Disturbance Attenuation with Multi-Sensing Servo Systems For High Density Storage Devices

Chee Khiang Pang

Disturbance Attenuation with Multi-Sensing Servo Systems For High Density Storage Devices

Chee Khiang Pang

M. Eng., B. Eng. (Hons.), NUS

Acknowledgments

First of all, I am grateful to my thesis advisors Prof. Ben M. Chen, Prof. Tong Heng Lee and Dr. Guoxiao Guo for giving me sound advice on control theory and offering me their valuable research directions. They have been great advisors and teachers and I thank them for their motivation and patience in grooming me into an independent researcher. Sometimes in life, it is not the length of contact but depth of communication that counts. I am still amazed by their technical expertise and will continue to learn from them whenever possible.

I wish to thank Prof. Frank L. Lewis of Automation and Robotics Research Institute, The University of Texas at Arlington. I'm truly amazed by his diligence and passion for research. I would also like to thank Dr. Masahito Kobayashi of Central Research Laboratory, Hitachi Ltd., for teaching me the many issues and problems in servo engineering for HDD industries. I would also like to take this opportunity to thank Dr. Zhao Yang Dong of School of Information Technology and Electrical Engineering, University of Queensland. He is a fantastic teacher and friend, and I sincerely appreciate his care and concern of my plight. I wish him all the best and am sure that we will have opportunity to work together again.

I am grateful to Ms. Wai Ee Wong for accompanying me to lunch and tea breaks. She has been a great friend and listener when my wife is abroad. I also wish to thank all the staffs and students of Mechatronics and Recording Channel Division, A*STAR Data Storage Institute and Central Research Laboratory, Hitachi Ltd., who had helped me in one way or another.

I have to thank my sisters Ms. Chia-Li Pang and Ms. Chia Mei Pang for

and indulge in unfettered reverie. To enjoy everyday as if it is the last, and be surrounded by truthful and faithful friends wherever I go.

I quote:

"To laugh often and much;

To win the respect of intelligent people and the affection of children;

To earn the appreciation of honest critics and endure the betrayal of false friends;

To appreciate beauty, to find the best in others;

To leave the world a bit better, whether by a healthy child, a garden patch or a redeemed social condition;

To know even one life has breathed easier because you have lived.

This is to have succeeded."∼ Ralph Waldo Emerson (1803–1882).

I will make it.

Summary

Track densities in magnetic recording demonstrations are projected to exceed 500,000 TPI (Tracks-Per-Inch) in the year 2007 and are still increasing. As such, data storage industries are also looking into probe-based storage systems actuated by MEMS (Micro-Electrical-Mechanical-Systems) for high density nanometer scale recording due to the superparamagnetic limitation in magnetic recording physics. This dissertation proposes novel control topologies and incorporates multi- and self-sensing solutions for stronger disturbance rejection capabilities with specific applications to with piezoelectric- and MEMS-actuated servo systems.

After a brief introduction of technological advances in magnetic storage and proposed solutions, system identification of mechanical actuators used in magnetic and probe-based storage systems will be detailed. Constraints and properties of future mobile high density data storage systems are also discussed.

Next, an OICA (Online Iterative Control Algorithm) using an RRO (Repeatable Run-Out) estimator and measured PES (Position Error Signal) tuned by minimizing the square of the $\mathcal{H}_2$-norm of the transfer function from NRRO (Non-RRO) to true PES is proposed for stronger NRRO rejection. The gradient estimates for parametric updates in the proposed OICA are independent of the dominant input and output disturbances in the measured PES spectra. To suppress input and output disturbances simultaneously, an add-on DDO (Disturbance Decoupling Observer) and DDOS (DO with extraneous Sensor) for stronger disturbance suppression are proposed, integrating theoretical developments from DDP (DD Problems), SPT (Singular Perturbation Theory) and practical DOs in sampled-data systems.

Extending the SPT to a LTI (Linear Time Invariant) mechanical system with rigid and flexible body modes, the VCM's (Voice Coil Motor) and induced PZT active suspension's dynamics are decomposed into fast and slow subsystems to tackle more DOFs (Degrees-Of-Freedom) via inner loop high frequency vibration suppression, using the piezoelectric elements in the suspension as a fast sensor and observer in a single stage HDD.

As SP control requires fast subsystem dynamics estimation, multi- and self-sensing servo systems for PZT- and MEMS-actuated devices will be introduced next. A novel nanoposition sensing scheme is proposed for dual-stage HDDs to incorporate cheap collocated sensors while retaining high SNR (Signal-to-Noise Ratio). The PZT microactuator is employed as a sensor and actuator simultaneously using SSA (Self-Sensing Actuation) and is used for AMD (Active Mode Damping) of the microactuator suspension's torsion modes and sway modes as well as decoupling the dual-stage loop for individual loop control and sensitivity optimization. The nanometer position sensing resolution with SSA is extended to CSSA (Capacitive SSA) scheme for the MEMS X-Y stage with 6 mm $\times$ 6 mm recording media platform actuated by capacitive comb drives and fabricated in DSI (Data Storage Institute) for probe-based storage systems. A robust decoupling control methodology for the MEMS micro X-Y stage is also proposed.

This dissertation presents sampled-data servo system designs to fulfill storage demands in data storage technologies which require robustness of control algorithms coupled with strong disturbance rejection capabilities for future mobile storage devices. Specific considerations on sensor fusion issues are made to improve track-following performance of mechanical actuators in magnetic and probe-based data storage systems.

Nomenclature

A/D	Analog-to-Digital
AFC	Anti-Ferromagnetically Coupled
AFM	Atomic Force Microscopy
AMD	Active Mode Damping
ARE	Algebraic Riccati Equation
BPI	Bits-Per-Inch
CMS	Coupled Master-Slave
CMOS	Complementary Metal Oxide Semiconductor
CSSA	Capacitive Self-Sensing Actuation
D/A	Digital-to-Analog
DDO	Disturbance Decoupling Observer
DDOS	Disturbance Decoupling Observer with extraneous Sensor
DDP	Disturbance Decoupling Problems
DIDO	Dual-Input-Dual-Output
DISO	Dual-Input-Single-Output
DMS	Decoupled Master-Slave
DOF	Degree-Of-Freedom
DRAM	Dynamic Random Access Memory
DSA	Dynamic Signal Analyser

DSI   Data Storage Institute

DSP   Digital Signal Processor

EMF   Electro-Motive Force

FEM   Finite Element Modelling

FIR   Finite Impulse Response

Gb   Gigabyte

HDD   Hard Disk Drive

HGST   Hitachi Global Storage Technologies

IBM   International Business Machines

IMP   Internal Model Principle

I/O   Input/Output

IVC   Initial Value Compensation

LDV   Laser Doppler Vibrometer

LMI   Linear Matrix Inequality

LPF   Low Pass Filter

LQG   Linear Quadratic Gaussian

LTI   Linear Time Invariant

Mb   Megabyte

MEMS   Micro-Mechanical-Electrical-Systems

MIMO   Multi-Input-Multi-Output

NMP   Non-Minimum Phase

NPM   Near-Perfect Modelling

NRRO   Non-Repeatable Run-Out

OICA   Online Iterative Control Algorithm

PES   Position Error Signal

PI   Proportional-Integral

PID   Proportional-Integral-Derivative

PMMA	PolyMethylMethAcrylate
PPF	Positive Position Feedback
PTOS	Proximate Time Optimal Servomechanism
PTP	Point-To-Point
PVDF	PolyVinylDeneFlouride
PZT	Pb-Zr-Ti (Lead-Zirconate-Titanate)
rpm	revolutions-per-minute
RRO	Repeatable Run-Out
R/W/E	Read/Write/Erase
SD	Sensitivity Disc
SEM	Scanning Electron Microscopy
SISO	Single-Input-Single-Output
SNR	Signal-to-Noise Ratio
SPM	Scanning Probe Microscopy
SPT	Singular Perturbation Theory
SRAM	Static Random Access Memory
SRF	Strain Rate Feedback
SSA	Self-Sensing Actuation
SSA-DMS	Self-Sensing Actuation Decoupled Master-Slave
SSTW	Self-Servo Track Writing
STW	Servo Track Writing
Tb	Terabyte
TMR	Track Mis-Registration
TPI	Tracks-Per-Inch
VCM	Voice Coil Motor
ZOH	Zero Order Hold

Contents

List of Figures

List of Tables

Chapter 1

Introduction

With the vast amount of information we carry with us ranging from MP3s (audio files encoded with algorithms devised by Moving Picture Experts Group using audio layer 3) to digital images *etc.* on the move everyday, data storage companies are constantly motivated to be innovative in proposing novel storage solutions to the world. Today, the humongous capacity and high transfer rate commodities offered ranging from conventional magnetic HDDs (Hard-Disk Drives) to SRAM (Static Random Access Memory), DRAM (Dynamic RAM), and Flash Memory *etc.* are becoming indispensable tools for many domestic and industrial electrical products. Typical applications include but are not limited to office and home usage (*e.g.* network servers and refrigerators *etc.*), to portable devices (*e.g.* mobile phones and digital cameras *etc.*).

1.1 Technological Advances in Data Storage

Although data storage industries are constantly researching on alternative storage solutions, HDDs remain as a cheap and important source of non-volatile storage. From the first huge magnetic drives manufactured by IBM's (International Business Machines) 'remote' research laboratory in San Jose [1] in 1956 to the small form factor drives produced by various HDD industries today, HDDs have come a long way and definitely caused a dramatic advancement in computer technologies. The history and progress of the HDD industry from HGST (Hitachi Global Storage Technologies) is shown the HDD Roadmap in Figure 1.1. It can be seen that
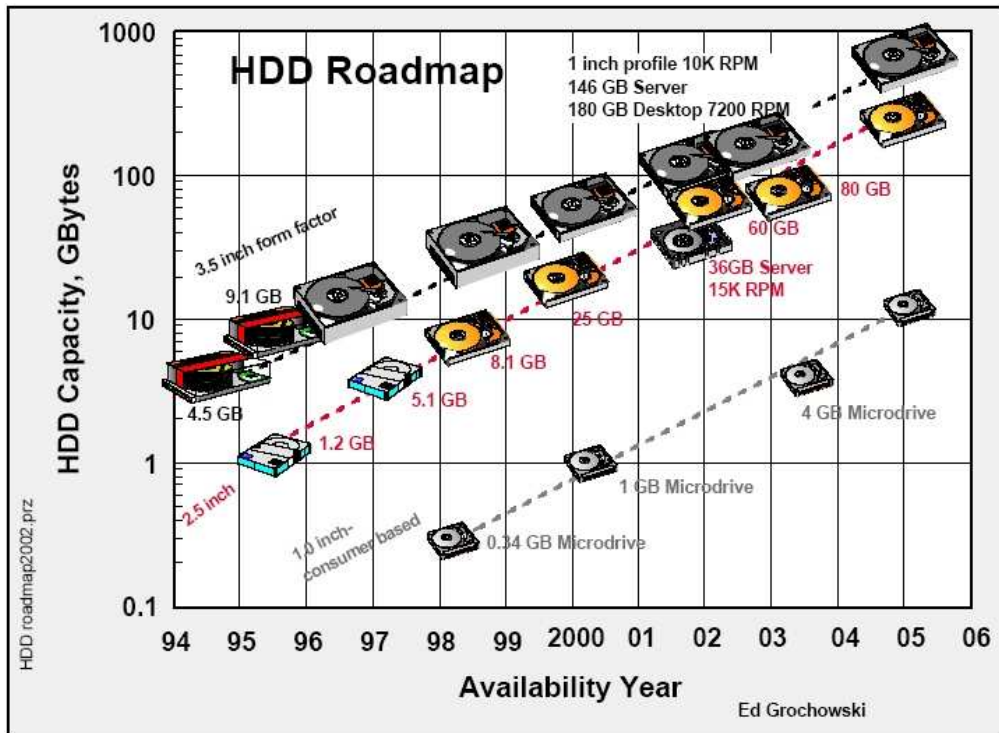
Figure 1.1: HDD roadmap showing exponential increase in data storage capacity vs time [31].

strong research efforts have been instilled to keep up with the exponential trend of increasing data storage capacities with HDDs of the same form factor. HDD

2

manufacturers are also making HDDs with higher rotation speed (to reduce access time) and smaller form factors (for usage in mobile electronic devices).

On the contrary, the price consumers have to pay for magnetic data storage in HDDs is decreasing at an exponential rate as can be seen in Figure 1.2 [31]. In the
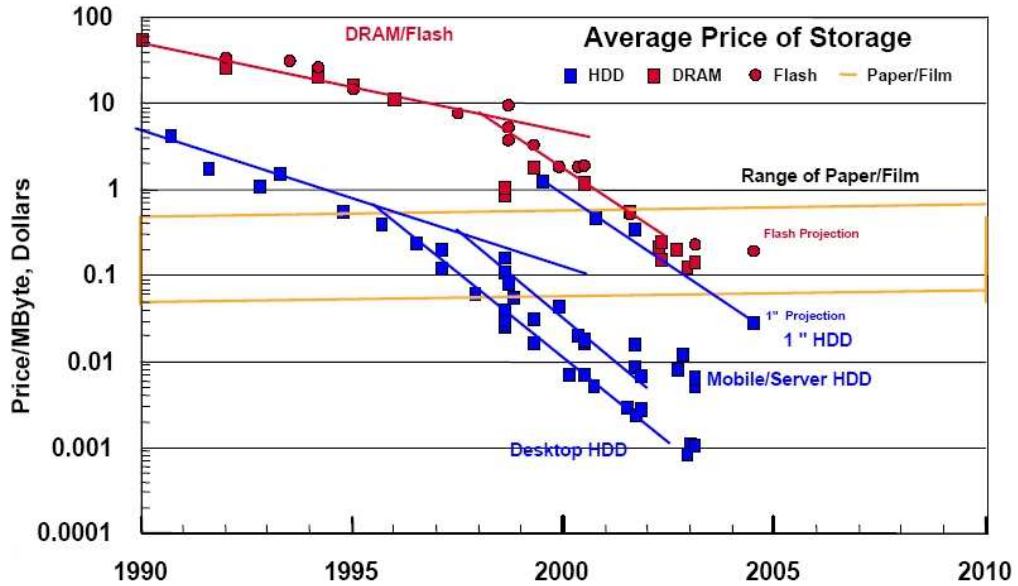
Figure 1.2: Average price per megabyte of storage in US$ vs time [31].

last decade, other rising and competing data storage technologies (*e.g.* DRAM and Flash Memory *etc.*) have compelled industries to reduce the selling price of their HDDs to retain their competitive edge. While HDDs still remain as the cheapest form of data storage in the short run, these up and coming novel technologies threaten the very existence of HDDs in the consumer data storage market.

In the 21st century, the nanometer (nm) will play a revolutionary role similar to the one played by the micrometer (μm) in the 20th century. The nanometer scale will presumably pervade the field of data storage. Future storage systems will be concentrated on portable devices which require ultra high data capacities, ultra high data transfer rates, coupled with strong disturbance rejection capabil-

3

ities. This translates into actuators in HDDs or other proposed storage systems to perform R/W/E (Read/Write/Erase) of nanometer sized data bits which are of nanometer proximity with one another.

Currently, we are already entering the magnetic storage restriction zone fuzzified by the superparamagnetic effect—a magnetic recording physics constraint which limits the size of magnetic domains to ensure data integrity when subjected to thermal fluctuations, as can be seen from the advanced storage roadmap in areal density shown in Figure 1.3. As such, strong research efforts are aimed at exploring
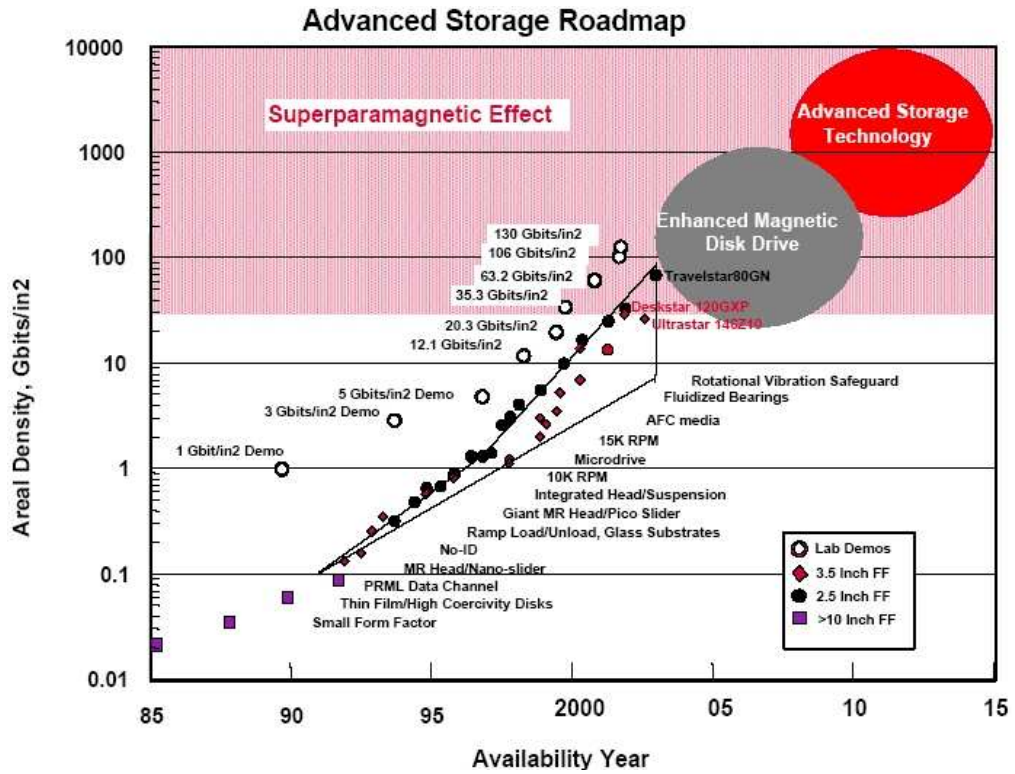
Figure 1.3: Advanced storage roadmap in areal density (GB/in^2) vs time [31].

various means to meet these challenges for magnetic recording technologies. In the short run, future storage devices will still be relying on incremental improvements of current magnetism-based storage systems in the enhanced magnetic disk drive zone as shown in Figure 1.3 [31]. Proposed solutions by far include improvements

in recording media *e.g.* AFC (Anti-Ferromagnetically Coupled) media, patterned media, perpendicular recording technologies and dual-stage HDDs. Dual-stage HDDs—by appending a secondary milli or microactuator onto the primary actuator VCM (Voice Coil Motor)—is seen by many as the solution for next generation of HDDs in the short run.

Besides firefighting with incremental improvements on current HDDs, several roadmap driven research ideas have been proposed to overcome the superparamagnetic limit as depicted in the advanced storage technology zone shown in Figure 1.3. One such proposal lies in probe-based storage devices which use thermomechanical properties of semiconductor cantilever tips actuated by MEMS (Micro-Mechanical-Electrical-Systems) devices to perform R/W/E of data bits (indentations) on a polymer media. The prototype was successfully demonstrated by IBM in the renowned "Millipede" project [21]. In the longer run, probe-based storage devices will be introduced into the consumer market, starting steadily from data storage for portable devices to other possible forms of tera bit density data storage devices [100]. In view of these trends, this dissertation concentrates on development of control methodologies with multi- or self-sensing capabilities for stronger disturbance rejection envisioned for use in future storage devices with specific applications to piezoelectric and MEMS-based actuators.

1.2   Magnetic Hard Disk Drives

An HDD is a high precision and compact mechatronics device. A typical commercial HDD consists of a disk pack, actuation mechanisms and a set of R/W heads, as shown in Figure 1.4. The major components in a typical HDD include:
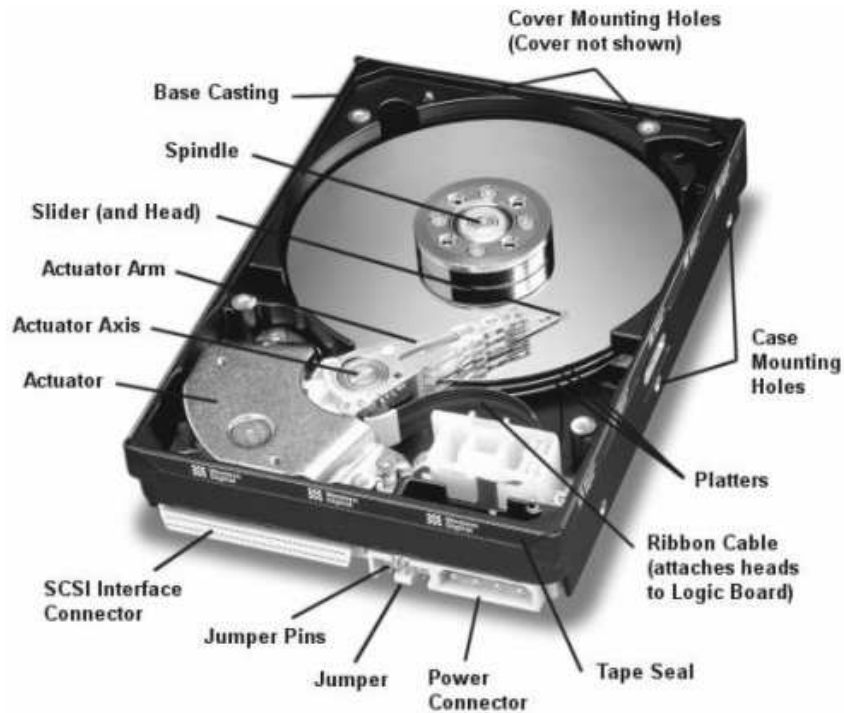
Figure 1.4: Inside a typical commercial HDD.

1. actuator arm driven by the VCM,

2. disks which contain data and servo address information,

3. head-suspension assembly to perform R/W actions on the disks,

4. actuator assembly which contains the VCM to drive the R/W head,

5. spindle motor assembly to make the disks rotate at a constant speed,

6. electronics card to serve as the interface to host computer, and

7. device enclosure which usually contains the base plate and cover to provide support to the spindle, actuator, and electronics card *etc.*

The disks are inserted into the spindle shaft (separated by spacers) and are rotated by the spindle motor. The R/W heads are mounted at the tip of the actuators

protected by the sliders. Due to the amount of air-flow generated by the high speed disk rotation, a very thin air bearing film is generated and hence the head-slider can float on the lubricant of the disks instead of being in contact with them.

In a typical operation, the HDD electronic circuits receive control commands from the host computer and the control signals are processed in the on-board DSP (Digital Signal Processor). The actuator on receiving the control signal will then move and locate the R/W heads to the target locations on the disks for the R/W process to take place. During this process the PES (Position Error Signal) and the track numbers are read from the disk for feedback control.

User data is recorded as magnetic domains on the disks coated with magnetic substrates in concentric circles called tracks. Typical HDD servo system consists of two types, namely the dedicated servo and embedded servo (or sector servo). The dedicated servo uses all the tracks on one disk surface of a disk pack to store servo information and is used in older generations HDDs. Currently, most HDDs employ the embedded servo method which divide the track into both storage of user data and servo information as most current HDDs have less disk platters. Furthermore, the non-collocated sensing and control in dedicated servo method introduces unacceptable manufacturing cost and noise in the HDD servo control loop. Using embedded servo, the encoded position in servo sectors can be demodulated into a track number as well as PES, which indicates the relative displacement of the head from the center of the nearest track. Interested readers are referred to [104] for in-depth discussions on different servo patterns as well as PES encoding and demodulation schemes.

1.3   Probe-Based Storage Systems

Fundamentally, probe-based storage systems are based on the SPM (Scanning Probe Microscopy) and AFM (Atomic Force Microscopy) technologies developed for characterizing the surface properties in small dedicated regions with ultra high resolution. Slight modifications at the tip in the SPM system allows the surface property of the medium to be changed in nanometer scale. With the bits corresponding directly to the size of the tip, probe-based storage systems have striking advantages in terms of areal density. A picture of a probe-based storage system successfully demonstrated by IBM is shown in Figure 1.5 below. The major com-
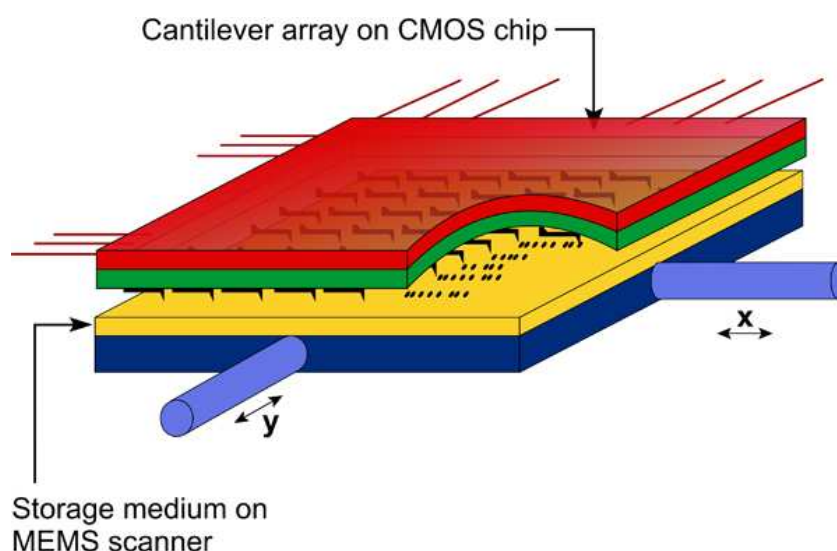
Figure 1.5: Illustration of a probe-based storage system [21].

ponents in a typical probe-based storage system include:

1. probes (consisting of a sharp tip on a cantilever),

2. polymer storage medium,

3. MEMS micro X-Y stage or MEMS scanner platform, and

4. control, signal processing and sensor electronics *etc.*

The nanometer wide tips of the probes perform the R/W/E operations by altering the surface physics of the polymer storage medium via either (i) thermal [21] (ii) electric [98] or even (iii) magnetic [9] properties on a small dedicated region. An ideal cantilever probe tip should be light (low inertia for fast R/W/E operations), yet stiff (high resonant frequencies with little parametric uncertainties) with surface scanning capabilities. While the in-plane sway mode is a bigger issue in actuators for HDDs where data is written in near concentric circles on the magnetic disks' surfaces with storage densities proportional to the number of these circles or tracks, the out-of-plane bending mode of the cantilever probes in probe-based storage systems is obviously more problematic as R/W/E operations of data are executed into the polymer medium, which affects the achievable bit and track pitch subsequently.

The polymer storage medium is bistable and bonded on the micro X-Y stage or scanner platform during fabrication. The interference between adjacent bits must be kept to a minimal with high retention of the states after R/W/E operations to safeguard the reliability and integrity of the written-in user data. For batch fabrication, small form factor and low cost, it is desirable for the micro X-Y stage to be fabricated using lithography processes. The micro X-Y stage with MEMS capacitive comb driven microactuators should move the recording platform with a fast response while maintaining small mechanical crosstalk (axial coupling).

Similar to HDDs, the control electronics consists of a DSP for signal processing (PES demodulation, read channel encoding/decoding and multiplexing/demultiplexing *etc.*) and control signal computations. Various controllers can take charge of I/O (Input/Output) scheduling, data distribution and reconstruction, host in-

terface and failure management. A DSP works as the "brain" of the probe-based storage system to receive, process and output control signals in a typical operation. On receiving reference commands, the micro X-Y stage is actuated to the desired locations with the help of thermal [21] or capacitive sensors. The probes will then rely on written in PES on dedicated servo fields for R/W/E operations to take place in an array operation. The simultaneous parallel operations of large number of probes boost the data access speed tremendously.

1.4 Modes of Operations

From the above, it can be seen there exist many inherent similarities between the two types of storage systems. Either HDD or probe-based storage systems, there are fundamentally three modes of operation for the data storage servo systems in general. The first mode is the track-seeking mode *i.e.* to move the R/W head (in HDDs) or tips (in probe-based storage systems) from the initial track to the target track within the shortest possible time. Using the track number, the servo controller can locate the R/W head to the desired track during track-seeking. The servo controllers for track-seeking operations are usually designed for time optimal criterion in a PTP (Point-To-Point) context. A good example of such methodologies is the PTOS (Proximate Time Optimal Servomechanism) employed in current HDDs and interested readers are kindly referred to works by Franklin *et al.* in [23].

Next, it is the track-settling mode. This process occurs once the actuator is less than one track pitch away from the target track. Due to the initial conditions of the actuators, the R/W head will be oscillating about the target track during the transient period. The track-settling controller should hence guide the R/W

head to be within a certain variance and tolerance with the center of the target track. The servo controller for track-settling operations are usually designed for compensating the actuators' initial states in an IVC (Initial Value Compensation) framework [129].

Finally, the head is maintained on the designated track with minimum error during the track-following mode. The same error signal PES is used to maintain the head on the track during track following. In this mode, the main objective of the track following controller is to stay as close to the center of the track as possible for the R/W/E operation to take place, in spite of the presence of external disturbances and measurement noise which in essence is PES variance control. The track-following process has to effectively reduce TMR (Track Mis-Registration), which is used to measure the offset between the actual head position and the track center. During track-following, TMR can also be defined as the 3σ value of PES. The three modes of operations are shown below in Figure 1.6.

Improving positioning accuracy during track-following control mode is essential in order to achieve a high recording density. As TPI continues to increase with decreasing track width at higher rotational speeds, external disturbances affecting the future storage servo system become significant in achieving higher TPI. This dissertation is concerned with the servo control aspects during track-following operations in HDDs and probe-based storage servo systems.

1.5 Motivation of Dissertation

Currently, it is reported that the track density would exceed 150,000 TPI [131] and the disk spin speed surpass 15000 rpm (revolutions-per-minute) in the year 2010.
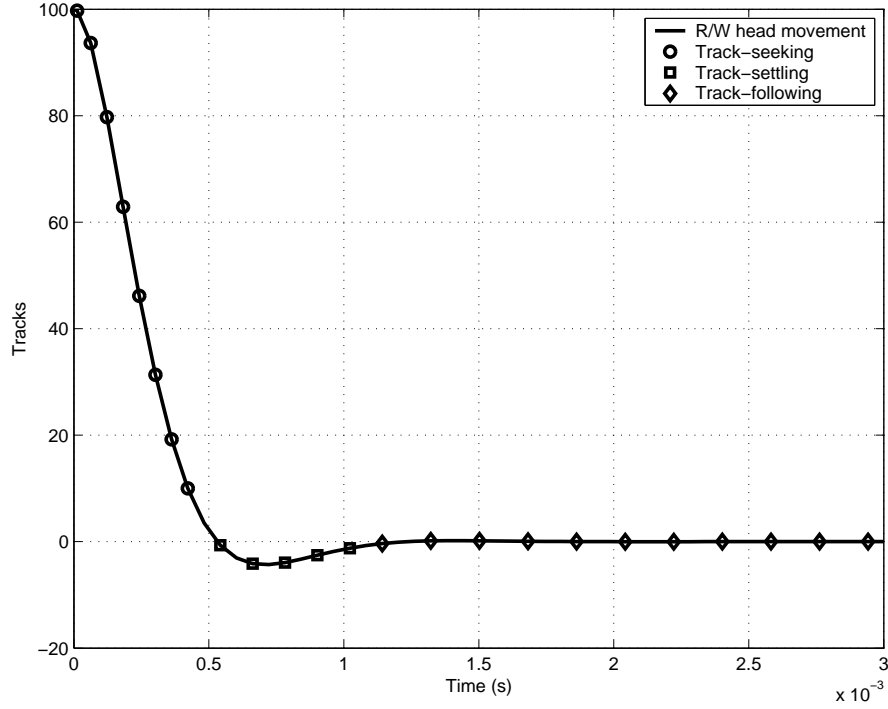
Figure 1.6: Typical R/W head position profile during track-seeking, settling and following control in a 100 track seek.

As the global demand for higher computational power increases, there is a corresponding need for better data storage devices to meet the demands of today's information explosion era. With the ever decreasing price per gigabyte in data storage devices, industries are also striving for mobile storage devices with smaller form factors to keep up with the trend of increasing track densities. It was also reported that ultra-high storage densities of up to 1 Tb/in ^{2} have been achieved on a very small form factor in the "Millipede" [21]. Future storage devices will have to be physically smaller, coupled with ultra high density and ultra fast data access rates. The trend of using piezoelectric and MEMS-based microactuators coupled with multi- or self-sensing schemes for higher bandwidth and stronger disturbance rejection capabilities are inevitable in future data storage servo systems.

Such ultra-high positioning accuracy translates directly into making the sen-

sitivity transfer function matrix have a small singular value to reduce or even suppress any amplification of the disturbances at high frequencies, where feedback is degrading the servo performance. Alternatively, reduction of $\mathcal{H}_2$- and $\mathcal{H}_\infty$-norms from disturbance sources to controlled output are also feasible candidate performance measures, the latter being commonly known as DDPs (Disturbance Decoupling Problems). Hence controller designs for future storage systems must ensure a low sensitivity servo system by loop shaping of sensitivity transfer matrix or minimizing $\mathcal{H}_2$- or $\mathcal{H}_\infty$-norms. Robust active vibration control algorithms are also essential to safeguard against variations of natural frequencies and damping ratios shifts in the piezoelectric or MEMS-based actuators mass produced by the data storage industries per day.

It is well known from control theory that the lowest sensitivity achievable by any control system is via state feedback, which is infeasible as measured PES is still the only available signal for feedback control, even when there are now more than one actuator (in dual-stage HDDs) or one degree of freedom (in probed-based storage systems). As such, placement of extra sensors ensure more states can be measured which alleviates controllers' orders. With SSA (Self-Sensing Actuation— using the actuator as a sensor simultaneously), cheap and non-intrusive collocated sensors with nanometer resolution can be incorporated. Together with PES, this newly acquired information in the novel data storage platforms will be used for servo control to enable high bandwidth and low sensitivity sampled-data systems.

1.6   Contributions and Organization

This dissertation concentrates on the study and development of high SNR (Signal-to-Noise Ratio) multi- or self-sensing servo systems using the electrical properties

of the piezoelectric and MEMS-based actuators in future storage devices. We will then focus on designing digital servo controllers to reduce the positive area in the sensitivity transfer function or $\mathcal{H}_2$- and $\mathcal{H}_\infty$-norms with and without the extraneous sensor information for enhanced disturbance rejection.

The original contributions of this dissertation are as follow:

1. Formulates an OICA (Online Iterative Control Algorithm) with and without extraneous sensor to reduce the square of $\mathcal{H}_2$-norm from disturbance sources to true PES for extra NRRO (Non-Repeatable Run-Out) rejection. Gradient estimates are obtained without prior knowledge of the dominant spectra of input and output disturbances in measured PES.

2. Designs an add-on DDO (Disturbance Decoupling Observer) and DDOS (DDO with extraneous Sensor) for enhanced disturbance suppression. Proposed DDO can achieve strong rejection of the dominant input and output disturbances simultaneously, with possible noise attenuation using the DDOS.

3. Applies the SPT (Singular Perturbation Theory) [56][57][62] and uses the PZT active suspension as fast sensor and observer for fast subsystem's dynamics estimation in a single stage HDD. The two time scale framework increases control effectiveness to control more DOF (Degrees-Of-Freedom) in flexible actuators.

4. Uses the PZT microactuator as a sensor and actuator simultaneously to actively damp its torsional and sway modes as well as achieving decoupling sensitivity in dual-stage HDDs. The cheap and nanometer resolution sensing capabilities improve robustness and decreases TMR.

5. Designs a high SNR CSSA (Capacitive Self-Sensing Actuation) scheme for MEMS devices actuated by capacitive comb drives. A robust decoupling control methodology of the designed micro X-Y stage is verified with simulation results.

The rest of the dissertation is organized as follow:

- Chapter 2 identifies the mathematical models of mechanical actuators used in HDDs and probe-based storage systems. The constraints and properties of these future storage sampled-data servo systems are also discussed.

- Chapter 3 explores the use of OICA and RRO estimator (with and without extraneous sensors) to optimize controller for extra NRRO rejection in a PZT actuated spinstand servo system.

- Chapter 4 details the use of add-on DDOs (Disturbance Decoupling Observers) with and without extraneous sensors to achieve disturbance decoupling effects and its application to a PZT actuated passive suspension for a spinstand servo system.

- Chapter 5 extends the SPT for a general LTI (Linear Time Invariant) mechanical system for vibration rejection in single stage HDDs using the PZT active suspension as a fast observer.

- Chapter 6 illustrates controller design examples for MIMO (Multi-Input-Multi-Output) systems in dual-stage HDDs as well as MEMS micro X-Y stage and proposes SSA with discussion on multi-sensing issues for enhanced disturbance rejection.

- Chapter 7 shows how the PZT microactuator can be employed as a sensor and actuator simultaneously for AMD (Active Mode Damping) to achieve a

low and decoupled sensitivity in dual-stage HDD servo systems.

- Chapter 8 designs a CSSA and robust decoupling controller for a designed micro X-Y stage actuated by MEMS in a proposed probe-based storage system.

- Chapter 9 summarizes the findings and results of this dissertation and presents some possible future research directions.

Chapter 2

High Density Data Storage Systems

In recent years, piezoelectric and MEMS actuators have attracted much attention and are envisaged by many researchers as actuators' solutions for future mobile data storage servo systems. This chapter covers the system identification of mechanical actuators used in dual-stage HDDs as well as MEMS probe-based storage systems. Constraints and properties of future storage sampled-data systems are also detailed with insights from theoretical analysis.

2.1 System Identification of Mechanical Actuators

Currently, the mechanical actuators used in high density data storage systems include the (i) VCM (Voice Coil Motor) in single-stage HDDs, (ii) piezoelectric actuators in spinstand servo system [120] or appended onto the VCM in suspension-

17

driven dual-stage HDDs [22], and (iii) MEMS-based actuators in slider-driven [40] or head-driven dual-stage HDDs [27] and also proposed probe-based storage systems [21]. In this section, system identification of these three types of mechanical actuators will be carried out and detailed.

2.1.1 VCM

In the conventional single stage actuation found in current HDDs, the VCM is the only actuator with the R/W head mounted on the tip of the suspension. Other components include a pivot (for rotary actuator), ball bearings, the arms commonly known as the "E" block, a flex cable, and suspensions to carry the sliders at their tips. The VCM is harnessed in between two very strong permanent magnets commonly called the yoke. When current is passed into the coil of the VCM, force and hence displacement is transduced to move the R/W heads. A picture of a VCM consisting of the above components is shown below in Figure 2.1.

Figure 2.1: A picture of a typical VCM.

By exciting the VCM at frequencies of interests, the displacement of the VCM

is measured by the LDV (Laser Doppler Vibrometer) non-intrusively. Swept sine excitation from the DSA (Dynamic Signal Analyzer) is introduced into the power amplifier and the frequency response of the VCM is captured and identified in MATLAB. A typical frequency response captured is plotted and shown in Figure 2.2.
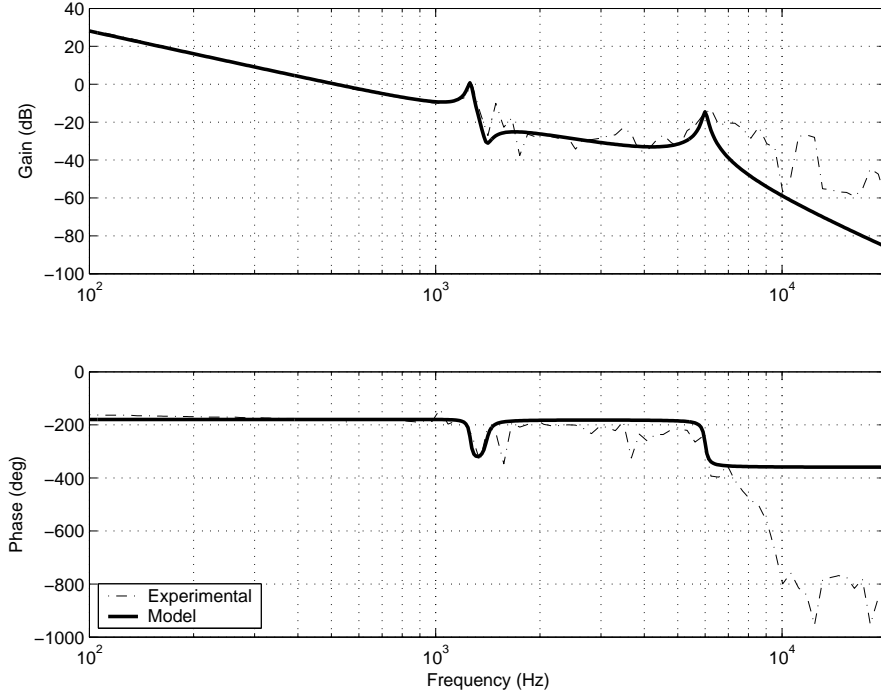
Figure 2.2: Frequency response of a VCM.

With prior knowledge from physical modelling and system identification [67], it can be shown that the VCM can be modelled as a double integrator with some flexible resonant poles and anti-resonant zeros. The overall transfer function of a VCM, $G_V(s)$, in s-domain can be expressed as

$$G_V(s) = \frac{K_V}{s^2} \prod_{i=1,j=1}^{m_V,n_V} \frac{s^2 + 2\zeta_{V,j}\,\omega_{V,j}s + \omega_{V,j}^2}{s^2 + 2\zeta_{V,i}\,\omega_{V,i}s + \omega_{V,i}^2} \qquad (2.1)$$

where m_V and n_V are the number of resonant poles and anti-resonant zeros, respectively. ζ_V and ω_V are the damping ratio and natural frequency of each mode,

19

respectively. K_V is the gain of the VCM.

For the VCM shown in Figure 2.2, the identified mathematical model $G_V(s)$ can be written as

$$
\begin{aligned}
G_V(s) & = \frac{1 \times 10^8}{s^2} \frac{s^2 + 2(0.05)(2\pi1.4 \times 10^3)s + (2\pi1.4 \times 10^3)^2}{s^2 + 2(0.03)(2\pi1.26 \times 10^3)s + (2\pi1.26 \times 10^3)^2} \cdots \\
& \times \frac{(2\pi6 \times 10^3)^2}{s^2 + 2(0.03)(2\pi6 \times 10^3)s + (2\pi6 \times 10^3)^2}
\end{aligned}
\tag{2.2}
$$

Minimum phase zeros are sometimes included to provide some phase lift. The mismatch in phase response is due to an unmodelled delay arising from the power amplifier and LDV measurement system, as well as unmodelled high frequency non-minimum phase zeros from the non-collocated actuator-sensor configuration in the VCM. However, this delay is omitted in (2.2) as the order of model $G_V(s)$ suffices in achieving control objectives to be discussed in future sections.

2.1.2 Piezoelectric Actuators

Piezoelectric actuators find applications in many micro-positioning applications, ranging from data storage to robot manipulators. In this section, system identification of a piezoelectric secondary actuator in a so-called dual-stage HDD is carried out.

Depending on the actuation mechanism, the secondary actuators can be categorized into (i) piezoelectric [107], (ii) electrostatic [27] and (iii) electromagnetic [55]. Alternatively, they can also be categorized according to their locations which include (i) suspension-based [22], (ii) slider-based [40] and (ii) head-based [27]. In this dissertation, a piezoelectric suspension-based secondary actuator is discussed. The piezoelectric element Lead-Zirconium-Titanate ceramic (Pb-Zr-Ti) is used usually. Hence, these actuators are also called PZT microactuators or

PZT active suspensions.

Piezoelectric ceramic material has high stiffness and generate large force by contraction and expansion. When actuated, the whole suspension length is moved and hence it yields a larger displacement range. PZT microactuators often employ the push-pull or shear design according to the direction of polarization of the piezoelectric materials. A picture of a push-pull PZT microactuator is shown in Figure 2.3 [80].
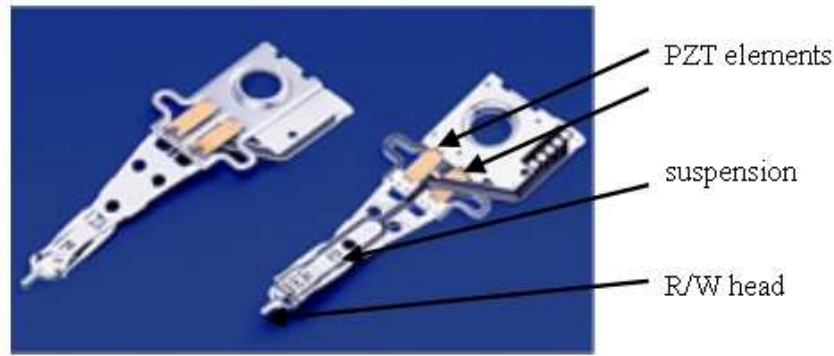
Figure 2.3: A picture of PZT microactuator [80].

A two strip setup of PZT active suspension is shown in Figure 2.3. Two small parallel strips of PZT elements can be found at the base of the suspension. When a voltage is applied to these elements, one PZT strip expands while the other contracts to deflect the entire suspension. Usually, the suspension-based microactuator designs can yield a stroke of about 1 μm with the first resonant mode in the range of 5–15 kHz. Ideally, the suspension should be stiff (high damping for less resonant modes and parametric uncertainties) yet light (for achieving high servo bandwidth and faster disturbance rejection via error correction) simultaneously. However, a light suspension makes it susceptible to effects of windage blowing across the entire actuation arm.

Using the same methodology as described previously in Section 2.1.1, the displacement of the PZT microactuator is measured by the LDV. Swept sine excitation from the DSA is introduced into the power amplifier and the frequency response of the secondary actuator is captured and identified in MATLAB. The frequency response of the PZT microactuator shown above in Figure 2.3 is captured and plotted in Figure 2.4.
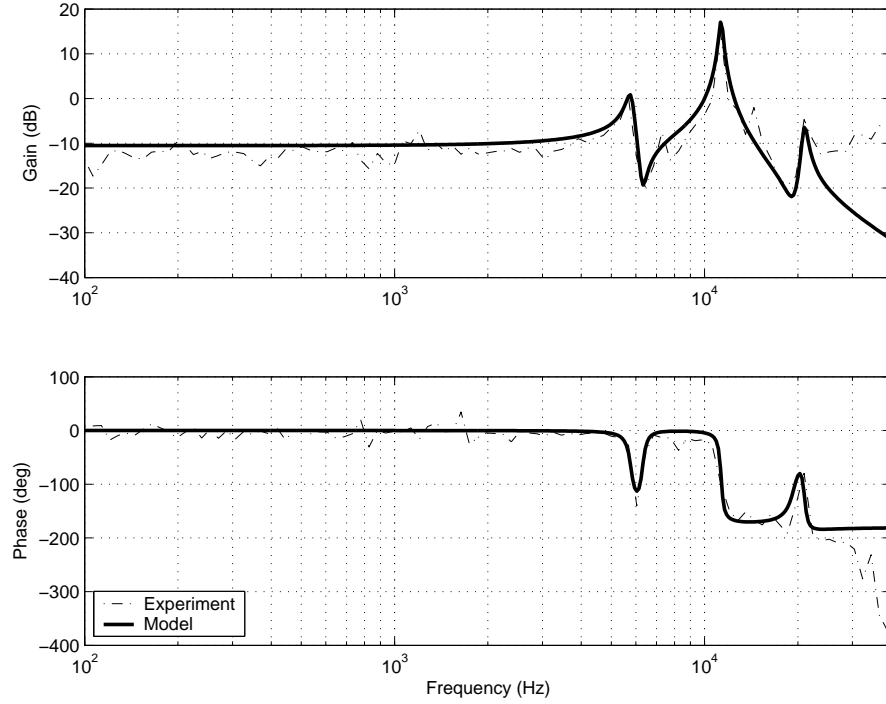
Figure 2.4: Frequency response of PZT microactuator.

It can be seen that the PZT microactuator can be modelled as a pure gain in a large range of frequencies coupled with high frequency resonant modes and anti-resonant zeros pairs. The overall transfer function of the PZT microactuator, $G_M(s)$, in s-domain can be expressed as

$$G_M(s) = K_M \prod_{i=1,j=1}^{m_M,n_M} \frac{s^2 + 2\zeta_{M,j}\,\omega_{M,j}s + \omega_{M,j}^2}{s^2 + 2\zeta_{M,i}\omega_{M,i}s + \omega_{M,i}^2} \tag{2.3}$$

where m_M and n_M are the number of resonant poles and anti-resonant zeros,

respectively, ζ_M and ω_M are the damping ratio and natural frequency of each mode, respectively, and K_M is the DC gain of the PZT microactuator.

The transfer function of the identified mathematical model can be written as $G_M(s)$ where

$$
\begin{aligned}
G_M(s) \;=\; & \frac{1.24 \times 10^9}{s^2 + 2(0.02)2\pi 21 \times 10^3 + (2\pi 21 \times 10^3)^2} \cdots \\
& \times \frac{s^2 + 2(0.025)2\pi 6.3 \times 10^3 + (2\pi 6.3 \times 10^3)^2}{s^2 + 2(0.03)2\pi 5.8 \times 10^3 + (2\pi 5.8 \times 10^3)^2} \cdots \\
& \times \frac{s^2 + 2(0.05)2\pi 19.5 \times 10^3 + (2\pi 19.5 \times 10^3)^2}{s^2 + 2\pi(0.015)2\pi 11.3 \times 10^3 + (2\pi 11.3 \times 10^3)^2}
\end{aligned}
\tag{2.4}
$$

It can be seen that the pole-zero pairs are all of minimum phase. It is worth noting that the PZT-actuated passive suspension used in a spinstand servo system [120] have a similar mathematical model, *i.e.* a pure gain low frequency behaviour coupled with high frequency resonant poles and anti-resonant zeros.

2.1.3 MEMS-based Actuators

MEMS-based actuators can be fabricated from standard process including wet bulk etching, wafer bonding, surface micromachining, deep trench silicon micromachining *etc.* similar to CMOS (Complementary Metal Oxide Semiconductor) processes. By aligning the actuators in a comb drive array, we can achieve nanometer positioning accuracy with the electrostatic attractive forces from the MEMS actuators. In this section, system identification of a fabricated MEMS micro X-Y stage is shown.

Many research institutes around the world are currently working on probe-based storage servo systems. While their approaches may differ, the main components used for high speed parallel R/W/E data are similar. Generally, a typical probe-based storage system consists of cantilever probe tips, a recording medium, a micro X-Y stage, and control electronics. In this dissertation, we present a pro-

posed probe-based storage servo system developed in A*STAR DSI (Data Storage Institute) an shown in Figure 2.5. For the rest of the dissertation, the MEMS
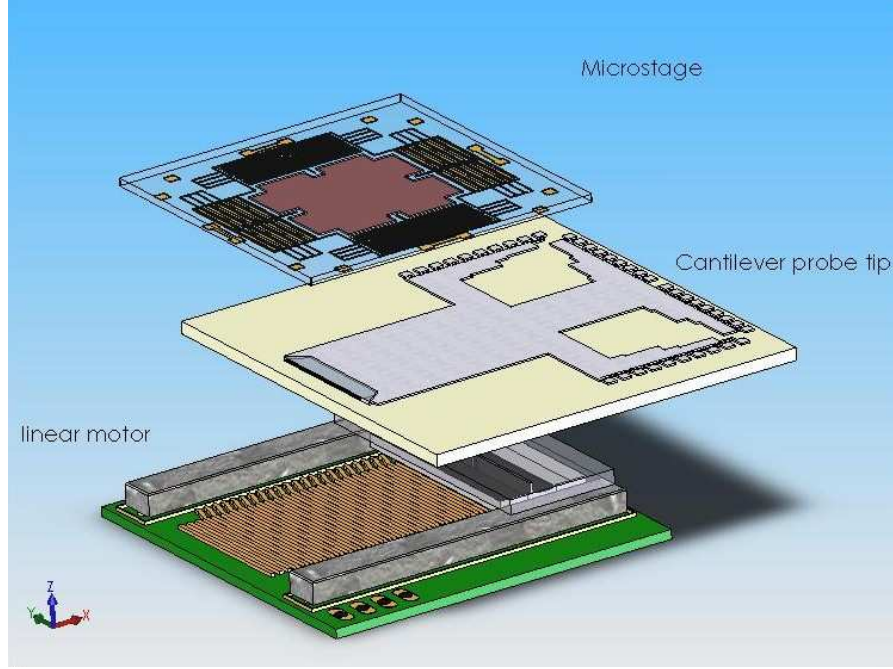
Figure 2.5: Components of proposed probe-based storage system "Nanodrive" developed in A*STAR DSI consisting of (i) cantilever probe tips (ii) linear motor and (iii) MEMS X-Y stage with recording medium.

micro X-Y stage in this platform will be used.

Using the data points of FEM (Finite Element Methods) from ANSYS, the identified mathematical model $G_{xx}(s)$ in the X-axis of the MEMS micro X-Y stage from the "Nanodrive" with first in-plane resonant frequency at 440 Hz is [70]

$$G_{xx}(s) = 20 \frac{(2\pi 400)^2}{s^2 + 2(0.0009)2\pi 400 s + (2\pi 400)^2} \tag{2.5}$$

The micro X-Y stage exhibits a small damping and out-of-phase characteristics at the resonant frequency and is perfectly symmetrical in actuator design. Due to the large gain at the resonant frequency the coupling effect between the main axes

cannot be ignored due the mechanical crosstalk during large span seeks. With the decoupling ratio between the main axes as 0.6%, the transfer functions of the MEMS micro X-Y stage in the Y-axis, $G_{yy}(s)$, as well as between the axes, $G_{xy}(s)$ and $G_{yx}(s)$, are

$$G_{yy}(s) = G_{xx}(s) \tag{2.6}$$

$$G_{xy}(s) = G_{yx}(s)$$

$$= 0.006G_{xx}(s) \tag{2.7}$$

As such, the transfer function of the MEMS micro X-Y stage in both axes is $G(s)$ with

$$G(s) = \begin{bmatrix} G_{xx}(s) & G_{xy}(s) \\ G_{yx}(s) & G_{yy}(s) \end{bmatrix}$$

$$= 20 \frac{(2\pi 400)^2}{s^2 + 2(0.0009)2\pi 400 s + (2\pi 400)^2} \begin{bmatrix} 1 & 0.006 \\ 0.006 & 1 \end{bmatrix} \tag{2.8}$$

and the frequency response the MEMS micro X-Y stage $G(s)$ is shown below in Figure 2.6. The dynamics of the micro stage in the Z-axis are unmodelled as the out-of-plane modes are uncontrollable.

It is worth noting that the MEMS-based actuators in slider-driven [40] or head-driven [27] dual-stage HDDs have a similar mathematical model, *i.e.* a second order transfer function with a main resonant mode of very small damping ratio (large amplitude) coupled with little high frequency uncertainties.
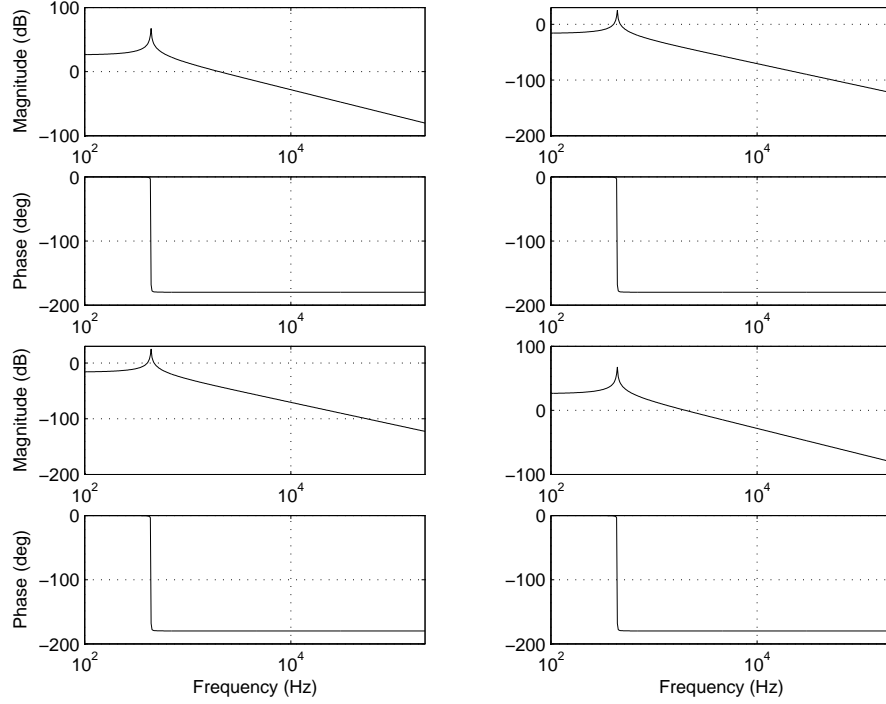
Figure 2.6: Frequency response of $G(s)$.

2.2 Constraints and Properties

By far, we see many inherent parallelism in data storage operations for HDDs and probe-based storage systems. Be it piezoelectric or MEMS-based, HDDs or probe-based storage systems, servo systems for future mobile storage devices harbour similar control limitations and identical properties. In this section, we will illustrate the constraints and properties of future storage devices using HDDs as an example for simplicity but without loss of generality.

Currently, HDDs use digital control with the help of fast DSPs. To enable better disturbance rejection and servo control, the sources of disturbances and noises should be modelled and known for this sampled-data system. Figure 2.7 shows the different sources of disturbances in the HDD servo control loop, which can be classified as the following:
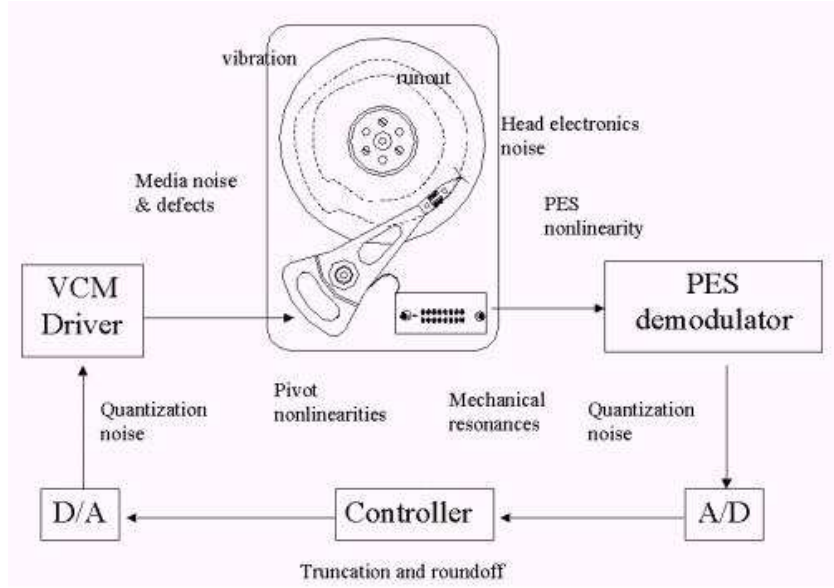
Figure 2.7: Sources of disturbance and noise in HDD servo control loop.

1. Input disturbance $d_i(s)$: Power amplifier noise, D/A (Digital-to-Analog) quantization error, pivot bearing friction, flexible cable torque, windage induced vibrations *etc.*;

2. Output disturbance $d_o(s)$: Suspension vibrations, disk fluttering and media defects *etc.*;

3. Noise $n(s)$: PES (Position Error Signal) demodulation noise and A/D (Analog-to-Digital) quantization error *etc.*

The measured PES is the error signal between the R/W head and the disk track center. The PES consists of two components: one component locked to spindle speed and phase known as the RRO (Repeatable Run-Out) and the other is the NRRO (Non-Repeatable Run-Out). RRO is synchronous to disk rotation and its harmonics with their main contributions coming from AC squeeze—sector to sector squeeze to adjacent tracks—and DC squeeze—mean distance between a large number of tracks—during the STW (Servo Track Writing) process where

27

servo tracks are pre-written on the disks in concentric circles. On the other hand, NRRO includes broad band white noise and some narrow band coloured noise with random phase and usually arises from spindle bearings and arm vibrations at frequencies outside the capabilities of the servo system.

1) Constraints: For simplicity but without loss of generality, consider a SISO (Single-Input-Single-Output) negative feedback control system with plant $G = \frac{N_G}{D_G}$ and controller $K = \frac{N_K}{D_K}$. N_G and N_K are the zero polynomials of G and K, respectively, while D_G and D_K are the pole polynomials of G and K, respectively. A future storage servo system during track-following control can be represented by the following block diagram in Figure 2.8.
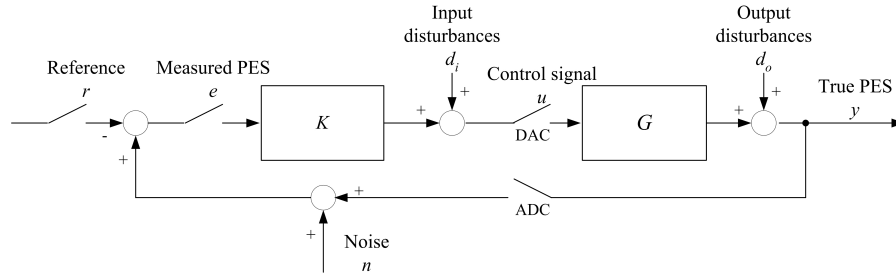
Figure 2.8: Block diagram of a typical future digital sampled-data storage system.

If the open loop transfer function L is given by $L = GK$, the following equation for true PES y with input disturbances d_i, output disturbances d_o and noise n can be obtained as

$$y = SG\,d_i + S\,d_o - T\,n \qquad (2.9)$$

with T and S as the complementary sensitivity transfer function and sensitivity

28

transfer function, respectively, defined by

$$T = \frac{L}{1+L} = \frac{\frac{N_G N_K}{D_G D_K}}{1 + \frac{N_G N_K}{D_G D_K}} = \frac{N_G N_K}{D_G D_K + N_G N_K} \tag{2.10}$$

$$S = \frac{1}{1+L} = \frac{1}{1 + \frac{N_G N_K}{D_G D_K}} = \frac{D_G D_K}{1 + N_G N_K} \tag{2.11}$$

The above equations hold for both continuous time and discrete time.

Remark 2.1 Zeros

The presence of anti-resonant zeros implies blocking of certain signal frequencies by G. From the derivation above in Equation (2.10), it can be seen that the zero polynomial of the open loop system L is the same as that of the closed-loop system T *i.e.* the zero locations are unaffected by feedback control. Hence it is apparent that the zeros will inhibit input disturbance d_i rejection capabilities (by G) as well as noise rejection and tracking capabilities (by T) at the frequencies of the anti-resonant zeros due to insufficient gain. As such, the feedback controller K in series compensation topology can counter the effects of stable anti-resonant zeros in G and T at best by placing corresponding stable poles in K [95].

Remark 2.2 Poles

Feedback control effectively causes the location of poles to be shifted and can be arbitrarily placed by designing K. An interesting observation on inspection of Equation (2.11) reveals that the zeros of S are effectively the poles of G and K. Hence to create notches in S for extra disturbance rejection and error correction, the gain of resonant poles of G are not compensated (in phase stabilization compensation [53]) or created by K (in peak filter designs *e.g.* [125]).

In a standard unity negative feedback configuration, there exists control conflicts and unavoidable trade-offs between attenuating disturbances and filtering out measurement error and noise. For good tracking performance and rejection of disturbances in low frequency region, good loop shaping techniques are essential to

avoid large control signals.

From Equation (2.9), it can be seen that a small S is ideal for disturbance rejection and a small T is good for insensitivity to measurement noise and high frequency uncertainties. But according to the definitions of S and T, the following identity always holds

$$S + T \equiv 1, \qquad\qquad \forall\, \omega \qquad\qquad (2.12)$$

S and T cannot be small simultaneously and in particular, $|S|$ and $|T|$ cannot be less than $\frac{1}{2}$ at the same time. Fortunately, this conflict can be resolved by making one transfer function small at a frequency band and the other small at another. This is possible by speculating the frequency spectra—the power spectra of references and disturbances are usually concentrated in the lower frequencies while the power spectra of measurement error and noise are in the high frequency range.

Knowing that $T = SL$ and design specifications on S and T, an intuitive approach to find stabilizing controller K is via closed-loop synthesis

$$
\begin{aligned}
K &= G^{-1}L \\
&= G^{-1}S^{-1}T \qquad\qquad (2.13)
\end{aligned}
$$

A problem now arises obviously as one has to choose among the many possible arbitrary combinations of S and T although their solution "shapes" are known. The properness and characteristics of plant G are ignored and the controller K derived via such a method might be causal, or even unstable if G is non-minimum phase.

A more common and easier solution is to use the open loop approach with $L = GK$. A good rule of thumb is to use high gain over low frequencies and decrease

the gain as rapidly as possible after the gain crossover frequency. Cascading a large number of LPFs (Low Pass Filters) is not admissible due to the amount of phase lag introduced. Using Bode's Stability Criterion, the typical magnitude shape of a compensated open loop transfer function of a negative feedback control system can be derived to have [24]

- Low frequency band: A large gain $\gg$ 0 dB and descending with a slope of $-20N$ dB/dec ($N \geq 2$);

- Mid frequency or crossover frequency band: Pass through 0 dB with $\approx$ -20 dB/dec for stability;

- High frequency band: A low gain $<$ 0 dB and descending with a slope of $-20N$ dB/dec ($N \geq 2$);

This method of controller design using open loop transfer function L will be used for controller designs in the rest of the dissertation.

Remark 2.3 Sensitivity

The sensitivity transfer function S is the transfer function from output disturbances d_o to to true PES y. As such, loop shaping methods put much emphasis on low frequency band to reject disturbance and enable better tracking. One loop shaping and controller design evaluation tool commonly used is the Nyquist plot. For brevity but without loss of generality, we will discuss in the continuous time domain and look at how the open loop transfer function $L(j\omega)$ and sensitivity transfer function $S(j\omega)$ are related on the Nyquist diagram. Figure 2.9 shows two typical Nyquist curves $L_1(j\omega)$ and $L_2(j\omega)$.

Since $S(j\omega) = \frac{1}{1+L(j\omega)}$ with $1 + L(j\omega)$ as the output return difference equation, the locus of $|S(j\omega)| = 1$ can be plotted as a unit disc with center at the critical
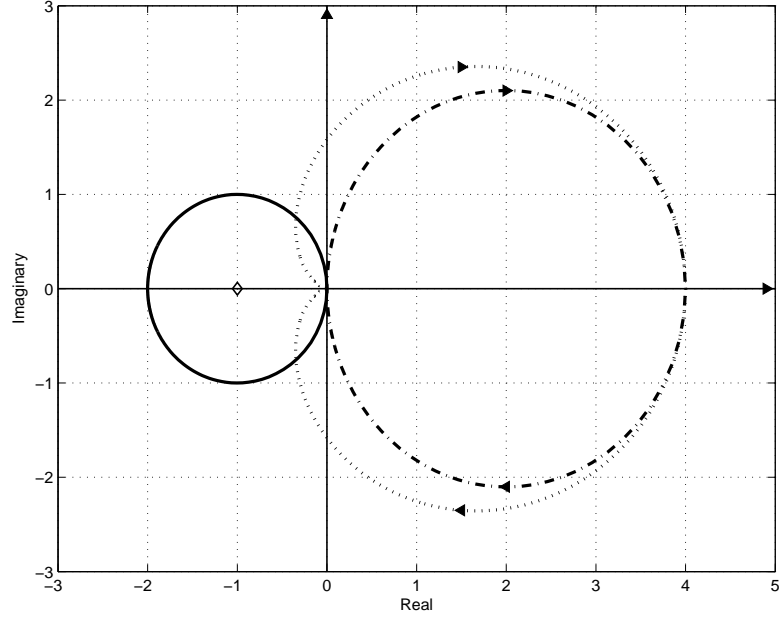
Figure 2.9: Nyquist plots. Solid: Sensitivity Disc (SD) with $|S(j\omega)| = 1$. Dotted: $L_1(j\omega)$. Dashed-dot: $L_2(j\omega)$.

point $(-1 + j0)$. We define this disc as "Sensitivity Disc" (SD). A $L(j\omega_-)$ outside SD will hence yield $|S(j\omega_-)| < 1$ and a $L(j\omega_+)$ inside SD will yield $|S(j\omega_+)| > 1$ for some frequencies ω_- and ω_+. $L(j\omega)$ touching the SD corresponds to unity gain or 0 dB on the Bode Diagram of $|S(j\omega)|$. $|S(j\omega)|$ is the reciprocal of the distance of $L(j\omega)$ to critical point $(-1 + j0)$.

As such, it can be seen from the example in Figure 2.9 that $L_2(j\omega)$ will have no positive area (or "hump") in the sensitivity function S. $L_1(j\omega)$ on the other hand cuts the SD for some $\omega \geq \omega_+$ and approaches the origin with phase angle more than $-\frac{\pi}{2}$. Negative feedback actually increases the sensitivity hump rather than decreases it at these frequencies ω_+.

With these ideas in mind, we will design our controllers to make $L_D(j\omega)$ [95]

1. far from and not touch SD. If this is not possible, make $L_D(j\omega)$ avoid SD

where the frequency spectra of the disturbances are concentrated;

2. approach the origin at $-\frac{\pi}{2} \leq \angle L_D(j\omega) \leq \frac{\pi}{2}$ as $\omega \to \infty$ so that SD is avoided. If this is not possible, make $|L_D(j\omega)| \approx 0$ at these frequencies;

3. do not encircle $(-1 + j0)$ clockwise for stability.

These tools and design considerations are valid for discrete time systems for frequencies below the Nyquist frequency.

Remark 2.4 Bode's Integral Theorem

Alternatively, we can use Bode's Integral Theorem to study the limitations of linear control systems. Bode's Integral Theorem was initially derived for systems with non-minimum phase zeros or even unstable poles. In such systems, the total area of the sensitivity function will be a positive value making it impossible to reduce the hump for disturbance rejection. This is intuitive due to the extra phase lag contribution compared to their stable counterparts, leaving a smaller phase margin. Hence much feedback is used for stabilization in addition to sensitivity reduction.

Theorem 2.1 *Continuous Bode's Integral Theorem [126]*

A continuous SISO, minimum phase LTI (Linear Time Invariant) system has the stable open loop transfer function $L(j\omega)$. The sensitivity transfer function of the unity negative feedback system is $S(j\omega) = \frac{1}{1+L(j\omega)}$. If the closed-loop system is stable, then

$$\int_0^\infty \ln |S(j\omega)| \, d\omega = -\frac{\pi}{2} K_s, \quad K_s = \lim_{s \to \infty} sL(s) \tag{2.14}$$

Corollary 2.1 When the relative degree of the open loop transfer function $L(s)$ is greater than or equal to two, $K_s = 0$ and so is the total area under the sensitivity transfer function S. For $|S(j\omega)| < 1$ over some frequency, then a necessary condition is that $|S(j\omega)| > 1$ over another frequency range, thereby causing a degra-

dation of disturbance rejection capabilities at frequencies whereby $|S(j\omega)| > 1$. This phenomenon is termed as the "waterbed" effect. In other words, the relative degree of the open loop system has to be unity for unity sensitivity at high frequencies which is not possible for the VCM in a single stage HDD, but feasible for a dual-stage HDD. For discrete time systems, the Discrete Bode's Integral Theorem is more stringent and their conclusions differs.

Theorem 2.2 *Discrete Bode's Integral Theorem [76]*

A discrete time SISO, minimum phase LTI system has the stable open loop transfer function $L(z)$. The sensitivity transfer function of the unity negative feedback system is $S(z) = \frac{1}{1+L(z)}$. If the closed-loop system is stable, then

$$\int_{-\pi}^{\pi} \ln |S(e^{j\phi})| \, d\phi = 2\pi(-\ln|K_z + 1|), \quad K_z = \lim_{z \to \infty} L(z) \tag{2.15}$$

and $\phi = \omega T$ and T is the sampling rate.

Corollary 2.2 When $G(z)$ is strictly proper, the Discrete Bode's Integral Theorem in Equation (2.15) reduces to

$$\int_{-\pi}^{\pi} \ln |S(e^{j\phi})| \, d\phi = 0 \tag{2.16}$$

This is the waterbed effect in discrete time domain.

The single stage HDD employing the VCM is hence bounded by the waterbed effect due to its low frequencies double integrator properties. It is worth noting that the transfer functions are periodic about Nyquist frequency $\frac{\pi}{T}$.

Corollary 2.3 When $G(z)$ is proper with $K_z < -2$ or $K_z > 0$, then the Discrete Bode's Integral Theorem in Equation (2.15) becomes

$$\int_{-\pi}^{\pi} \ln |S(e^{j\phi})| \, d\phi < 0 \tag{2.17}$$

This implies that some loop shaping technique is possible and may not be bounded

34

by the waterbed effect. Sensitivity reduction and disturbance attenuation is possible for a zero relative degree system (*e.g.* a dual-stage HDD employing PZT- or MEMS-actuated suspensions/sliders/heads) with proper controller design.

Corollary 2.4 When $G(z)$ is proper with $-2 < K_z < 0$, the Discrete Bode's Integral Theorem in Equation (2.15) implies that

$$\int_{-\pi}^{\pi} \ln \, |S(e^{j\phi})| \, d\phi > 0 \tag{2.18}$$

and feedback control is now degrading sensitivity and performance rather than improving it. The conclusion is similar to that of non-minimum phase systems.

As such for the VCM in a single stage HDD with non-minimum zeros and delay, overall positive sensitivity is unavoidable. However, the problem can be alleviated with the development of in-phase VCM [5] with possible reduction to Corollary 2.2. This restricts the overall positive sensitivity area to zero and within the limits of the waterbed effect.

2) Properties: Future storage devices employing piezoelectric and MEMS-based actuators with multi- or self-sensing capabilities have small form factors coupled with ultra high access speeds and storage densities. Besides using the positive area of the sensitivity transfer function as a measure of disturbance rejection capabilities in a servo system, reduction of system norms are also an indicative measure of control system performance. In this subsection, we define and discuss the common system norms as indices as effectiveness of controller design with their physical interpretations.

Definition 2.1 Continuous $\mathcal{H}_2$-norm [102]

Consider a continuous time SISO transfer function $G(s)$. The $\mathcal{H}_2$ norm of $G(s)$ is

defined as

$$||G||_2 = \sqrt{\frac{1}{2\pi} \int_{-\infty}^{\infty} G(j\omega)G(-j\omega)\,d\omega} \qquad (2.19)$$

By Parseval's Theorem, the frequency domain integral can be converted into time domain as

$$||G||_2 = \sqrt{\int_{0}^{\infty} g^2(t)\,dt} \qquad (2.20)$$

where $g(t)$ is the weighting function or impulse response with Dirac delta function from disturbance to true output.

Definition 2.2 Discrete $\mathcal{H}_2$-norm [102]

Consider a discrete time SISO transfer function $G(z)$. The $\mathcal{H}_2$ norm of $G(z)$ is defined as

$$||G||_2 = \sqrt{\frac{1}{2\pi} \int_{-\pi}^{\pi} G(e^{j\omega})G(e^{-j\omega})\,d\omega} \qquad (2.21)$$

By Parseval's Theorem, the frequency domain integral can be converted into discrete time domain as

$$||G||_2 = \sqrt{\sum_{k=0}^{\infty} g^2(k)} \qquad (2.22)$$

where $g(k)$ is the weighting function or impulse response sequence with Dirac delta function from disturbance to true output.

Reduction of $\mathcal{H}_2$-norm is commonly seen as a performance index for control system to minimize average disturbance energy over all frequencies. In fact, minimization of $\mathcal{H}_2$-norm of transfer function T_{yw} of the disturbance sources w to true PES y results in highest achievable TPI in HDDs. When the collected PES samples N are large enough in HDDs, the limit of the $\mathcal{H}_2$-norm of T_{yw} can be expressed as [64]

$$||T_{yw}||_2 = \sqrt{\frac{1}{N-1} \sum_{k=1}^{N} y^2(k)} \qquad (2.23)$$

assuming that the sampled variance is an unbiased estimate of the unknown true PES variance.

Definition 2.3 Continuous $\mathcal{H}_\infty$-norm [102]

Consider a continuous time SISO transfer function $G(s)$. The $\mathcal{H}_\infty$-norm of $G(s)$ is defined as

$$||G||_\infty = \sup_\omega \overline{\sigma}\left[G(j\omega)\right] \tag{2.24}$$

where $\overline{\sigma}\left[.\right]$ denotes the largest singular value.

Definition 2.4 Discrete $\mathcal{H}_\infty$-norm [102]

Consider a discrete time SISO transfer function $G(z)$. The $\mathcal{H}_\infty$-norm of $G(z)$ is defined as

$$||G||_\infty = \sup_{-\pi \leq \omega \leq \pi} \overline{\sigma}\left[G(e^{j\omega})\right] \tag{2.25}$$

$\mathcal{H}_\infty$ optimization reduces the worst case gain of worst frequency of disturbance energy amplification over all frequencies. As such, the $\mathcal{H}_\infty$-norm is also the maximum value of the gain of maximum singular value in the transfer function matrix T_{yw}. Reduction of $\mathcal{H}_2$- and $\mathcal{H}_\infty$-norms (or even simultaneously in mixed sensitivity problems) to the extent of even disturbance decoupling are common approaches in controller designs for data storage servo systems.

The choice of a sampling frequency is important to ensure that the dominant dynamics of the plant to be controlled are captured. At the same time, it is essential to ensure that the sampled-data control system with ZOH (Zero Order Hold) is of minimum phase by adhering to the guidelines depicted in [6]. Coupled with higher processing speeds in new generation of DSPs, higher PES SNR (digital PES demodulation and dual even multiple frequency [120]) and novel PES demodulation schemes (obtaining PES from user data [45][121] *etc.*), sampling frequencies in

HDDs are getting higher without much reduction in user data storage space. The usage of secondary actuators in dual-stage HDDs also prompt for an increase in sampling frequencies due to higher servo bandwidth and higher frequency dynamics of the appended secondary actuator. With upcoming technologies of perpendicular recording and servo patterned media, sampling frequencies comparable to that using embedded servo are fast becoming a reality.

On probe-based storage systems, high sampling rates are feasible due to usage of dedicated servo patterns [21]. As such, high sampling frequencies for digital controllers mimicking their analog counterparts with little degradation in performance are feasible.

2.3   Summary

In this chapter, system identification of mechanical actuators used in dual-stage HDDs (employing PZT microactuators) and MEMS-based micro X-Y stage are detailed and discussed. The standard unity feedback control system is analyzed based on a SISO framework in terms of poles and zeros. The inherent constraints are discussed with analysis on sensitivity transfer function S and Bode's Integral Theorems (continuous and discrete). Future storage devices have similar properties in terms of sensor fusion and sampling rate selection, and performance measurement yardsticks in terms of sensitivity and system norms ($\mathcal{H}_2$- and $\mathcal{H}_\infty$-norms) reduction.

In the next chapter, an OICA (Online Iterative Learning Control) is proposed for extra NRRO rejection by reducing the $\mathcal{H}_2$-norm of transfer from NRRO disturbance sources to true PES on a PC-based spinstand servo system reported

in [120]. Gradient estimates are obtained without prior knowledge of the spectra of dominant input and output disturbances in measured PES.

Chapter 3

Disturbance Rejection with Iterative Control using Experimental Gradient Estimates

The exact spectra of disturbances and noises affecting precise servo positioning required for high density storage in future HDDs are time-varying and remain unknown. In this chapter, an OICA (Online Iterative Control Algorithm) by setting measured PES into the servo system to achieve high track densities through minimizing the square of the $\mathcal{H}_2$-norm of the transfer function from NRRO (Non-Repeatable Run-Out) disturbance sources to true PES without solving AREs and LMIs is proposed. To prevent the parameters from being trapped in a local minima, an online RRO estimator is constructed to extract NRRO components for gradient estimates. Experimental results on a spinstand servo system show an improvement of 22% in 3σ NRRO and suppression of spectrum of baseline NRRO.

3.1 Background

In the HDD industry, the areal density is continuously growing and targeting at achieving above 1 Tb/in^2 through perpendicular recording technologies. In turn, the demand for higher track density increases which requires a position accuracy of about 400 kTPI. However, there are many contributing factors that limit the achievable track density. One of the major contributors is the NRRO generated from the disk media and spindle vibration, which is induced by the windage noise within the disk stack.

Considerable efforts have been made to design servo control systems that reduce the effect of vibrations on operation of HDDs, especially on the NRRO error induced by the spindle motor and head media defects. As with all HDD designs, the efficiency of controlling vibrations and structural noise depends on the dynamic behavior of the overall system considering the parametric variations among HDDs in terms of resonant frequencies, length, mass, force (or torque) constant, R/W element, *etc.* Designers are continually challenged to bring all of these elements together to produce the optimal design that meets the criteria for the various applications designed for. Self-optimizing controller designs are hence essential for the millions of HDDs produced by the industries per day.

Several robust and optimal controller design methods have been proposed. Herrmann *et al.* used μ-synthesis via D-K iteration for robust stability control of different HDDs in [39]. Goh *et al.* [29] and Lee *et al.* [64] solved AREs (Algebraic Riccati Equations) for minimization of $\mathcal{H}_\infty$ and $\mathcal{H}_2$ criterions in HDDs, respectively. However due to the small time constants of the actuators involved and high servo bandwidth required by HDDs for stronger error rejection, numerical instabilities often arise due to ill-conditioned system matrices prompting servo designers

to doubt the integrity of the solutions.

More recently, Hao *et al.* in [37] and Park *et al.* in [97] used performance index-based rules to tune track-following controller and repetitive controller for minimum TMR (Track Mis-Registration). Jia *et al.* reinject measured PES into the servo system for more precise RRO estimation in [48]. Reinjection of collected information into the servo system for gradient estimates is also well documented by Hjalmarsson *et al.* in [41].

In this chapter, an OICA is proposed to tune the controller parameters to minimize the square of the $\mathcal{H}_2$-norm from disturbance of unknown spectra to true PES for more effective NRRO rejection. An RRO estimator is constructed via averaging measured PES and NRRO information is extracted from the difference between measured PES and estimated RRO. The gradients are computed by reinjecting the NRRO into closed-loop system similar to that suggested in [41] without having to solve AREs and LMIs for high density storage experiments. The proposed methodology can be readily applied to STW and especially SSTW (Self-STW) processes in HDD industries to prevent error propagation issues raised by Ye *et al.* in [130].

3.2 Control Problem Formulation

The block of servo control system in HDDs with input disturbances d_i, output disturbances d_o and noise n contaminating true PES y is shown in Figure 3.1. From Figure 3.1, the true PES y can be derived by the following relation

$$
\begin{aligned}
y &= \frac{P}{1 + C(\mu)P} d_i + \frac{1}{1 + C(\mu)P} d_o - \frac{C(\mu)P}{1 + C(\mu)P} n \\
&= S(\mu)P\, d_i + S(\mu)\, d_o - T(\mu)\, n
\end{aligned}
\tag{3.1}
$$
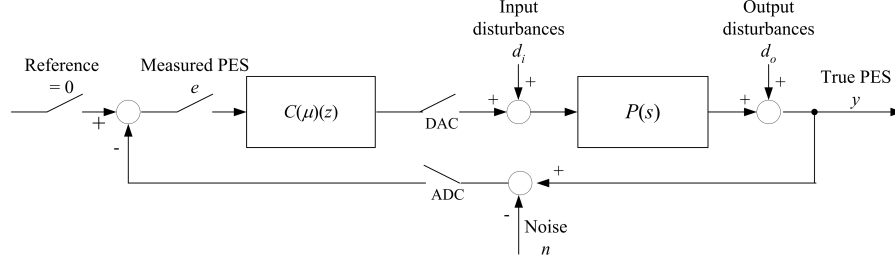
Figure 3.1: Block diagram of servo control system with input disturbances d_i, output disturbances d_o and noise n contaminating true PES y.

where μ is a vector of controller parameters. $S(\mu)$ and $T(\mu)$ denote the sensitivity and complementary sensitivity transfer functions of the stable closed-loop servo system parameterized by μ respectively.

For high TPI in future HDDs, the TMR budget will have to be minimized when the HDD servo system is subjected to the input disturbances d_i, output disturbances d_o and noise sources n packed as vector w. Now let the transfer function of the disturbance sources w to true PES y be defined as T_{yw}. When the number of collected PES samples N are large enough in HDDs, the limit of the $\mathcal{H}_2$-norm of T_{yw} can be expressed as [64]

$$||T_{yw}||_2 = \sqrt{\frac{1}{N-1}\sum_{k=1}^{N} y^2(k)} \tag{3.2}$$

assuming that the sampled variance is an unbiased estimate of the unknown true PES variance σ_{PES}^2. We propose the following quadratic cost function to minimize the square of $\mathcal{H}_2$-norm in Equation (3.2) (or variance of true PES y) parameterized by μ

$$
\begin{aligned}
J(\mu) &= ||T_{yw}||_2^2 \\
&= \frac{1}{N-1}\sum_{k=1}^{N} y^2(k)
\end{aligned}
\tag{3.3}
$$

As measured PES e remains as the only accessible quantity, minimizing the

43

square of TMR of true PES y is done via minimizing the square of TMR of measured PES e *i.e.* the controller parameterized by μ^* minimizing the measured PES e also minimizes the true PES y. It should be noted that the measured PES e consists of RRO and NRRO components. The proof of this argument is found in the appendix of [37] and is omitted here.

The optimal controller parameter μ^* is thus defined as

$$\mu^* = \min_{\mu \in \Sigma} J(\mu) \tag{3.4}$$

where Σ is the set of all stabilizing controllers. By finding the partial derivative of $J(\mu)$ with respect to μ

$$\frac{\partial J}{\partial \mu} = \frac{2}{N-1} \sum_{k=1}^{N} y(k) \frac{\partial y}{\partial \mu}(k) \tag{3.5}$$

and set it to 0, we can obtain the minima (local or global) μ^* directly. While it is not mathematically tractable to find a direct solution to Equation (3.5) with the main obstacle being evaluating $\frac{\partial y}{\partial \mu}(k)$, we observe that by taking partial derivative of Equation (3.1) with respect to control parameter μ at each iteration i, the following equation hold

$$
\begin{aligned}
\frac{\partial y}{\partial \mu} &= -\frac{P^2}{[1+C(\mu)P]^2}\frac{\partial C}{\partial \mu}d_i - \frac{P}{[1+C(\mu)P]^2}\frac{\partial C}{\partial \mu}d_o \cdots \\
&\quad + \frac{C(\mu)P^2}{[1+C(\mu)P]^2}\frac{\partial C}{\partial \mu}n - \frac{P}{1+C(\mu)P}\frac{\partial C}{\partial \mu}n \\
&= -S(\mu)^2 P^2 \frac{\partial C}{\partial \mu}d_i - S(\mu)^2 P \frac{\partial C}{\partial \mu}d_o + C(\mu)S(\mu)^2 P^2 \frac{\partial C}{\partial \mu}n - S(\mu)P \frac{\partial C}{\partial \mu}n \\
&= -S(\mu)P\frac{\partial C}{\partial \mu}\left[S(\mu)P\,d_i + S(\mu)\,d_o - C(\mu)S(\mu)P\,n + n\right] \\
&= -S(\mu)P\frac{\partial C}{\partial \mu}\left[S(\mu)P\,d_i + S(\mu)\,d_o - T(\mu)\,n + n\right] \tag{3.6}
\end{aligned}
$$

Substituting Equation (3.1) into Equation (3.6), the partial derivative $\frac{\partial y}{\partial \mu}$ can also be expressed as

$$\frac{\partial y}{\partial \mu} = -S(\mu)P\frac{\partial C}{\partial \mu}\left[y + n\right] \tag{3.7}$$

44

which implies a numerical gradient estimate of the required $\frac{\partial y}{\partial \mu}$ at current iteration i can be obtained by filtering $(y+n)$ with partial derivative of controller with respect to controller parameter vector $\frac{\partial C}{\partial \mu}(\mu)$ and shock transfer function $S(\mu)P$.

Using the proposed scheme, $\frac{\partial y}{\partial \mu}$ is not affected by input disturbances d_i and output disturbances d_o at the current iteration i as can be seen from Equation (3.7). Only noise n permeates through to the gradient estimate. However if we assume that the noise n is of zero mean, then the effects of n on the gradient estimate of cost function $\frac{\partial J}{\partial \mu}$ will be negligible if N is large as can be seen from Equation (3.5) due to summation. As such, Equation (3.7) can be rewritten as

$$\frac{\partial y}{\partial \mu} \approx -S(\mu)P\frac{\partial C}{\partial \mu}\,e \tag{3.8}$$

with zero reference since only measured PES e is available and hence the gradient estimate of cost function $\frac{\partial J}{\partial \mu}$ will be a sufficiently accurate unbiased estimate.

Remark 6.1 If $C(\mu)$ is a FIR (Finite Impulse Response) filter of the form

$$\begin{aligned}
C(\mu)(z^{-1}) &= \mu_0 + \mu_1 z^{-1} + \cdots + \mu_n z^{-n} \\
&= \boldsymbol{\mu}^T \boldsymbol{\xi}(z^{-1})
\end{aligned} \tag{3.9}$$

where $\boldsymbol{\mu} = [\mu_0 \quad \mu_1 \quad \cdots \quad \mu_n]^T$ and $\boldsymbol{\xi} = [z^0 \quad z^{-1} \quad \cdots \quad z^{-n}]^T$, then the partial derivative of controller with respect to controller parameter vector $\frac{\partial C}{\partial \mu}$ is given by

$$\frac{\partial C}{\partial \mu} = \boldsymbol{\xi}(z^{-1}) \tag{3.10}$$

or a vector of delay operators.

Remark 6.2 From Equation (3.7), it can be seen that we can use an online approach by injecting the result as input disturbance d_i to be filtered by shock transfer function $S(\mu)P$ and then filtering the new measured PES e offline with $\frac{\partial C}{\partial \mu}$ to obtain the required gradient estimate $\frac{\partial y}{\partial \mu}$ required for computing the gradient of

cost function $\frac{\partial J}{\partial \mu}$ using Equation (3.5). However due to control signal saturation (leading to closed-loop instability) of actuators used for nanopositioning in storage systems, this method is not used in this chapter.

Remark 6.3 Alternatively, we can set measured PES e as reference into servo system (which in essence is filtering by sensitivity transfer function $S(\mu)$) and then post-filtering the new measured PES offline with $\frac{\partial C}{\partial \mu}$ and mathematical model of plant P to obtain $\frac{\partial y}{\partial \mu}$ required for computing the gradient of cost function $\frac{\partial J}{\partial \mu}$ using Equation (3.5). This method—though less satisfactory as we rely on the accuracy of the mathematical model of plant P but sufficiently accurate during experimental implementations—will be used and explored in future sections of this chapter.

3.3   Online Iterative Control Algorithm

Assuming that the initial conditions of the plant and the controllers are the same in all experiments and the experiment interval N is sufficiently large when compared to the time constants of the closed-loop system, we will detail the gradient estimation of $\frac{\partial y}{\partial \mu}$ with and without extraneous sensor in the subsequent sections.
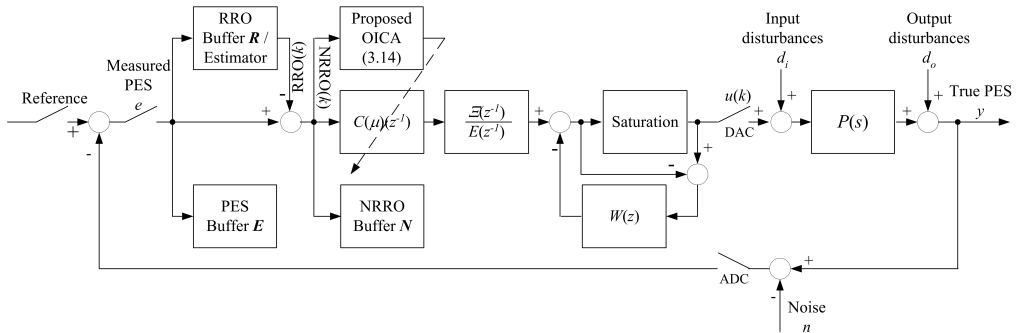
Figure 3.2: Block diagram of spinstand experiment setup with RRO estimator, anti-windup compensator $W(z)$ and actuator saturation considerations.

3.3.1 RRO Estimator

Before we use NRRO components for estimating gradient of $\frac{\partial y}{\partial \mu}$, an online RRO estimator is constructed to extract NRRO components from measured PES e. It is assumed that the NRRO components are of zero mean.

Most of the RRO components enter the servo loop as output disturbances d_o, which is valid as most of the RRO components arise from spindle rotation. By ensembled averaging measured PES e stored in PES buffer $\boldsymbol{E}$ and dividing by sensitivity transfer function $S(\mu)$ at each iteration i offline, the RRO estimator can be constructed and stored in RRO buffer $\boldsymbol{R}$ as shown in Figure 3.2. The NRRO components can then be obtained by the difference between measured PES e from PES buffer $\boldsymbol{E}$ and output of RRO buffer $\boldsymbol{R}$. The RRO components are not used for gradient estimations to prevent the OICA from being "trapped" in a local optimum due to insufficient persistent excitation. After RRO compensation, the servo problem can be reformulated into a disturbance rejection problem with NRRO as output disturbance sources. Any nonlinear media and head effects are considered as initial conditions of the disturbance rejection problem with unknown disturbance input spectrum. The NRRO components will be used as reference for the gradient estimation of $\frac{\partial y}{\partial \mu}$ as shown in Figure 3.2.

3.3.2 Gradient Estimation using NRRO without Extraneous Sensor

Firstly we set measured PES e as reference into the closed-loop servo system as suggested in Remark 3 with RRO compensation as shown in Figure 3.2. The resultant data now consists of NRRO components and is used to obtain the gradient $\frac{\partial y}{\partial \mu}$

in Equation (3.8). The experimental estimate $\frac{\partial y}{\partial \mu}$ using NRRO components can be obtained from Equation (3.8) by post-filtering with $\frac{\partial C}{\partial \mu}$ and plant model P as suggested earlier in Remark 3 of Section 3.2. As such, we can expect more adjustments (hence loop shaping) at frequencies of high sensitivity and plant's resonant modes from the shock transfer function $S(\mu)P$.

Using these data and the previously stored NRRO data, we use Equation (3.5) to calculate the partial derivative of cost function with respect to controller parameter $\frac{\partial J}{\partial \mu}$ at current iteration i. This gradient will be essential for controller parameter update which will be detailed in future subsections.

3.3.3 Gradient Estimation using NRRO with Extraneous Sensor

With additional sensors (*e.g.* using SSA to estimate displacement in piezoelectric actuators [87]), we can improve the gradient update and tuning algorithm derived earlier. Assume that the extraneous sensor introduces a measurement noise n_s. As such, the measured true PES y_s from the extraneous sensor is given by

$$y_s = y + n_s \tag{3.11}$$

and the gradient $\frac{\partial y}{\partial \mu}$ using NRRO components after subtracting from RRO estimator can be obtained using Equation (3.7) as

$$\frac{\partial y}{\partial \mu} = -S(\mu)P\frac{\partial C}{\partial \mu}\left[y_s + n + n_s\right] \tag{3.12}$$

Similarly assuming the noise source from the new sensor n_s to be of zero mean, an experimental estimate of gradient $\frac{\partial y}{\partial \mu}$ can be obtained as

$$\frac{\partial y}{\partial \mu} \approx -S(\mu)P\frac{\partial C}{\partial \mu}\,y_s \tag{3.13}$$

The experimental gradient estimate $\frac{\partial y}{\partial \mu}$ using NRRO components with extraneous sensor can be obtained from Equation (3.13) after subtracting y_s from RRO estimator offline constructed from previous subsection and post-filtering with $\frac{\partial C}{\partial \mu}(\mu)$ with the shock transfer function model $S(\mu)P$.

Although additional sensor incurs extra cost, the main advantage of the extraneous sensor is obvious as reinjecting measured PES e into the servo system as suggested in the previous section becomes redundant. The convergence time of the proposed OICA will hence be halved and similar to that without extraneous sensor, the experimental gradient estimate $\frac{\partial y}{\partial \mu}$ is independent of disturbances sources d_i and d_o. The unbiased gradient estimate will be sufficiently accurate if the noise levels from both the servo system n and sensor n_s are low.

Similarly using these data and the previously stored NRRO data, we use Equation (3.5) to calculate the partial derivative of cost function with respect to controller parameter $\frac{\partial J}{\partial \mu}$ at current iteration i.

3.3.4 Parametric Update

With the developments derived with and without extraneous sensor, the controller parameter vector μ is then updated with the following iterative algorithm at the end of each iteration i

$$
\begin{aligned}
\mu(i+1) &= \mu(i) - \frac{\partial J}{\partial \mu}(i) \\
&= \mu(i) - \frac{2}{N-1} \sum_{k=1}^{N} y(k) \frac{\partial y}{\partial \mu}(k)
\end{aligned}
\tag{3.14}
$$

The updating algorithm in Equation (3.14) is in essence a steepest decent algorithm $i.e.$ the parameters are updated in the direction of steepest drop in gradient of $J(\mu)$. The proof of parametric convergence is detailed in [15] and omitted here.

49

The convergence rate is not as rapid as that using the Gauss-Newton method but is essential for real time implementation to save computational cycles and power from having to evaluate matrix inverse.

3.4 System Evaluation

To demonstrate the effectiveness of our proposed OICA, the control scheme without extraneous sensor will be substantiated with simulation and experimental results on the PC-based servo system setup on a spinstand as reported by Wong *et al.* in [120].

3.4.1 Spinstand Servo System

For our simulation and experiments, the Guzik spinstand (Model S1701A)[36] is used. The existing head cartridge of the spinstand is modified to integrate a small piezoelectric actuator (of dimensions 3 mm × 3 mm) near to the R/W head. The width of the write head element used, is about 10.5 μin and the width of the GMR (Giant Magnetoresistive Head) read element is about 8.4 μin. In this experiment, the track pitch is 9 μin as documented in [120]. The block diagram of the spinstand setup is shown in Figure 3.3. A close-up view of the head cartridge with piezoelectric PZT (Pb-Zr-Ti) actuator is shown in Figure 3.4.

The controlled plant is thus having four components: the PZT amplifier, PZT actuator, the head cartridge base and a passive suspension with the HGA (Head Gimbal Assembly). The experimental frequency response of the spinstand setup using calibrated measured PES e (without control) is shown in Figure 3.5. We can see that the PZT head cartridge plant model has the first in plane structural
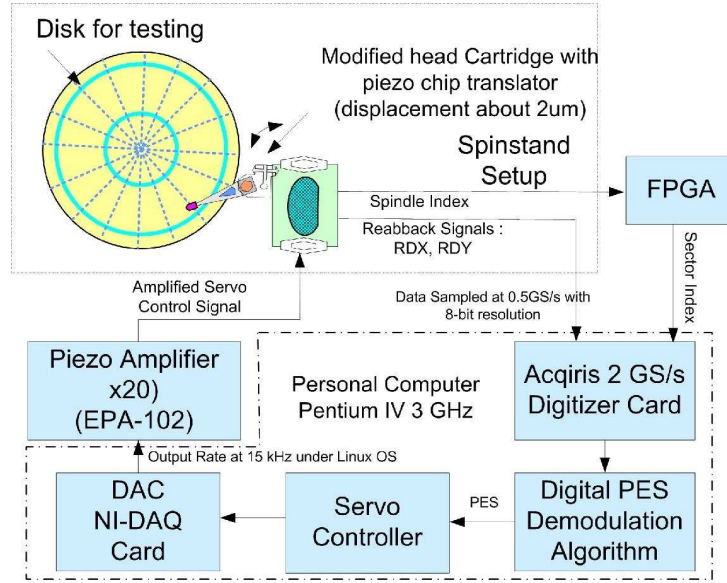
Figure 3.3: Block diagram of spinstand servo system architecture [120].
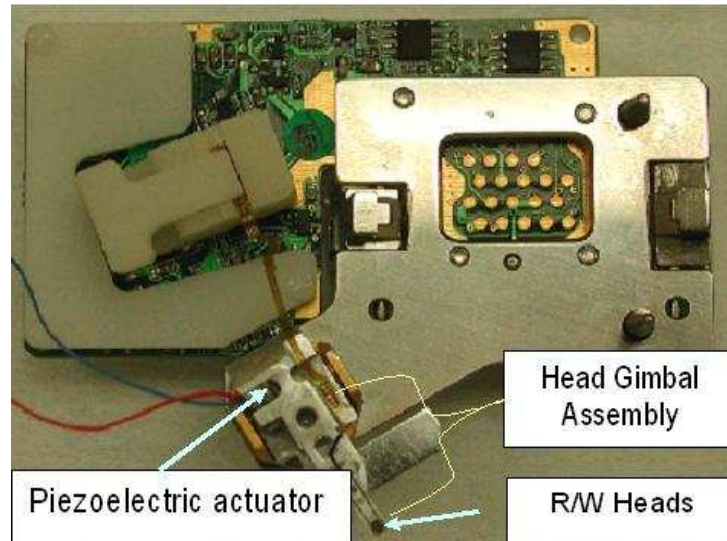
Figure 3.4: Modified head cartridge with piezoelectric (PZT) actuator, HGA and R/W head [120].

resonance from sway mode at 4.2 kHz with a displacement range of about 140 μin.

The plant is discretized via ZOH method and a sampling time of 65 μs is chosen
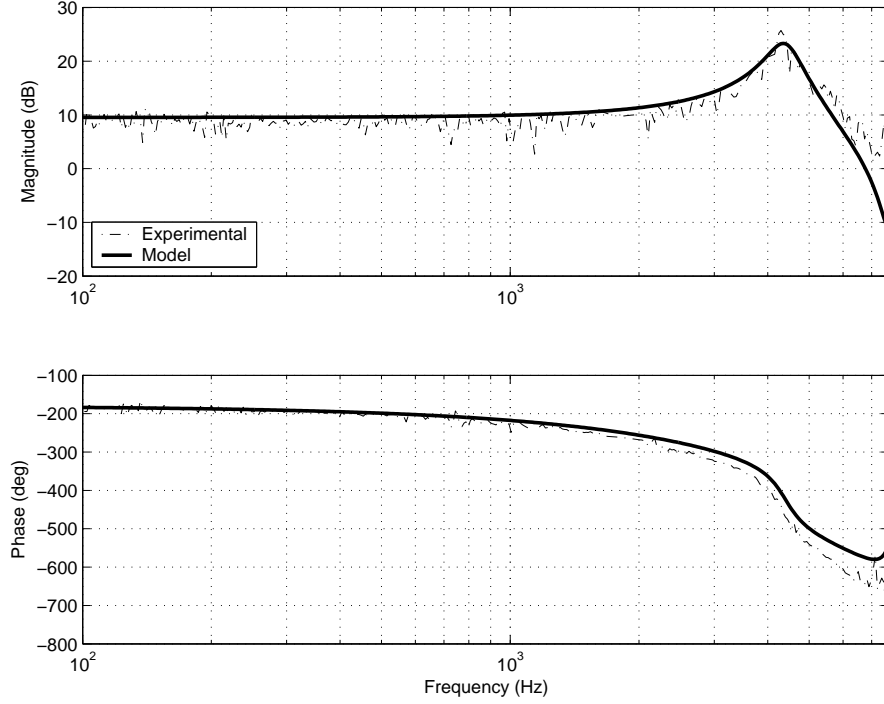
Figure 3.5: Frequency response of spinstand head cartridge with PZT actuator using measured PES.

according to PC-based servo system setup specifications and required computation time as reported previously in [120]. The transfer function of the identified PZT-actuated passive suspension plant model in z-domain is

$$P(z) = -3.3291z^{-1}\frac{z + 0.8862}{z^2 + 0.3695z + 0.7236} \tag{3.15}$$

To demonstrate the effectiveness of the proposed OICA, a nominal feedback controller $\frac{U(z)}{E(z)}$ which is in essence a lag controller cascaded with an approximate plant inverse designed using the guidelines in [95]

$$\frac{U(z)}{E(z)} = -0.051079\frac{z - 0.04321}{z - 1}\frac{z^2 + 0.3695z + 0.7236}{(z - 0.1658)^2} \tag{3.16}$$

is used to ensure low sensitivity according to Discrete Bode's Integral Theorem.

Rewriting Equation (3.16) into filter form

$$\begin{aligned} \frac{U(z^{-1})}{E(z^{-1})} &= \frac{U(z^{-1})}{\Xi(z^{-1})} \frac{\Xi(z^{-1})}{E(z^{-1})} \\ &= \frac{-0.05108 - 0.01666z^{-1} - 0.03615z^{-2} + 0.001597z^{-3}}{1 - 1.331z^{-1} + 0.3589z^{-2} - 0.02748z^{-3}} \end{aligned}$$

(3.17)

and augmenting the pole polynomial $\frac{\Xi(z^{-1})}{E(z^{-1})}$ to form the shaped plant to be controlled, parametric updates will be done only on the coefficients of the zero polynomial $\frac{U(z^{-1})}{\Xi(z^{-1})}$ to prevent closed-loop instability. Hence, the zero polynomial $\frac{U(z^{-1})}{\Xi(z^{-1})}$ can be expressed as a FIR filter $C(\mu)(z^{-1})$ parameterized by vector μ

$$\begin{aligned} C(\mu)(z^{-1}) &= \mu_0 + \mu_1 z^{-1} + \mu_2 z^{-2} + \mu_3 z^{-3} \\ &= \boldsymbol{\mu}^T \boldsymbol{\xi}(z^{-1}) \end{aligned}$$

(3.18)

and the FIR filter is parameterized by vector $\boldsymbol{\mu} = [\mu_0 \quad \mu_1 \quad \mu_2 \quad \mu_3]^T$ with $\boldsymbol{\xi}(z^{-1})$ as a vector of delay operators as mentioned earlier in Remark 1 of Section 3.2. $C(\mu)(z^{-1})$ is initialized to coefficients of zero polynomial $\frac{U(z^{-1})}{\Xi(z^{-1})}$ in Equation (3.17).

To prevent controller and actuator saturation, a simple and effective anti-windup compensator $W(z)$ of the form

$$W(z) = \alpha z^{-1}$$

(3.19)

with $0 < \alpha \leq 1$ is included as seen in Figure 3.2. $W(z)$ works only when the control signal is saturated. The induced oscillations during parametric adaptations during large-span seek operations are also greatly reduced.

For the spinstand servo architecture, the time responses of NRRO and corresponding control signal before OICA are plotted in Figure 3.6. A 3σ NRRO of 0.7823 μin translating to 127 kTPI at 10% tolerance is observed. The experimental spectra of PES, RRO and NRRO is shown in Figure 3.7.

53
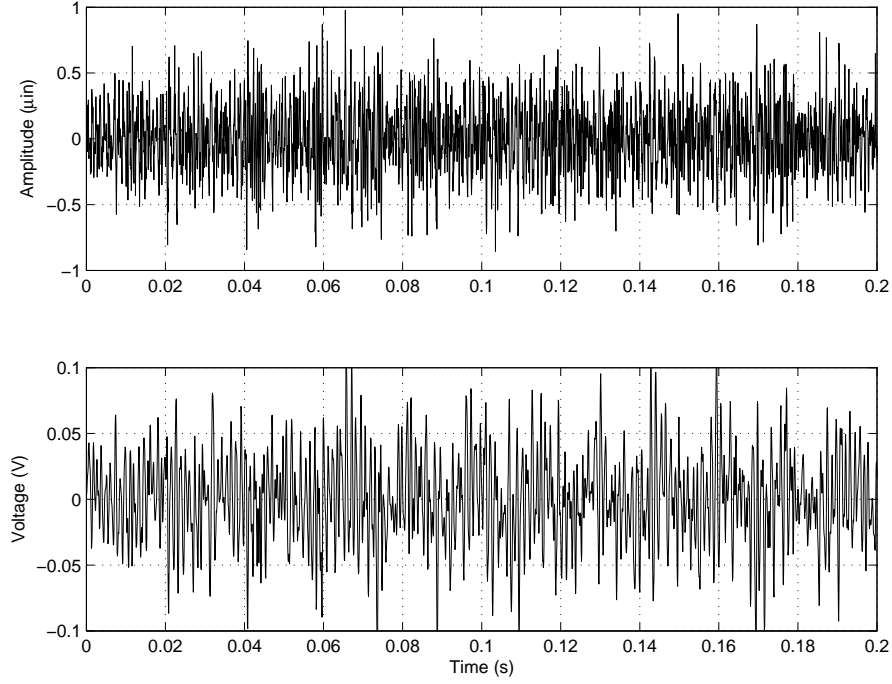
Figure 3.6: Time traces of NRRO (top) and control signal (bottom) before OICA tuning.

It should be noted that the less than exemplary responses obtained (corresponding to lower kTPI) in the figures are due to usage of an earlier generation spindle motor.

3.4.2 Performance Evaluation

In this section, the spinstand setup described in the previous subsection is used to illustrate the effectiveness of the proposed OICA scheme to NRRO rejection. The OICA consists of collecting N samples of measured PES e (chosen to be at least 2 revolutions of the spindle speed) for constructing an online RRO estimator at each update as shown in Figure 3.2. For our experiments, the spindle rotation speed is 4000 rpm and five spindle revolutions are used. As such, $N = 1154$ and the
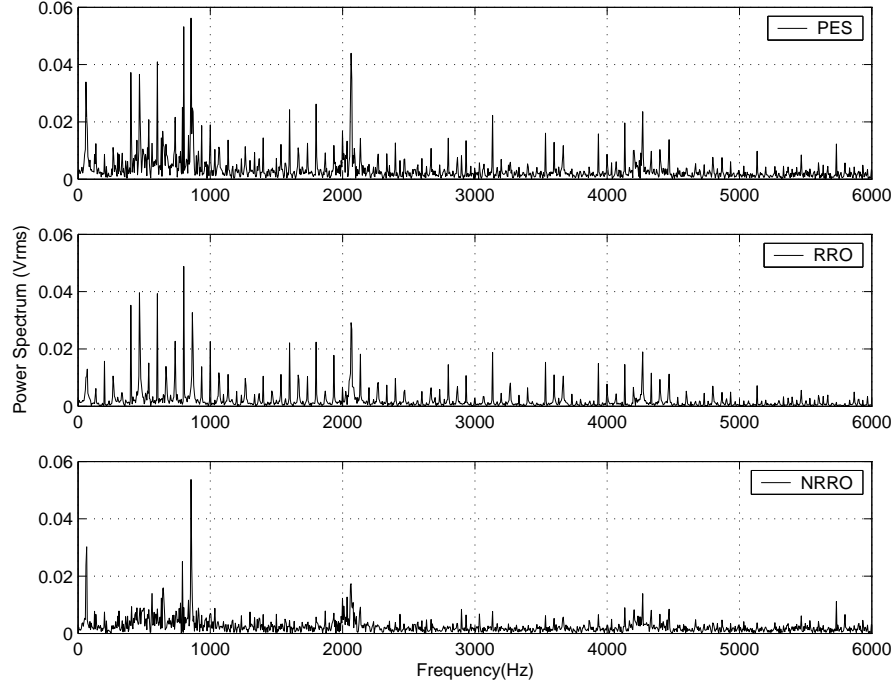
Figure 3.7: Experimental measured spectra of PES, RRO and NRRO in spinstand servo before OICA tuning.

lengths of the PES buffer $\boldsymbol{E}$, RRO buffer $\boldsymbol{R}$ and NRRO buffer $\boldsymbol{N}$ are set as N. It should be noted that the FIR filter $C(\mu)$ is not updated during the first iteration which is used for data logging.

FIR filter $C(\mu)$

Using the proposed OICA, the evolution of the FIR filter $C(\mu)$ after ten iterations of OICA is shown in Figure 3.8. It can be seen that the notch filter originally designed to attenuate the gain of the PZT actuator's sway mode at 4.2 kHz is shifted to 4.8 kHz. The effects and explanations will be investigated with experimental measured PES e later.

The FIR filter's parameters μ_0 to μ_3 after ten iterations of OICA are shown in

55
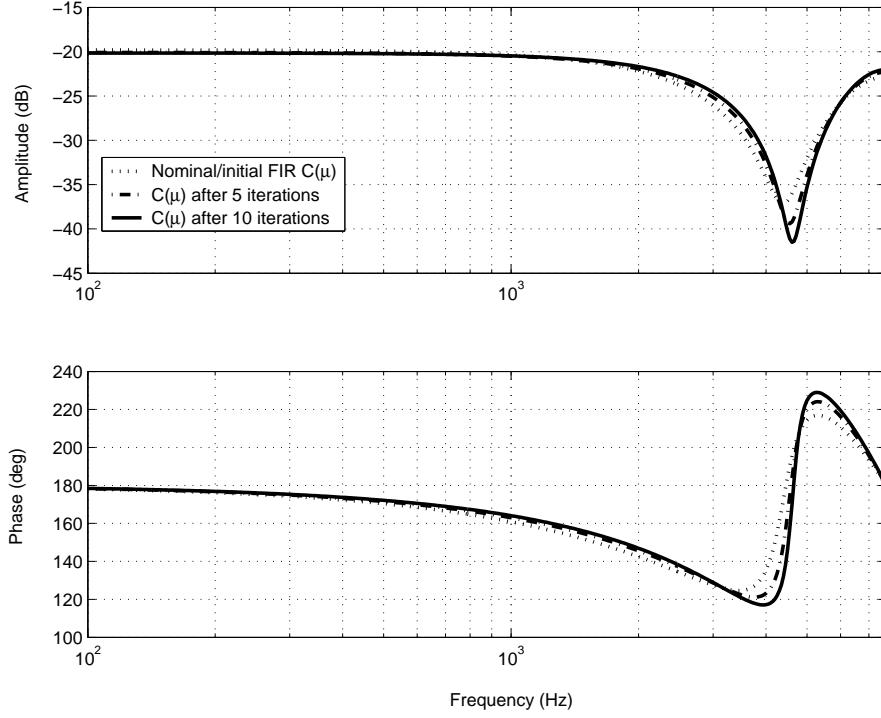
Figure 3.8: Frequency responses of FIR filter $C(\mu)$ during OICA. Dotted: nominal/initial FIR filter $C(\mu)$. Dashed-dot: after five iterations of OICA tuning. Solid: after ten iterations of OICA tuning.

Figure 3.9. Although the steepest descent method of parametric updating method is used, the parameters typically converge to their optimal values *i.e.* $\mu = \mu^*$, after 6 iterations of OICA tuning.

Robustness Analysis

The robustness margin of the proposed OICA is investigated with simulation examples using the same set of collected PES, RRO and NRRO data during the ten iterations of OICA as mentioned in the previous subsection. The effects of variations in natural frequencies of the actuators and different initial controller conditions are mimicked by perturbing the gain and notch frequency (initially at
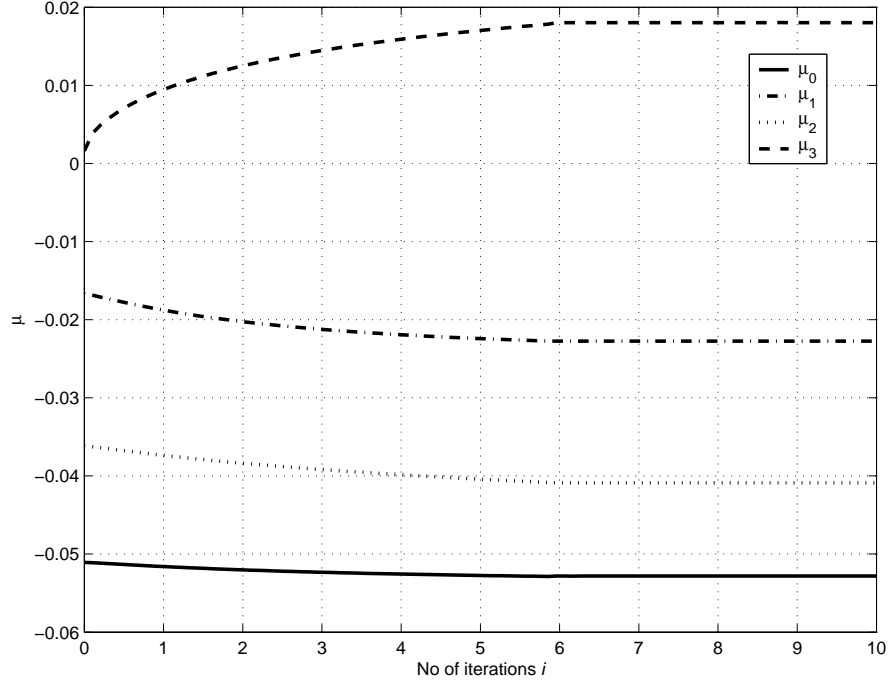
Figure 3.9: FIR filter $C(\mu)$ parameters μ_0 to μ_3.

natural frequency of PZT actuator's in-plane sway mode of 4.2 kHz) with $\pm 10\%$ variations. The frequency responses of the perturbed, nominal and optimal FIR filter are shown in Figure 3.10.

Using the proposed OICA, both the perturbed and nominal FIR filters converge to optimal FIR filter $C(\mu^*)$. However, the rate of convergence depends on the size of norm of difference between the initial controller parameter and that of optimal parameter vector μ^*. For the case of -10% shift in gain and notch frequency shown in Figure 3.10, ten iterations are needed while only three iterations are required for $+10\%$ shift in gain and notch frequency.
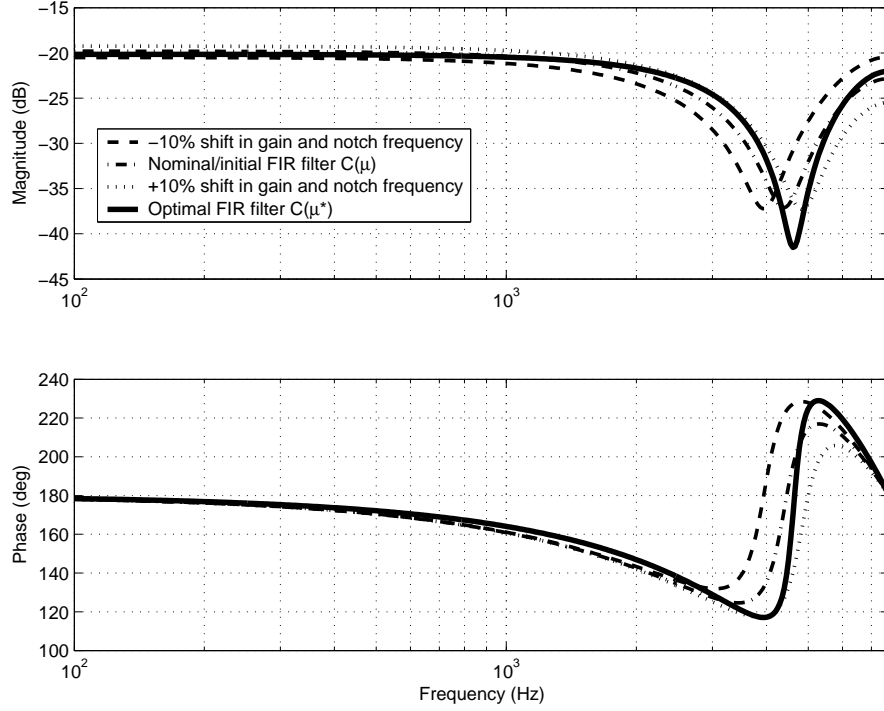
Figure 3.10: Frequency responses of FIR filter $C(\mu)$ with $\pm10\%$ shift in gain and notch frequency. Dash: -10% shift in gain and notch frequency. Dash-dot: nominal/initial FIR filter. Dot: +10% shift in gain and notch frequency. Solid: optimal FIR filter $C(\mu^*)$.

Frequency Responses

The open loop transfer functions using nominal controller and that with FIR filter $C(\mu)$ after being tuned using the proposed OICA algorithm for six iterations is shown in Figure 3.11. With the same controller order, the proposed OICA achieves better disturbance rejection even without prior knowledge of the disturbance model or increase the open loop gain crossover frequency for higher bandwidth.

The frequency response of the sensitivity transfer function is shown in Figure 3.12. The proposed OICA seeks to increase the gain at the resonant modes to create an attenuation notch in the sensitivity transfer function around the resonant

58
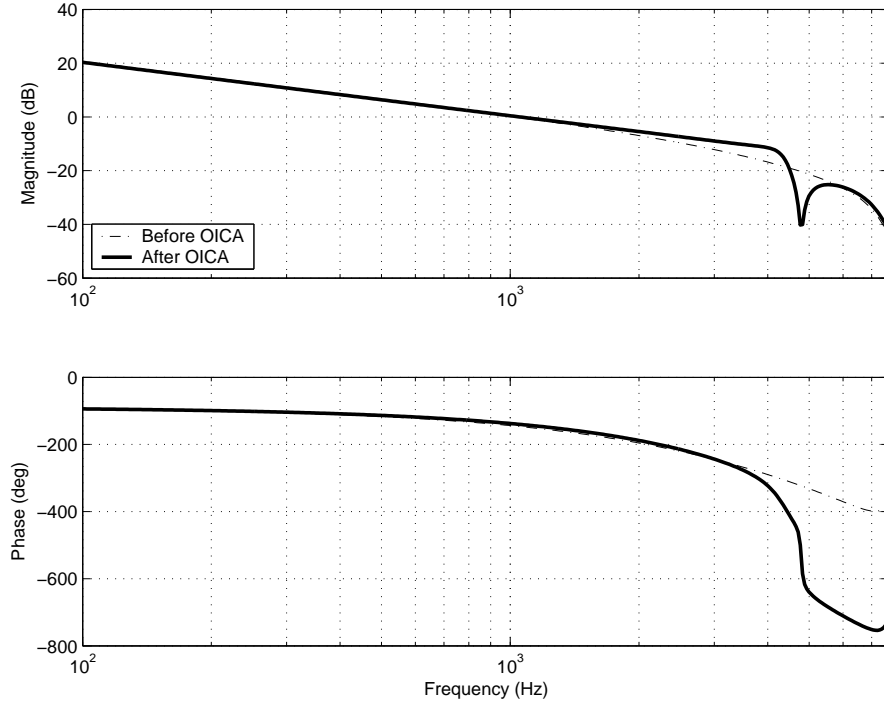
Figure 3.11: Frequency responses of open loop transfer functions. Dashed-dot: before OICA tuning. Solid: after six iterations of OICA tuning.

mode frequency region of 3–5 kHz where the PZT actuator's in-plane sway mode is and much of the high frequency NRRO spectrum is trapped. Another notch in sensitivity transfer function of smaller magnitude is also created at around 5–7 kHz region where much high frequency NRRO is concentrated at as shown earlier in Figure 3.7.

Time Responses

The time responses of the NRRO and control signal after six iterations of OICA are shown in Figure 3.13. A 3σ NRRO of 0.6101 μin translating to 164 kTPI at 10% tolerance is observed. It can be seen from Figures 3.6 and 3.13 that much of the variance of NRRO is reduced after six iterations of OICA tuning. The improvement
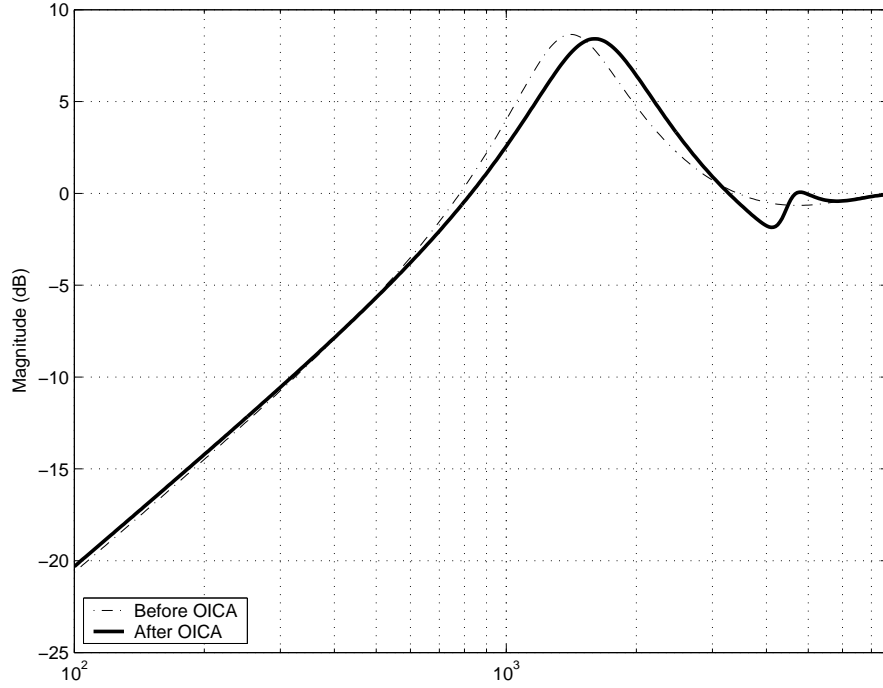
Figure 3.12: Magnitude responses of sensitivity transfer functions. Dashed: before OICA tuning. Solid: after six iterations of OICA tuning.

in time domain shows a 22% reduction in 3σ NRRO over the nominal controller when computed and the histograms are shown in Figure 3.14.

The power spectra of the experimental NRRO before and after proposed OICA is shown in Figure 3.15. As can be seen in the NRRO spectrum before OICA in Figure 3.7, much NRRO is trapped in the frequency region 3–5 kHz corresponding to the PZT actuator's sway mode at resonant frequency of 4.2 kHz and also in the high frequency region of about 5–7 kHz. With the attenuation notches in the sensitivity transfer function created at these frequency regions, the improvement in NRRO spectrum after OICA shows much amplitude reduction as shown in Figure 3.15. The base line curve at most frequencies is also effectively suppressed by the controller after the proposed OICA tuning.
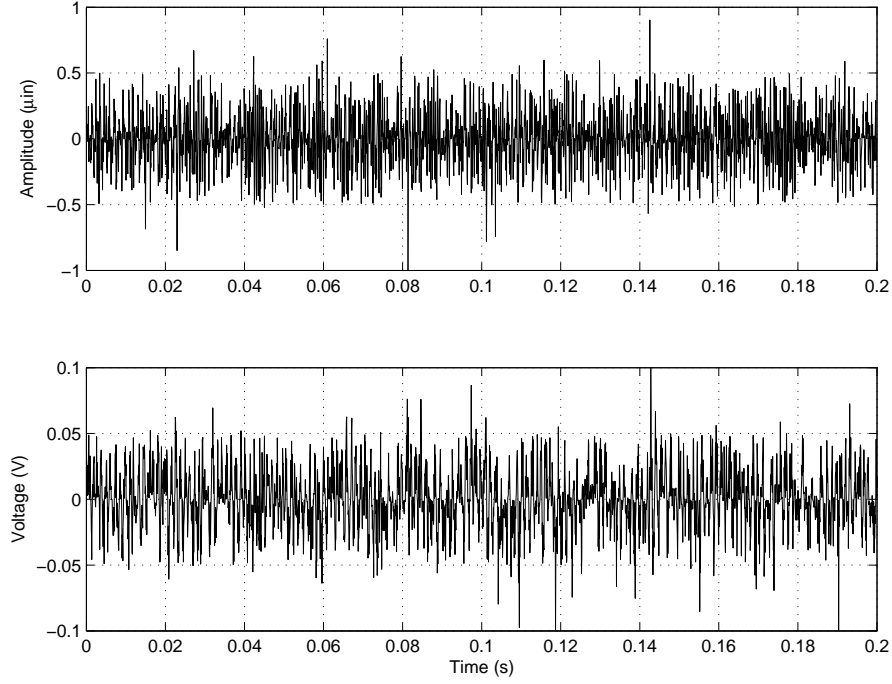
Figure 3.13: Time traces of NRRO (top) and control signal (bottom) after six iterations of OICA tuning.

3.5 Summary

In this chapter, an OICA (Online Iterative Control Algorithm) is proposed to minimize the square of $\mathcal{H}_2$-norm of T_{yw}, hence avoiding any ill-conditioned numerical issues commonly encountered when solving AREs and LMIs in robust and optimal controller synthesis for HDDs. The TMR budget is optimized for achieving higher recording densities via stronger NRRO rejection in future HDDs without prior knowledge of the dominant input and output disturbances spectra in measured PES. Experimental results using proposed OICA tuning for a third order FIR on a spinstand servo system show an improvement of 22% in 3σ NRRO and much baseline NRRO rejection without increase in servo bandwidth.

In the next chapter, we design add-on DDO (Disturbance Decoupling Ob-
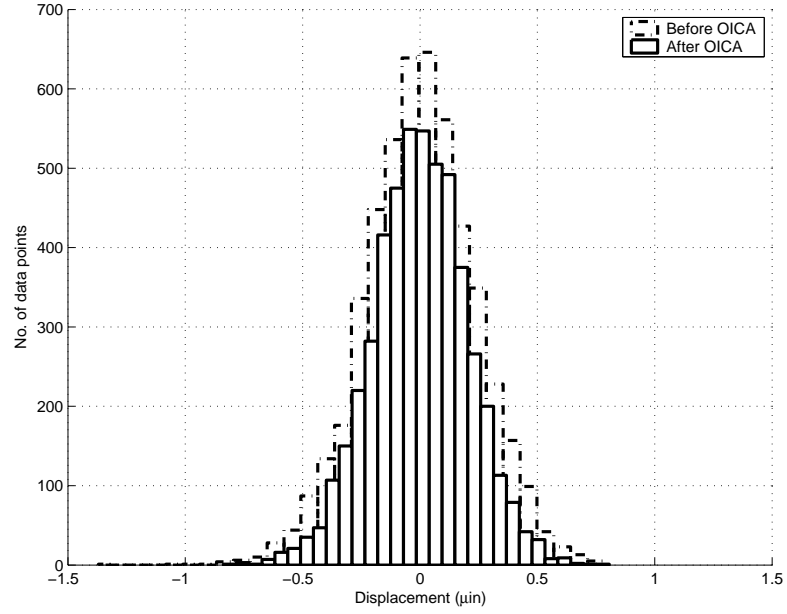
Figure 3.14: Histograms of NRRO spectra. Dashed-dot: before OICA tuning. Solid: after six iterations of OICA tuning.

servers) and DDOS (DDO with extraneous Sensors) to suppress these dominant input and output disturbances simultaneously. Concurrent suppression of noise is also feasible by using the proposed DDOS.
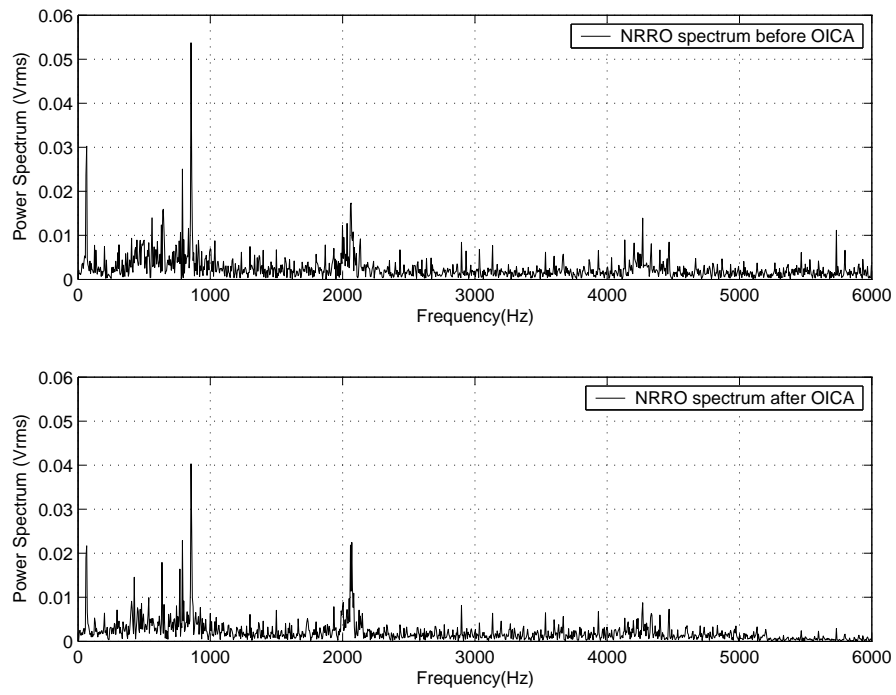
Figure 3.15: Experimental NRRO spectra. Top: before OICA tuning. Bottom: after six iterations of OICA tuning.

Chapter 4

Disturbance Suppression via Disturbance Decoupling Observers using Singular Perturbation

Precise servo control systems require strong disturbance rejection capabilities for accurate positioning in the nanometer scale. In this chapter, an add-on DDO (Disturbance Decoupling Observer) and DDOS (DO with extraneous Sensor) are proposed for stronger disturbance suppression. The control methodology uses a nominal plant model and its inverse to reject input and output disturbances simultaneously in sampled-data systems, with the plant inverse controller approximated by tuning a single parameter ε. Experimental results on a PZT actuated servo system with air flow of mean speed of 50 m/s corresponding to 15000 rpm in today's high end HDDs show an improvement of 69.2% of 3σ PES (Position Error Signal) during track-following.

4.1 Background

Reduction of $\mathcal{H}_2$- and $\mathcal{H}_\infty$-norms from disturbance sources to controlled output remain an important measure of designing servo systems for precision servo systems. These demands of ultra high and precise servo positioning accuracy directly translate into a high bandwidth servo system for ultra strong disturbance and vibration rejection capabilities. While the disturbance sources can be generally classified as periodic and aperiodic, most current disturbance rejections schemes are concerned with tackling them independently. Interested readers are referred to works by Duan *et al.* [20] for feedforward periodic RRO compensation and Pang *et al.* [92] for online iterative control of aperiodic NRRO rejection in HDDs.

To tackle the disturbance sources simultaneously, the effects of disturbances should be cancelled before they affect the true controlled output. This effectively requires making the sensitivity transfer function matrix S or $\mathcal{H}_2$- and $\mathcal{H}_\infty$-norms from output disturbance sources to controlled output to zero, the latter being commonly known as DDPs (Disturbance Decoupling Problems). Several disturbance decoupling (setting the norms to zero) and almost disturbance decoupling (almost zero) schemes have been proposed. Lin *et al.* in [66] explicitly parameterized in a single parameter which solves the well-known $\mathcal{H}_\infty$-ADDPMS ($\mathcal{H}_\infty$-Almost DDP with Measurement feedback and with internal Stability) for discrete-time linear systems. Chen *et al.* extended the framework and applied to disturbance decoupling control of a piezoelectric bimorph actuator with hysteresis in [11] successfully.

Alternatively, improved disturbance rejection capabilities via the construction of disturbance observers have also been introduced by Ohnishi in [81]. White *et al.* constructed a disturbance observer for improved track-following capabilities in HDDs without additional sensors in [118]. Goodwin also showed that introduction

of these schemes are highly cost effective and attractive alternatives to embedding sensors which are susceptible to measurement noise in [30].

In this chapter, an add-on DDO and DDOS into current sampled-data systems to mimic disturbance decoupling effects are proposed. The proposed DDO uses the identified discretized plant model and its inverse to reject input disturbances and output disturbances simultaneously. The nominal plant inverse is obtained by tuning a single parameter ε to approximate the causality of the improper plant inverse. The proposed control methodology is evaluated with simulation and experimental results on a PZT actuated passive suspension mounted on a head cartridge for usage on a spinstand as reported in [120].

4.2   Disturbance Decoupling Observer

For simplicity but without loss of generality, we consider the following SISO (Single-Input-Single-Output) digital sampled-data servo control system regulation problem with proposed DDO as shown in Figure 4.1.

The control signal u is given by

$$
\begin{aligned}
u &= u_k + u_o \\
&= Ke + z^{-\Delta}\widetilde{G}^{-1}\widehat{G}u + z^{-\Delta}\widetilde{G}^{-1}e
\end{aligned}
\tag{4.1}
$$

where $\widehat{G}$ is the identified discretized mathematical model of the plant to be controlled $G(s)$ using a ZOH equivalence at a chosen sampling rate the stable pole-zero pairs of plant $G(s)$ remain in the unit disc using the guidelines depicted in [6]. Δ is an integer included to prevent computational singularity and its choice will be detailed in future sections. $\widetilde{G}^{-1}$ is the proper and minimum phase inverse of the $\widehat{G}$. The procedure to obtain $\widetilde{G}^{-1}$ will be proposed in the next section.

66
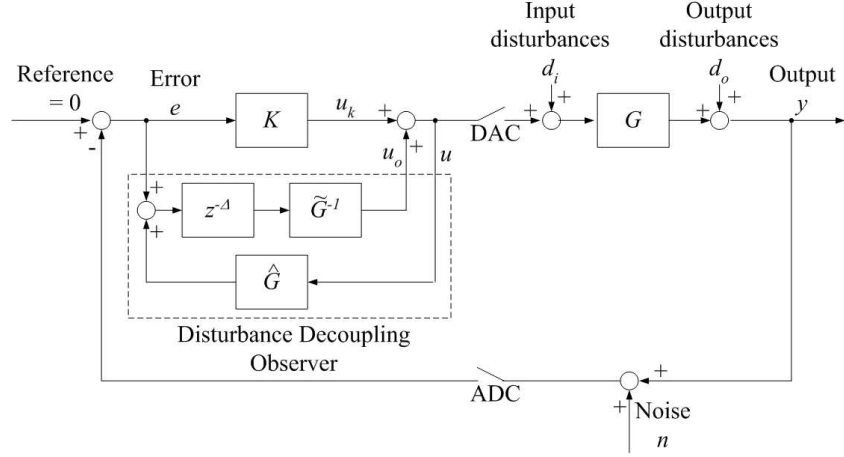
Figure 4.1: Block diagram of servo sampled-data control system with proposed DDO.

Straight forward manipulation results in

$$
\begin{aligned}
y &= d_o + G d_i + G u \\
&= \frac{1 - z^{-\Delta}\widetilde{G}^{-1}\widehat{G}}{1 - z^{-\Delta}\widetilde{G}^{-1}\widehat{G} + GK + z^{-\Delta}\widetilde{G}^{-1}G}\left(do + G d_i\right)\cdots \\
&\quad - \frac{GK + z^{-\Delta}\widetilde{G}^{-1}G}{1 - z^{-\Delta}\widetilde{G}^{-1}\widehat{G} + GK + z^{-\Delta}\widetilde{G}^{-1}G}\, n
\end{aligned}
\tag{4.2}
$$

The main motivation of the proposed DDO comes from the renowned IMP (Internal Model Principle) which includes $\widehat{G}$ as part of the feedback controller for state estimation. $\widetilde{G}^{-1}$ compensates for the resonant poles and anti-resonant zeros of the plant as well as decreases the relative degree of the open loop transfer function for lower sensitivity.

The results can be expanded to MIMO (Multi-Input-Multi-Output) framework if G is square and non-singular.

4.2.1 Complete Disturbance Suppression

In view of Equation (4.2), we propose the following

Theorem 3.1 *Consider the following optimization problem*

$$V = \arg\min_{\mu} \left\| 1 - z^{-\Delta} \widetilde{G}^{-1}(\mu)\widehat{G} \right\|_{\infty} \tag{4.3}$$

subject to $\Delta = 0$ and the constraint

$$\widetilde{G}^{-1}(\mu) \in R\mathcal{H}_{\infty} \tag{4.4}$$

we can obtain perfect disturbance suppression with proposed DDO if the plant G is proper and of minimum phase.

Proof 3.1 Assuming a chosen sampling frequency f_s such that the pole-zero pairs of stable plant G remain in the unit disc [6] and non-minimum phase behaviour of the plant is removed. The ZOH discrete equivalence of plant G with model $\widehat{G}$ can be written in standard state-space formulation as

$$x(k+1) = \Phi x(k) + \Gamma u(k) \tag{4.5}$$

$$y(k) = Hx(k) + Ju(k) \tag{4.6}$$

where Φ, Γ, H and J are the sampled-data system state matrix quadruple. The plant inverse model $\widetilde{G}^{-1}$ can then be obtained via

$$\begin{bmatrix} \Phi & \Gamma \\ H & K \end{bmatrix}^{-1} = \begin{bmatrix} \Phi - \Gamma J^{-1}H & \Gamma J^{-1} \\ -J^{-1}H & J^{-1} \end{bmatrix} \tag{4.7}$$

From Equation (4.2), the first term becomes zero and we have only

$$y = -n \tag{4.8}$$

which shows that the proposed DDO cancels the input disturbances d_i and output disturbances d_o. Only the effects of measurement and sensor noise permeate to the true controlled output y. $\square$

While this method extends only to stable and proper systems (translating to direct feedthrough from control signal u to output y), it is not viable for physical systems which are generally low pass in nature. Moreover due to the constraint of $S + T = 1$ where S is the sensitivity transfer function and T being the complementary sensitivity transfer function, Theorem 3.1 makes $S = 0$ or an infinite bandwidth servo system which is not achievable in practice.

4.2.2 Almost Disturbance Suppression

Most physical systems are strictly proper with high frequency roll-off characteristics in nature. As such if the digital inverse model $\widetilde{G}^{-1}$ can only be approximated up to high frequencies—for *e.g.* using ZPET (Zero Phase Error Tracking) algorithm proposed by Tomizuka in [110] or the NPM (Near Perfect Modeling) methodology proposed by Pang *et al.* in [95]—before Nyquist frequency in sampled-data systems to prevent unbounded control signals. The disturbance rejection capabilities of the proposed DDO is deteriorated, with the performance of the servo system now determined by the proximity of the inverse plant model $\widetilde{G}^{-1}$ and the true plant inverse $\widehat{G}^{-1}$ at most frequencies. The effects of measurement and sensor noise n will also be attenuated by the complementary sensitivity transfer function.

Obviously, $J = 0$ if G is strictly proper as the relative degree of G is now at least one. While Theorem 3.1 still holds, Proof 3.1 does not as singularity now occurs when evaluating J^{-1} in Equation (4.7). As such, we propose the following simple methodology using a SP (Singular Perturbation) approach [56][57]

Proposition 3.1 *Consider Theorem 3.1 and the inverse dynamics problem posed in Equation (4.7). The singularity encountered in $J = 0$ is avoided using a SP technique by first introducing ε into the state space representation of strictly*

proper plant G

$$\dot{x} = Ax + Bu \tag{4.9}$$

$$y = Cx + \varepsilon u \tag{4.10}$$

where A, B, and C are the system state matrix triple with $0 < \varepsilon \ll 1$. After ZOH discretization, the singular perturbed system is invertible using Equation (4.7).

Similarly, we assume a chosen sampling frequency f_s such that the pole-zero pairs of singular perturbed system remain in the unit disc [6] and non-minimum phase behaviour of the plant is removed. The proof is now straightforward and ε acts as a controller tuning parameter. If we choose $0 < \varepsilon \ll 1$, the sensitivity transfer function S also approaches zero and we get the following approximation

$$y \approx -n \tag{4.11}$$

The geometric interpretation $S + T = 1$ is shown in Figure 4.2. It is worth noting that using the SP approach, decreasing ε has the effect of increasing bandwidth of the servo system (better disturbance suppression) and the size of norm of vector T (hence reducing the size of norm of vector S) without decreasing the size of θ where θ is the angle between S and T. A small θ is hence ideal as a large θ causes large peaks in the largest singular values of both S and T.

4.2.3 Choice of Delay Order

However, the proposed SP method is sensitive to effects of high frequency measurement and sensor noise. In practice, this method of evaluating the plant inverse $\widehat{G}^{-1}$ deteriorates when the relative degree of the plant is large. This is apparent due to the large differentiating effects at high frequencies on attempting plant inversion.
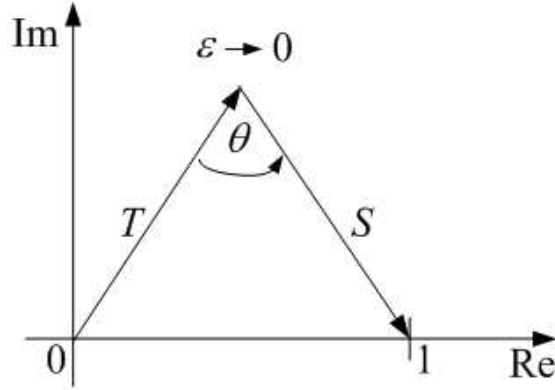
Figure 4.2: Geometric interpretation of feedback control constraint $S + T = 1$.

As such, the delay element is included to compensate for the relative degree by placing excess deadbeat poles. A rule of thumb for choosing Δ is to set it as the difference between the relative degree and two. The inclusion of the delay term with an appropriate choice of Δ increases θ and also avoids large peaks in S and T.

4.3 Disturbance Decoupling Observer with Extraneous Sensor

Addition of sensors to control systems are known to enhance servo performance and reduce the order of observers used in controller designs. In this section, we introduce a DDOS when additional information is available for feedback control with state measurements. This can be obtained via embedding additional sensors or SSA, the latter being more ideal as it requires only cheap electronics while achieving sensor-actuator collocation pair [87].

Similarly, consider the following SISO digital sampled-data servo control system regulation problem with proposed DDOS as shown in Figure 4.3.
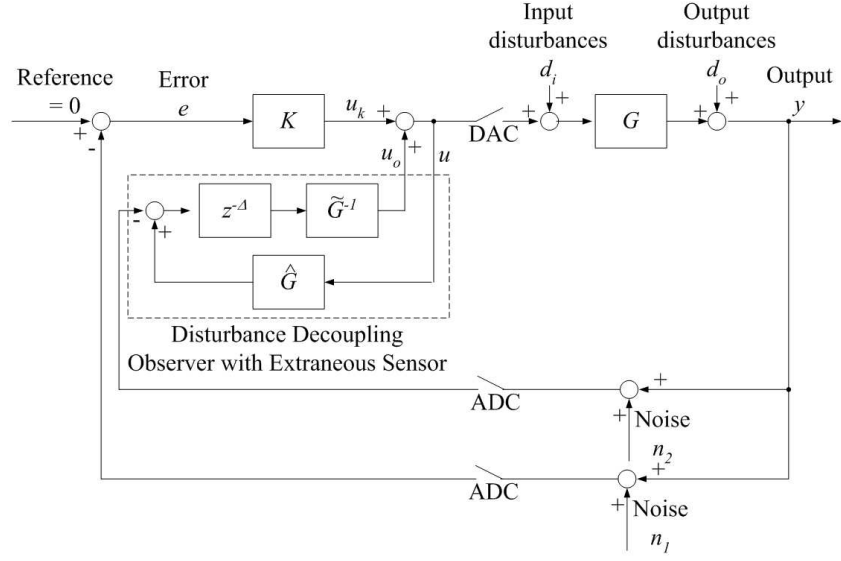
Figure 4.3: Block diagram of servo sampled-data control system with proposed DDOS.

The control signal u is given by

$$
\begin{aligned}
u &= u_k + u_o \\
&= Ke + z^{-\Delta}\widetilde{G}^{-1}\Big(\widehat{G}u - y - n_2\Big)
\end{aligned}
\tag{4.12}
$$

where n_2 is the noise introduced by the additional sensor. It is assumed that the noise sources n_1 and n_2 are mutually uncorrelated.

Straight forward manipulation again yields the following relation

$$
\begin{aligned}
y &= d_o + Gd_i + Gu \\
&= \frac{1 - z^{-\Delta}\widetilde{G}^{-1}\widehat{G}}{1 - z^{-\Delta}\widetilde{G}^{-1}\widehat{G} + GK + z^{-\Delta}\widetilde{G}^{-1}G}\Big(do + Gd_i\Big) \cdots \\
&\quad - \frac{GK}{1 - z^{-\Delta}\widetilde{G}^{-1}\widehat{G} + GK + z^{-\Delta}\widetilde{G}^{-1}G}\, n_1 \cdots \\
&\quad - \frac{z^{-\Delta}\widetilde{G}^{-1}G}{1 - z^{-\Delta}\widetilde{G}^{-1}\widehat{G} + GK + z^{-\Delta}\widetilde{G}^{-1}G}\, n_2
\end{aligned}
\tag{4.13}
$$

Similarly, the results can be expanded to MIMO framework if G is square and non-singular.

4.3.1 Complete Disturbance Suppression with Extraneous Sensor

With the new results and additional actuator information, we propose the following

Theorem 3.2 *Consider Theorem 3.1 and the inverse dynamics problem posed in Equation (4.7). We can achieve perfect disturbance suppression using the additional sensor with the noise sources n_1 and n_2 attenuated by T and S, respectively, where T and S are the nominal complementary sensitivity and sensitivity transfer functions, respectively.*

Proof 3.2 Refer to the control block diagram with proposed DDOS depicted in Figure 4.3. By setting $u_o = 0$, the nominal complementary sensitivity transfer function T and sensitivity transfer function S are given by

$$T = \frac{GK}{1 + GK} \tag{4.14}$$

$$S = \frac{1}{1 + GK} \tag{4.15}$$

If Theorem 3.3.1 is satisfied, then the true controlled output y in Equation (4.13) reduces to

$$y = -\frac{GK}{1 + GK} n_1 - \frac{1}{1 + GK} n_2$$

$$= -Tn_1 - Sn_2 \quad \square \tag{4.16}$$

Dissimilar to the DDO where the noise n permeates to the true controlled output y, the DDOS using an extraneous sensor offers attenuation of nominal noise n_1 with nominal complementary sensitivity transfer function T which is in essence a low pass filter. The noise source n_2 introduced by the additional sensor becomes an output disturbance to the nominal control loop. This implies that

additional output information—though same measurement—can be used to achieve disturbance rejection and noise attenuation simultaneously assuming that noise sources n_1 and n_2 are uncorrelated. As such, the effects of noise on including additional sensor can be removed with any loop shaping design for low sensitivity.

4.3.2   Almost Disturbance Suppression with Extraneous Sensor

Analogous to the almost disturbance suppression in DDO, the almost disturbance suppression with extraneous sensor in DDOS avoids the singularity encountered in $J = 0$ for physical systems by using the SP technique with $0 < \varepsilon \ll 1$ [56][57] as mentioned in the previous section.

Proposition 3.2 *Consider Theorem 3.1, Theorem 3.2 and the inverse dynamics problem posed in Equation (4.7). The singularity encountered in $J = 0$ is avoided using a SP technique by first introducing ε into the state space representation of strictly proper plant G*

$$\dot{x} \;=\; Ax + Bu \tag{4.17}$$

$$y \;=\; Cx + \varepsilon u \tag{4.18}$$

where A, B, and C are the system state matrix triple with $0 < \varepsilon \ll 1$. After ZOH discretization, the singular perturbed system is invertible using Equation (4.7).

Similarly, we assume a chosen sampling frequency f_s such that the pole-zero pairs of singular perturbed system remain in the unit disc [6] and non-minimum phase behaviour of the plant is removed. Equation (4.7) can now be used with ε as a controller tuning parameter. When $0 < \varepsilon \ll 1$, we get the following approximation

for true controlled output y

$$y \approx -Tn_1 - Sn_2 \qquad (4.19)$$

We achieved almost disturbance suppression with simultaneous attenuation of noise sources n_1 and n_2, not possible without additional sensor information.

4.4   Industrial Application

In this section, we shall evaluate the effectiveness of the proposed DDO scheme for simplicity but without loss of generality. Simulation and experiments are conducted on a PZT actuated head cartridge reported by Wong *et al.* in [120] and shown in Figure 4.4.
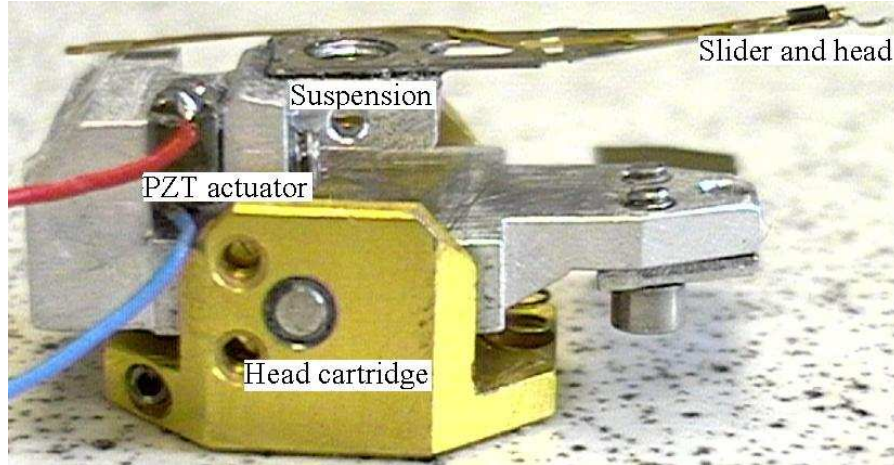
Figure 4.4: PZT-actuated head cartridge with mounted passive suspension carrying a slider and R/W head used in a spinstand.

It is worth noting that the PZT active suspension commonly envisaged for usage in future dual-stage HDDs can also be used. The nominal DDO is chosen to illustrate the effectiveness of our proposed schemes as it is well known from control

theory that additional sensors improve servo performance if SNR (Signal-to-Noise Ratio) and resolution of the sensors are satisfactory. Also, we expect the DDOS to perform better if extraneous sensors are available as the propositions and problem formulations for both DDO and DDOS are inherently similar.

The frequency response of the PZT actuated head cartridge with passive suspension is shown in Figure 4.5. The nominal plant model of the PZT actuated
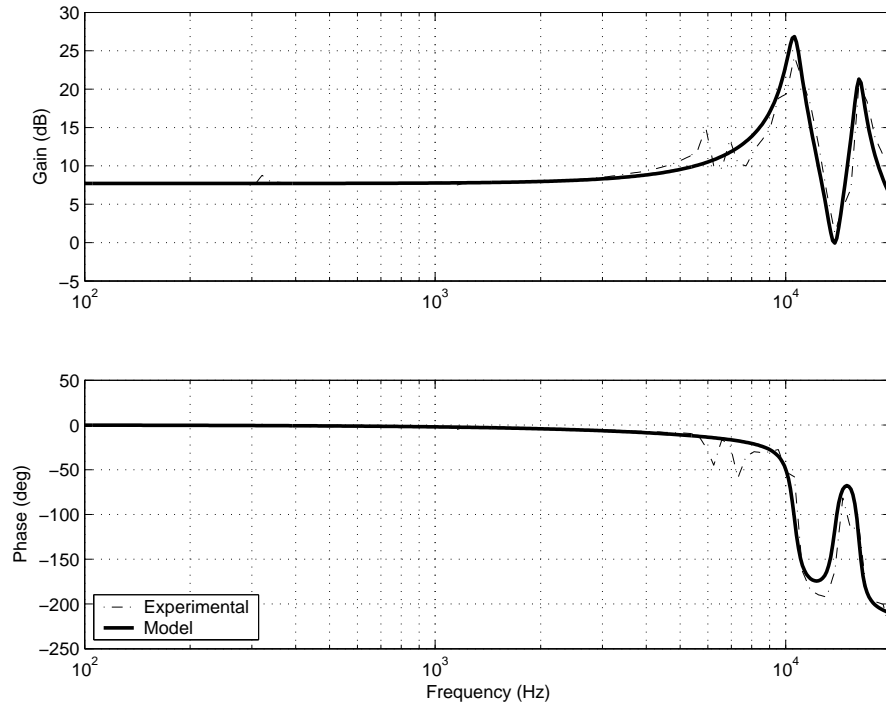
Figure 4.5: Frequency response of the PZT actuated head cartridge with mounted passive suspension.

head cartridge $G(s)$ is identified with resonant poles at 10.6 kHz and 16.2 kHz as well as anti-resonant zeros at 13.8 kHz. For our application, the sway modes at these frequencies are identified while the torsional modes at 5.6 kHz and 7.1 kHz are not included as they are out-of-plane (weakly uncontrollable). $G(s)$ is then discretized via a ZOH at a sampling rate f_s of 40 kHz so that the stable pole-zero pairs of $G(s)$ remain in the unit disc [6]. The transfer function of the discretized

plant $G(z)$ is identified as

$$G(z) = \frac{1.6919(z + 0.9729)(z^2 - 0.2433z + 0.8912)}{(z^2 - 0.854z + 0.9151)(z^2 + 0.2329z + 0.9033)} \qquad (4.20)$$

The relative degree of the $G(z)$ is unity and hence Δ is set to zero.

For the digital controller $K(z)$, a practical integrator (by setting pole at 10 Hz instead of origin to prevent actuator saturation from very large low frequency gain) in series with a low pass filter of corner frequency at 5 kHz is used. An extra zero is placed near Nyquist frequency of 20 kHz to reduce the relative degree of $K(z)$ without affecting mid frequency performance, thereby achieving low sensitivity [95]. To tackle the resonant modes, digital notch filters are constructed to attenuate the large gains of the sway modes at 10.6 kHz and 16.2 kHz caused by the PZT actuated passive suspension. As such, the transfer function of $K(z)$ considering the practical integrator, low pass filter, extra zero, notch filters and a gain to ensure the gain crossover frequency is at 3.5 kHz is given by

$$\begin{aligned} K(z) &= 0.033049 \frac{z + 0.998}{z - 0.998} \frac{z + 0.222}{z - 0.4361} \frac{z^2 + 1.623z + 0.9667}{z^2 + 1.287z + 0.5597} \cdots \\ &\quad \times \frac{z^2 + 0.2405z + 0.9707}{z^2 + 0.1632z + 0.3367} \end{aligned} \qquad (4.21)$$

The frequency response of $K(z)$ is shown in Figure 4.6.

4.4.1 Simulation Results

To illustrate the effectiveness of our proposed DDO, simulations are carried out with reference to a "standard" DO used for track following operations in HDD servo control as detailed by White *et al.* in [118]. For the standard DO, the Q-filter is designed to be a second order transfer function of unity DC gain and damping with natural frequency at 3.5 kHz, corresponding to the gain crossover frequency of the
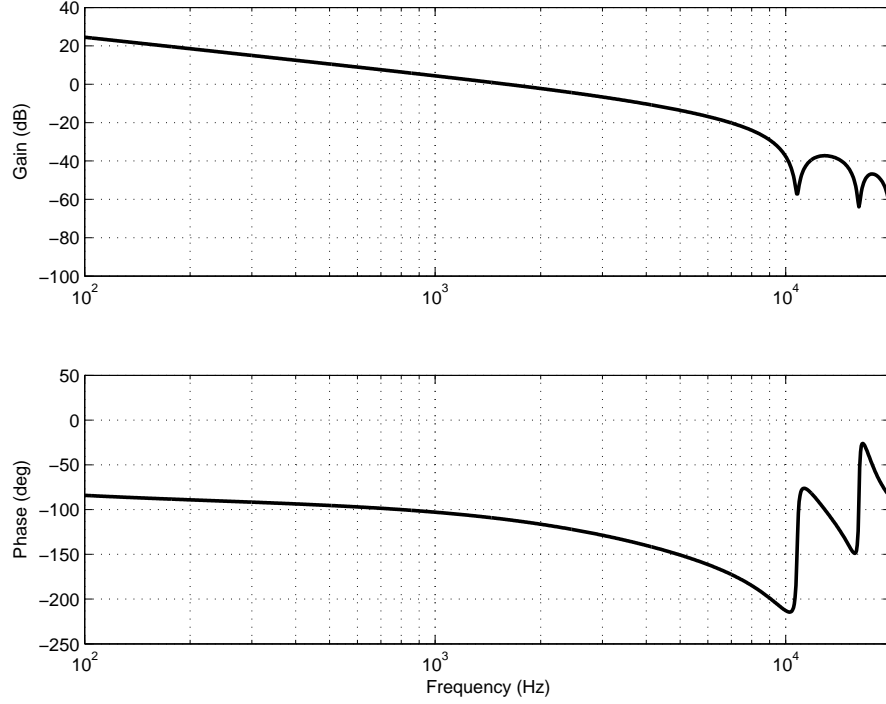
Figure 4.6: Frequency response of designed controller $K(z)$.

nominal open loop transfer function. The plant inverse is designed according to ZPET methodology detailed by White *et al.* in [118] and Tomizuka in [110].

Choice of ε

The performance of the proposed DDO is dependent on the accuracy of the plant inverse model $\widehat{G}^{-1}$. The frequency response of $\widehat{G}^{-1}(z)G(z)$ for different values of ε is shown in Figure 4.7. From the above, it can be seen that decreasing ε effectively increases the frequency range where the $\widehat{G}^{-1}(z)G(z) = 1$. However, further reduction of ε results in a larger peak at high frequencies which degrades closed-loop stability. Decreasing ε also increases the high frequency gain of the controller, resulting in amplification of measurement noise and high frequency signal amplification which might saturate the actuators. The authors recommend a
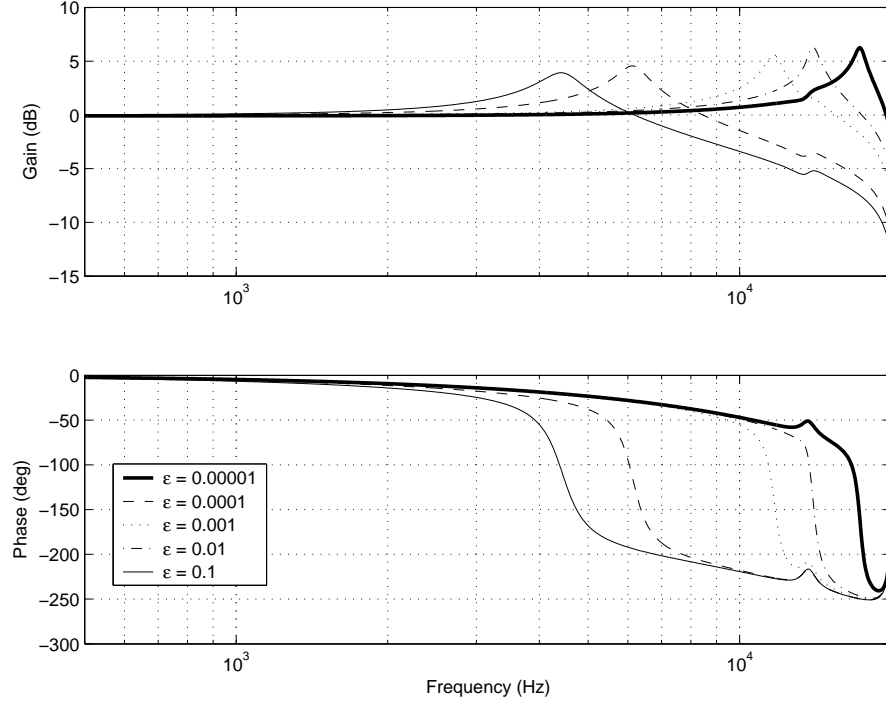
Figure 4.7: Frequency response of $\widehat{G}^{-1}(z)G(z)$ for different values of ε.

range of $1 \times 10^{-4} \leq \varepsilon \leq 5 \times 10^{-3}$ for a compromise between performance of the DDO and noise attenuation. For the rest of our discussions, an $\varepsilon = 1 \times 10^{-3}$ is used.

Frequency Responses

The simulated frequency responses of the open loop transfer functions without DO, with a standard DO and with our proposed DDO are shown in Figure 4.8. The standard DO shapes the frequency response of the open loop transfer function at high frequencies (after gain crossover frequency) with increased phase lifting and reduced roll-off. The increased phase margin corresponds to a "lighter" servo system, increasing the phase margin for robust stability and reduces the seek time during short-span tracking operations. The reduced roll-off translates to a sensi-
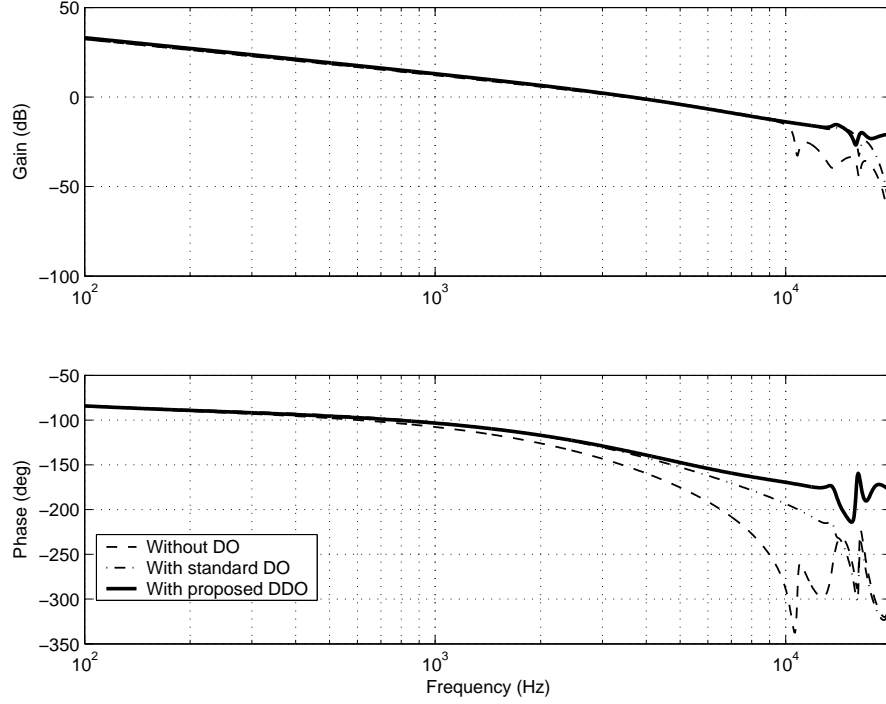
Figure 4.8: Frequency responses of open loop transfer functions. Dashed: without DO. Dashed-dot: with standard DO. Solid: with proposed DDO.

tivity transfer function with reduced positive area (or "hump") after gain crossover frequency and hence impedes amplification of high frequency disturbances at frequencies where feedback control is degrading servo performance [95].

With the proposed DDO, the low frequency gain is increased while maintaining the same gain crossover frequency at 3.5 kHz with alleviated phase delay and roll-off simultaneously as can be seen from Figure 4.8. Due to parallel compensation, the open loop transfer function is able to achieve a higher bandwidth via the approximate plant inverse model $\widehat{G}^{-1}$ which compensates for the stable pole-zero pairs in plant G. The low frequency disturbance rejection performance is improved, coupled with an even lower positive area in sensitivity transfer function. This is verified with the simulated frequency responses of the sensitivity transfer functions S shown in Figure 4.9. Stronger error rejection is achieved with the proposed
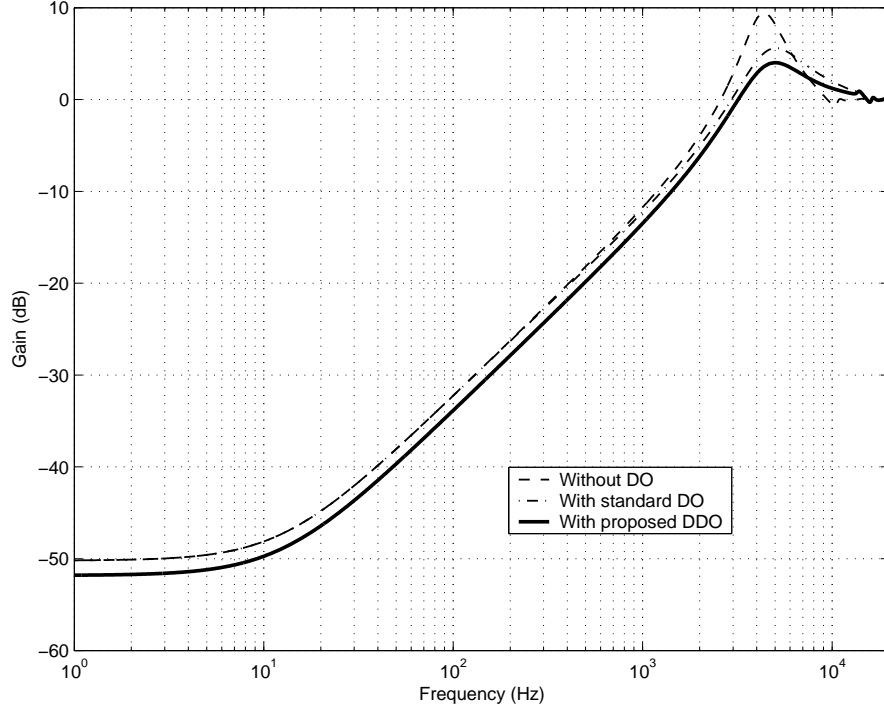
Figure 4.9: Frequency responses of sensitivity transfer functions S. Dashed: without DO. Dashed-dot: with standard DO. Solid: with proposed DDO.

DDO even though the gain crossover frequency is maintained at 3.5 kHz for all three cases.

The proposed DDO is linear and hence is still bounded by the "waterbed" effect as depicted by Discrete Bode's Integral Theorem [76]. While much sensitivity reduction can be seen at most frequencies, the excavated sensitivity area at low frequencies and the "hump" is actually (and automatically) distributed evenly over high frequencies for low sensitivity up to Nyquist frequency *i.e.* the gain of the sensitivity transfer function reaches 0 dB more gradually but with a smaller amplitude. This phenomenon can be observed for the frequency response of the sensitivity transfer function as shown in Figure 4.9 using the proposed DDO.

PES Test

To demonstrate the effectiveness of our proposed DDO scheme, simulations are carried out to evaluate the 3σ PES or TMR (Track Mis-Registration) during track following control operations where σ is the standard deviation. The identified vibration and noise sources models reported by Du *et al.* in [18] with a Fujitsu fluid bearing spindle motor HDD rotating at 5400 rpm is used to emulate output disturbances d_o and noise n, respectively. While the torque disturbance reported in [18] is not applicable, a low frequency sinusoid of $0.01 \sin(2\pi 50t)$ is used to simulate the effects of input disturbances d_i. The simulated measured PES e without DO, with a standard DO and with the proposed DDO are shown in Figure 4.10. An improvement of 79.5% in 3σ PES is observed.
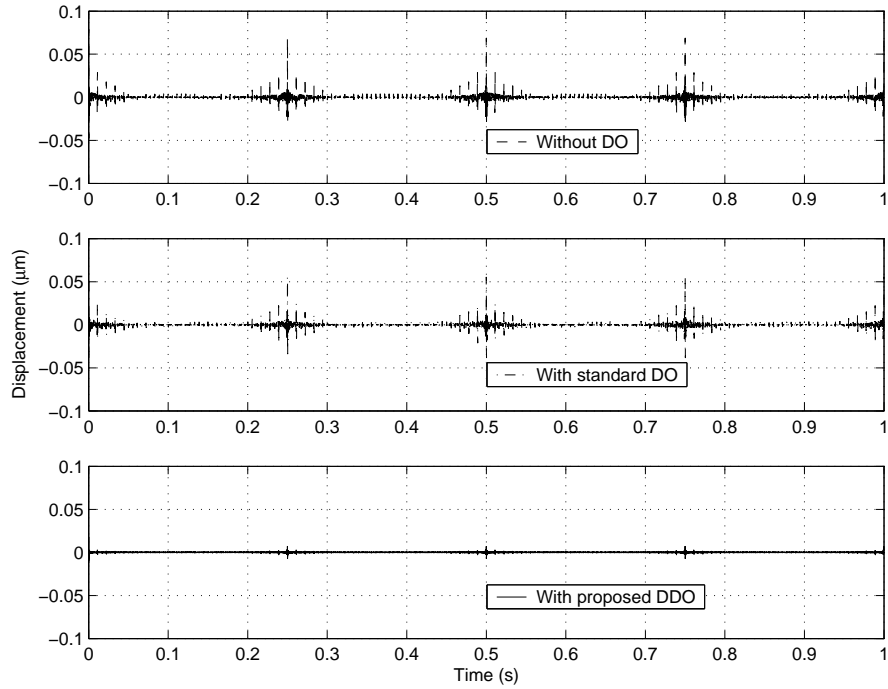
Figure 4.10: Simulation results of measured PES e. Dashed: without DO. Dashed-dot: with standard DO. Solid: with proposed DDO.

82

The standard DO improves the 3σ PES from 0.0083 μm to 0.0074 μm (a 16.0% improvement) while the proposed DDO is able to reduce the 3σ PES further to 0.0017 μm, corresponding to a 79.5% improvement. The histograms of measured PES e without DO, with a standard DO and with the proposed DDO are shown in Figure 4.11. The variance of PES is greatly reduced.
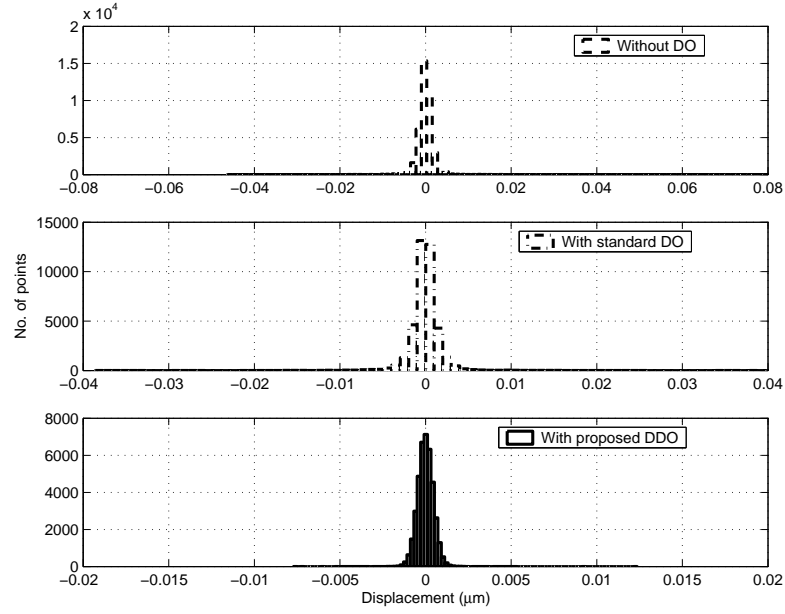
Figure 4.11: Histogram of measured PES e. Dashed: without DO. Dashed-dot: with standard DO. Solid: with proposed DDO.

Robustness Analysis

For the algorithm to be used by data storage industries in mass production, the performance of the proposed DDO should be robustly stable. To demonstrate the robustness of the proposed control scheme, we perturb the dynamics of the PZT actuated head cartridge with mounted passive suspension by up to $\pm10\%$ as shown in Figure 4.12.
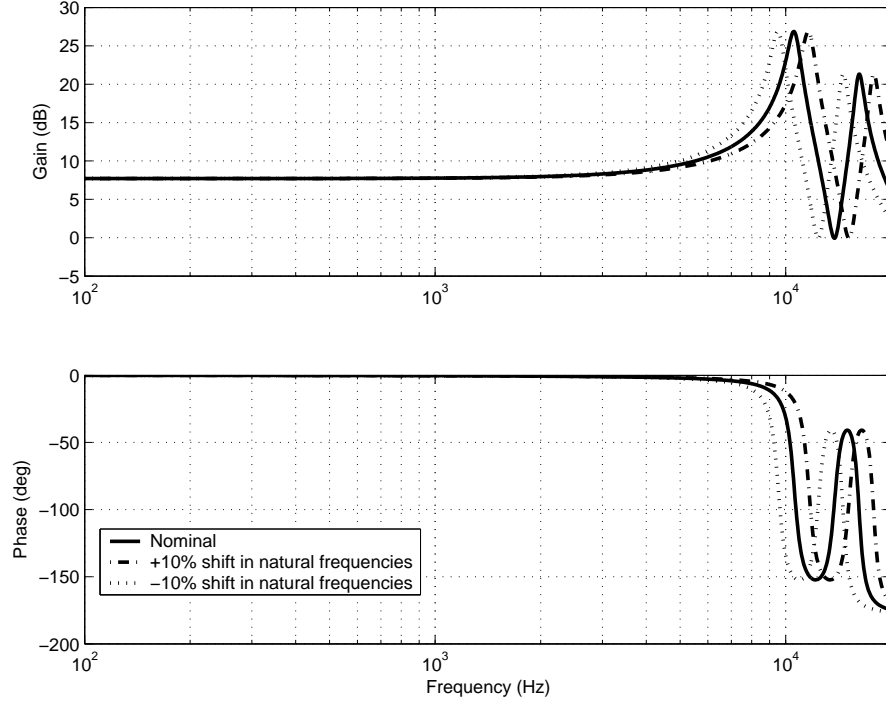
Figure 4.12: Frequency responses of perturbed PZT-actuated head cartridge with mounted passive suspension by $\pm 10\%$ in natural frequncies.

The controller design for high bandwidth remains stable for the range of frequency uncertainties. However, degradation in percentage reduction of measured PES e employing the proposed DDO occurs when the shifts in resonant frequencies exceed more than $\pm 7\%$ as can be seen in Figure 4.13 although the nominal closed-loop remains robustly stable.

4.4.2 Experimental Results

For our experiments, the LDV (Laser Doppler Vibraometer) is used as a displacement sensor to measure the displacement of the R/W head non-intrusively and the measured voltage output is collected as measured PES e.
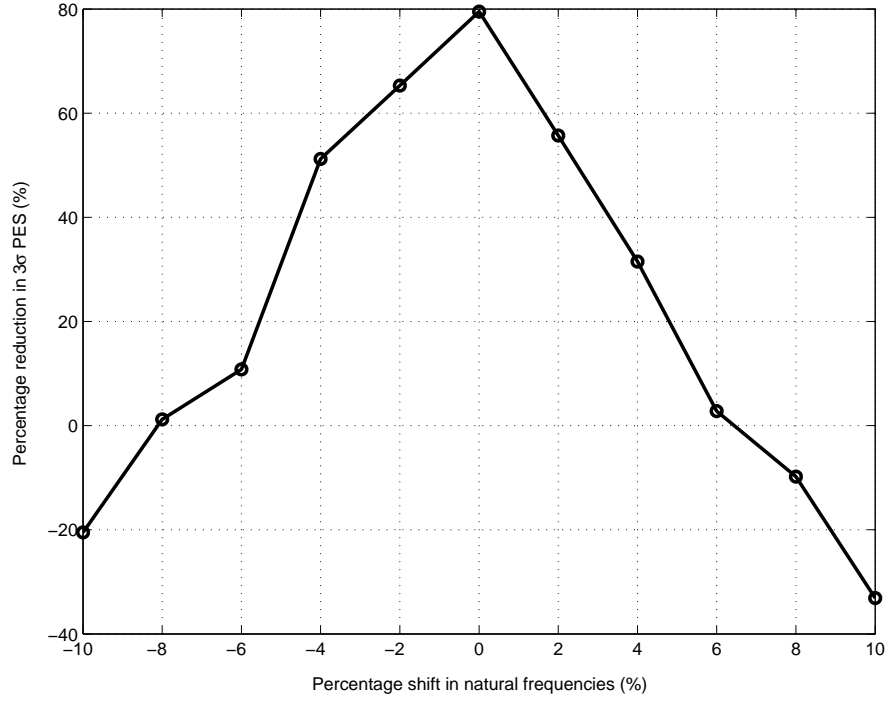
Figure 4.13: Graph of percentage reduction in 3σ PES vs percentage shift in resonant and anti-resonant frequencies.

Frequency Responses

The experimental frequency response of open loop transfer function with the proposed DDO is shown in Figure 4.14. The corresponding experimental frequency response of sensitivity transfer function S and complementary sensitivity transfer function T are drawn in Figure 4.15.

From the figures above, it can be seen that experimental results tally well with the simulated frequency responses of open loop transfer function in Figure 4.8 as well as sensitivity and complementary sensitivity transfer functions in Figure 4.9.
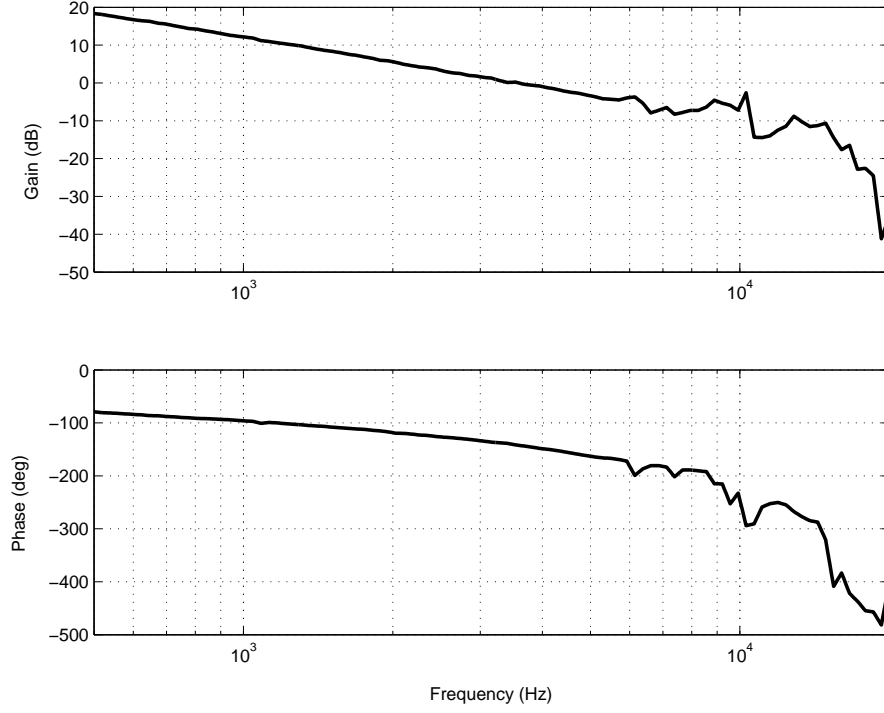
Figure 4.14: Frequency response of experimental open loop transfer function with DDO.

Disturbance Rejection Test

In this section, we conduct experiments to showcase the effectiveness of the proposed control scheme in rejecting input disturbances d_i and output disturbances d_o simultaneously.

By closing the loop with $K(z)$ only and setting a zero reference, the measured PES e from the LDV and the corresponding control signal u is shown in Figure 4.16. A low frequency measurement noise of about 20 Hz from the LDV is observed. The 3σ measured PES e is about 0.0174 μm for the length of data logged.

By including the proposed DDO with $K(z)$ and setting a zero reference, the measured PES e and the corresponding control signal u is shown in Figure 4.17.
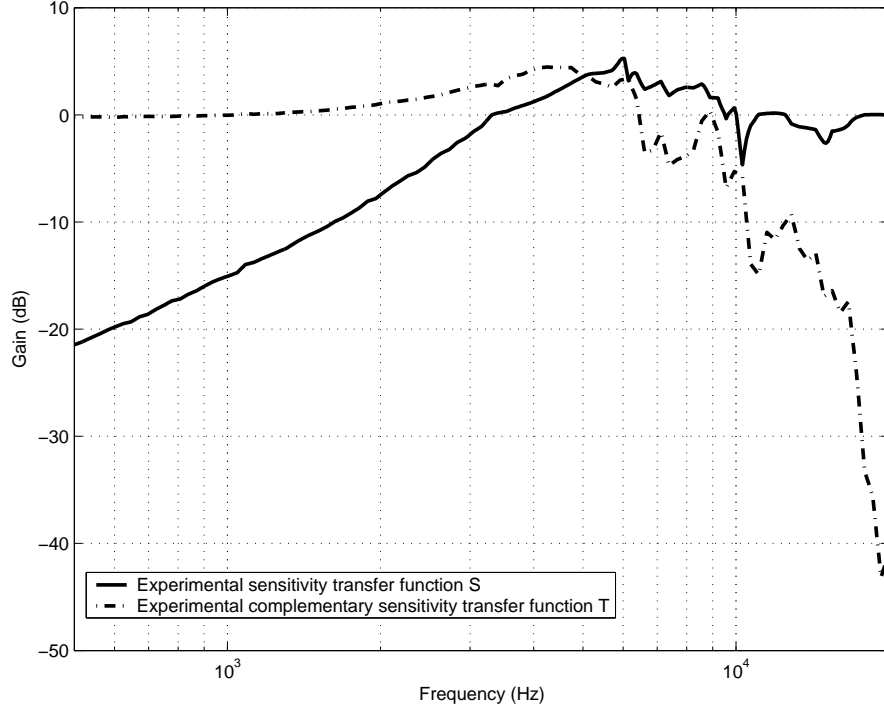
Figure 4.15: Experimental frequency responses of sensitivity transfer functions with DDO.

The 3σ measured PES e is now about 0.0136 μm and hence a 16% improvement in 3σ measured PES e from 0.0174 μm to 0.0136 μm is obtained.

While the improvement seems trivial, we emulate a HDD environment using airflow with the centrifugal fan turned on as shown in Figure 4.18. The windage across the entire passive suspension arm and air flow induced suspension vibrations are considered as input disturbances d_i and output disturbances d_o to the HDD servo system. The wind tunnel linearizes and concentrates the air flow and hence increases the airflow's mean speed to about 50 m/s, corresponding to the amount of airflow the R/W head experiences at the OD (Outer Diameter) of a 2.5" disk at a fast spindle rotation speed of 15000 rpm in current high end HDDs for servers. The air flow from the wind tunnel is directed at the entire passive suspension arm while the measure PES e is collected at the R/W head using LDV.
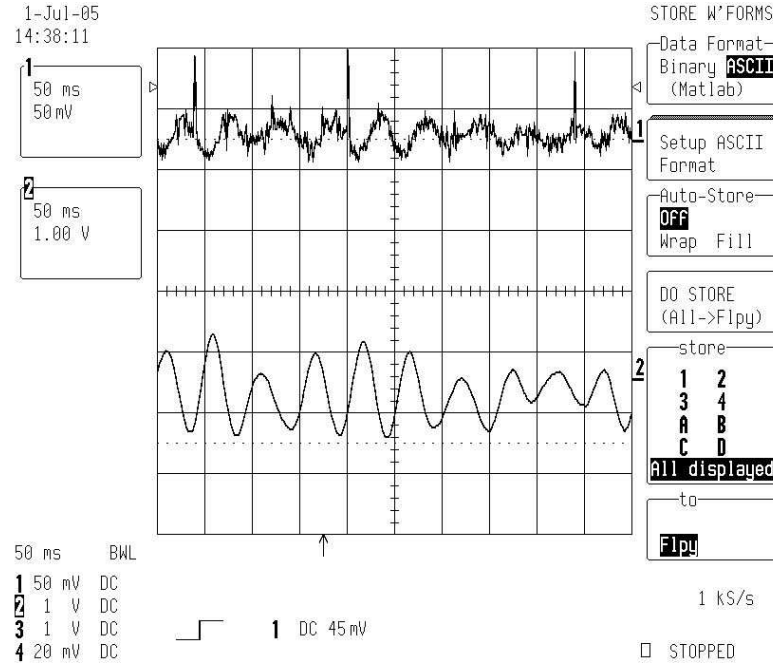
Figure 4.16: Measured PES e in channel 1 (top) and control signal u in channel 2 (bottom) with nominal controller $K(z)$ only, *i.e.* without DDO.

With $K(z)$ only, the measured PES e and the corresponding control signal u is shown in Figure 4.19. Although a high servo bandwidth of up to 3.5 kHz and low sensitivity controller are used, the amount of air flow on the passive suspension causes the R/W head to be deviated from the track centre on a large magnitude. The 3σ measured PES e now becomes 0.0578 μm with a horrendous deterioration of up to 230%.

By including the proposed DDO, the experiment is repeated with the centrifugal fan on. The measured PES e and the corresponding control signal u is shown in Figure 4.20. The 3σ measured PES e is now about 0.0178 μm and hence a 69.2% improvement in 3σ measured PES e from 0.0578 μm to 0.0178 μm is observed. The DDO constricts the effects of input and output disturbances to bring the standard deviation of measured PES e near to the case without the centrifugal fan on.
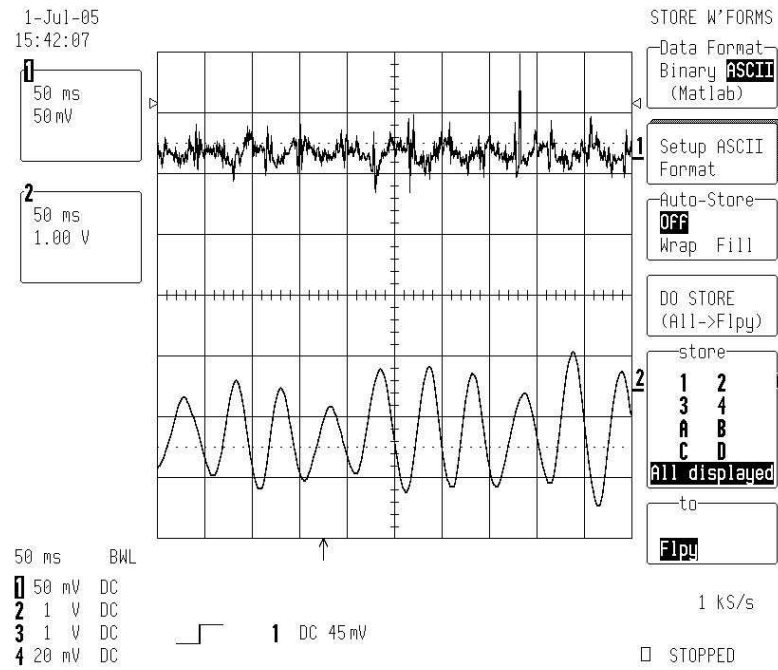
Figure 4.17: Measured PES e in channel 1 (top) and control signal u in channel 2 (bottom) with controller $K(z)$ and proposed DDO.
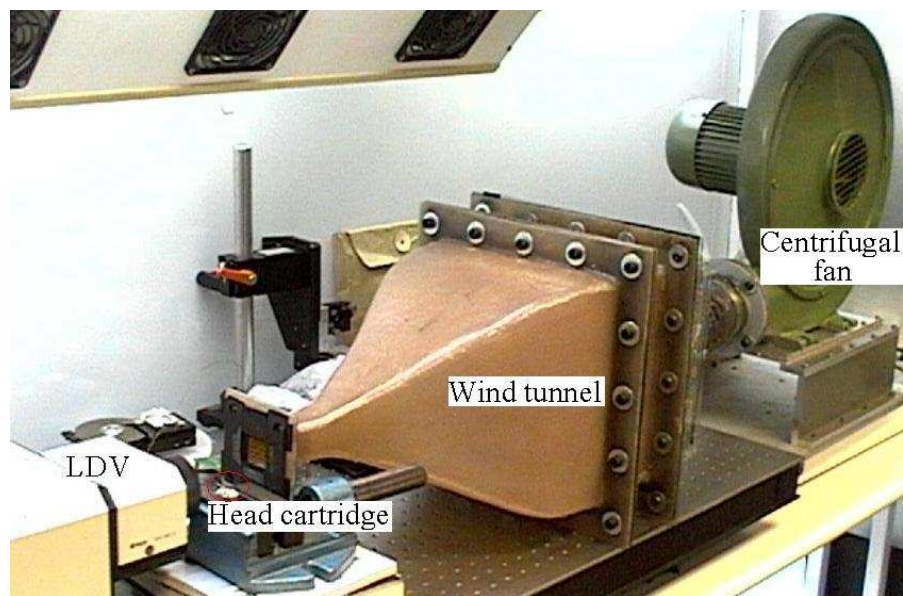
Figure 4.18: Experiment setup showing LDV, PZT actuated passive suspension on head cartridge, a centrifugal fan and wind tunnel.
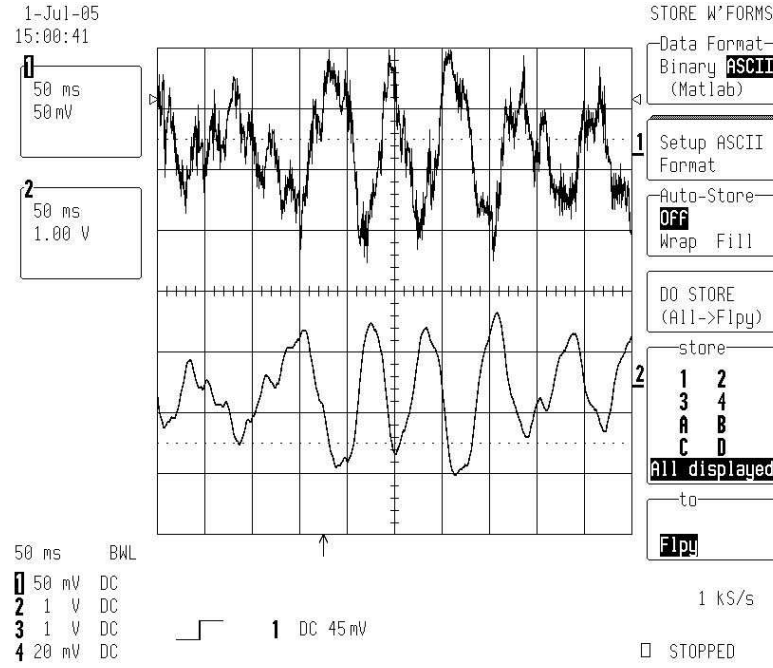
Figure 4.19: Measured PES e in channel 1 (top) and control signal u in channel 2 (bottom) with controller $K(z)$ only, *i.e.* without DDO with the centrifugal fan on.

4.5 Summary

In this chapter, a practical DDO (Disturbance Decoupling Observer) and DDOS (Disturbance Decoupling Observer with extraneous Sensor) are proposed for stronger disturbance rejection in precise sampled-data servo systems. The proposed schemes are parameterized by a single parameter ε using a SP (Singular Perturbation) approach, and are capable of rejecting input disturbances d_i and output disturbances d_o simultaneously, with possible simultaneous attenuation of noise sources from sensors using the DDOS. Experimental results on a PZT actuated head cartridge with mounted passive suspension in a servo spinstand shows an improvement of 69.2% of 3σ PES during track-following when air flow of mean speed of 50 m/s corresponding to 15000 rpm in today's high end HDDs mimicking input disturbances and output disturbances d_i and d_o, respectively, is channelled on it.

90
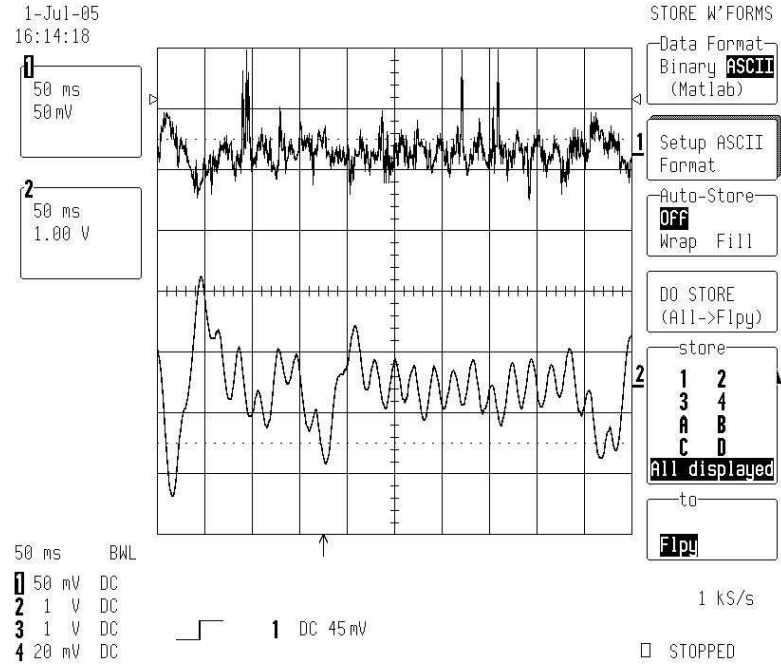
Figure 4.20: Measured PES e in channel 1 (top) and control signal u in channel 2 (bottom) with controller $K(z)$ and proposed DDO with the centrifugal fan on.

In the next chapter, we will further explore the application of SPT (Singular Perturbation Theory) in [56][57] and extended in [62] to a single stage HDD with the PZT microactuator exploited as a fast sensor and observer.

Chapter 5

Singular Perturbation Control for Vibration Rejection with PZT Actuator as Sensor and Fast Observer

Position sensors other than the R/W head are not embedded into current HDDs due to SNR and nanometer resolution issues. Moreover, non-collocated sensor fusion creates non-minimum phase zero dynamics which degrades tracking performance. In this chapter, the SPT (Singular Perturbation Theory) [57][62] is applied to decompose the VCM's and induced PZT active suspension's dynamics into fast and slow subsystems respectively. The PZT active suspension is used as a fast sensor and observer estimating the fast subsystem dynamics online. The controller design procedure is decoupled and control effectiveness is increased to tackle more DOFs (Degrees-Of-Freedom) via inner loop vibration suppression with measured high frequency VCM's and PZT active suspension's dynamics from the piezoelec-

tric elements in the suspension. Experimental results on a commercial HDD with LDV show effective suppression of the VCM and PZT active suspension's flexible resonant modes as well as an improvement of 39.9% in 3σ PES during track following when compared to conventional notch-based servos.

5.1   Background

Currently, HDDs remain as the mainstream of cheap non-volatile mass data storage devices. With increasing consumer demands for portable high density storage HDDs, future mobile devices are still relying on magnetism-based storage methodologies despite facing the renowned superparamagnetic effect by venturing into perpendicular recording technologies. Future HDDs will continue to need strong disturbance rejection capabilities for ultra high data capacities and ultra fast data transfer rates. But fortunately, improvements in sensor fabrication technologies coupled with low cost DSPs (Digital Signal Processors) allow high SNR, high resolution sensors, and enhanced servo algorithms to be embedded into future HDDs while retaining economic competitiveness.

It is well known from control theory that extraneous sensors alleviate controllers' orders and improve servo performance. Incorporation of additional sensors for active vibration control in HDDs has been studied in *e.gs.* [44][65] and [87] to actively damp the resonant modes of actuators together with PES. However, non-collocated sensor fusion results in non-minimum phase zero dynamics in the closed-loop system which degrades tracking performance. By using SP (Singular Perturbation) control [57][62], we can decompose the plant to be controlled into fast and slow subsystems as well as design their controllers independently for internal stability. In fact, by relaxing the tracking requirement to ensure that the

93

slow dynamics are used for tracking the desired trajectory, we can get minimum phase zero dynamics even with non-collocated actuator-sensor pairs.

In this chapter, the rigid and flexible modes of a VCM with mounted PZT-actuated active suspension (or PZT active suspension for short) are decomposed into their slow and fast subsystems, respectively, in a two time scale framework. The piezoelectric elements in the PZT active suspension are used as a sensor to detect the high frequency dynamics of the VCM and PZT active suspension for high frequency inner loop compensation in active damping of the actuators' flexible resonant modes. This approach is more robust than digital notch filters, and slow controller design for the rigid body modes used in track-seeking or track-following operation mode is independent of the inner loop controller used for high frequency vibration control. More importantly, it increases the control effectiveness of the servo system since the flexible modes increase the DOFs of the VCM *i.e.* more DOFs than number of control inputs. This systematic procedure also works for general nonlinear HDD models including pivot friction and flex cable nonlinearities *etc.*

5.2 Singular Perturbation Theory for LTI Mechanical Systems

For a general LTI mechanical system, its state space representation can be written as

$$
\begin{bmatrix} \dot{x}_R \\ \varepsilon \dot{x}_F \end{bmatrix} = \begin{bmatrix} A_{RR} & A_{RF} \\ A_{FR} & A_{FF} \end{bmatrix} \begin{bmatrix} x_R \\ x_F \end{bmatrix} + \begin{bmatrix} B_R \\ B_F \end{bmatrix} u_V
$$

(5.1)

and the output y_V of the mechanical system is given by

$$y_V \;=\; \begin{bmatrix} C_R & C_F \end{bmatrix} \begin{bmatrix} x_R \\ x_F \end{bmatrix} \tag{5.2}$$

$[x_R^T \;\; x_F^T]^T \in R^n$, $u_V \in R^m$ and $y \in R^p$ are the states, control input and output of the mechanical system with appropriate dimensions of n, m and p, respectively. ε is a small positive scalar ($0 < \varepsilon \ll 1$) which represents that the flexible mode dynamics are much faster than the rigid body modes. In fact, ε can be used as a tuning parameter such that the rigid body dynamics x_R are developed along time scale t while the flexible mode dynamics x_F are developed along time scale $\tau = \frac{t}{\varepsilon}$ to yield $\frac{d}{d\tau} x_F = \varepsilon \dot{x}_F$.

The SP design technique involves rewriting the system dynamics into slow and fast subsystems assuming that they operate on different time scales and which make them independent of each other [57][62]. This technique allows decoupled controller design while increasing the control effectiveness which is essential for controlling more DOFs than dimensions of control inputs. In the following subsection, we shall decompose a general LTI mechanical system into slow (denoted by superscript $^-$) and fast (denoted by superscript $^\thicksim$) subsystems respectively.

5.2.1 Slow Subsystem

The slow subsystem dynamics are obtained by setting $\varepsilon = 0$ together with the corresponding slow variables. As such, the slow manifold equation is obtained by

$$0 \;=\; A_{FR}\bar{x}_R + A_{FF}\bar{x}_F + B_F \bar{u}_V$$

$$\therefore \bar{x}_F \;=\; -A_{FF}^{-1}\big(A_{FR}\bar{x}_R + B_F\bar{u}_V\big) \tag{5.3}$$

which in essence is an algebraic equation. Obviously, A_{FF} is assumed to be invertible which is obtained from the fast subsystem dynamics to be mentioned in

the next subsection. Substituting Equation (5.3) into the first equation of Equation (5.1), the slow system dynamics can be obtained as

$$\dot{\bar{x}}_R \;\;=\;\; \left(A_{RR} - A_{RF}A_{FF}^{-1}A_{FR}\right)\bar{x}_R + \left(B_R - A_{RF}A_{FF}^{-1}B_F\right)\bar{u}_V \tag{5.4}$$

Similarly, substituting Equation (5.3) into output Equation (5.2), the output of the slow subsystem $\bar{y}_V$ is then given by

$$\bar{y}_V \;\;=\;\; \left(C_R - C_F A_{FF}^{-1}A_{FR}\right)\bar{x}_R - C_F A_{FF}^{-1}B_F\bar{u}_V \tag{5.5}$$

It is worth noting that there is a direct feedthrough term in the slow subsystem which reduces the relative degree (properness) of the slow subsystem and must be confronted in any design.

5.2.2   Fast Subsystem

In deriving the fast subsystem dynamics, we work in the fast time scale with $\tau = \frac{t}{\varepsilon}$ and hence the top equation in Equation (5.1) can be written as

$$\frac{d}{d\tau}x_R \;\;=\;\; \varepsilon\dot{x}_R \approx 0 \tag{5.6}$$

assuming that the rigid body dynamics do not change much in the fast time scale and hence $\tilde{x}_R \approx 0$.

Similarly, the bottom equation in Equation (5.1) can be written as

$$\begin{aligned}
\varepsilon\frac{d}{dt}x_F \;\;&=\;\; \frac{d}{d\tau}(\bar{x}_F - \tilde{x}_F) \\
&=\;\; A_{FR}\bar{x}_R + A_{FF}(\bar{x}_F + \tilde{x}_F) + B_F(\bar{u}_V + \tilde{u}_V)
\end{aligned} \tag{5.7}$$

Using the slow manifold equation in Equation (5.3), the state equation of the fast dynamics can be obtained as

$$\frac{d}{d\tau}\tilde{x}_F \;\;=\;\; A_{FF}\tilde{x}_F + B_F\tilde{u}_V \tag{5.8}$$

96

with the assumption that $\frac{d}{d\tau}\bar{x}_F = 0$ or the slow parts of the flexible modes do not vary much in the fast time scale τ.

The output of the fast subsystem is hence given by

$$\tilde{y}_V = C_F \tilde{x}_F \tag{5.9}$$
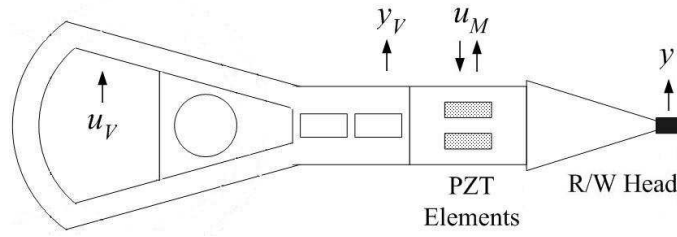
Figure 5.1: Picture of a VCM with mounted PZT active suspension (not drawn to scale) showing input (arrow to actuator) and output/measurement signals (out of actuator) respectively.

5.3   System Identification

In a conventional HDD, the VCM is the only actuator with the R/W head mounted on the tip of the suspension. Typically, a VCM can be represented by rigid body dynamics (low frequency double integrator) and flexible mode dynamics (high frequency resonant modes, including suspension modes) respectively. In this section, we shall identify the state matrices required for subsystem decomposition using experiment frequency responses.

A picture of a typical VCM is with mounted PZT active suspension is shown in Figure 5.1. For our application, A_{RF} is assumed to be negligible as the rigid

and flexible modes are mechanically decoupled or the flexible resonant modes are assumed to have little or no induced dynamics on the bulky VCM. Similarly, A_{FR} is also assumed to be negligible as the flexible resonant modes occur at high frequencies where the gain of the rigid body is very small due to at least -40 dB/dec amplitude reduction from its low frequency double integrator properties.

By exciting the VCM at u_V, the frequency response of the VCM with PZT active suspension measured from y is shown below in Figure 5.2. Both the VCM's
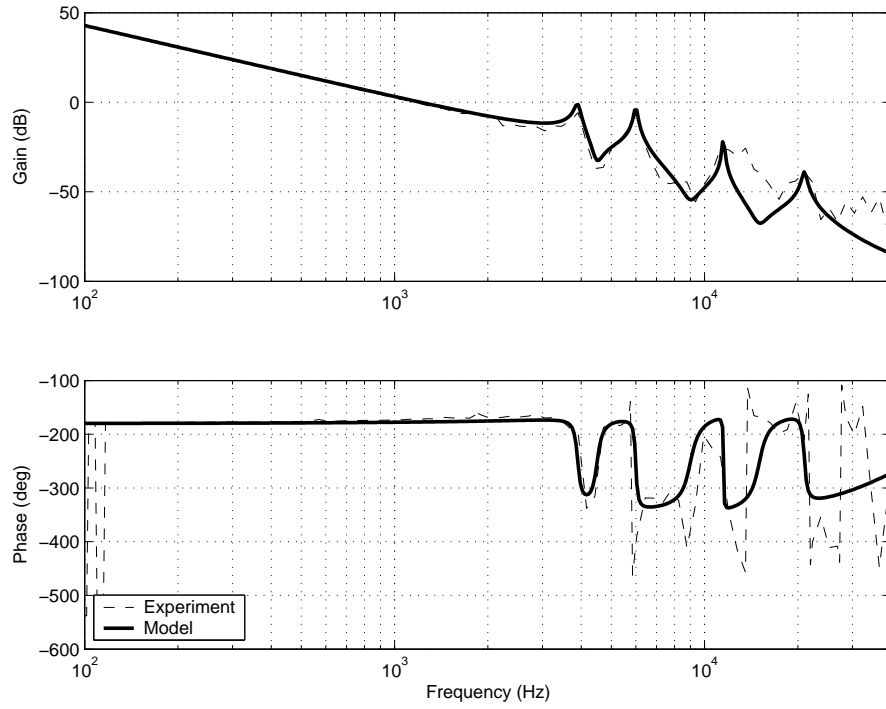
Figure 5.2: Frequency response of transfer function from u_V to y.

and PZT active suspension's flexible resonant modes are excited and identified.

The identified mathematical model of $\frac{y(s)}{u_V(s)}$ is

$$
\begin{aligned}
\frac{y(s)}{u_V(s)} &= \frac{2974514.7531}{s^2} \frac{s^2 + 1696s + 7.994 \times 10^8}{s^2 + 980.2s + 6.005 \times 10^8} \cdots \\
&\times \frac{s^2 + 5655s + 3.198 \times 10^9}{s^2 + 754s + 1.421 \times 10^9} \frac{s^2 + 9425s + 8.883 \times 10^9}{s^2 + 361.3s + 5.221 \times 10^9} \cdots \\
&\times \frac{s^2 + 2.513 \times 10^5 s + 6.317 \times 10^{10}}{s^2 + 3958s + 1.741 \times 10^{10}}
\end{aligned}
\tag{5.10}
$$

The fitted mathematical model is less than exemplary but is sufficient in picking up the essential rigid and flexible resonant modes.

It can be seen from Figure 5.2 that the flexible modes consist of VCM and induced PZT active suspension's resonant modes. In the following subsections, we shall detail the procedures for determining the state space representation of the VCM with mounted PZT active suspension in the form of Equations (5.1) and (5.2) with identified experimental frequency responses.

5.3.1 Transfer Function Identification

Before we identify the rigid body dynamics, the frequency responses of the VCM from u_V to y_V and the PZT active suspension from u_M to y is shown below in Figures 5.3 and 5.4 respectively. It can be seen that the VCM itself has identified rigid body mode (low frequency double integrator) and flexible modes (high frequency resonant modes) at 3.9 kHz and 6.0 kHz. It is worth noting that the PZT active suspension is employed solely as a sensor and fast observer for our application to detect high frequency dynamics of a VCM and PZT active suspension. As such, Figure 5.4 serves as a good reference for the sufficiency of a reduced order model to isolate flexible modes arising from the VCM and PZT active suspension required for SP control.

The PZT active suspension has identified flexible modes at 5.9 kHz, 11.5 kHz
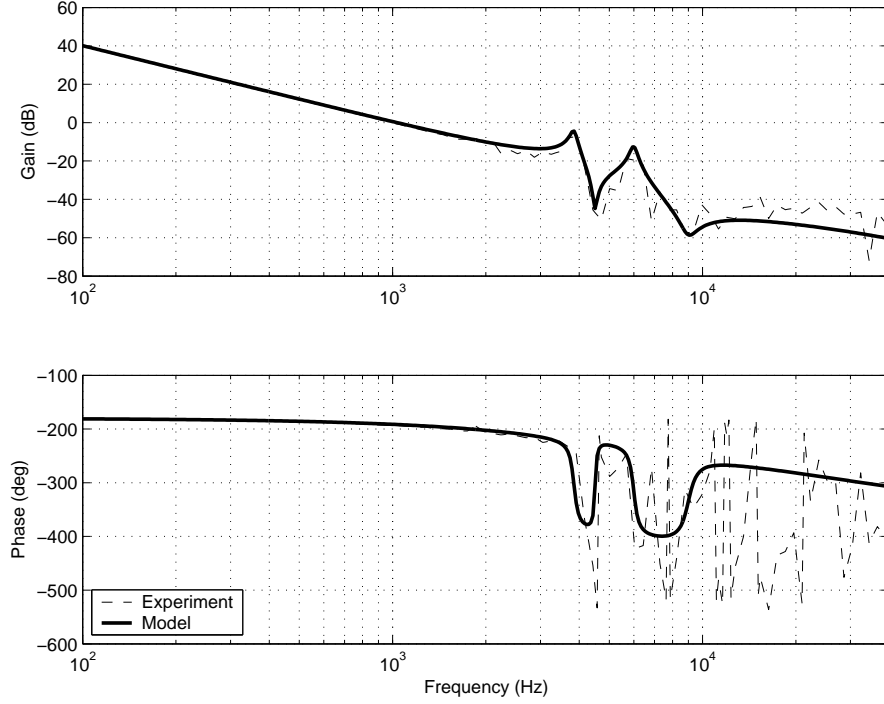
Figure 5.3: Frequency response of transfer function from u_V to y_V (*i.e.* only "E"-block).

and 21.0 kHz respectively.

Flexible Body

To obtain the flexible body dynamics $V_F(s)$ of the VCM with mounted PZT active suspension, the low frequency integrators are subtracted from transfer function $\frac{y(s)}{u_V(s)}$ with lifted DC gain (to match that in Figure 5.2) to form $V_F(s)$ given by

$$
\begin{aligned}
V_F(s) &= -355.9008 \frac{s + 1.421 \times 10^5}{s^2 + 980.2s + 6.005 \times 10^8} \frac{s^2 + 1471s + 1.002 \times 10^9}{s^2 + 754s + 1.421 \times 10^9} \cdots \\
&\times \frac{s^2 + 1766s + 4.784 \times 10^9}{s^2 + 361.3s + 5.221 \times 10^9} \frac{s^2 + 6860s + 1.611 \times 10^{10}}{s^2 + 3958s + 1.741 \times 10^{10}}
\end{aligned}
\tag{5.11}
$$

and $V_F(s)$ will be used for identification of the fast subsystem.
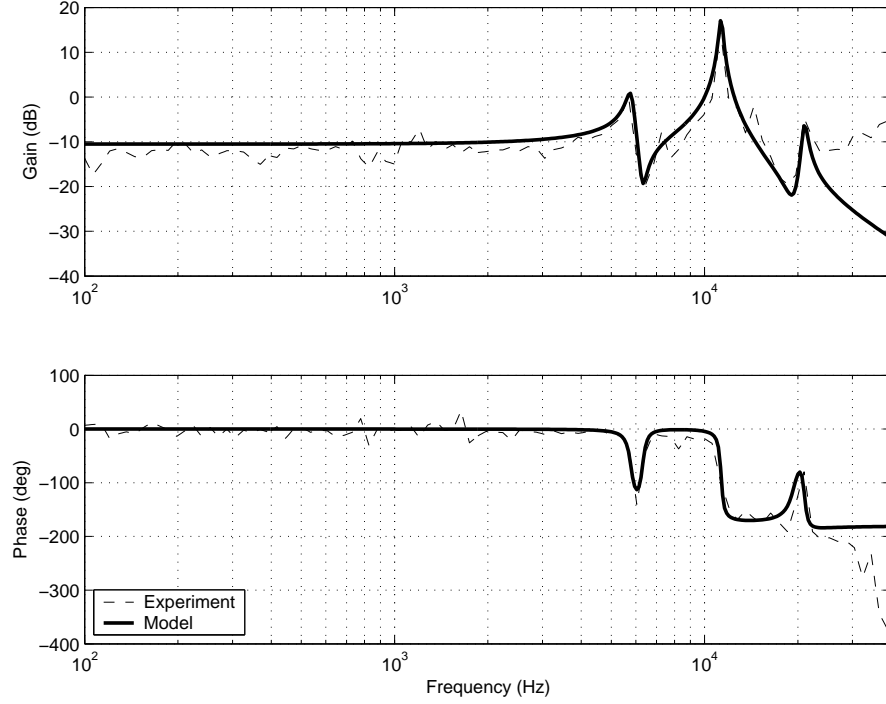
Figure 5.4: Frequency response of transfer function from u_M to y.

Rigid Body

As such, the rigid body dynamics $V_R(s)$ of the VCM with mounted PZT active suspension are given by the isolated low frequency integrators with lifted DC gain described above (or difference between Equations (5.10) and (5.11)) to form

$$V_R(s) = \frac{355.9s + 5.5 \times 10^7}{s^2} \tag{5.12}$$

and $V_R(s)$ will be used to identify the slow subsystem in the following subsection.

5.3.2   Subsystem Identification

With the identified state matrices for the VCM with mounted PZT active suspension in Equations (5.1) and (5.2), the fast and slow subsystems operating on two different time scales as detailed in Section 5.2 earlier now can be identified.
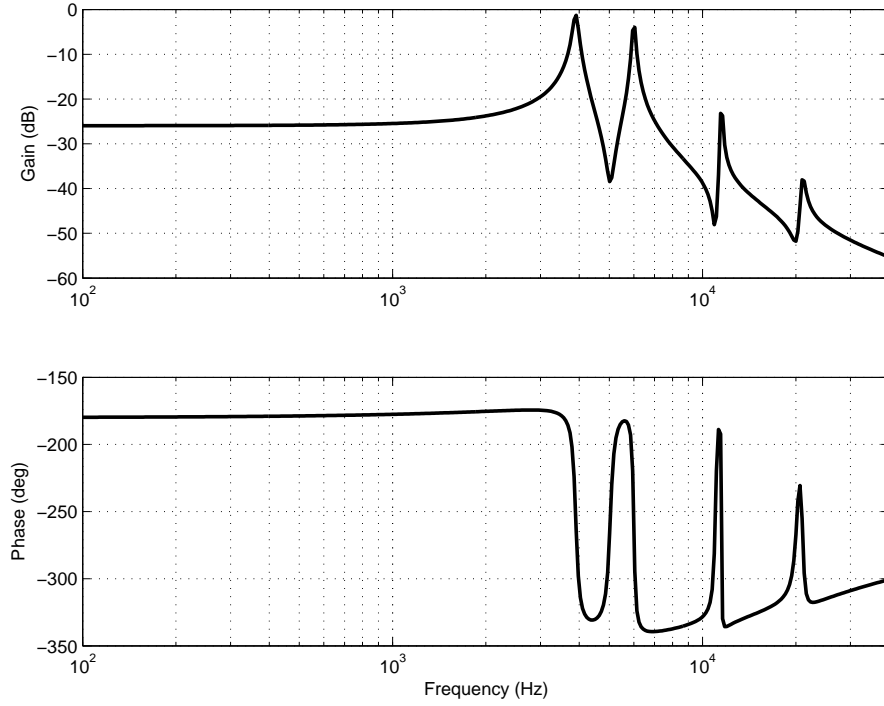
Figure 5.5: Frequency response of fast subsystem $\tilde{G}_V$ from $V_F(s)$ after decomposition.

Fast Subsystem $\tilde{G}_V$

To obtain the fast subsystem state $\tilde{G}_V$ and its space matrix triple (A_{FF}, B_F, C_F), $V_F(s)$ is rewritten in state space representation with x_F as the state. Obviously, the pair (A_{FF}, B_F) is stabilizable and A_{FF} is invertible which makes SP control possible. The frequency response of $\tilde{G}_V$ is shown in Figure 5.5. It can be seen from Figure 5.5 that flexible resonant modes at natural frequencies 3.9 kHz, 6.0 kHz (from VCM and PZT active suspension), 11.5 kHz and 21.0 kHz are captured and retained.

Slow Subsystem $\bar{G}_V$

Similarly, $V_R(s)$ is then rewritten in state space representation with x_R as the state to obtain the state space triple (A_{RR}, B_R, C_R). Using Equations (5.4) and (5.5), the dynamics of the slow subsystem $\bar{G}_V$ can be obtained in transfer function form as

$$
\begin{aligned}
\bar{G}_V &= \frac{\bar{y}_V(s)}{\bar{u}_V(s)} \\
&= \frac{-0.05037s^2 + 355.9s + 5.5 \times 10^7}{s^2}
\end{aligned}
\tag{5.13}
$$

The frequency response of $\bar{G}_V$ is shown in Figure 5.6. It can be seen from Figure 5.6
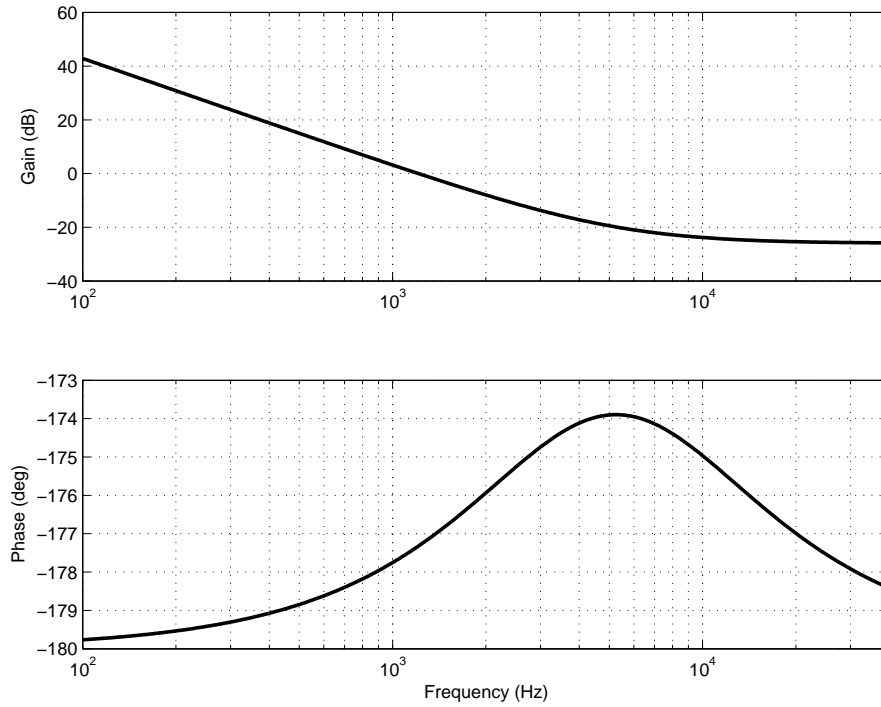
Figure 5.6: Frequency response of slow subsystem $\bar{G}_V$ after system decomposition.

that the low frequency integrators with lifted DC gain are captured and retained. It is worth noting from Equation (5.13) that the introduction of the feedthrough term makes the slow subsystem $\bar{G}_V$ proper.

5.4 Estimating High Frequency Dynamics

For SP control to be feasible, the fast dynamics of $\tilde{G}_V$ should be estimated or measured for vibration rejection using inner loop compensation. This translates directly into construction of an estimator for state reconstruction or real time measurements of the VCM's and PZT active suspension's high frequency dynamics. In this section, we will use the latter by employing the piezoelectric material in PZT active suspension as a sensor solely to obtain these flexible mode's vibratory signals in both the VCM and PZT active suspension. This is possible as when piezoelectric materials (*e.g.* PZT elements) are subjected to strain, charges arise on the surface of the material and hence setting up an electric field, analogous to back EMF (Electro-Motive Force) in electromagnetic systems.
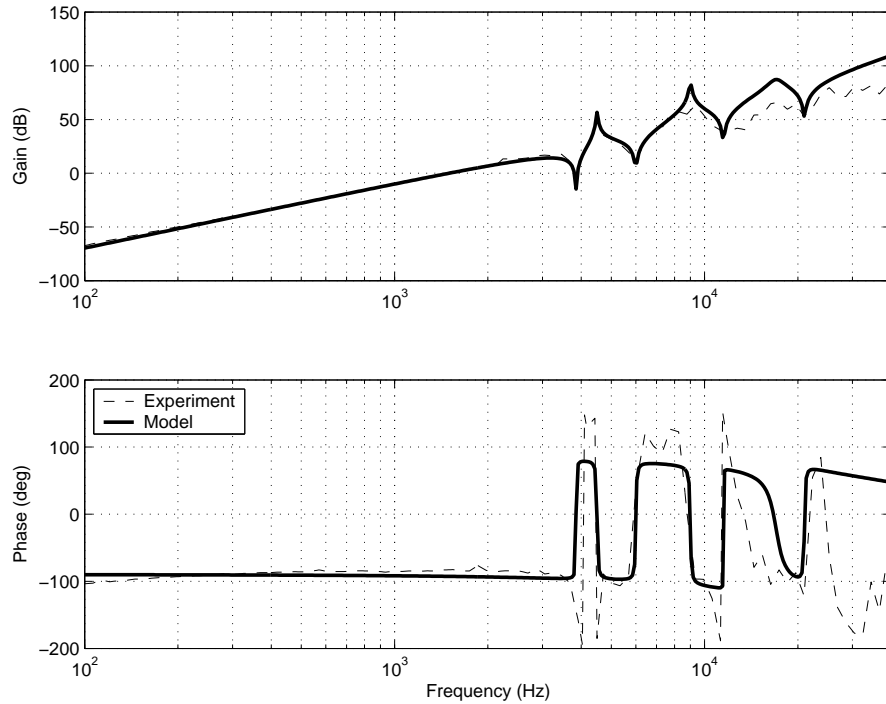
Figure 5.7: Frequency response of transfer function from y to u_M using PZT active suspension as a sensor and fast observer.

For our experiments, a Brüel and Kjær signal conditioning amplifier of gain 10 and band pass corner frequencies of 10 Hz and 30 kHz is used. Using a similar methodology to that detailed in [87], swept sine excitation is injected at u_V while y measured from the LDV is connected to channel 1 and u_M from the PZT active suspension through the amplifier output is connected to channel 2 of the DSA (HP 35670A model). The frequency response of transfer function from y to u_M is measured and shown in Figure 5.7.

It can be seen from Figure 5.7 that the estimation is effective at most frequencies and the frequencies of the anti-resonant zeros correspond to the natural frequencies of the VCM and PZT active suspension. The online state estimator measured u_M from amplifier to y has differentiator effects and can be identified with the following non-causal transfer function as

$$
\begin{aligned}
\frac{u_M(s)}{y(s)} &= 1.2841 \times 10^{-16} s^3 \frac{s^2 + 96.76s + 5.852 \times 10^8}{s + 2.513 \times 10^5} \cdots \\
&\times \frac{s^2 + 301.6s + 1.421 \times 10^9}{s^2 + 226.2s + 7.994 \times 10^8} \frac{s^2 + 72.26s + 5.221 \times 10^9}{s^2 + 565.5s + 3.198 \times 10^9} \cdots \\
&\times \frac{s^2 + 1319s + 1.741 \times 10^{10}}{s^2 + 1.068 \times 10^4 s + 1.141 \times 10^{10}}
\end{aligned}
\tag{5.14}
$$

and the high frequency VCM's and PZT active suspension's dynamics can hence be easily estimated online through a digital inverse of Equation (5.14) from the output of the amplifier as detailed in the next section This method is shown to have high SNR and nanometer resolution estimation and interested readers are referred to [87] for an in-depth analysis which is not reiterated in this chapter.

5.5 Design of Controllers

According to SPT, the overall control signal u_V is given by $u_V = \bar{u}_V + \tilde{u}_V$, where $\bar{u}_V$ and $\tilde{u}_V$ are designed separately using the slow and fast subsystems respectively.

Ensuring that the pair (A_{FF}, B_F) is stabilizable, the composite control u_V results in the following overall state trajectories given by

$$
\begin{aligned}
x_R &= \bar{x}_R + O(\varepsilon) \\
x_F &= \bar{x}_F + \tilde{x}_F + O(\varepsilon)
\end{aligned}
\tag{5.15}
$$

where $O(\varepsilon)$ denotes the terms of order ε according to a theorem by Tikhonov. This independent design of two control inputs practically increases the control effectiveness of the system and the fast control signal $\tilde{u}$ is a boundary layer correction that suppresses high frequency vibrations analogous that with sliding mode control.

In fact this procedure is equivalent to direct design of a state feedback on the system without any direct or inverse time scaling as we will be using in this section. As such, it possess better numerical properties as ill-conditioned scenarios (from the large gains and small time constants in HDDs) are commonly encountered during controller synthesis and optimization designs using $\mathcal{H}_2$ or $\mathcal{H}_\infty$ techniques.
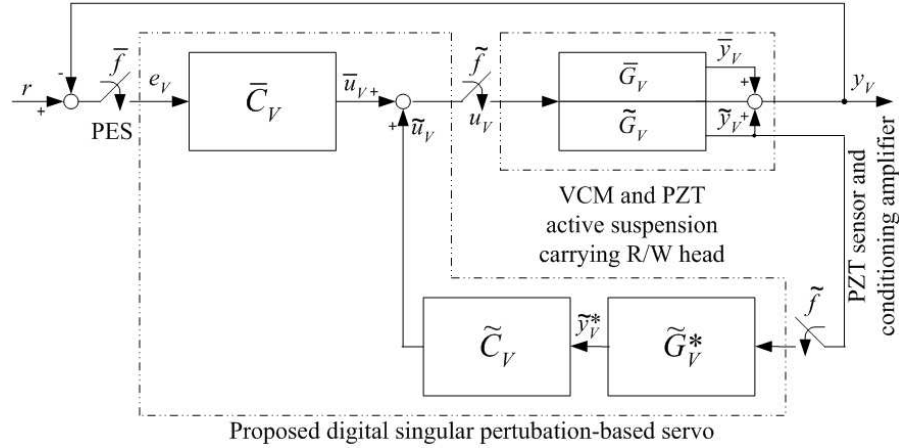
Figure 5.8: Block diagram of proposed SP-based servo system.

The proposed SP control topology using PZT active suspension as sensor to determine VCM's high frequency dynamics is shown below in Figure 5.8. The

superscripts $^-$, $\tilde{}$ and * denote slow subsystems, fast subsystems and estimates respectively. The slow controller $(\bar{C}_V)$ and fast controllers $(\tilde{C}_V$ and $\tilde{G}_V^*)$ operate at slow frequency $\bar{f}$ and fast frequency $\tilde{f} = \frac{\bar{f}}{\varepsilon}$ respectively. The fast subsystem dynamics $\tilde{y}_V$ are measured from the PZT active suspension through a signal conditioning amplifier and estimated through $\tilde{G}_V^*$.

5.5.1 Fast Subsystem Estimator

For fast inner loop compensation to be implementable, the high frequency dynamics of the VCM and PZT active suspension as mentioned in Section 5.4 should be available. By designing the fast subsystem estimator $\tilde{G}_V^*$ as the inverse of Equation (5.14)

$$
\begin{aligned}
\tilde{G}_V^*(s) \;=\; & \frac{7.787803 \times 10^{15}}{s^3} \frac{s + 2.513 \times 10^5}{s^2 + 96.76s + 5.852 \times 10^8} \cdots \\
& \times \frac{s^2 + 226.2s + 7.994 \times 10^8}{s^2 + 301.6s + 1.421 \times 10^9} \frac{s^2 + 565.5s + 3.198 \times 10^9}{s^2 + 72.26s + 5.221 \times 10^9} \cdots \\
& \times \frac{s^2 + 1.068 \times 10^4 s + 1.141 \times 10^{10}}{s^2 + 1319s + 1.741 \times 10^{10}}
\end{aligned}
\tag{5.16}
$$

the high frequency dynamics estimate $\tilde{y}^*$ can be obtained online using the output of the amplifier (from measured u_M) as input. This low pass filter removes much measurement noise from the online estimator which permits a low order fast controller $\tilde{C}_V$ to be designed.

5.5.2 Fast Controller

To calculate the fast control signal $\tilde{u}$, we can design any standard LQG, $\mathcal{H}_2$ or even $\mathcal{H}_\infty$ output feedback controller for high frequency inner loop compensation. For our design, the nice in phase properties of the PZT active suspension as shown

in Figure 5.2 is exploited and a low order lead compensator of the form is used

$$\tilde{C}_V = \kappa \frac{s + 6283}{s + 1.257 \times 10^5} \tag{5.17}$$

as fast controller $\tilde{C}_V$ and $1 < \kappa \leq 20$ is tuned to balance between the amount of suppression of high frequency vibrations and stability to the amount of sensing noise tolerable in the output of the servo system. In fact, $\tilde{C}_V$ is analogous to a high gain PD control commonly used for controlling robot manipulators [62]. For the rest of our discussions, we have chosen $\kappa = 100$.

5.5.3 Slow Controller

As the slow subsystem contains mainly of the rigid body modes (low frequency double integrator), the lag-lead compensator recommended in [87] augmented with a low pass filter

$$\bar{C}_V(s) = K_V \frac{s + \frac{2\pi f_V}{2\alpha}}{s + 2\pi 10} \frac{s + \frac{2\pi f_V}{\alpha}}{s + 2\alpha 2\pi f_V} \frac{\frac{\alpha \pi f_V}{2}}{s + \frac{\alpha \pi f_V}{2}} \tag{5.18}$$

using $5 < \alpha < 10$ is used. K_V can be calculated by setting $|\bar{C}_V(j2\pi f_V)\bar{G}_V(j2\pi f_V)| = 1$ where $\bar{G}_V$ is the slow subsystem identified in previous section. The lag portion of the controller is used to increase the low frequency gain for low frequency disturbance rejection and tracking accuracy and acts as the outer slow loop for disturbance rejection. The lead portion of the controller increase phase margin to ensure stability during crossover region and speeding up of the rigid mode in the VCM. An additional low pass filter is cascaded to increase the high frequency roll-off and stability of the stiffened VCM and PZT active suspension due to a reduced relative degree after inner loop compensation. For our design, we have chosen $\alpha = 5$ and $f_V = 700$ at about one-fifth of the natural frequency of the first in-plane resonant sway mode.

5.6 Performance Evaluation

In this section, the effectiveness of our proposed SP control scheme is verified with simulation studies and experimental implementations.

5.6.1 Simulation Studies

For demonstration purposes, the commonly used notch-based servo (using digital notch filters to attenuate gain of control signals at natural frequencies to prevent excitation of the flexible resonant modes) is compared with the proposed SP-based servo.
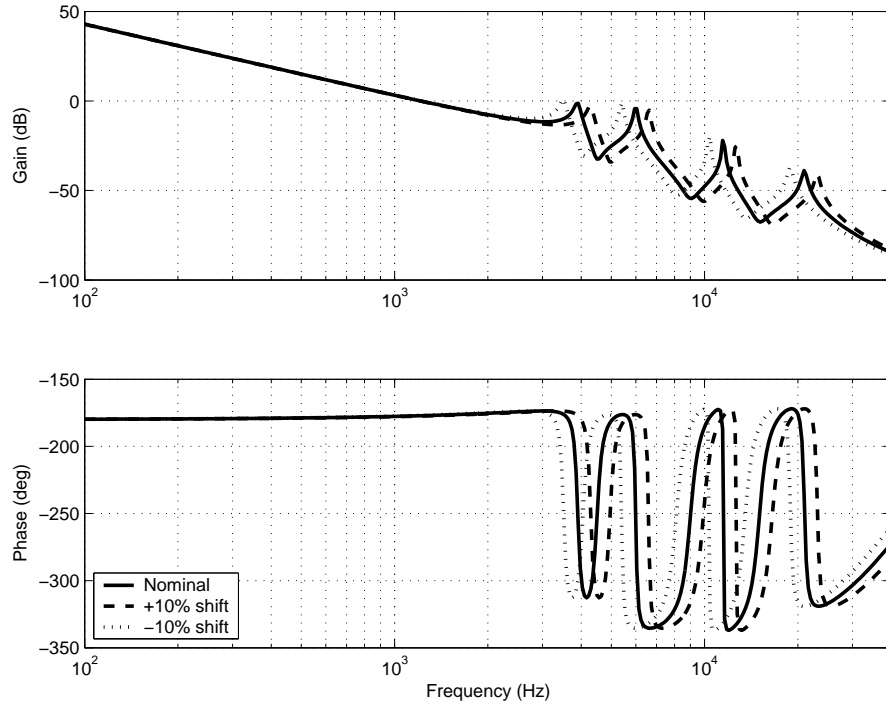
Figure 5.9: Frequency response of transfer function from u_V to y with $\pm 10\%$ shift in natural frequencies of the flexible modes.

Robustness Analysis

To demonstrate the robustness of the proposed SP-based servo, the natural frequencies of the flexible modes in the VCM and PZT active suspension are perturbed by $\pm 10\%$ as shown below in Figure 5.9.
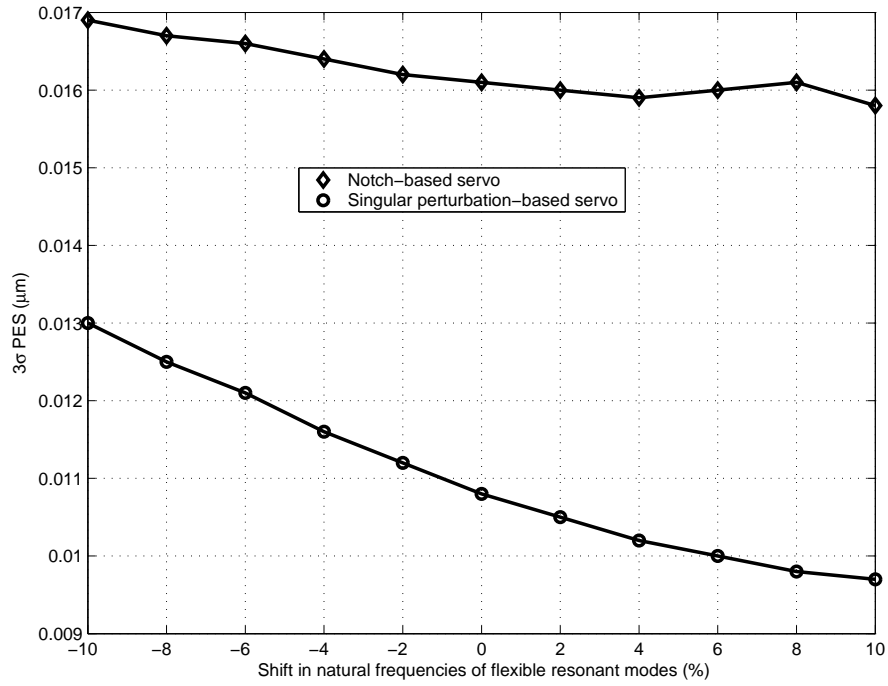
Figure 5.10: Percentage variation of natural frequency of flexible modes (%) vs 3σ PES (μm) in VCM and PZT active suspension with respect to the nominal frequencies.

The identified vibration and noise models reported by Du *et al.* in [19] for a STW (Servo Track Writing) process with a spindle motor rotating at 5400 rpm are used to emulate input torque disturbances $d_i(s)$, output disturbances $d_o(s)$, and
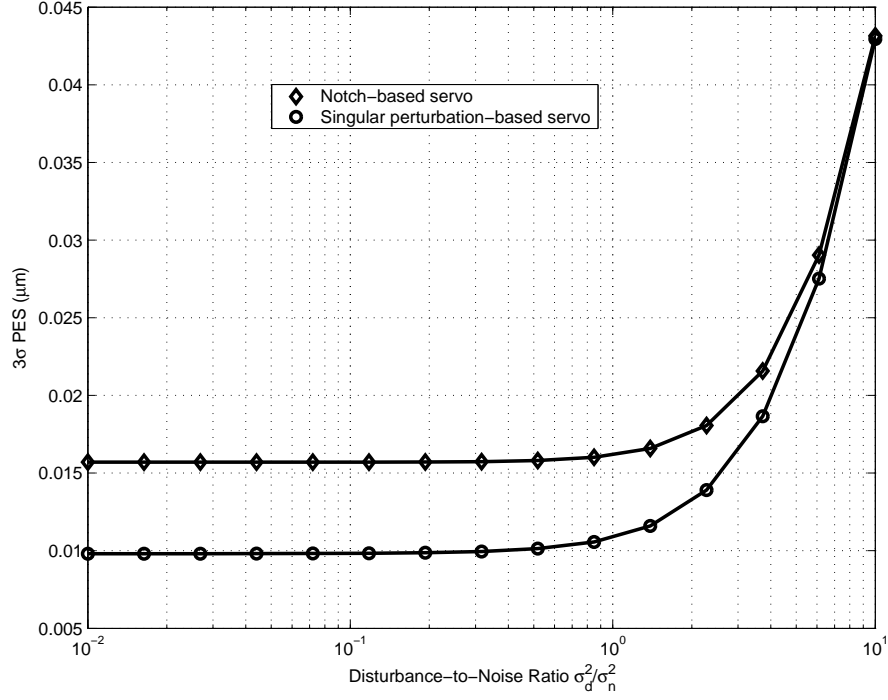
Figure 5.11: 3σ PES (μm) vs DNR.

noise sources $n(s)$ of today's high end HDDs. The transfer functions are given by

$$
d_i(s) \;=\; \frac{159.9}{s^2 + 113.1s + 3.198 \times 10^5} \tag{5.19}
$$

$$
\begin{aligned}
d_o(s) \;=\;& 0.00163 \frac{s^2 - 2.691s + 5.262 \times 10^5}{s^2 + 0.754s + 3.948 \times 10^5} \frac{s^2 - 585.6s + 3.765 \times 10^6}{s^2 + 0.2011s + 1.011 \times 10^6} \cdots \\
& \times \frac{s^2 + 4161s + 2.008 \times 10^7}{s^2 + 245s + 1.668 \times 10^7} \frac{s^2 + 2402s + 5.634 \times 10^8}{s^2 + 477.5s + 5.701 \times 10^8} \tag{5.20}
\end{aligned}
$$

and noise source $n(s)$ is of Gaussian distribution with zero mean and a variance of 0.001.

Simulations are then carried out to obtain the 3σ PES with perturbation of the natural frequencies and plotted in Figure 5.10. As can be seen from Figure 5.10, SP-based servo is robust to fluctuations in natural frequencies, with improved disturbance rejection capabilities at natural frequency variations in the high frequency region. An improvement of up to 38.2% in 3σ PES is observed at nominal natural frequencies of the flexible modes.

111
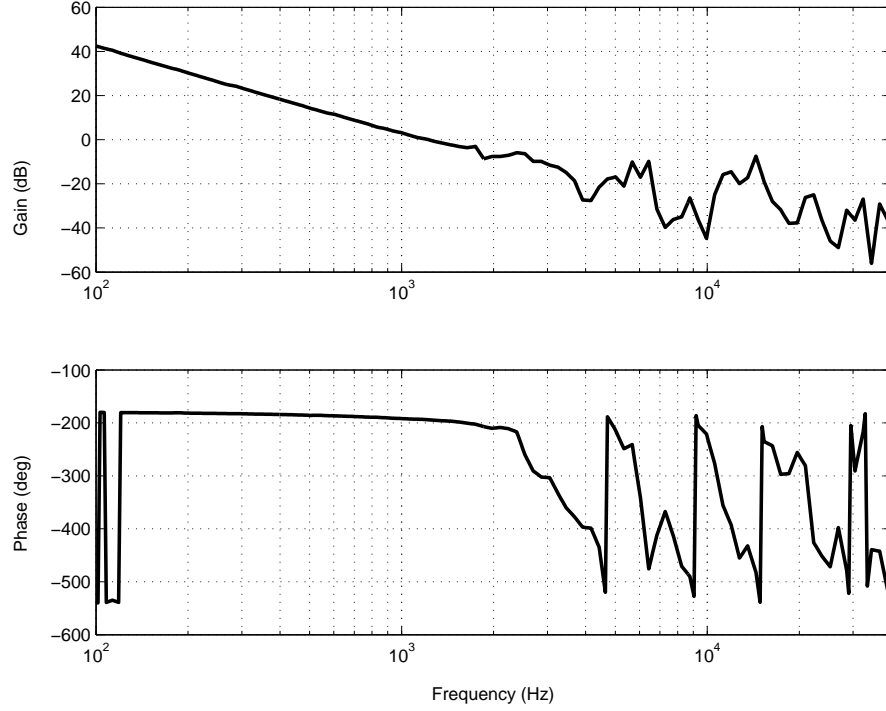
Figure 5.12: Frequency response of transfer function from u_V to y using PZT active suspension as a sensor with high frequency inner loop compensation.

Disturbance-to-Noise Ratio (DNR)

In this section, we define a performance index called DNR (Disturbance-to-Noise Ratio) which is the ratio of output disturbance power to measurement noise power *i.e.* DNR= $\frac{\sigma_d^2}{\sigma_n^2}$. Simulations are then executed to evaluate the proposed SP-based servo as a high pass filter is used for inner loop compensation which is generally undesirable for HDD control (due to high PES sensing noise).

By simulating DNR from 0.01 to 10 (which translates from a noise level of a hundred times higher than output disturbance to a tenth smaller), the 3σ PES is plotted in Figure 5.11. It can be seen that the proposed SP-based servo scheme works well even when noise level is high, when compared to that of conventional notch-based servo.

5.6.2 Experimental Implementation

For our experiments, the digital controllers are discretized via bilinear transformation and a nominal slow sampling frequency $\bar{f}$ of 5 kHz with $\varepsilon = 0.0625$ is chosen. Due to the parametrization by ε, the fast controller $\tilde{C}_V$ and estimator $\tilde{G}_V$ and are discretized at a fast sampling frequency $\tilde{f}$ of 80 kHz where $\tilde{f} = \frac{\bar{f}}{\varepsilon}$. It is interesting to note this formulation is analogous to that using multi-rate digital control with slow controller operating on measured PES at nominal sampling frequency and fast controllers in inner loop mimicking high sampling frequency from higher spindle rotation speeds (more PES data).
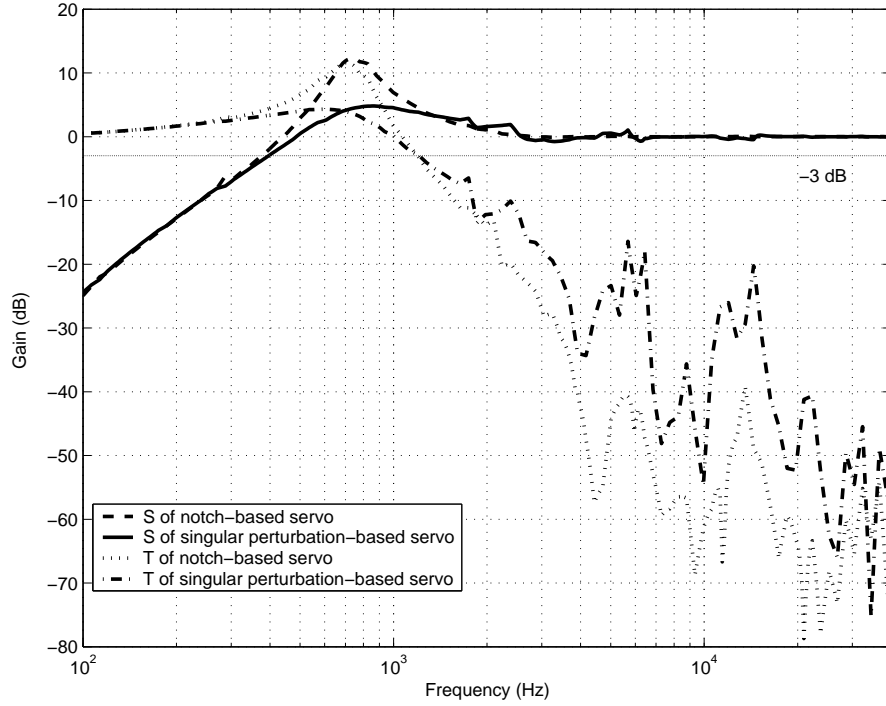
Figure 5.13: Frequency response of sensitivity transfer functions with proposed SP-based servo and conventional notch-based servo.

Frequency Responses

The frequency response of transfer function from u_V to y using PZT active suspension as a sensor with high frequency inner loop compensation is shown below in Figure 5.12. The VCM's and PZT active suspension's flexible resonant modes at 3.9 kHz, 6.0 kHz, 11.5 kHz and 21.0 kHz are effectively damped with a reduced relative degree.
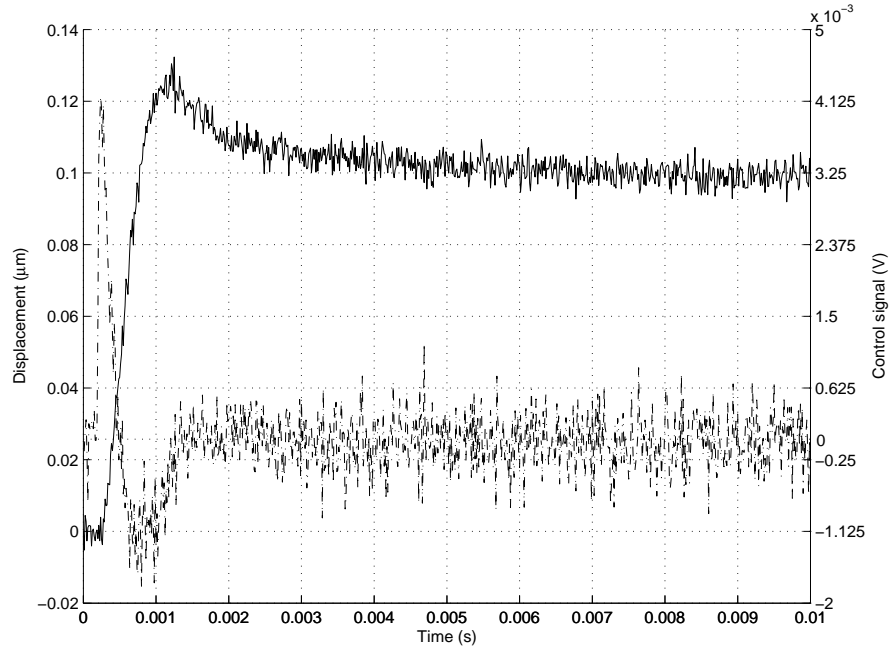
Figure 5.14: Experimental step response using conventional notch-based servo. Solid: displacement measured at tip of PZT active suspension. Dash-dot: control signal.

The VCM's flexible modes at 3.9 kHz and 6.0 kHz and the PZT active suspension's flexible modes at 5.9 kHz, 11.5 kHz and 21.0 kHz are effectively damped with proposed SP-based servo. As such, we can expect a possible higher servo bandwidth and low sensitivity with reduced relative degree as verified with the experimental sensitivity transfer functions S of proposed SP-based servo and con-

ventional notch-based servo shown below in Figure 5.13.

SP-based servo offers stronger vibration suppression capabilities with a higher bandwidth and lower sensitivity such that high frequency disturbances would not be amplified by the servo loop [95]. However, the complementary sensitivity transfer functions T of the proposed schemes shown in Figure 5.13 reveal that a smaller roll-off at high frequencies (although at the same closed-loop bandwidth) is obtained for SP-based servo.
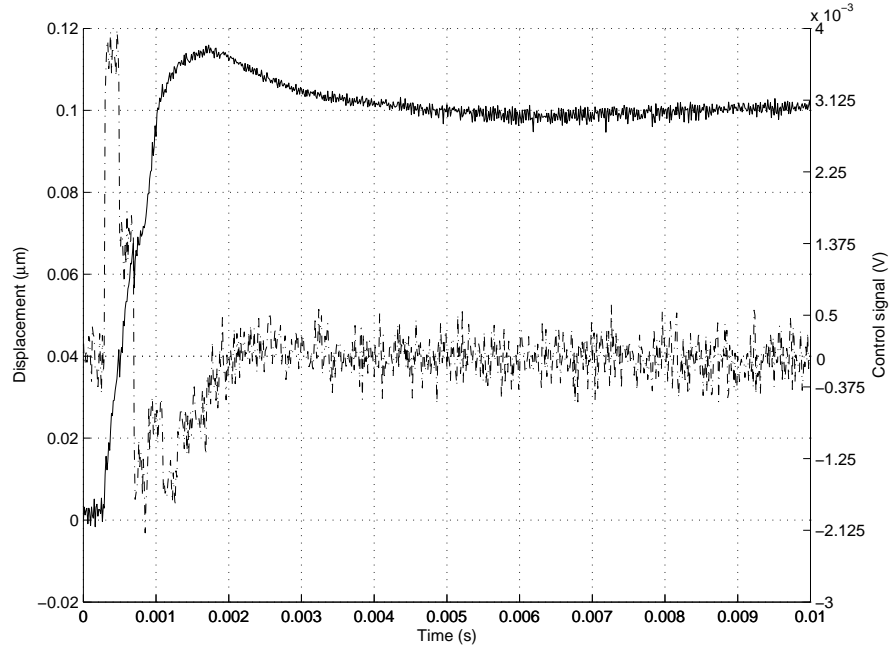
Figure 5.15: Experimental step response using proposed SP-based servo. Solid: displacement measured at tip of PZT active suspension. Dash-dot: control signal.

Time Responses

A linear track-following controller is normally used for short-span seeks in HDDs. For comparison purposes, the gain crossover frequency of both conventional notch-based servo and proposed SP-based servo are set at 700 Hz. The experimental

115

step responses of 0.1 μm using conventional notch-based servo and the proposed SP-based servo are shown in Figures 5.14 and 5.15 respectively. The slow control signal $\bar{u}_V$ and fast control signal $\tilde{u}_V$ are shown in Figure 5.16.
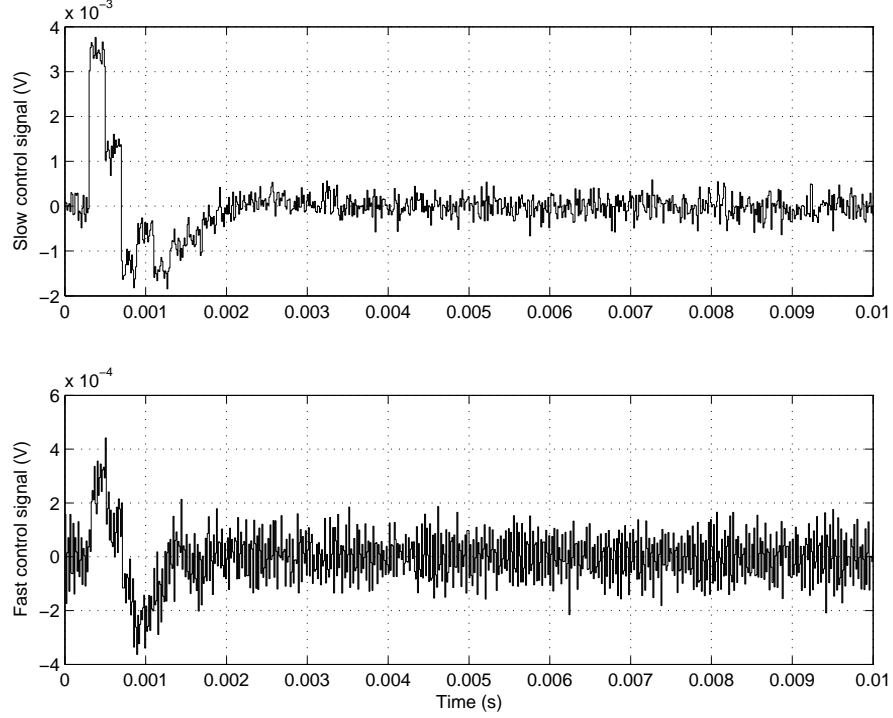
Figure 5.16: Control signals using proposed SP-based servo. Top: slow control signal $\bar{u}_V$. Bottom: fast control signal $\tilde{u}_V$.

It can be seen from the Figures 5.14 and 5.15 that the induced oscillations using proposed SP-based servos are also highly suppressed by the fast control signal $\tilde{u}_V$. However, the SP-based servo offers a smaller overshoot due to active vibration control but a slower seek and settling time is traded-off. This is expected as the tracking requirements are relaxed in a SP framework [62] and tracking is done by the slow subsystem (hence rigid body modes). Also, fast inner loop active vibration control results in phase reduction from 2 kHz to 3.9 kHz where the first resonant mode of the VCM occurs as can be seen from Figures 5.2 and 5.12. This

translates directly into a delay which results in a slower seek response. However, it should be noted that a much higher gain crossover frequency (corresponding to faster seek and settling times) can be designed and achieved for the proposed SP-based servo as the first in-plane resonant mode is well-damped as shown in Figure 5.12 earlier.
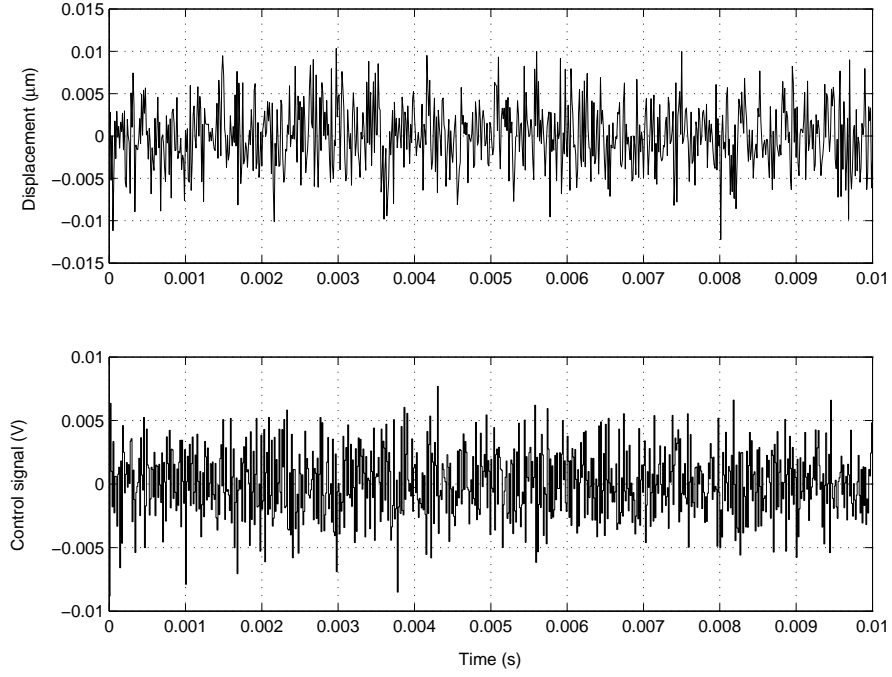
Figure 5.17: Experimental PES y measured with LDV using conventional notch-based servo. Top: displacement measured at tip of PZT active suspension. Bottom: control signal.

Next to mimic the effects of disturbance and noise sources during track-following, the vibration models described earlier from [19] are injected into the closed-loop systems during experiment. The experimental PES y measured with LDV using conventional notch-based servo and the proposed SP-based servo are shown in Figures 5.17 and 5.18 respectively. The corresponding experimental slow control signal $\bar{u}_V$ and fast control signal $\tilde{u}_V$ are shown in Figure 5.16.

117
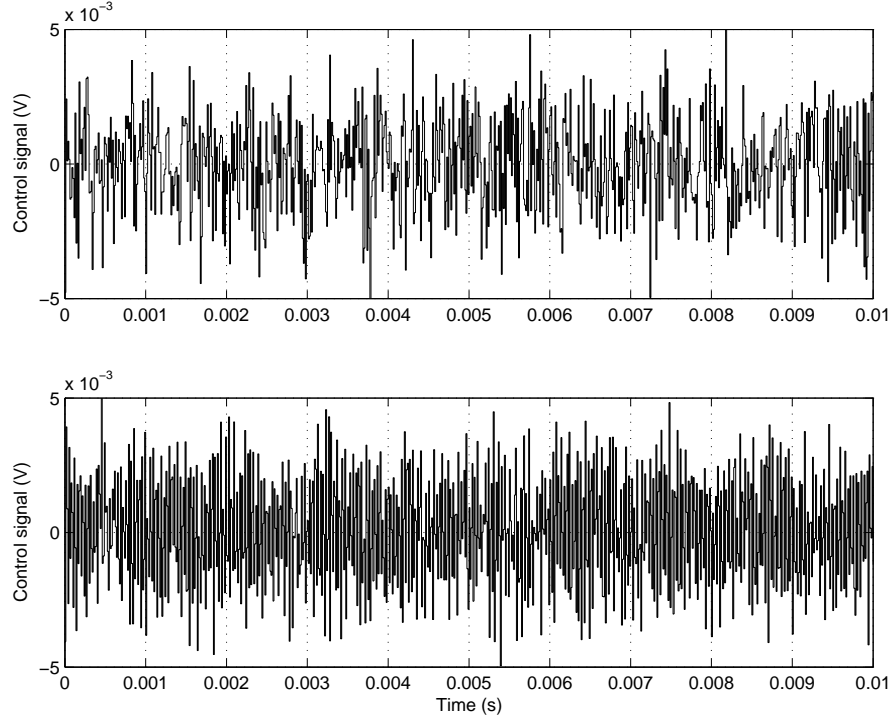
Figure 5.18: Experimental PES y measured with LDV using proposed SP-based servo. Top: displacement measured at tip of PZT active suspension. Bottom: control signal.

An improvement of experimental 3σ PES from 0.0248 μm in Figure 5.17 to 0.0149 μm (39.9%) in Figure 5.18 is observed. The histograms of the above PES data are plotted in Figure 5.20, revealing a tighter tolerance and much reduction in variance of PES.
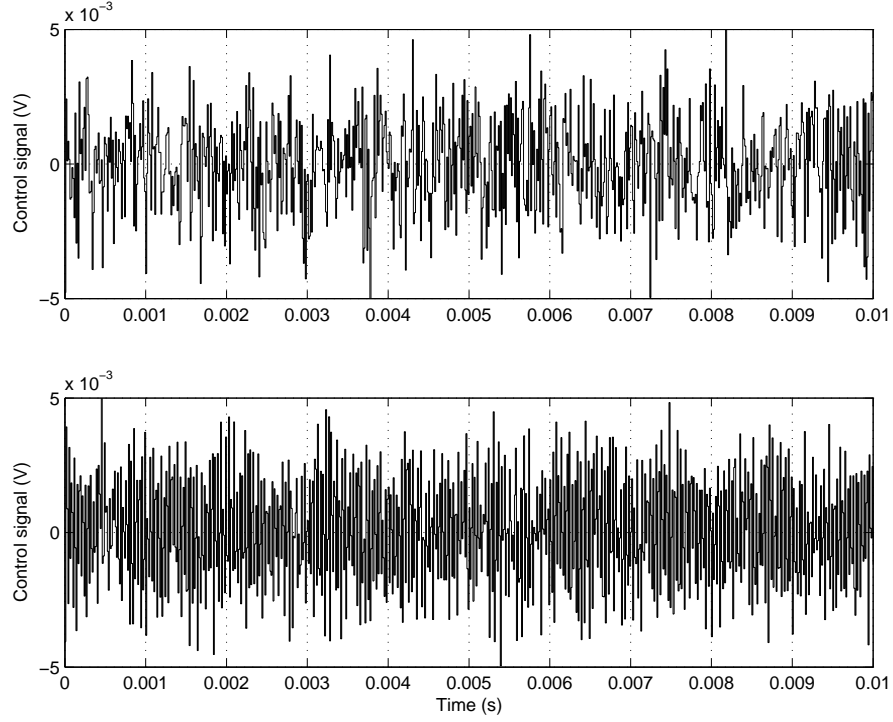
Figure 5.19: Control signal using proposed SP-based servo. Top: Slow control signal $\bar{u}_V$. Bottom: fast control signal $\tilde{u}_V$.

5.7 Summary

In this chapter, a SP (Singular Perturbation) controller design method is proposed for stronger vibration suppression in VCM and PZT active suspension using the piezoelectric elements in the suspension as a sensor to detect the actuators' high frequency dynamics. The slow and fast controllers are designed independently parameterized by a single parameter ε for time scale separation. Experimental results show effective suppression of the VCM's flexible modes at 3.9 kHz and 6.0 kHz as well as PZT active suspension's flexible modes at 5.9 kHz, 11.5 kHz and 21.0 kHz with an improvement of 39.9% in 3σ PES during track-following.

In the following chapter, we extend the active sensing methodology to MIMO (Multi-Input-Multi-Output) multi-sensing data storage servo systems. Controller
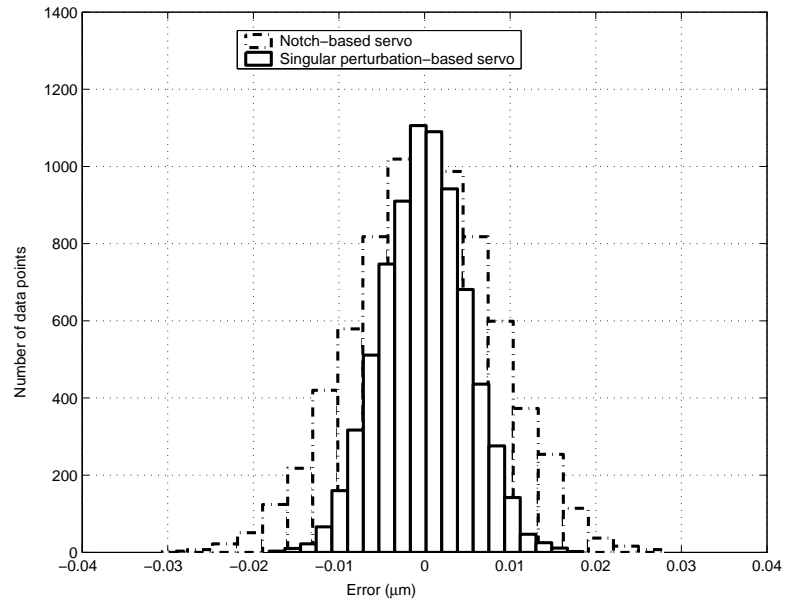
Figure 5.20: Histogram of experimental PES y measured with LDV using conventional notch-based servo and proposed SP-based servo.

design examples and SSA (Self-Sensing Actuation) feasibility studies are also executed for dual-stage HDDs as well as MEMS probe-based storage systems.

Chapter 6

Multi-Sensing Track-Following Servo Systems

With the improvements in disturbance rejection performance by incorporation of extraneous sensors and active-sensing methodologies covered in previous chapters, this chapter discusses about the feasibility of employing multi- and even self-sensing servo systems using the mechanical actuators as sensors and actuators simultaneously. Track-following controller examples are also detailed for MIMO (Multi-Input-Multi-Output) data storage servo systems in dual-stage HDDs employing PZT suspension-based secondary actuators as well as MEMS probe-based storage systems.

6.1 Example of Dual-Stage HDD Control

In a dual-stage HDD servo system, the secondary actuator is of a much smaller dimension compared to the VCM. Usually mounted on the VCM, the R/W head

is then placed onto the tip of the secondary actuator.

However, the secondary actuators (commonly known as microactuators) have a very small displacement range (0.2–2 μm) and hence is not suitable for track-seeking operation. As such, track-seeking is done by the primary actuator VCM and the secondary actuator will be active in the track-following mode. Care has to be taken to prevent saturation of the secondary actuator which will tend to destabilize the servo loop when linear controllers are used. Nonlinear controllers can be used for short span seek of several tracks to tackle the effect of actuator saturation effectively [34].

In a dual-stage HDD using PZT suspension-based secondary actuator, only the relative displacement PES is available. As such, SISO (Single-Input-Single-Output) design structures are usually employed on the VCM and microactuator loop separately and then combine the results into a complete dual-stage loop. This method gives actual insight into the working principles of the two actuators at different frequency ranges. The different control topologies will be discussed in this section.

Assume the following nomenclature with G_V and G_M as VCM and PZT microactuator models, and C_V and C_M as controllers for VCM and PZT microactuator, respectively. Also, L_D is the open loop transfer function of the dual-stage control loop, respectively. S_V, S_M and S_D are the sensitivity functions of the VCM loop, PZT microactuator loop and overall dual-stage control loop. T_V, T_M and T_D are the closed-loop transfer functions (or complementary sensitivity functions) of the VCM loop, PZT microactuator loop and dual-stage control loop, respectively. We will detail the commonly used types of dual-stage control topologies and present a simulation example.

1) Parallel configuration: Although a multivariable control method using DIDO (Dual-Input-Dual-Output) feedback is ideal, it is not feasible in HDD servo system as measured PES remains as the only available output signal. As such, the following DISO (Dual-Input-Single-Output) configuration is proposed. The functional block diagram of this structure is shown below in Figure 6.1. It should be noted that the effects of disturbances and noises are omitted in the block diagram.
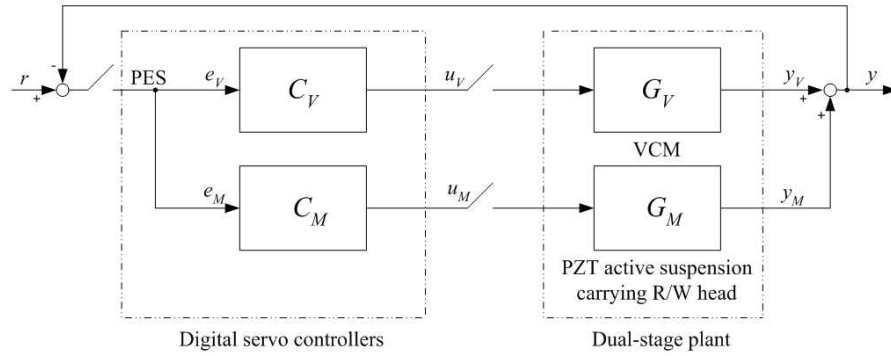
Figure 6.1: Parallel configuration.

The corresponding open loop, sensitivity and complementary sensitivity transfer functions of the parallel configuration are L_D, S_D and T_D, respectively with

$$L_D = C_V G_V + C_M G_M \tag{6.1}$$

$$S_D = \frac{1}{1 + C_V G_V + C_M G_M} \tag{6.2}$$

$$T_D = \frac{C_V G_V + C_M G_M}{1 + C_V G_V + C_M G_M} \tag{6.3}$$

It can be seen that the gain crossover frequency of the dual-stage control loop is higher than that using single stage actuation. Also, the sensitivity function is similar to that of the single stage actuation with the addition of $C_M G_M$ in the denominator. This implies that disturbance suppression and rejection is more effective in the dual-stage control loop. Control designs in parallel structure usually end

123

up with $|C_V G_V| \gg |C_M G_M|$ in the low frequency range and $|C_V G_V| \ll |C_M G_M|$ in the high frequency range. This frequency allocation allows the PZT microactuator to "work" in the higher frequency range enabling disturbance rejection while the VCM functions in the lower frequencies during error correction.

Amongst the various works done on HDD dual-stage servo control using the parallel structure, Schroeck *et al.* proposed their developed so-called PQ-method [105]. The PQ-method is a systematic procedure that simplifies the DISO (Dual-Input-Single-Output) plant into a fictitious SISO (Single-Input-Single-Output) system for successive loop closures design in the frequency domain.

2) Master-slave configuration: The primary advantage of a master-slave configuration is to put priority onto one actuator than the other [33], making the microactuator respond faster to external disturbance by being the "master" and the bulky VCM as the "slave" to compensate for slower variations in the relative displacement between the actuators.

The master-slave configuration comes in a slight variation, namely the CMS (Coupled Master-Slave) structure and the DMS (Decoupled Master-Slave) structure. Both configurations require a microactuator model as part of the VCM controller to estimate the microactuator output and is used to drive the VCM. The functional block diagram of the CMS configuration is shown in Figure 6.2.

The corresponding open loop, sensitivity and complementary sensitivity transfer functions of the CMS configuration are L_D, S_D and T_D, respectively with

$$L_D = (1 + C_V G_V)C_M G_M \tag{6.4}$$

$$S_D = \frac{1}{1 + C_M G_M + C_V G_V C_M G_M} \tag{6.5}$$

$$T_D = \frac{(1 + C_V G_V)C_M G_M}{1 + C_M G_M + C_V G_V C_M G_M} \tag{6.6}$$
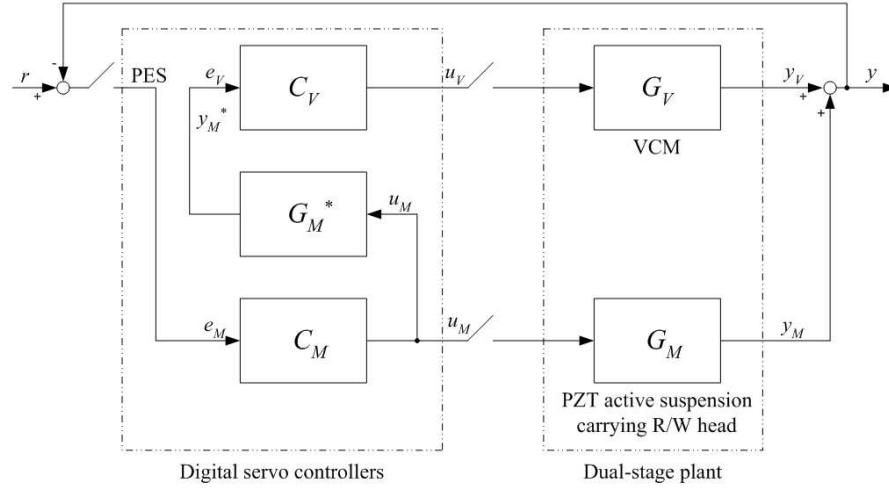
Figure 6.2: Coupled master slave configuration.

For the DMS topology, the difference between PES and the estimated PZT microactuator's displacement (which in essence is the error signal for the VCM path) is channelled back into the VCM controller. The DMS scheme is more preferable to that of the CMS (and other configurations mentioned above) as the error signal is split into two independent control loops. The functional block diagram of the DMS configuration is shown below in Figure 6.3.
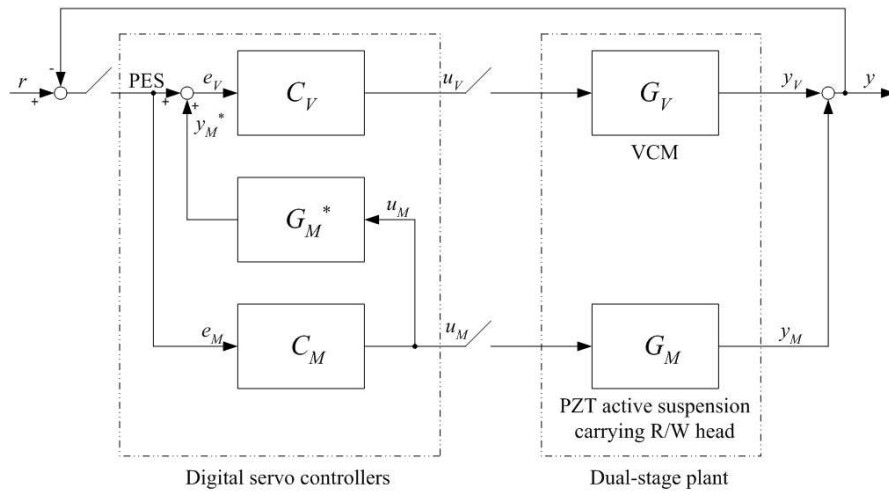
Figure 6.3: Decoupled master slave configuration.

The corresponding open loop, sensitivity and complementary sensitivity transfer functions of the DMS configuration are L_D, S_D and T_D, respectively with

$$L_D = (1 + C_M G_M)C_V G_V + C_M G_M \tag{6.7}$$

$$S_D = S_V S_M \tag{6.8}$$

$$= \frac{1}{(1 + C_M G_M)(1 + C_V G_V)} \tag{6.9}$$

$$T_D = \frac{(1 + C_M G_M)C_V G_V + C_M G_M}{(1 + C_M G_M)(1 + C_V G_V)} \tag{6.10}$$

Note that the sensitivity function of the DMS structure is the product of the sensitivity function of the VCM loop and the PZT microactuator loop. Obviously, the DMS design can be converted into the parallel design when the VCM controller C_{VP} is designed as

$$C_{VP} = (1 + C_M G_M)C_V \tag{6.11}$$

Implementation will be eased as the loops can be closed independently and dual-stage closed-loop stability will be ensured. Also, better disturbance rejection is enabled with the product of the individual path sensitivity functions. However, the performance of the master-slave configuration depends highly on the effectiveness of the estimator. If the estimator gives an actuator output which is close to the actual displacement of the microactuator ($y_M \approx y_M^*$), then disturbance rejection capabilities and servo performance will be enhanced. This is because the difference of the sensor output and the estimated microactuator output gives a good estimate of the VCM output.

Amongst the various works done on dual-stage control using the DMS structure, Kobayashi *et al.* designed a phase-stable controller for the PZT actuated-suspension using their proposed second phase margin index to retain the large gain of the resonant poles for notches in the sensitivity transfer function [53]. Peng *et*

126

al. used the developed CNF (Composite Nonlinear Feedback) control law for the VCM to reduce the rise time for a seek command in a dual-stage HDD [99]. Pang *et al.* proposed a NPM (Near Perfect Modelling) method to construct a virtual PZT actuated-suspension digital model inverse to reduce the dual-stage sensitivity using Discrete Bode's Integral Theorem [95].

The existence of structural resonant modes in both the VCM and PZT microactuator will not be able to meet the above criterion as the gain of the actuators are very high at resonant frequencies. These large gain at the lightly damped poles cause not only oscillations in the step response but also instability in the closed-loop servo system due to poor gain and phase margins. As such, several resonance compensation methods have been proposed to tackle these flexible resonant modes. The commonly used control practices will be covered in the following subsection.

Resonant Mode Compensation Methods

1) Gain stabilization: To avoid the open loop transfer function L_D from touching -1 or the 0 dB line in the magnitude of frequency response, gain stabilization of the resonant modes are commonly used to suppress the energy (hence gain) of the resonant modes at the resonant frequencies by attenuating the signal power to avoid the excitation of the associated structural modes. As such, notch filters are commonly used and is seen as the "conventional" approach [1]. Moreover, they are easy to design and implement and hence recommended in HDD literature over low pass filters for their sharper reduction in magnitude of gain at the resonant frequencies.

A drawback of these filters are that they are not robust to parameter variation— a resonant frequency shift might cause instability of the closed-loop system. Also,

they are sensitive to transients of residual vibrations [112] and large initial conditions of the VCM at the end of track-seeking mode.

2) Phase stabilization: Contrary to notch filter designs, phase stabilization methods involve design of lead compensators to drive the open loop transfer function L_D away from -1 or the $-180°$ line in the phase response via phase lifting. Using phase stabilization techniques, the large gain of the resonant modes are retained in L_D and hence notches will appear in the gain of the sensitivity transfer function S_D at the frequencies of the resonant modes. As such, stronger vibration and disturbance rejection capabilities are enhanced at the resonant frequencies. An impressive application of phase stabilization technique for dual-stage servo is documented in [53] to tackle effects of windage on the PZT active suspension.

3) Inverse control: If the system contains minimum phase pole-zero pairs (which is typical of PZT actuated systems), an approximate plant inverse controller can be constructed to make the system behave like a pure gain up high frequencies. This technique not only compensates for the large gain at the resonant modes but also increases the gain of the anti-resonant zeros.

It is well known from linear systems theory that the zeros of a system are unaltered by feedback control *i.e.* the anti-resonant zeros of the open loop system are the same as those of the closed-loop system. As such, inverse control allows the actuator to "reach" the desired locations behaving as a pure gain for better error correction, especially at the frequencies of the anti-resonant zeros. Moveover, inverse control reduces the relative degree of the closed-loop system up to high frequencies which makes the actuator "lighter" and hence a higher servo bandwidth.

While a perfect plant inverse is not realizable in causal controller designs for physical systems, the designs and effectiveness of an approximate plant inverse

controller will have to be carefully evaluated and substantiated. An example of inverse control of PZT microactuator for high bandwidth and low sensitivity dual-stage servo control is illustrated in [95].

4) Active control with embedded sensors: While measured PES remains as the only information in HDD servo systems, addition of sensors to pick up extra actuator's information (*e.g.* displacement and velocity) is intuitive. Several methods including employing (i) rotational accelerometers [44] (ii) PZT compound actuator as an instrumented suspension [59] (iii) one of the two PZT strips in an active suspension [65] as sensor and (iv) using the PZT elements as sensors and actuators simultaneously [87][128] have been proposed. Together with measured PES, active vibration controllers are synthesized for improved disturbance rejection capabilities.

For ease of design and illustration but without loss of generality, the gain stabilization method employing digital notch filters will be used here. Suppose the VCM and PZT microactuator have resonant modes at natural frequency $f_{R,i}$ and damping ratio $\zeta_{R,i}$ which can be represented by the following transfer function $R_i(s)$

$$R_i(s) = \frac{(2\pi f_{R,i})^2}{s^2 + 2\zeta_{R,i}(2\pi f_{R,i})s + (2\pi f_{R,i})^2} \tag{6.12}$$

where $(0 < \zeta_{R,i} < 1)$. An intuitive notch filter design $N_i(s)$ for each resonant mode $R_i(s)$ would be

$$N_i(s) = \frac{(2\pi f_{D,i})^2}{(2\pi f_{R,i})^2} \frac{s^2 + 2\zeta_{R,i}(2\pi f_{R,i})s + (2\pi f_{R,i})^2}{s^2 + 2\zeta_{D,i}(2\pi f_{D,i})s + (2\pi f_{D,i})^2} \tag{6.13}$$

to ensure perfect cancellation of the resonant mode. $\sqrt{2} < \zeta_{R,i} \leq 1$ is usually chosen to replace the lightly damped poles to more well-damped ones. When $f_{R,i} = f_{D,i}$, some degradation in phase response is still apparent at the resonant frequency $f_{R,i}$. A high pass notch using $f_{D,i} > f_{R,i}$ can be constructed to reduce and even remove the phase loss.

Notch filters are recommended in HDD literature over low pass filters for a sharper reduction in magnitude. The notch filters are low order and are easy to design and implement. A setback of these filters are that they are not robust to parameter variations. A resonant shift might cause instability of the closed-loop system.

For our simulation, the notch filters $N_i(s)$ are designed by replacing the small damping ratio of each resonant modes with unity at $f_{R,i} = f_{D,i}$. $N_i(s)$ is then discretized at a sampling rate of $f_s = 50$ kHz using pole-zero matching.

VCM Controller

Many control strategies have been implemented and tested on dual-stage servo systems. Optimal LQG (Linear Quadratic Gaussian)/LTR(Loop Transfer Recovery) or post modern $\mathcal{H}_2/\mathcal{H}_\infty$ controllers usually result in very high order controllers whose performance has little improvement over traditional ones.

The VCM plant model will be that shown in Equation (2.2). Assume that the compensated VCM plant can be viewed as a double integrator at frequencies of interest after pre-compensation with notch filters $N_i(s)$

$$G_V(s) \approx \frac{1 \times 10^8}{s^2} \tag{6.14}$$

We propose a double-lag controller with complex zeros of the form

$$C_V(s) = K_V \frac{s^2 + 2\zeta_{KV}(2\pi f_{KV}) + (2\pi f_{KV})^2}{s(s + \pi f_s)} \tag{6.15}$$

where $\zeta_{KV} < \frac{\sqrt{2}}{2}$ is used. f_{KV} is the frequency of the notch created by the complex zeros and f_s is the Nyquist frequency. For our simulations, $\zeta_{KV} = 0.4714$ and $f_{KV} = 100$ is used. K_V is calculated by setting $|C_V(j2\pi f_V)G_V(j2\pi f_V)| = 1$

where $f_V = 1000$ is the gain crossover frequency of the VCM path. Using the proposed complex zero compensator in the low frequency, we can see from Figure 6.4 that the lag portion of the controller is increased for enhanced low frequency disturbance rejection without increasing the gain crossover frequency (hence open loop bandwidth). More importantly, it allows faster phase recovery with the notch for a better phase margin during crossover region and speeding up of the double integrator rigid mode in the VCM while maintaining robustness. The compensated open loop transfer function has a -20 dB/dec slope during crossover and -40 dB/dec before and after crossover frequency of 1000 Hz as can be seen from Figure 6.5.
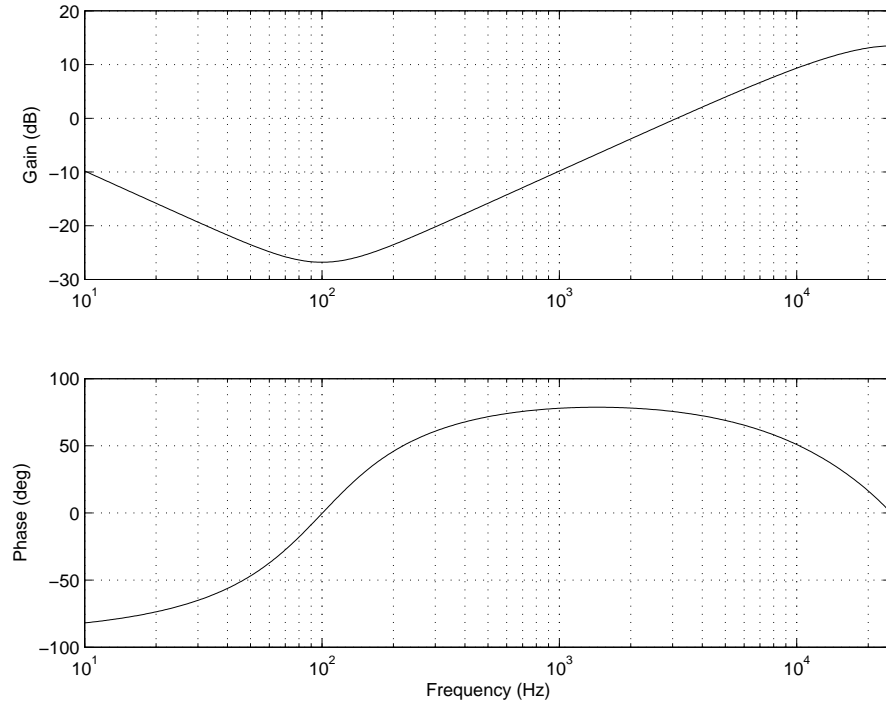
Figure 6.4: Frequency response of PID-type controller.
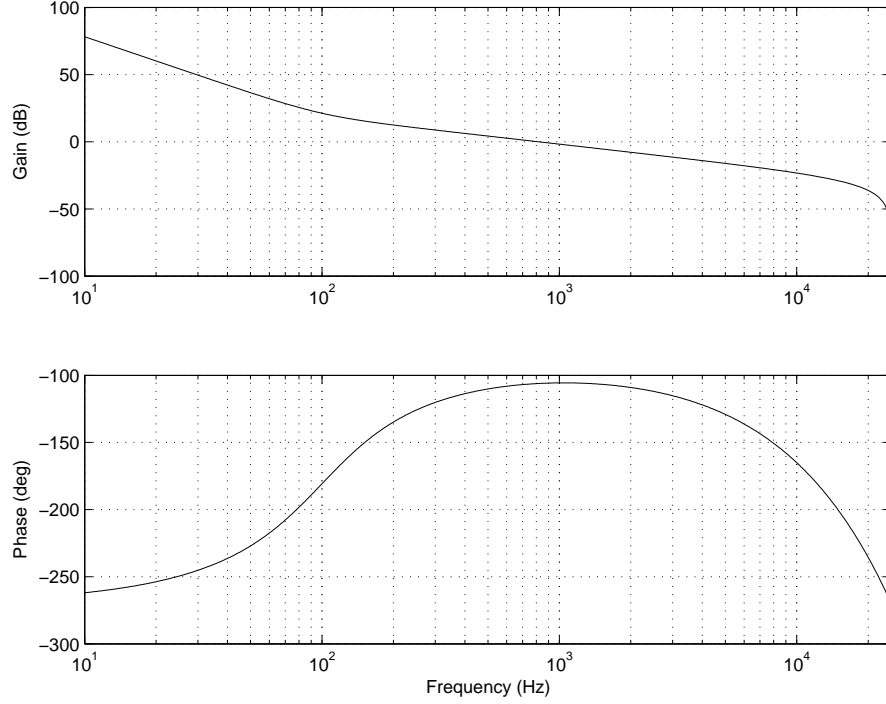
Figure 6.5: Open loop frequency response of VCM path.

PZT Microactuator Controller

For demonstration of PZT microactuator control, the PZT microactuator model
in Equation (7.4) will be used. Similarly, assume that the PZT microactuator can
be viewed as a second order low pass transfer function at frequencies of interest
after pre-compensation with notch filters $N_i(s)$

$$G_M(s) \approx 0.282 \frac{(2\pi 1 \times 10^4)^2}{s^2 + 2(1)2\pi 1 \times 10^4 s + (2\pi 1 \times 10^4)^2} \qquad (6.16)$$

The secondary actuator path can then be stabilized by a simple PI-type lag com-
pensator for low dual-stage sensitivity [95]

$$C_M(s) = K_M \frac{s + \pi f_s}{s + 2\pi 2.5 \times 10^3} \qquad (6.17)$$

where K_M can be found with the relation $|C_M(j2\pi f_M)G_M(j2\pi f_M)| = 1$ with f_M as
the gain crossover frequency for the microactuator path. The frequency response
of the PZT microactuator controller $C_M(s)$ is shown in Figure 6.6.

In this example, $f_M = 3000$ Hz. The open loop transfer function has a -20 dB/dec slope during crossover as shown in Figure 6.7. For the combined dual-stage control, a DMS structure will be used for our simulations.
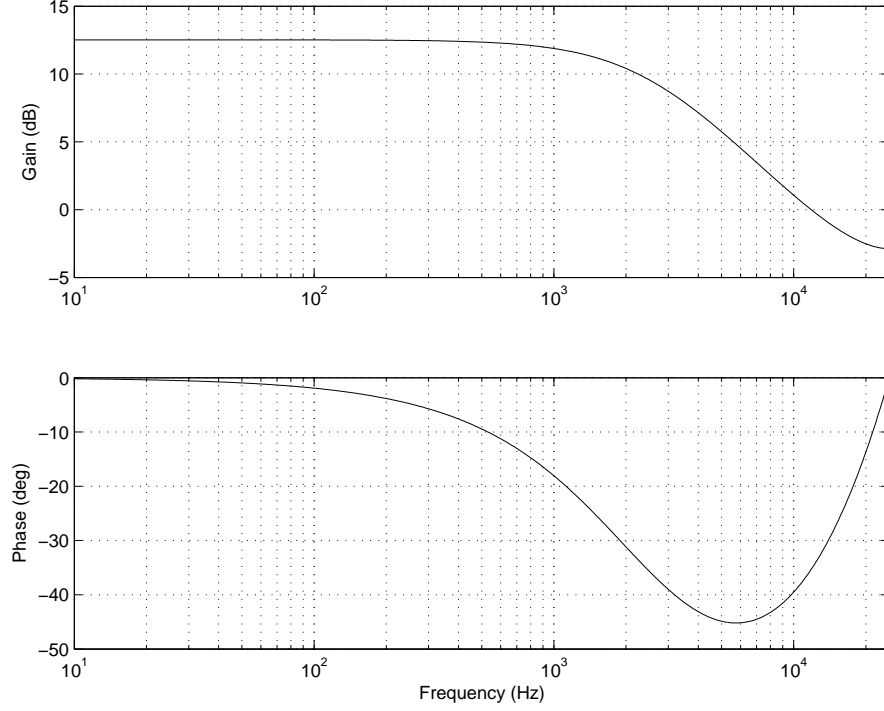
Figure 6.6: Frequency response of PZT microactuator controller.

Simulation Results

In this section, simulation results of the above dual-stage controller design will be evaluated.

1) Frequency responses: The open loop frequency responses of dual-stage L_D, VCM path $C_V G_V$ and PZT microactuator path $C_M G_M$ are plotted in Figure 6.8. Figure 6.9 shows the sensitivity and complementary sensitivity transfer function of the dual-stage servo loop S_D and T_D, respectively. A high closed-loop bandwidth and improved sensitivity can be observed. As such, strong disturbance rejection
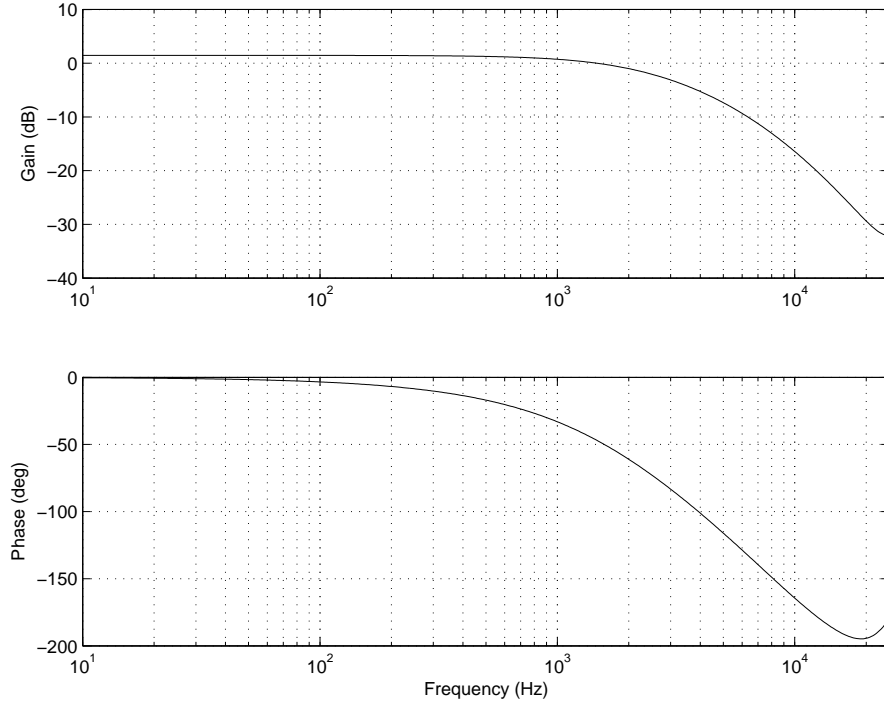
Figure 6.7: Open loop frequency response of PZT microactuator path.

capabilities are ensured.

2) Time responses: The 0.1 μm step response of the combined actuation is shown in Figure 6.10. The overshoot of the dual-stage servo system is reduced by the secondary actuator with decreased rise time.

From Figures 6.8 and 6.10, it can be seen that the two actuators do not compete with each other during actuation which causes destructive interferences. At about the so-called handover frequency (where the gain responses of the VCM and PZT microactuator intersect) of about 600 Hz, the phase difference between the VCM output and PZT microactuator output is about 100°.

The design specifications achieved are shown in Table 6.1 and are acceptable by industrial standards.
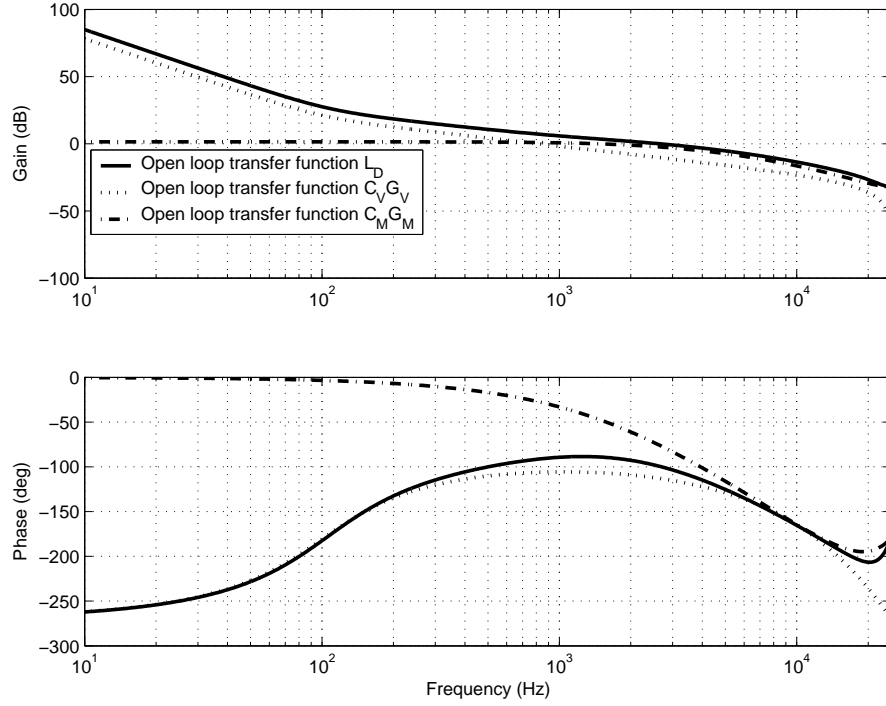
Figure 6.8: Open loop frequency response of dual-stage control using DMS structure.

Table 6.1: Design specifications achieved with dual-stage servo control

Open loop crossover frequency	$\approx$	3 kHz
Gain margin	$\geq$	20 dB
Phase margin	$\geq$	60°
Rise time	$<$	1 ms
Percentage overshoot	$<$	10%
Peak of sensitivity function	$\leq$	5 dB

6.2 Self-Sensing Actuation in Piezoelectric Actuators

Common piezoelectric materials currently employed as actuators/sensors include the PVDF (PolyVinylDeneFlouride), a semicrystalline polymer film and the PZT

135
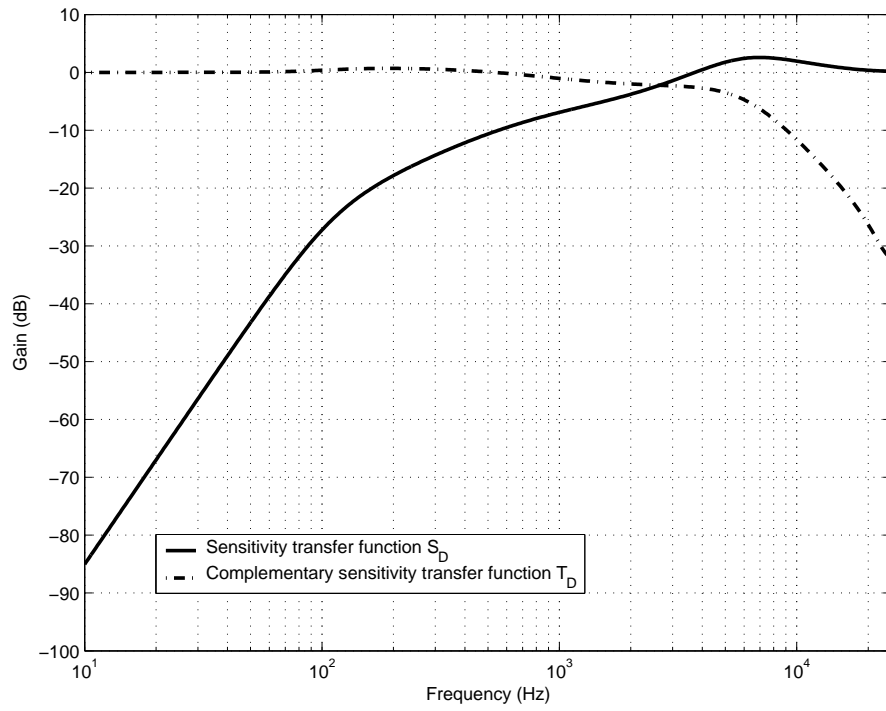
Figure 6.9: Sensitivity transfer functions of dual-stage control using DMS structure.
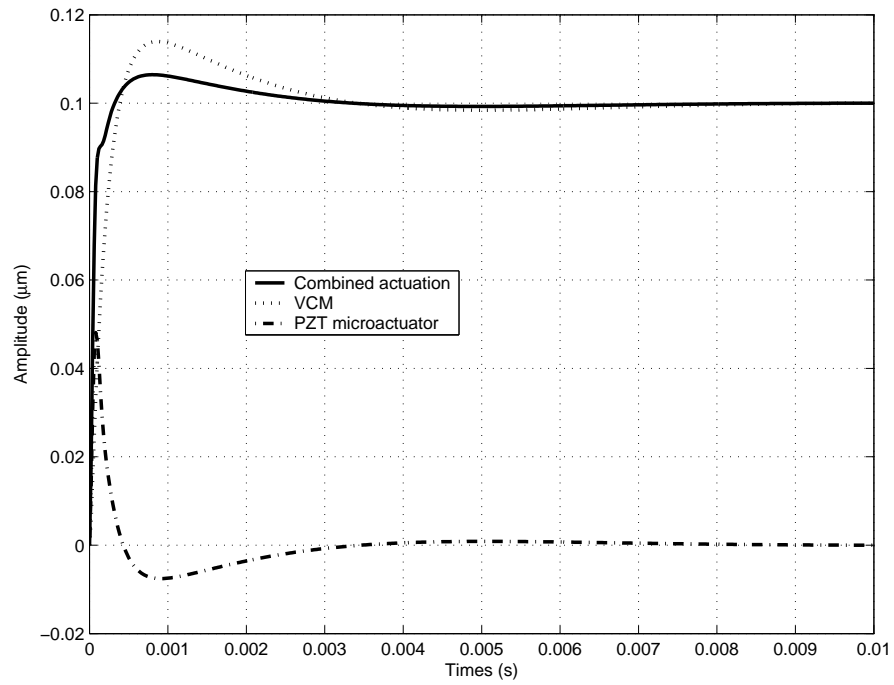
Figure 6.10: Step response using DMS structure.

136
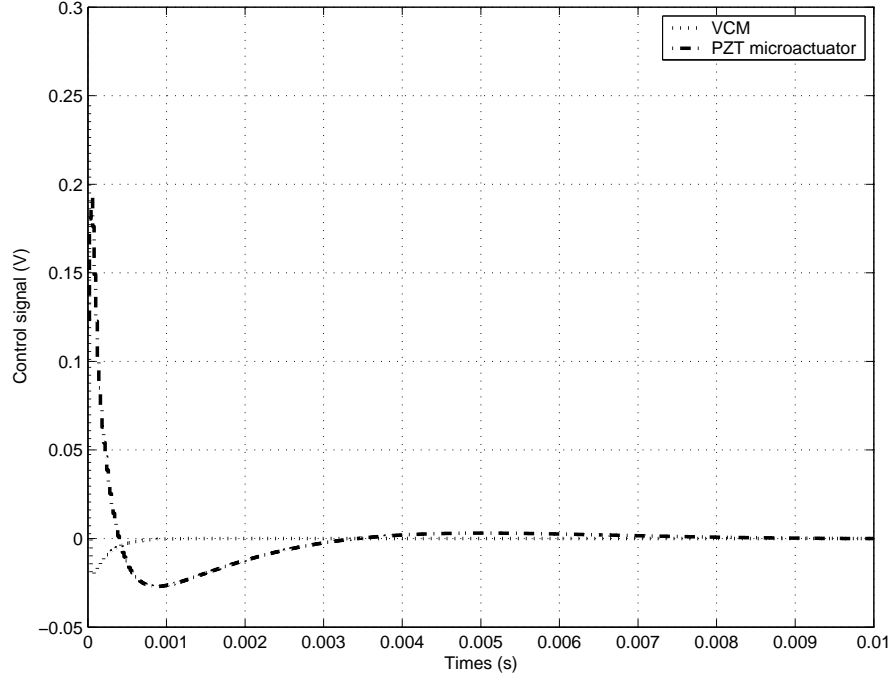
Figure 6.11: Control signals for step response.

(Lead-Zirconate-Titanate) element. The piezoelectric property is made possible by excessive exposure of the ceramic to strong electric field during the manufacturing process, thus inducing permanent dipoles in the material. When electrically polarized, the dipoles respond collectively to produce an expansion and hence mechanical strain within the material, leading to perpendicular displacement. Conversely when piezoelectric materials are subjected to strain, charges arise on the surface of the material and hence setting up an electric field, analogous to back EMF (Electro-Motive Force) in magnetic systems. These properties allow the piezoelectric material to function as an actuator and sensor respectively.

Self-Sensing Actuation, or SSA, uses the piezoelectric material as an actuator and sensor *simultaneously*. The piezoelectric material can be modelled as a capacitance in series with a variable voltage source, the capacitor representing the dipoles and the variable voltage source representing the electric field setup by the dipoles

during actuation. If the capacitance of the piezoelectric material is known, one can decouple the variable voltage (hence strain/displacement information) using a bridge circuit.

SSA has already been applied to many practical engineering problems, *eg.* control of robot manipulators and cantilever beams (see [87] and the references therein). SSA is attractive in active control applications because the actuator and sensor arrangement is a truly collocated (or in many applications near collocated) pair. Moreover when applied to dual-stage HDDs, SSA requires only additional cheap electronic circuitry and does not reduce the effective actuation of the PZT microactuator. The PZT elements in the PZT microactuator is modelled as a capacitor C_{PZT} in series with a dependent voltage source v_M as shown below in Figure 6.12.
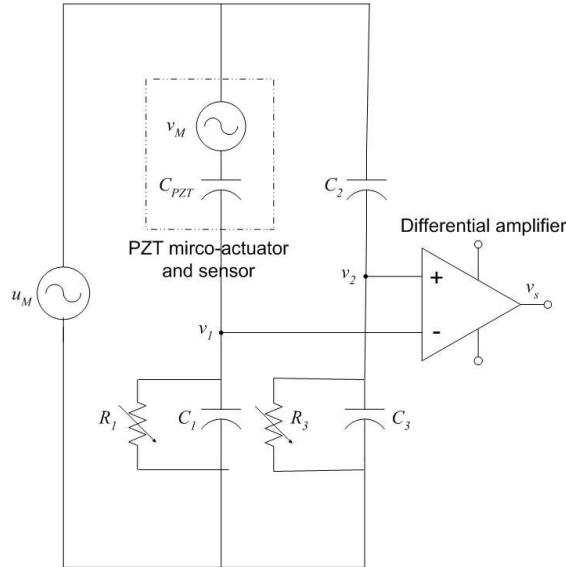
Figure 6.12: Piezoelectric bridge circuit for SSA.

When the bridge circuit is subjected to control voltage u_M, the PZT microactuator is actuated to give displacement y_M. The voltage v_M generated is hence

proportional to y_M (arising from mechanical strain) of the PZT microactuator, and can be then be decoupled from u_M using a differential amplifier. As such, we can obtain the following equations from Figure 6.12

$$v_1 = \frac{C_{\text{PZT}}}{C_1 + C_{\text{PZT}}}(u_M - v_M) \tag{6.18}$$

$$v_2 = \frac{C_2}{C_2 + C_3}u_M \tag{6.19}$$

$$v_s = v_2 - v_1$$

$$= \left(\frac{C_{\text{PZT}}}{C_1 + C_{\text{PZT}}} - \frac{C_2}{C_2 + C_3}\right)u_M + \frac{C_{\text{PZT}}}{C_1 + C_{\text{PZT}}}v_M \tag{6.20}$$

The measured capacitance C_{PZT} of the PZT elements in the PZT microactuator is about 160 μF. Resistors R_1 and R_3 are sometimes placed in parallel with capacitors C_1 and C_3 to prevent DC drifts. By making capacitors $C_1 = C_2 = C_3 = C_{\text{PZT}}$, the bridge circuit is balanced and a PZT microactuator displacement estimator is established with

$$v_s = \frac{C_{\text{PZT}}}{C_1 + C_{\text{PZT}}}v_M$$

$$= \frac{v_M}{2} \tag{6.21}$$

As such, v_M is decoupled from the control signal u_M and can be used for control purposes. The only trade-off we have is that a larger control signal u_M is needed for the same amount of displacement actuation as compared to no bridge circuit. The feasibility of using SSA in dual-stage HDDs will be detailed in the next chapter.

6.3 Example of MEMS Micro X-Y Stage Control

In this section, an example of MEMS micro X-Y stage control is presented. A $\mathcal{H}_2$ output feedback controller is designed for the MIMO plant.

Rewriting the dynamics of the MEMS micro X-Y $G(s)$ from Equation (2.8) into standard state-space representation Σ, we have

$$\Sigma : \begin{cases} \dot{x} &=& Ax + Bu + Ew \\ y &=& C_1 x + D_1 w \\ z &=& C_2 x + D_2 u \end{cases} \tag{6.22}$$

where $x \in R^n$, $y \in R^p$, $z \in R^q$, $w \in R^l$ and $u \in R^m$ are state variables, measurement, controlled output, disturbance and control signal, respectively. For our simulations, we have chosen $E = 0.01B$, $D_1 = 2 \times 10^{-3} I$ and $D_2 = 0$. As such, the controlled output z has no feedthrough term and standard perturbation approach will be used to tackle the singular problem [102].

Define a new controlled output

$$\begin{aligned} \tilde{z} &=& \begin{bmatrix} z \\ \varepsilon x \\ \varepsilon u \end{bmatrix} \\ &=& \begin{bmatrix} C_2 \\ \varepsilon I \\ 0 \end{bmatrix} x + \begin{bmatrix} D_2 \\ 0 \\ \varepsilon I \end{bmatrix} u \end{aligned} \tag{6.23}$$

and the matrices with disturbance inputs become

$$\begin{aligned} \tilde{E} &=& \begin{bmatrix} E & \varepsilon I & 0 \end{bmatrix} \\ \tilde{D}_1 &=& \begin{bmatrix} D_1 & 0 & \varepsilon I \end{bmatrix} \end{aligned} \tag{6.24}$$

with a sufficiently small positive scalar ε. With this augmentation scheme, the problem is transformed to that of the regular case and the singular problem can be solved for the perturbed plant $\tilde{\Sigma}$ as

$$\tilde{\Sigma} : \begin{cases} \dot{x} &=& Ax + Bu + \tilde{E}\tilde{w} \\ y &=& C_1 x + \tilde{D}_1 \tilde{w} \\ \tilde{z} &=& \tilde{C}_2 x + \tilde{D}_2 u \end{cases} \tag{6.25}$$

$\mathcal{H}_2$ Suboptimal Control

As the problem is now formulated into a regular case, the solution to the regular $\mathcal{H}_2$ output feedback problem can be obtained by solving the following $\mathcal{H}_2$ ARE (Algebraic Riccati Equation) [102]

$$A^T P_2 + P_2 A + \tilde{C}_2^T \tilde{C}_2 - (P_2 B + \tilde{C}_2^T \tilde{D}_2)(\tilde{D}_2^T \tilde{D}_2)^{-1}(\tilde{D}_2^T \tilde{C}_2 + B^T P_2) = 0 \quad (6.26)$$

for a unique positive semi-definite solution $P_2 \geq 0$ and the following ARE

$$Q_2 A^T + A Q_2 + \tilde{E}\tilde{E}^T - (Q_2 C_1^T + \tilde{E}\tilde{D}_1^T)(\tilde{D}_1 \tilde{D}_1^T)^{-1}(\tilde{D}_1 \tilde{E}^T + C_1 Q_2) = 0 \quad (6.27)$$

for a unique positive semi-definite solution $Q_2 \geq 0$. The state feedback gain F_2 and estimator gain K_2 are given by

$$F_2 = -(\tilde{D}_2^T \tilde{D}_2)^{-1}(\tilde{D}_2^T \tilde{C}_2 + B^T P_2) \quad (6.28)$$

$$K_2 = -(Q_2 C_1^T + \tilde{E}\tilde{D}_1^T)(\tilde{D}_1 \tilde{D}_1^T)^{-1} \quad (6.29)$$

Using $\varepsilon = 0.005$, we obtain the following values of P_2, F_2, Q_2 and K_2 with MATLAB as

$$P_2 = \begin{bmatrix} 0.0004 & 0.0057 & 0.0000 & 0.0000 \\ 0.0057 & 0.1719 & 0.0000 & 0.0015 \\ 0.0000 & 0.0000 & 0.0004 & 0.0057 \\ 0.0000 & 0.0015 & 0.0057 & 0.1719 \end{bmatrix} \quad (6.30)$$

$$F_2 = 1 \times 10^4 \begin{bmatrix} -0.1932 & -2.9149 & -0.0006 & -0.0175 \\ -0.0006 & -0.0175 & -0.1932 & -2.9149 \end{bmatrix} \quad (6.31)$$

$$(6.32)$$

$$
Q_2 = 1 \times 10^{-3}
\begin{bmatrix}
0.1095 & 0.0290 & -0.0003 & -0.0002 \\
0.0290 & 0.0256 & -0.0002 & -0.0002 \\
-0.0003 & -0.0002 & 0.1095 & 0.0290 \\
-0.0002 & -0.0002 & 0.0290 & 0.0256
\end{bmatrix}
\tag{6.33}
$$

$$
K_2 =
\begin{bmatrix}
-234.0227 & -0.0235 \\
-128.6627 & 0.3717 \\
-0.0235 & -234.0227 \\
0.3717 & -128.6627
\end{bmatrix}
\tag{6.34}
$$

The dynamic $\mathcal{H}_2$ suboptimal output feedback controller Σ_2^c is then given by

$$
\Sigma_2^c :
\begin{cases}
\dot{v} &= (A + BF_2 + K_2C_1)v - K_2y \\
u &= F_2v
\end{cases}
\tag{6.35}
$$

and its frequency response is shown below in Figure 6.13. The best achievable $\mathcal{H}_2$-norm γ_2^* of the closed-loop system from $\tilde{w}$ to z (*i.e.* $T_{z\tilde{w}}$) is given by

$$
\begin{aligned}
\gamma_2^* &= \sqrt{\mathrm{tr}(\tilde{E}^T P_2 \tilde{E}) + \mathrm{tr}[(A^T P_2 + P_2 A + \tilde{C}_2^T \tilde{C}_2)Q_2]} \\
&= 1.1279
\end{aligned}
\tag{6.36}
$$

where $\mathrm{tr}(\boldsymbol{.})$ denotes the trace operation.

The frequency response of largest open loop singular value is shown in Figure 6.14. The synthesized $\mathcal{H}_2$ suboptimal output feedback controller effectively phase-stabilizes the MEMS micro X-Y stage with lead compensation at crossover frequency of about 4.5 kHz.

The frequency response of the largest singular value of closed-loop transfer function T_{zw} from disturbance w to controlled output z is shown in Figure 6.15. It can be seen that the proposed $\mathcal{H}_2$ control scheme has strong disturbance rejection capabilities over all frequencies.
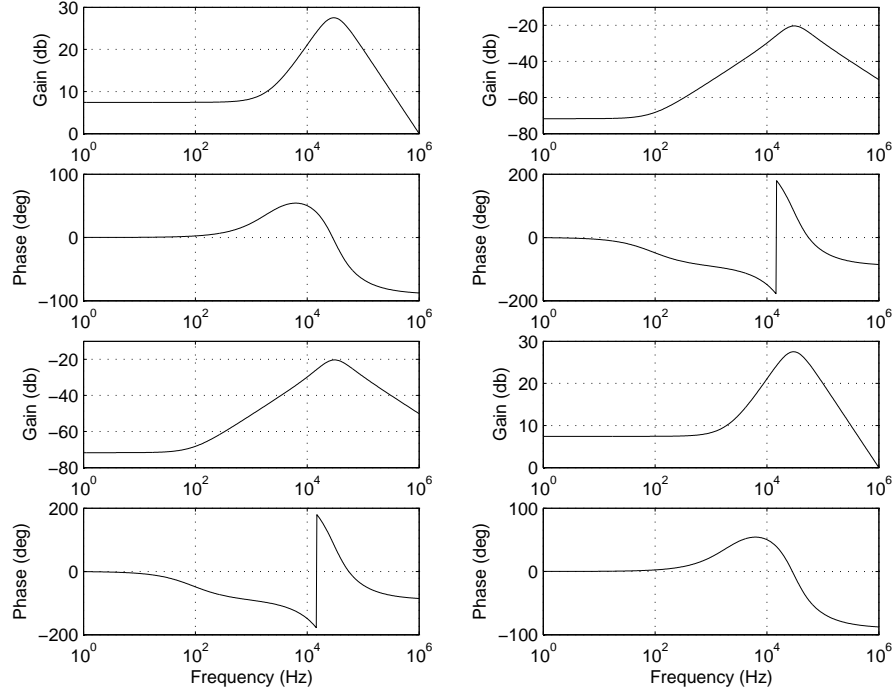
Figure 6.13: Frequency response of synthesized $\mathcal{H}_2$ suboptimal output feedback controller Σ_2^c.

6.4 Capacitive Self-Sensing Actuation in MEMS-based Actuators

Using the fact that the capaitance C_{MEMS} of the comb drives in the MEMS micro X-Y stage is proportional to the area of overlap A according to this equation

$$C_{\mathrm{MEMS}} = \frac{\varepsilon_r \varepsilon_o A}{d} \qquad (6.37)$$

which is proportional to displacement of the MEMS micro X-Y stage for the same comb width, we can design a bridge circuit similar to that of the piezoelectric actuator case in Figure 6.12 to decouple the capacitance information, which is linear with displacement of the MEMS micro X-Y stage.

However, the capacitance of MEMS-based devices are usually in the pico or
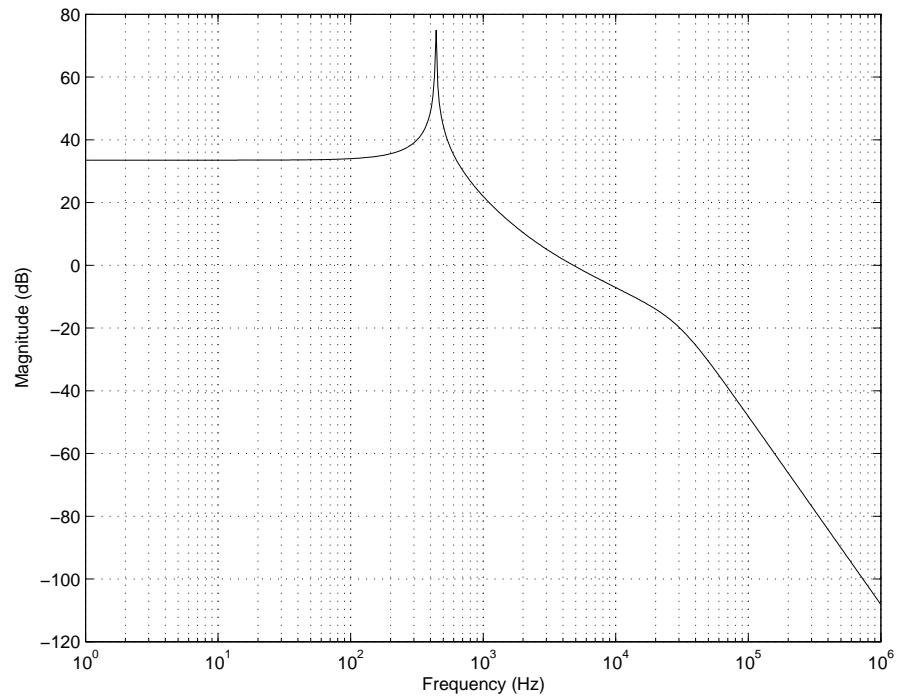
Figure 6.14: Magnitude response of largest open loop singular value.
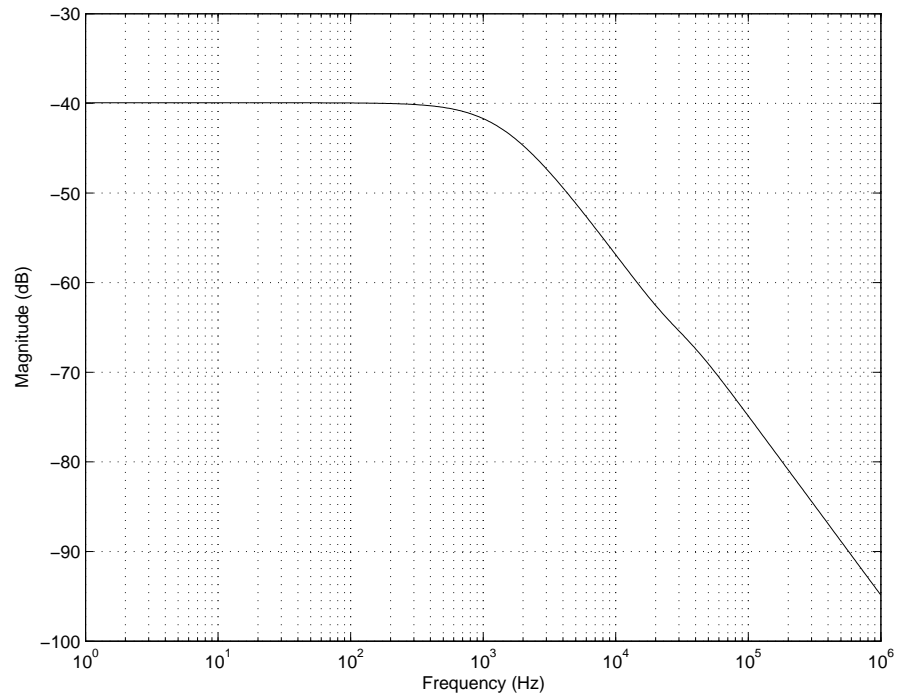
Figure 6.15: Magnitude response of largest singular value of T_{zw}.

144

even femto Farad region. When actuated in micro or even nanometers, the SNR (Signal-to-Noise Ratio) of a simplistic bridge circuit will be very low. As such, modifications to the original bridge circuit yields the following schematic for CSSA (Capacitive Self-Sensing Actuation) in MEMS-based actuators
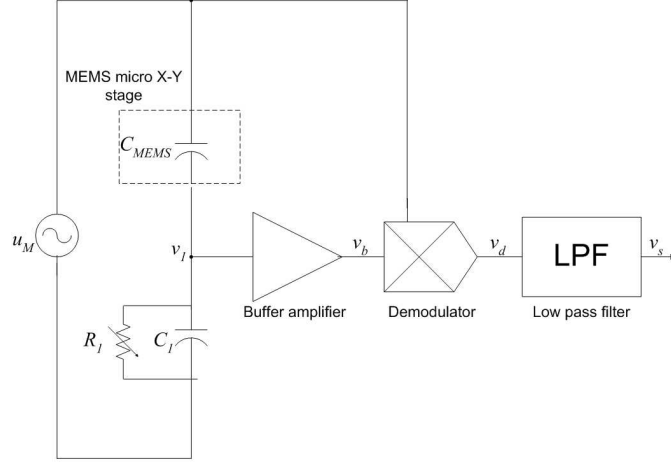
Figure 6.16: MEMS-based bridge circuit for CSSA.

Assume that the signal generator u_M produces a sinusoid $U \sin \omega t$. As such, the following equations hold

$$v_1 = \frac{C_{\text{MEMS}}}{C_1 + C_{\text{MEMS}}} U \sin \omega t \tag{6.38}$$

$$v_b = K_a v_1 \tag{6.39}$$

$$v_d = v_b u_M$$

$$= K_a v_1 U \sin \omega t$$

$$= \frac{U^2 K_a C_{\text{MEMS}}}{C_{\text{MEMS}} + C_1} \sin^2 \omega t$$

$$= \frac{U^2 K_a C_{\text{MEMS}}}{2(C_{\text{MEMS}} + C_1)} (1 - \cos 2\omega t) \tag{6.40}$$

where K_a is the gain of the buffer amplifier. After passing through the LPF (Low Pass Filter), the high frequency sinusoid at 2ω is demodulated and we can obtain v_s

as

$$v_s = \frac{U^2 K_a C_{\mathrm{MEMS}}}{2(C_{\mathrm{MEMS}} + C_1)} \tag{6.41}$$

and hence we can intrapolate C_{MEMS} to be

$$C_{\mathrm{MEMS}} = -\frac{2v_s C_1}{2v_s - U^2 K_a} \tag{6.42}$$

which is proportional to the area of overlap A (hence displacement) of the MEMS micro X-Y stage in both axial directions. The effectiveness of the proposed circuit will be detailed in future chapters. The above derivations exclude the effects of resistor R_1 which is commonly included to prevent drifting effects of the capacitance after prolonged operations.

The modulator and demodulator are added to reduce the sensor noise level. Unlike in magnetic storage systems where PES is obtained when the R/W head moves over servo sectors on the spinning disks, PES has to be generated in probe-storage systems by artificially vibrating the MEMS micro X-Y stage at a frequency ω to obtain readback signal. After PES demodulation, the MEMS micro-stage is actuated to the desired position with a new computed u_M from the obtained PES. To obtain PES at the new location, the MEMS micro X-Y stage is vibrated at ω again and the procedure is repeated in capacitive self-sensing.

It should be noted that any sinusoid of frequency that has unity gain within the closed-loop bandwidth of the MEMS micro X-Y stage can be used.

6.5 Summary

In this chapter, controller designs for MIMO (Multi-Input-Multi-Output) systems in dual-stage HDDs (employing PZT microactuator) and MEMS-based mi-

cro X-Y stage are presented. The feasibilities of incorporating SSA (Self-Sensing Actuation)—employing the actuator as a sensor and actuator simultaneously—are also detailed with respect to high density data storage systems.

In the next chapter, we extend the direct design compensation methodology in SPT (Singular Perturbation Theory) without time scaling to a dual-stage HDD using SSA (Self-Sensing Actuation) by employing the PZT microactuator as secondary actuator and sensor simultaneously. A high SNR (Signal-to-Noise Ratio) with nanometer sensing resolution is achieved for AMD (Active Mode Damping) of the PZT microactuator's torsional and sway modes.

Chapter 7

Self-Sensing Actuation for Nanopositioning and Active Mode Damping in Dual-Stage HDDs

Position sensors other than the R/W heads are not embedded into current HDDs due to cost, resolution and SNR issues. Moreover, the "optimal" location for placing these sensors is still unknown. In this chapter, the PZT elements in the PZT suspension-based microactuator are used as a secondary actuator and a displacement sensor simultaneously with SSA. The proposed displacement estimation circuit produces an estimated PZT microactuator's displacement with high SNR and nanometer resolution comparable to that measured from the LDV. A robust AMD (Active Mode Damping) controller is then designed to damp the PZT microactuator suspension's torsion modes and sway mode, as well as decoupling the HDD dual-stage servo into two distinct loops for individual sensitivity optimization.

7.1 Background

In today's information explosion era, HDDs find their applications in many home and portable electronic devices. As such, industries are striving for HDDs with smaller form factors and higher recording density simultaneously to meet the storage demands of consumers. These pushing factors translate into stringent requirements for servo positioning to enable high recording densities. With the demonstration of more than 200 kTPI at end of 2004, the track density of HDD product is expected to double by the end of 2006.

Such a high-track density requires a higher precision servo system, which cannot be achieved by the current HDDs employing the VCM as the sole actuator. The VCM limits the bandwidth extension in the single-stage servo system because of its mechanical resonances and high frequency uncertainties. As such, dual-stage actuation is seen by many as the solution for next generation of HDDs.

In a typical proposed dual-stage HDD, a small secondary actuator (*e.g.* PZT suspension-based microactuator, or PZT microactuator for short) is appended piggyback on the VCM for fine positioning. As the effective stroke range of the PZT microactuator is limited, it is easily saturated which leads to instability of the dual-stage servo system if unconsidered [34]. Also, the electrical and mechanical characteristics of the PZT element is still not well developed and understood. The stiffness of the suspension remains an issue, hence unlike optical drives where dual-stage actuation is introduced with much celebrated success, secondary actuation is still not implemented into current magnetic HDDs. PES remains as the only available information for feedback control when there are now two distinct actuators to be controlled.

On adding sensors for active control in HDDs, Huang *et al.* [44] used rotational accelerometers to damp the VCM butterfly mode in a single-stage HDD, Li *et al.* [65] split the two PZT strips in a PZT-actuated suspension and use one strip of PZT element as actuator and the other as sensor for active vibration control in a dual-stage HDD. While Lee *et al.* [59] used the PZT elements in the entire compound actuator solely as a position sensor.

In this chapter, SSA employing the PZT element as a secondary actuator, and displacement sensor is explored simultaneously. This idea was first brought to HDD industry by Sasaki in 1999, but since then no results were documented till recently where [128] and [86] appeared simultaneously. Yamada *et al.* in [128] used the strain and strain rate information from SSA for active vibration control of the PZT microactuator using PPF (Positive Position Feedback) and SRF (Strain Rate Feedback), respectively. Pang *et al.* however, focused on the SNR issues in using the PZT microactuator with SSA and used the PZT microactuator's displacement information for AMD of the PZT microactuator for dual-stage sensitivity optimization.

With the natural collocation of the actuator and sensor, we propose a simple and robust AMD controller for the PZT microactuator. Together with PES, the PZT microactuator's displacement information is used to decouple the dual-stage servo system into two loops for track-following controller design and individual sensitivity optimization.

7.2 Dual-Stage Servo Systems

The main classifications of HDD dual-stage servo systems in ascending order of size are (i) the head-based: where the microactuator is attached between the slider and the R/W head; (ii) the slider-based: where the microactuator is inserted between the suspension and the slider; and (iii) the suspension-based: where the microactuator is placed between the arm of VCM and the suspension. Depending on the location in which the microactuator is placed, the control topology and design for a dual-stage HDD differs. The slider- and head-based microactuators are manufactured by the MEMS technology, and are hence known as MEMS microactuators. In our discussions and experiments, we are using the suspension-based microactuators actuated by PZT elements, or PZT microactuators for short.

Among the many dual-stage control designs described in the previous chapter, the modified DMS dual-stage control structure with saturation as shown in Figure 7.1 is considered here for its simplicity and effectiveness in dealing with microactuator saturation issues [34]. Similar to the conventional DMS dual-stage control structure, the VCM is driven by its decoupled loop error signal e_V as can be seen from Figure 7.1. If G_M^* produces a good estimation y_M^* such that $y_M^* \approx y_M$, we can obtain decoupling of the two actuator loops. This enables individual loop control and sensitivity optimization for better disturbance rejection capabilities.

Because of the limited displacement range of the microactuator, the control efforts for the two actuators should be distributed properly when designing respective controllers to prevent saturation of the microactuator. An effective dual-stage loop should adhere to the guidelines given in [50] so that the actuators will not conflict with each other's control authority, causing negative interferences.
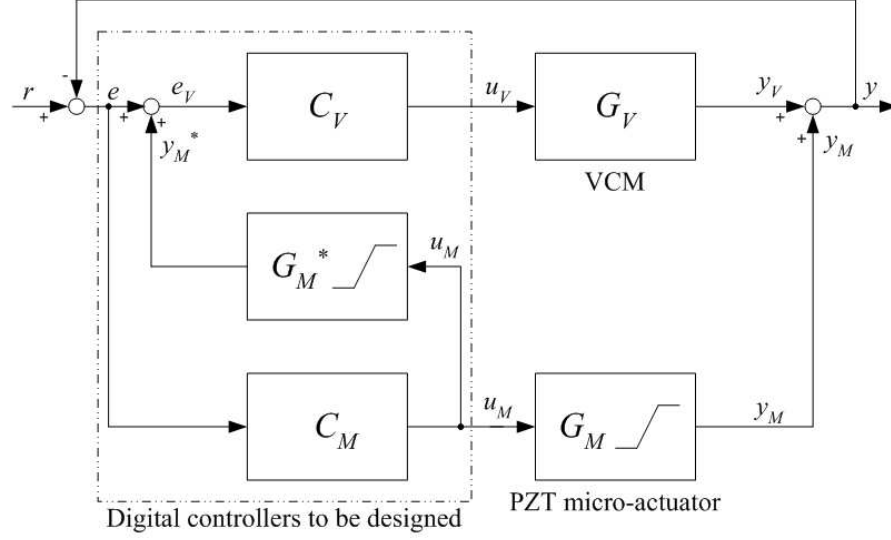
Figure 7.1: Modified decoupled master-slave configuration with PZT microactuator saturation considerations [34].

In this chapter, we propose an SSA-DMS dual-stage control topology as shown in Figure 7.2. Unlike the conventional DMS structure where only PES is used, this proposed SSA-DMS control topology uses PES and the estimated PZT microactuator's displacement y_M^* obtained from SSA for feedback control. The digital inverse of displacement estimation circuit $H_B^{-1}(z)$ replaces the off-line estimator G_M^* in the conventional DMS configuration to obtain a real time estimated y_M^* for actively decoupling the dual-stage loop so that controller designs and sensitivity optimization for the VCM and the PZT microactuator can be carried out independently. Further, y_M^* is also used in the AMD controller C_D to damp the PZT microactuator suspension's torsion modes and sway mode in the inner loop compensation, which was previously impossible if y_M^* arising from the displacement estimation circuit H_B using SSA was unavailable. The details on design of C_V, H_B^{-1}, C_D and C_M are presented in future sections.

152
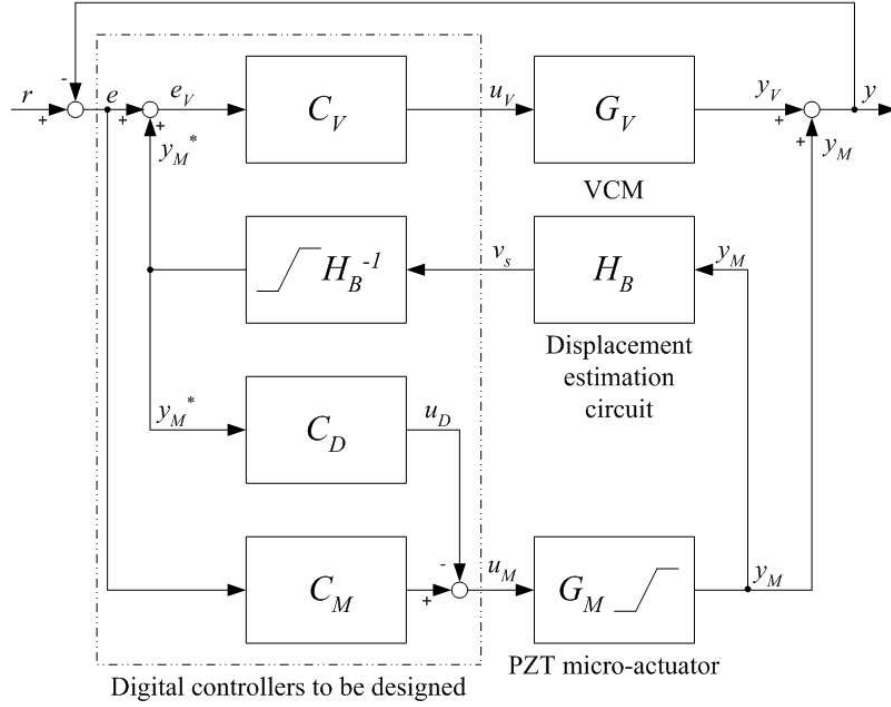
Figure 7.2: Proposed SSA-DMS dual-stage control topology.

7.3 Online Estimation of PZT Micro-actuator's Displacement

In this section, we shall detail the procedure in obtaining an online estimation of PZT microactuator's displacement y_M^*. The SNR and resolution of the estimated y_M^* will also be compared to the measured y_M from the LDV.

7.3.1 Self-Sensing Actuation (SSA)

For our experiments, we establish the SSA circuit shown previously in Figure **??** to estimate a real time PZT microactuator's displacement y_M^*. A differential amplifier setup consisting of the HP1142A differential probe control (with power module) and Brüel and Kjær voltage amplifier for low noise and high gain amplification is

used. The frequency response of the differential amplifier setup with a gain of 10 is shown in Figure 7.3.
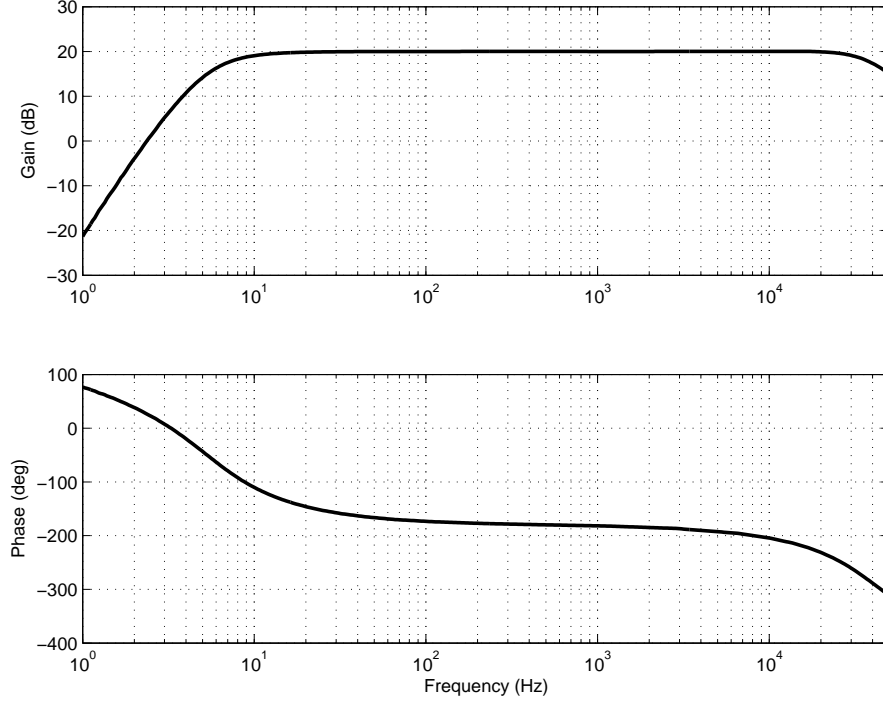
Figure 7.3: Frequency response of differential amplifier setup consisting of HP1142A differential probe control and Brüel and Kjær voltage amplifier.

It should be noted that any high-speed, low-noise instrumentation amplifiers (*e.g.* AD524 from Analog Devices) can be used. The differential amplifier setup has constant gain with little phase distortion from 100 Hz to 10 kHz.

7.3.2   Identification of Displacement Estimation Circuit

The PZT microactuator displacement estimation circuit H_B consists of the PZT micro-ctuator/sensor and the differential amplifier setup. As v_M (hence v_s) arises from y_M, H_B should be modelled by a transfer function $H_B(s) = \frac{v_s(s)}{y_M(s)}$. Making the VCM stationary, we connect y_M measured from the LDV to channel 1 and v_s

from the differential amplifier setup output to channel 2 of the DSA. The frequency response of $H_B(s)$ is measured with swept sine excitation and is shown below in Figure 7.4.
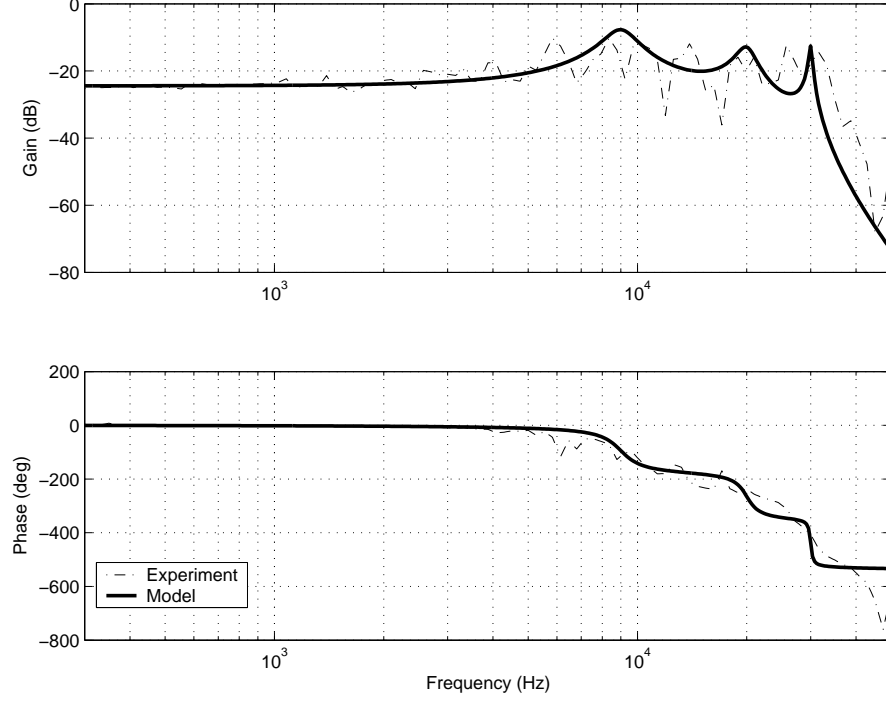
Figure 7.4: Frequency response of displacement estimation circuit H_B.

To identify $H_B(s)$, the following sixth order transfer function is used

$$H_B(s) \;=\; K_B \frac{\omega_1^2}{s^2 + 2\zeta_1\omega_1 s + \omega_1^2} \frac{\omega_2^2}{s^2 + 2\zeta_2\omega_2 s + \omega_2^2} \frac{\omega_3^2}{\tau} \frac{s+\tau}{s^2 + 2\zeta_3\omega_3 s + \omega_3^2} \quad (7.1)$$

The values of K_B, ζ_i, ω_i and τ for $i = 1, 2$ and 3 are shown in Table 7.1.

7.3.3 Performance Analysis

A digital inverse of $H_B(s)$, $H_B^{-1}(z)$, is constructed at a sampling frequency f_s of 100 kHz to provide an estimate of the PZT microactuator displacement y_M^*.

Table 7.1: Parameters of $H_B(s)$

K_B	0.06
ζ_1	0.2
ζ_2	0.09
ζ_3	0.03
ω_1	$2\pi 9 \times 10^3$
ω_2	$2\pi 20 \times 10^3$
ω_3	$2\pi 30 \times 10^3$
τ	$2\pi \times 10^3$

The model inverse $H_B^{-1}(s)$ is constructed as

$$
H_B^{-1}(s) = \frac{\tau \omega_\beta^5}{K_B \omega_1^2 \omega_2^2 \omega_3^2} \frac{s^2 + 2\zeta_1 \omega_1 s + \omega_1^2}{(s+\tau)(s+\omega_\beta)} \cdots
$$
$$
\times \frac{s^2 + 2\zeta_2 \omega_2 s + \omega_2^2}{(s+\omega_\beta)^2} \frac{s^2 + 2\zeta_3 \omega_3 s + \omega_3^2}{(s+\omega_\beta)^2} \tag{7.2}
$$

where $\omega_\beta = \frac{\pi f_s}{\beta}$ and $1 \leq \beta < 1.2$ is chosen usually so that the $H_B^{-1}(s)$ is realizable. The poles are chosen near the Nyquist frequency $\frac{f_s}{2}$ to maximize the dynamic range of H_B^{-1}. A saturation function is also included to mimic the saturation of the PZT microactuator.

While a sixth order transfer function is computationally intensive, it is still more efficient than the eight order estimator G_M^* (digital PZT microactuator model as shown in Figure 7.10) used in conventional DMS control structures. With the inverse dynamics available, v_s is channelled into the digital inverse $H_B^{-1}(z)$ so that its output y_M^* estimates the PZT microactuator's displacement y_M measured using the LDV. This allows us to evaluate the effectiveness of PZT microactuator displacement estimation circuit H_B in nanoposition sensing for usage in dual-stage

HDDs.

SNR Analysis

For brevity but without loss of generality, the performance of the sensor circuit is examined with sinusoids of frequencies at 10 kHz and 30 kHz for illustration purposes. This is done by making the VCM stationary and exciting the PZT microactuator with $u_M = 10\sin(2\pi10 \times 10^3 t)$ V and $u_M = 10\sin(2\pi30 \times 10^3 t)$ V, respectively. The time responses of the measured PZT microactuator's displacement y_M using a LDV and the estimated displacement y_M^* from the digital inverse $H_B^{-1}(z)$ are shown below in Figures 7.5 and 7.6.

The phase difference between the two signals is due to phase loss during sampling and imperfect modelling of H_B. However, this phase difference is small as can be seen from the frequency response of measured PZT microactuator's displacement from LDV y_M to estimated PZT microactuator's displacement y_M^* to be shown in the next subsection, and is negligible as can be seen from the experimental results which will be presented in future sections.

If we reduce the source level of control signal u_M further, it can be seen from Figures 7.7 and 7.8 below that the estimated PZT microactuator's displacement y_M^* still resembles y_M measured from the LDV well with high SNR at nanometer resolution and accuracy even when the PZT microactuator is actuating at ±5 nm and ±10 nm in radial directions.

The measured y_M from the LDV becomes distorted when the PZT microactuator is actuating at about ±5 nm in radial directions as shown in Figure 7.8. However, the PZT SNR is low only when the PZT microactuator is actuated to less than 2 nm (not shown) which makes the displacement estimation circuit H_B

Figure 7.5: Time responses with $u_M = 10\sin(2\pi 10 \times 10^3 t)$ V. Top: PZT microactuator's displacement y_M measured from LDV with resolution of 0.5 μm/V. Bottom: Estimated PZT microactuator's displacement y_M^* from digital bridge circuit inverse $H_B^{-1}(z)$. The PZT microactuator is actuating at about ± 37.5 nm in radial directions.

comparable to that measurements from the LDV in nanometer resolution.

Correlation Analysis

By setting the peak-to-peak level of u_M to 2 V corresponding to the PZT microactuator actuating at about ± 8 nm in radial directions, the frequency response of measured PZT microactuator's displacement from LDV y_M to estimated PZT microactuator's displacement y_M^* is shown in Figure 7.9.

Figure 7.6: Time responses with $u_M = 10 \sin(2\pi 30 \times 10^3 t)$ V. Top: PZT microactuator's displacement y_M measured from LDV with resolution of 0.5 μm/V. Bottom: Estimated PZT microactuator's displacement y_M^* from digital bridge circuit inverse $H_B^{-1}(z)$. The PZT microactuator is actuating at about ± 37.5 nm in radial directions.

It can be seen from Figure 7.9 that the estimated PZT microactuator's displacement y_M^* correlates well with measured PZT microactuator's displacement from LDV y_M from about 300 Hz onwards even at small displacements of ± 8 nm. This makes the displacement estimation circuit H_B effective only in the higher frequencies, which is tolerable as low frequency error rejection is mainly done by the VCM. The high frequency accuracy is also essential for effective inner loop compensation via AMD control to actively damp the high frequency PZT microactuator's torsion and sway modes to be discussed in future sections.
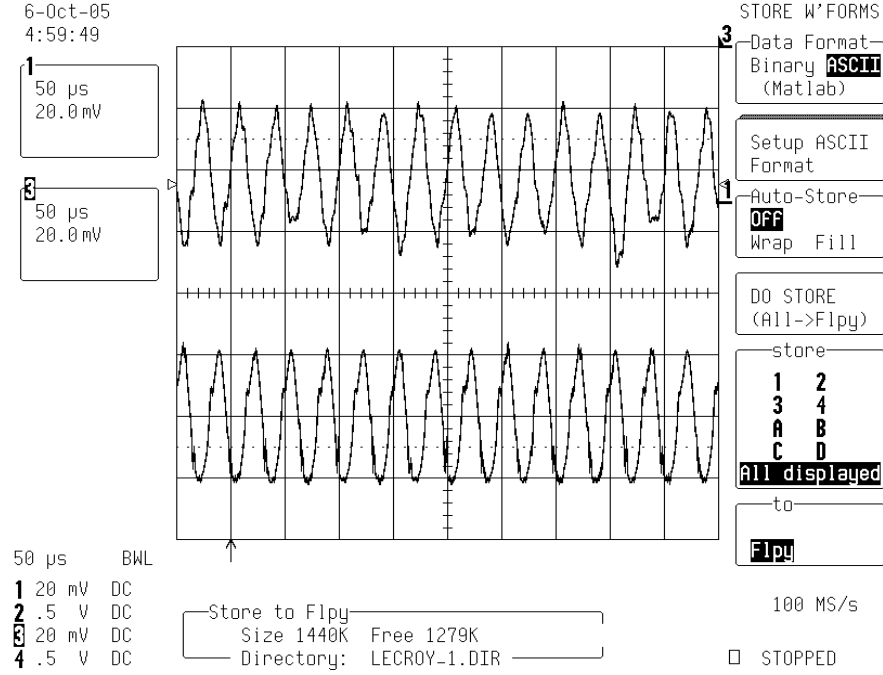
Figure 7.7: Time responses with $u_M = 2.5\sin(2\pi 30 \times 10^3 t)$ V. Top: PZT microactuator's displacement y_M measured from LDV with resolution of 0.5 μm/V. Bottom: Estimated PZT microactuator's displacement y_M^* from digital bridge circuit inverse $H_B^{-1}(z)$. The PZT microactuator is actuating at about ± 10 nm in radial directions.

7.4 SSA-DMS Dual-Stage Controller Design

With the measured PES and online estimated PZT microactuator's displacement y_M^*, we can proceed to design the SSA-DMS dual-stage track-following and AMD controllers in Figure 7.2. The designs of the VCM controller C_V and the PZT microactuator controller C_M are discussed in Sections 7.4.1 and 7.4.3, respectively. The AMD controller design using y_M^* is discussed in Section 7.4.2.
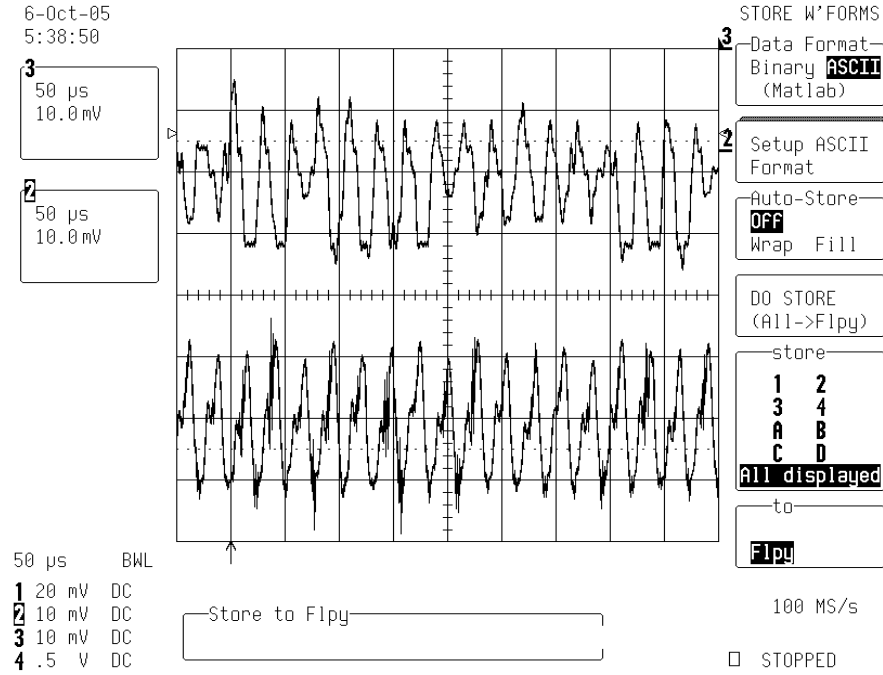
Figure 7.8: Time responses with $u_M = 1.2\sin(2\pi 30 \times 10^3 t)$ V. Top: PZT microactuator's displacement y_M measured from LDV with resolution of 0.5 μm/V. Bottom: Estimated PZT microactuator's displacement y_M^* from digital bridge circuit inverse $H_B^{-1}(z)$. The PZT microactuator is actuating at about ± 5 nm in radial directions.

7.4.1 VCM Controller

Suppose the dominant VCM resonant modes are compensated by notch filters and the compensated model can be approximated by a double integrator in the frequencies of interest. A lag-lead compensator recommended in [34] is used as the VCM controller. This design methodology uses the lag portion of the controller to increase the low frequency gain for low frequency disturbance rejection and tracking accuracy. The lead portion of the controller increases phase margin to ensure stability during crossover region. This design also requires the servo designer to tune only one parameter α for the desired gain crossover frequency f_V. A slight
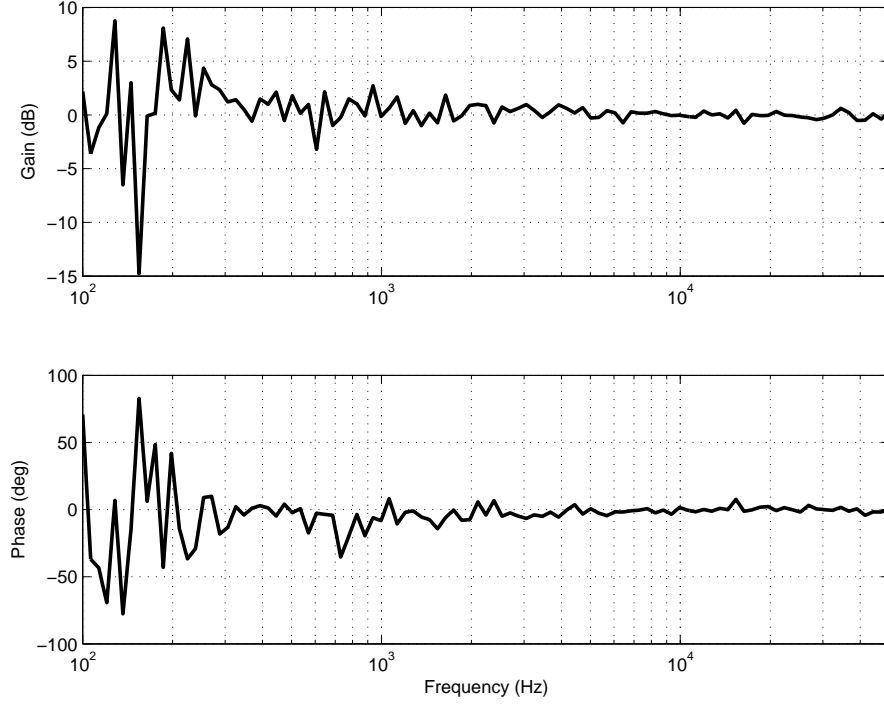
Figure 7.9: Frequency response of measured PZT microactuator's displacement from LDV y_M to estimated PZT microactuator's displacement y_M^*. The PZT microactuator is set to actuate at about ± 8 nm in radial directions.

modification is made and the controller takes the following form [95]

$$C_V(s) = K_V \frac{s + \frac{2\pi f_V}{2\alpha}}{s + 2\pi 10} \frac{s + \frac{2\pi f_V}{\alpha}}{s + 2\alpha 2\pi f_V} \tag{7.3}$$

with $5 < \alpha < 10$ used typically. K_V can be calculated by setting the VCM path gain crossover frequency at f_V with $|C_V(j2\pi f_V)G_V(j2\pi f_V)| = 1$.

7.4.2 Active Mode Damping (AMD) Controller

In conventional HDDs, non-collocation of actuators (VCM) and sensor (R/W head) exists. However with SSA, the collocation of PZT microactuator and PZT microactuator's displacement sensor issue is nearly achieved. The estimated PZT microactuator's displacement y_M^* can be used for many control methodologies, *e.g.* DISO

(Dual-Input Single-Output) robust control synthesis. In this section, we present a robust AMD controller design for damping the PZT microactuator suspension's torsion modes and sway modes.

The PZT microactuator behaves like a pure gain in low frequencies coupled with a number of resonant poles and anti-resonant zeros at high frequencies as can be seen below in Figure 7.10.
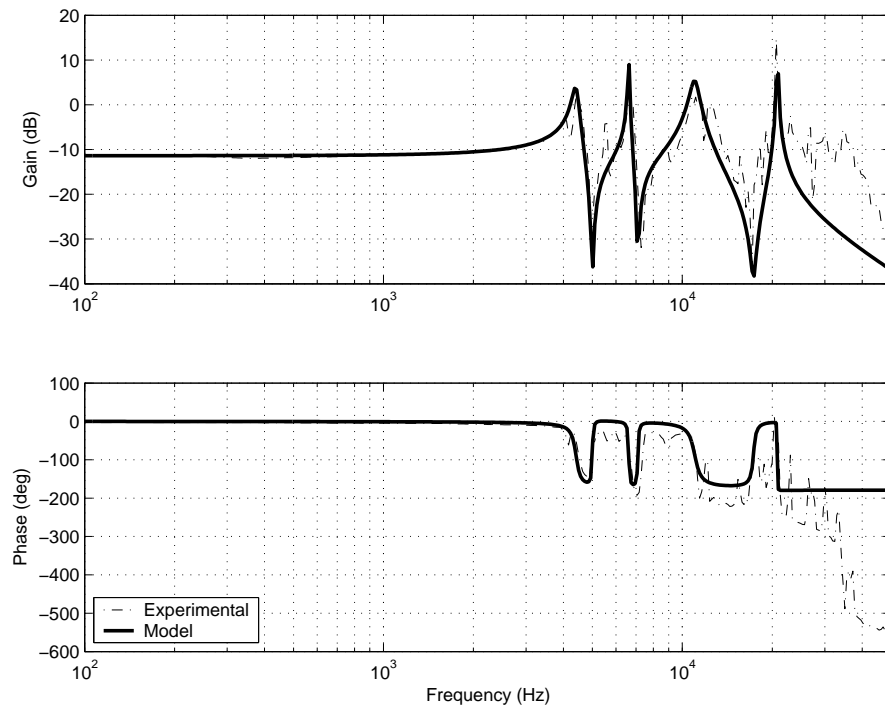
Figure 7.10: Frequency response of PZT microactuator.

The identified model $G_M(s)$ is

$$G_M(s) = 0.9875 \frac{s^2 + 2(0.01)(2\pi 5 \times 10^3)s + (2\pi 5 \times 10^3)^2}{s^2 + 2(0.05)(2\pi 4.41 \times 10^3)s + (2\pi 4.41 \times 10^3)^2} \cdots$$
$$\times \frac{s^2 + 2(0.01)(2\pi 7.1 \times 10^3)s + (2\pi 7.1 \times 10^3)^2}{s^2 + 2(0.01)(2\pi 6.62 \times 10^3)s + (2\pi 6.62 \times 10^3)^2} \cdots$$
$$\times \frac{s^2 + 2(0.03)(2\pi 17.3 \times 10^3)s + (2\pi 17.3 \times 10^3)^2}{s^2 + 2(0.07)(2\pi 11 \times 10^3)s + (2\pi 11 \times 10^3)^2} \cdots$$
$$\times \frac{(2\pi 20.8 \times 10^3)^2}{s^2 + 2(0.001)(2\pi 20.8 \times 10^3)s + (2\pi 20.8 \times 10^3)^2}$$

$$(7.4)$$

The PZT microactuator suspension has identified torsion modes at 4.31 kHz and 6.52 kHz and sway mode 21.08 kHz.

We propose an AMD controller $C_{D,i}(s)$ for each resonant mode i as

$$C_{D,i}(s) = K_{D,i} \frac{s + \frac{\omega_{n,i}}{\varepsilon_i}}{s + \frac{\kappa_i \omega_{n,i}}{\varepsilon_i}} \frac{s + \omega_{n,i}}{s + \frac{\varepsilon_i \omega_{n,i}}{\kappa_i}} \qquad (7.5)$$

to increase the damping ratios (hence smaller amplitudes) of the PZT microactuator suspension's torsion modes and sway mode. $K_{D,i}$ is set to ε_i in most cases. ε_i and κ_i are tuning parameters. $1 < \varepsilon_i \leq P$ is chosen usually for robustness against natural frequency variations P %, where $P < 3$ for most physical systems. $5 < \kappa_i < 15$ is then chosen to determine the amount of phase lift required to stabilize the resonance mode at the natural frequency $\omega_{n,i}$. The overall AMD controller C_D is given by

$$C_D(s) = \prod_{i=1}^{N} C_{D,i}(s) \qquad (7.6)$$

where $N = 3$ in this case.

Phase lead compensators are sometimes added to reduce the phase loss introduced by the AMD controllers and to increase the gain of the PZT microactuator's displacement for high frequency mode detection. C_D is general case of traditional PPF vibration controller [25] with additional minimum phase zeros. The zeros

prevent causality issues in PPF arrangements and improves the robust stability margin of the closed-loop system as will be illustrated later. The proposed AMD controller in essence increases the gain of each resonant mode but stabilizes the PZT microactuator loop using a phase lead from the zeros at $\frac{\omega_{n,i}}{\varepsilon_i}$, which is a common result when using optimal control methods such as $\mathcal{H}_\infty$ loop shaping techniques.

Assuming the PZT microactuator G_M has resonant modes at natural frequencies $\omega_{n,i}$, with the AMD controller C_D in the feedback path as shown in Figure 7.2. The following equation closed-loop equation holds

$$\frac{y_M(s)}{u_M(s)} = \frac{G_M(s)}{1 + C_D(s)G_M(s)} \tag{7.7}$$

if the closed-loop system is stable. The gains of the modes are suppressed by the AMD controller at the frequencies $\omega_{n,i}$ of the resonant modes effectively by a factor of $\frac{1}{|C_D(j\omega_{n,i})|}$

$$\begin{aligned}
\left|\frac{y_M(j\omega_{n,i})}{u_M(j\omega_{n,i})}\right| &= \left|\frac{G_M(j\omega_{n,i})}{1 + C_D(j\omega_{n,i})G_M(j\omega_{n,i})}\right| \\
&\approx \frac{|G_M(j\omega_{n,i})|}{|C_D(j\omega_{n,i})G_M(j\omega_{n,i})|} \\
&= \frac{1}{|C_D(j\omega_{n,i})|} \tag{7.8}
\end{aligned}$$

if $|C_D(j\omega_{n,i})G_M(j\omega_{n,i})| >> 1$.

The simulated frequency responses of AMD controller $C_D(s)$ and the open loop transfer function $C_D(s)G_M(s)$ is shown in Figure 7.11. With $C_D(s)$ in the feedback path as shown in Figure 7.2 and Equation (7.7), the loop is closed to damp the PZT microactuator suspension's torsion modes and sway mode. Figure 7.12 shows that the PZT microactuator suspension's torsion modes at 4.31 kHz and 6.52 kHz as well as sway mode at 21.08 kHz are all damped by the AMD controller C_D. The oscillations causing deviation of the R/W head from the track center during reading process are hence greatly reduced.
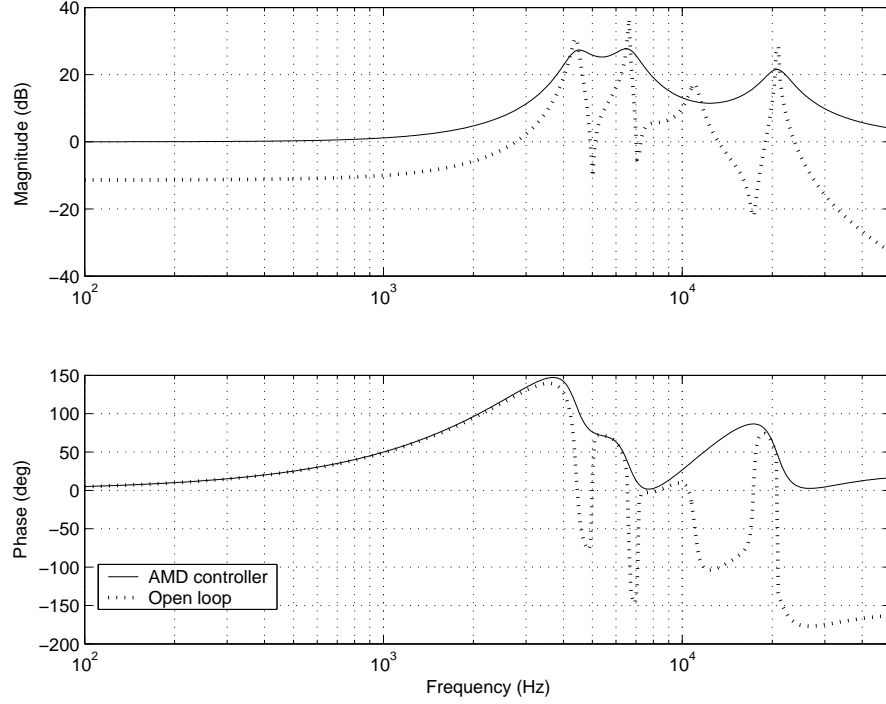
Figure 7.11: Simulated frequency responses of PZT microactuator with AMD.

However from Figure 7.12, it can also be seen that the proposed AMD controller $C_D(s)$ is more effective in suppressing the sway mode of the PZT microactuator at 21.08 kHz (> 30 dB) than the torsion modes at 4.31 kHz and 6.52 kHz (≈ 5 dB). This is apparent as the estimated PZT microactuator's displacement y_M^* from the displacement estimation circuit H_B is only effective in measuring in-plane components (making in-plane sway modes controllable) of the PZT microactuator and not the torsion modes (out-of plane weakly controllable modes). The PZT microactuator's displacement estimation circuit H_B is a scalar signal and hence the control effectiveness of the system is reduced due to more DOFs (Degrees-Of-Freedom) in the PZT microactuator's suspension than control inputs.

The simulated step responses of the PZT microactuator with and without the proposed AMD controller C_D are shown below in Figure 7.13. The transfer
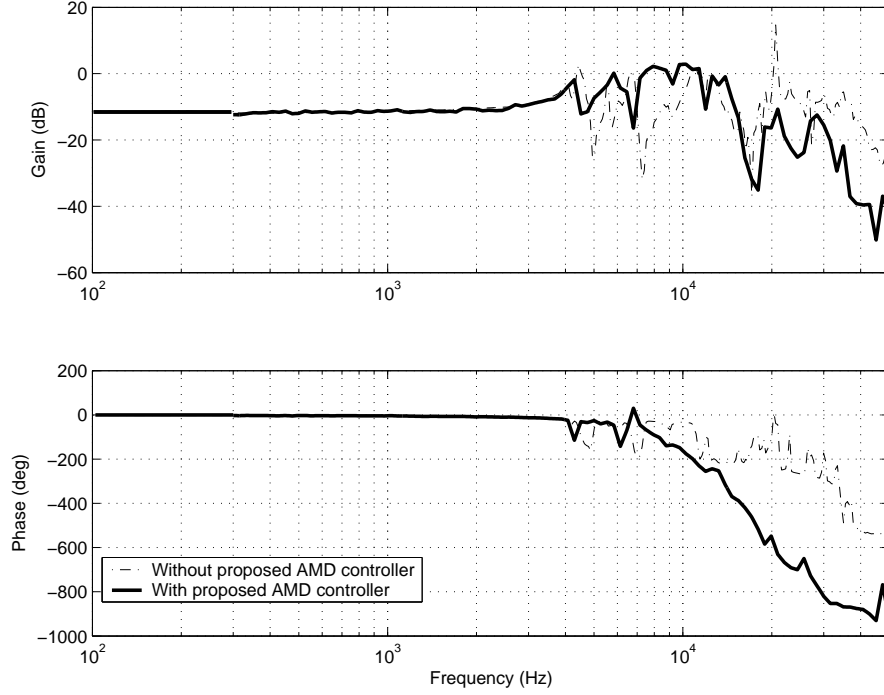
Figure 7.12: Experimental frequency responses of PZT microactuator.

function of the step response with AMD controller $y_{\text{AMD}}(s)$ is given by

$$
\begin{aligned}
y_{\text{AMD}}(s) \;=\; & \frac{1260897508.4794}{s(s^2 + 7380s + 3.808 \times 10^8)} \frac{(s + 3.142 \times 10^5)^2}{s^2 + 1148s + 9.809 \times 10^8} \cdots \\
& \times \frac{s^2 + 5542s + 7.678 \times 10^8)}{(s^2 + 2.51 \times 10^4 s + 1.468 \times 10^9)} \frac{s^2 + 314.2s + 9.87 \times 10^8}{s^2 + 539.3s + 1.958 \times 10^9} \cdots \\
& \times \frac{s^2 + 8319s + 1.73 \times 10^9}{s^2 + 4.074 \times 10^4 s + 6.199 \times 10^9} \cdots \\
& \times \frac{s^2 + 446.1s + 1.99 \times 10^9}{s^2 + 5.717 \times 10^5 s + 8.846 \times 10^{10}} \cdots \\
& \times \frac{s^2 + 3261s + 1.182 \times 10^{10}}{s^2 + 1.208 \times 10^4 s + 1.232 \times 10^{10}} \cdots \\
& \times \frac{s^2 + 2.614 \times 10^4 s + 1.708 \times 10^{10}}{s^2 + 1.644 \times 10^4 s + 4.248 \times 10^{10}}
\end{aligned}
\tag{7.9}
$$

7.4.3 PZT Micro-Actuator Controller

With the main resonant modes of the PZT microactuator dampened, we proceed to identify the mathematical model of the PZT microactuator with AMD control.
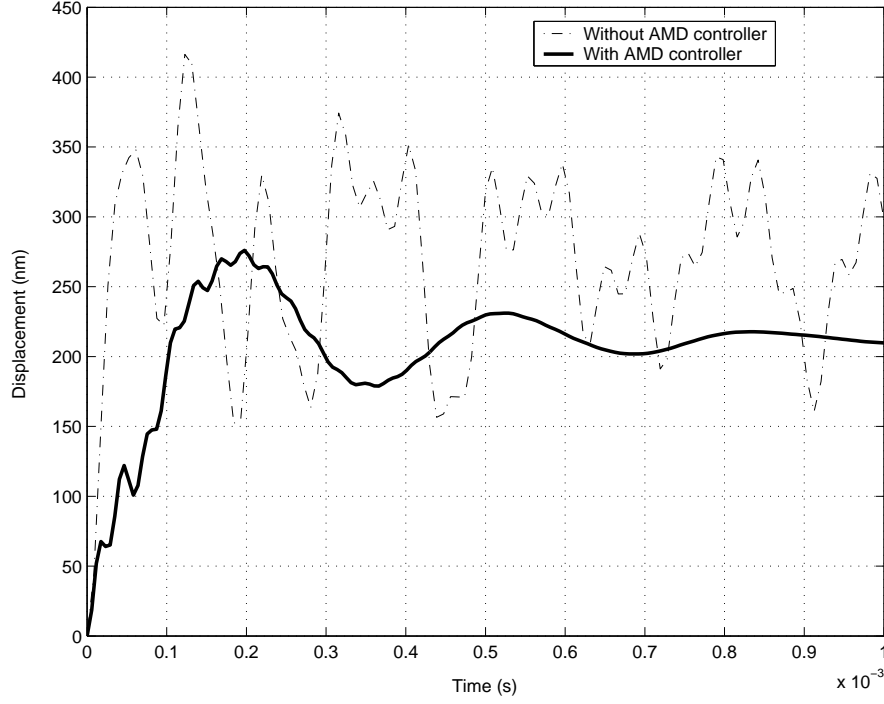
Figure 7.13: Simulated step responses of PZT microactuator with and without AMD.

In this section, a track-following controller $C_M(s)$ is designed for this identified model.

Let the transfer function of the PZT microactuator with AMD control from $u_M(s)$ to $y_M(s)$ be $G_M^C(s)$ where the superscript C indicates the presence of AMD controller. Using a second order model, we identify G_M^C as

$$G_M^C(s) = 0.25 \frac{(2\pi 9 \times 10^3)^2}{s^2 + 2(0.04)(2\pi 9 \times 10^3)s + (2\pi 9 \times 10^3)^2} \qquad (7.10)$$

The frequency responses from experiment and mathematical model are plotted in Figure 7.14. A low order model is used for identifying G_M^C, which suffices as the gain stabilization of the PZT microactuator loop is used and the amplitudes of the PZT microactuator's resonant modes with AMD control are all very small.
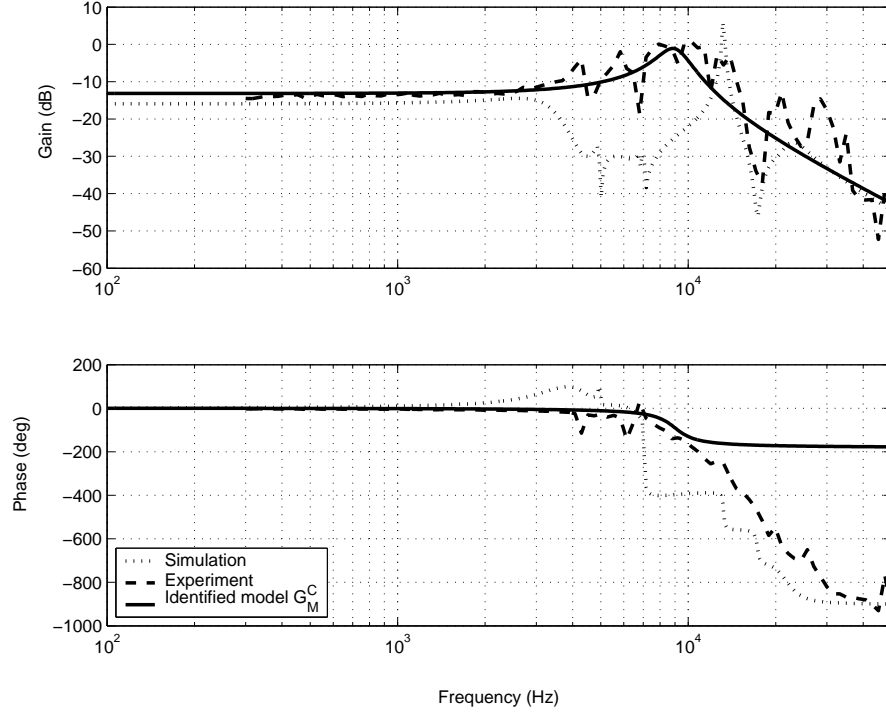
Figure 7.14: Identified model of PZT microactuator with AMD control.

Using the model of G_M^C, the PZT microactuator track-following controller of the form

$$C_M(s) = K_M \frac{1}{s^2} \frac{s + 2\pi \frac{f_M}{\beta}}{s + 2\pi \beta f_M} \tag{7.11}$$

is used to control G_M^C. f_M is the gain crossover frequency of the open loop PZT microactuator path and β is a tuning parameter for intended disturbance attenuation. $1 < \beta \leq 1.2$ is used typically, and K_M can be found with the relation $|C_M(j2\pi f_M)G_M(j2\pi f_M)| = 1$.

The PZT microactuator controller C_M is in essence a double integrator in series with a lead compensator. The lead compensator is added to improve phase margin at the gain crossover frequency and hence closed-loop stability in the PZT microactuator loop. Integrators are placed to ensure steady-state accuracy in the PZT microactuator loop required for fast tracking and error rejection. Also, the

integrators are essential to test the effectiveness of the bridge circuit in estimating the PZT microactuator's displacement, and at the same time filter the high frequency noise in the displacement estimation circuit H_B. β can be used to tune the damping ratio of the closed-loop system. For implementation purposes, a slight modification to the above proposed controller in Equation (7.11) becomes

$$C_M(s) = K_M \frac{\sigma^2}{(s+\sigma)^2} \frac{s + 2\pi \frac{f_M}{\beta}}{s + 2\pi\beta f_M} \tag{7.12}$$

where σ is chosen to be $\sigma < 100$. This practical modification prevents a large low frequency gain which saturates the PZT microactuator and causes integrator windup.

7.5   System Evaluation

In this section, we investigate the robustness of the proposed AMD controller $C_D(s)$. The performance of the proposed dual-stage control topology, sensitivity transfer functions of the VCM loop, PZT microactuator loop and dual-stage loop are presented. The 3σ PES of using the different control schemes are also be compared.

7.5.1   Robustness Analysis

To illustrate the robustness of the proposed AMD controller C_D, we carry out simulations with $\pm 10\%$ shift in natural frequencies of the modes in the PZT microactuator as shown in Figure 7.15.

The corresponding closed-loop transfer functions and step responses are shown in with the same designed AMD controller $C_D(s)$ are shown in Figure 7.16 and Figure 7.17 respectively. From these figures, it can be seen that the proposed AMD
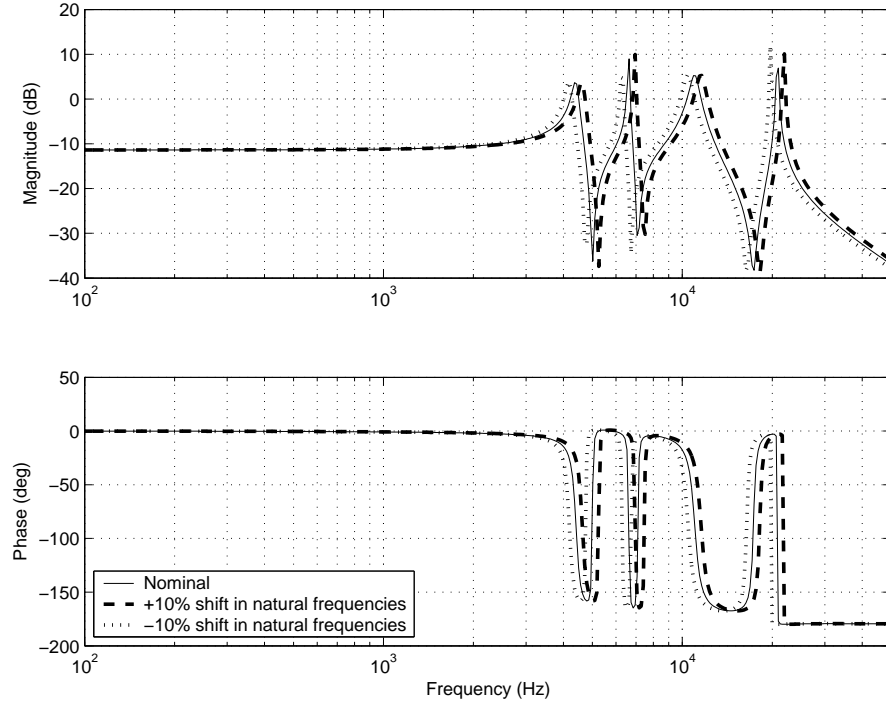
Figure 7.15: Frequency responses of PZT microactuator with $\pm 10\%$ shift in natural frequencies.

controller C_D is robust to resonant frequencies shifts up to $\pm 10\%$ using phase stabilization, hence avoiding the use of notch filters required for attenuating the gain of the modes. This method avoids the use of digital notch filters to attenuate the gain of the resonance modes as they are sensitive to transients of residual vibrations [112] and not robust to parametric variations. Shifts in natural frequencies often results in mode splitting and spill-over phenomena which compromises the closed-loop stability of the closed-loop system.
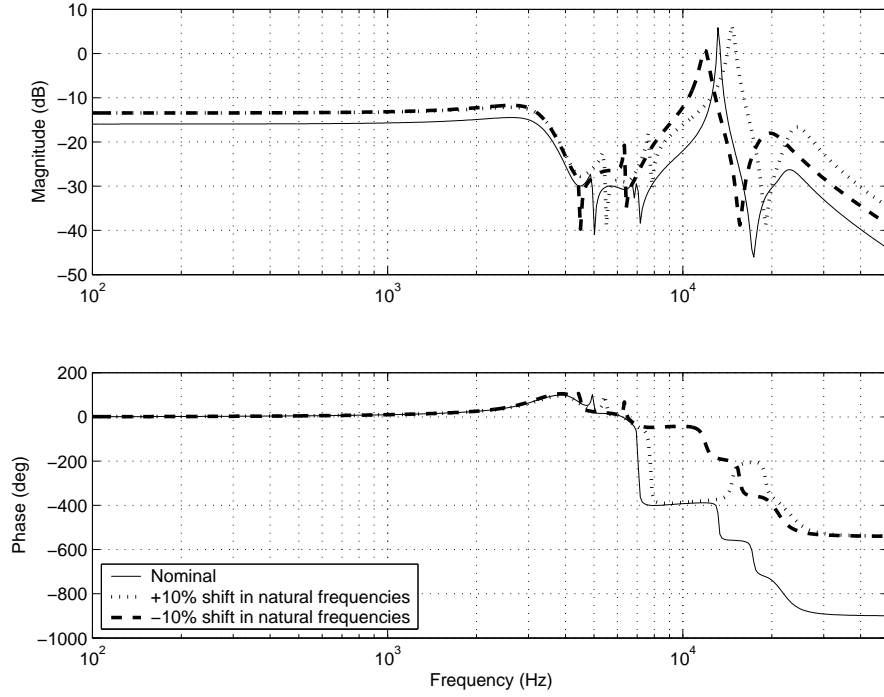
Figure 7.16: PZT microactuator's inner closed-loop transfer functions.

7.5.2 Decoupling Analysis

Referring to the SSA-DMS dual-stage control topology in Figure 7.2, the following equations hold:

$$L_D = (1 + C_M G_M) C_V G_V + C_M G_M \tag{7.13}$$

$$S_D = \frac{1}{(1 + C_M G_M)(1 + C_V G_V)}$$

$$= S_M S_V \tag{7.14}$$

$$T_D = \frac{(1 + C_M G_M) C_V G_V + C_M G_M}{(1 + C_M G_M)(1 + C_V G_V)} \tag{7.15}$$

where L_D, S_D and T_D are the dual-stage open loop, sensitivity, and complementary sensitivity transfer functions, respectively. S_V and S_M are the sensitivity transfer functions of the VCM path and PZT microactuator path, respectively.

The sensitivity transfer function of the dual-stage servo system S_D is the

172
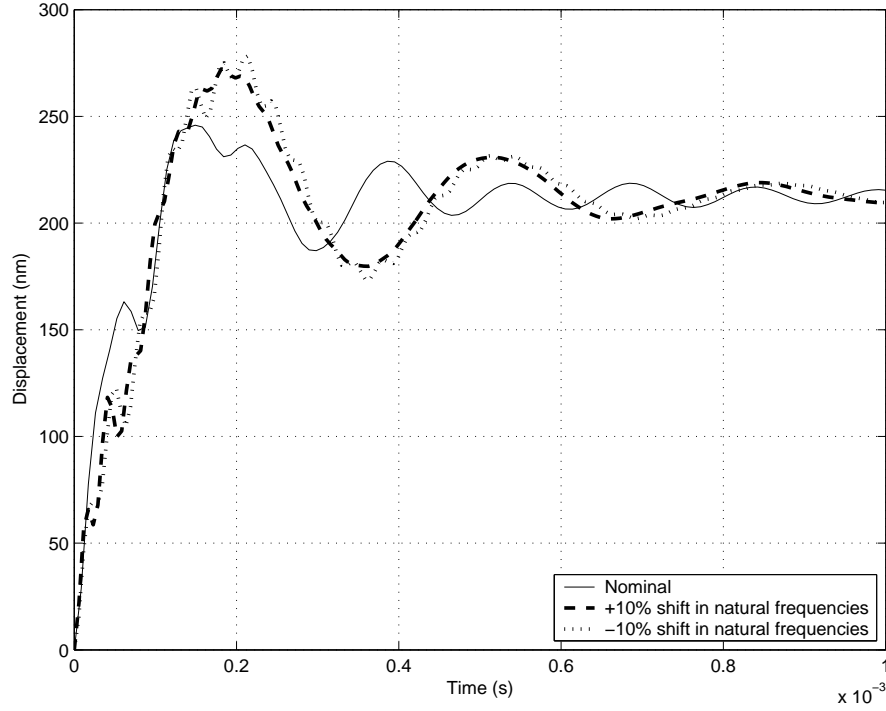
Figure 7.17: Simulated step responses of PZT microactuator with $\pm 10\%$ shift in natural frequencies.

product of the sensitivities of the VCM path and PZT microactuator path. As such, these sensitivity transfer functions are a measure of the extent of decoupling between the VCM path and PZT microactuator path.

For our design and experiment, we set f_M to be about 3 kHz. This high gain crossover frequency—translating directly into a high dual-stage open loop gain crossover frequency—is normally not achievable without AMD control, as the first dominant resonant mode of the PZT suspension-based microactuator is usually at 5–10 kHz. As no notch filters are used, two integrators are used for a high gain reduction rate of about -40 dB/dec after gain crossover frequency f_M for closed-loop stability by keeping loop gain less than unity. The integrators are also important in sensitivity optimization via loop shaping of the dual-stage open loop transfer function. The high roll-off rate after f_M causes the dual-stage open

loop in the Nyquist plot to avoid the unit circle centered at $-1 + j0$, a region where feedback increases the sensitivity rather than decreases it. The simulated sensitivity transfer functions of the VCM loop S_V, PZT loop S_M, dual-stage loop with and without AMD are shown in Figure 7.18.
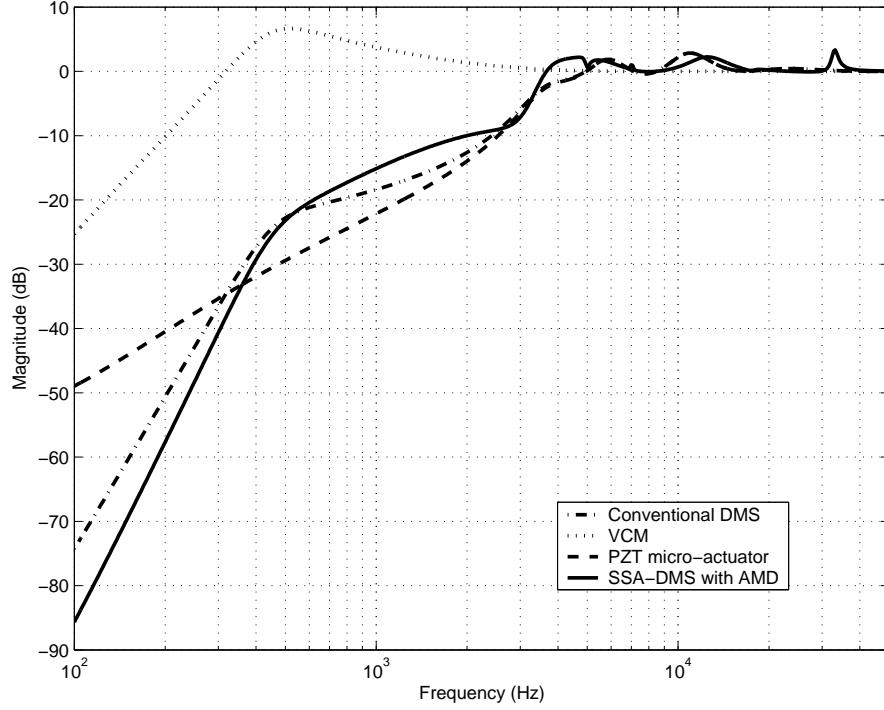
Figure 7.18: Simulated sensitivity transfer functions of different control schemes.

The experimental sensitivity transfer functions S_V, S_M and S_D are shown in Figure 7.19. It can be seen from the sensitivity transfer functions that indeed $S_D = S_V S_M$. However due to the high gain feedback from the SSA loop, the low frequency gain of the PZT microactuator in C_M is decreased to prevent saturation of the PZT microactuator. The estimated PZT microactuator's displacement y_M^* decouples the VCM path and PZT microactuator path into two distinct loops for individual path's sensitivity optimization. This method of using the real time PZT microactuator's displacement estimation y_M^* is far more accurate and robust to parameter as well as environmental variations. S_D is shaped
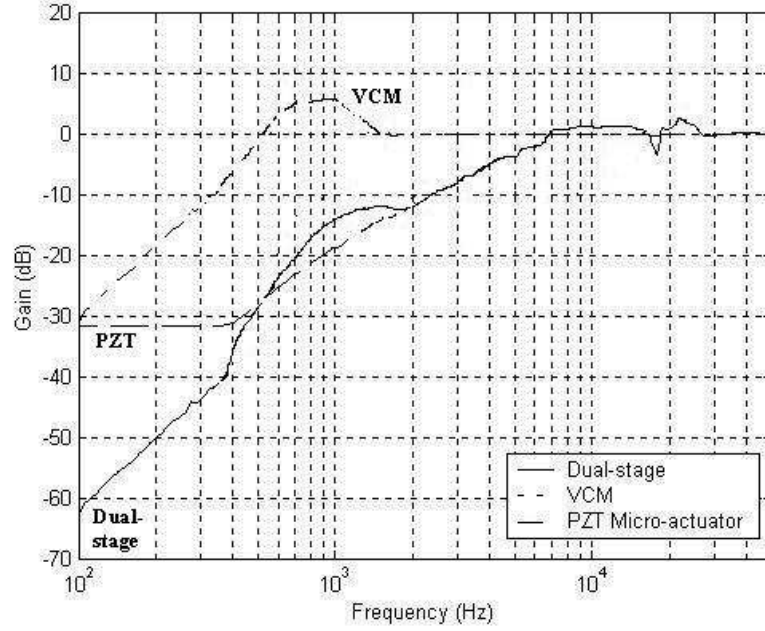
Figure 7.19: Experimental sensitivity transfer functions using proposed SSA-DMS dual-stage control topology.

independently such that the lag portion of the VCM controller C_V is used for low frequency disturbance rejection capabilities and tracking performance while the AMD controller C_D and integrators in the PZT microactuator controller C_M are used to ensure a low sensitivity in the high frequency sensitivity after crossover frequency. The low sensitivity hump retains good disturbance rejection capabilities and avoids amplification of output disturbances at higher frequencies [95].

7.5.3 PES Test

For simulation purposes, additive zero mean white noise with variance of 0.01 is added to the PZT microactuator's displacement to mimic sensing noise in the PZT elements. The 3σ PES of different control schemes used in the PZT microactuator loop for a dual-stage HDD is shown in Figure 7.20, using vibration and noise models

by Du *et al.* in [18].
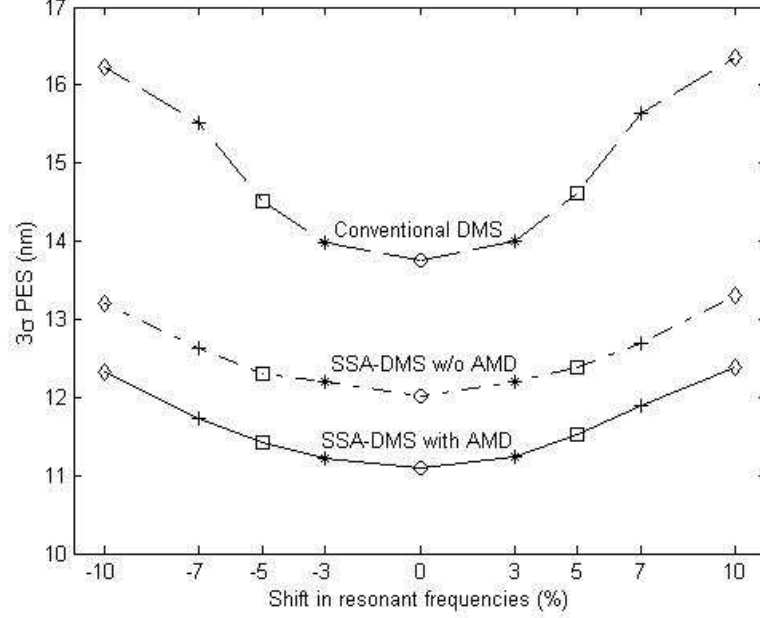
Figure 7.20: Comparison of 3σ PES with different control schemes.

The conventional DMS scheme uses digital notch filters to attenuate the gain of the resonant modes in the PZT microactuator as depicted in Figure 7.1. In the SSA-DMS scheme, digital notch filters together with $C_D = 0$ are used as shown in Figure 7.2. The main difference between conventional and SSA-DMS schemes is that it is SSA-DMS is able to pick up real time PZT microactuator's displacement while the conventional DMS scheme relies on an off-line estimator to estimate the displacement. The SSA-DMS with AMD control topology includes the proposed AMD controller C_D to damp the PZT microactuator's torsion modes and sway modes.

It can be seen that AMD control is robust for $\pm 10\%$ shifts in frequencies of the resonant modes ω_R. When SSA-DMS and AMD are employed simultaneously, better servo positioning and disturbance rejection capabilities are achieved with a

reduction of up to 20% in 3σ PES.

7.6 Summary

In this chapter, SSA (Self-Sensing Actuation) is used to construct a cheap and collocated PZT microactuator's displacement sensor with nanoposition resolution. The proposed displacement estimation circuit H_B estimates the PZT microactuator's displacement y_M with high correlation and high SNR without compromising the effective actuation of the PZT microactuator. y_M^* is used to design a robust AMD controller to actively damp the PZT microactuator suspension's torsion modes and sway mode, as well as decouple the dual-stage loop. Experimental results show attenuation of PZT microactuator's suspension modes by 5 dB and sway mode by 30 dB with low sensitivity. A reduction of up to 20% in 3σ PES is also observed. Also, the proposed dual-stage servo loop is effectively decoupled, and sensitivities in the VCM path and PZT microactuator path can be optimized individually to obtain a low sensitivity hump servo system. An improvement of 3σ PES by up to 20% is also observed when both SSA and AMD control is employed simultaneously.

With the successful implementation of SSA in piezoelectric actuators, a CSSA (Capacitive SSA) is proposed for a micro X-Y stage fabricated in DSI (Data Storage Institute) envisaged for usage in future probe-based storage systems in the following chapter. A robust decoupling control scheme based on open loop $\mathcal{H}_\infty$ loop shaping controller synthesis [28] is designed for the micro X-Y stage for high bandwidth and enhanced vibration rejection servo system.

Chapter 8

Capacitive Self-Sensing Actuation and Robust Decoupling Control of MEMS Micro X-Y Stage

To tackle the superparamagnetic effect in conventional magnetic data storage, MEMS-based scanning-probe based storage systems have been proposed [21]. In this chapter, a micro X-Y stage with 6 mm × 6 mm recording media platform actuated by capacitive comb drives is designed and fabricated in DSI. The prototype of the micro X-Y stage is fabricated by micromachining techniques with the integration of the 40 nm thickness PMMA (PolyMethyl-MethAcrylate) recording media and FEA (Finite Element Analysis) of the proposed platform shows that the first two modes of the micro X-Y stage are in plane modes at 440 Hz. The displacement of the media platform can achieve 20 μm with the driving voltage of 55 V. A CSSA (Capacitive Self-Sensing Actuation) circuit and robust decoupling control scheme is proposed and presented.

8.1 Background

Portable consumer electronics such as MP3 players, digital cameras, video recorders and cell phones *etc.* require high-density data storage devices with smaller sizes and form factors. As such, traditional data storage devices such as magnetic hard disk drives, semiconductor memories (*e.g.* compact-flash and smart-media) have limited volumetric densities and storage capacities. However with MEMS as an enabling technology, it is very promising to develop small micro-fabricated motors and actuators to replace spinning disks in a new type of low-cost high-capacity storage device such as MEMS-based probe storage devices [21][116][115][96]. Conventionally, thermal sensors are embedded to detect the tip position for PID and LQG servo control.

Several studies have been reported on probe storage devices using a combination of a micro X-Y stage and a micro-probe array. Choi *et al.* in [14] fabricated an electromagnetic micro X-Y stage to drive recording media. Bonding and assembling processes are required since the permanent magnets must be fitted into the proper position to align with the micro-coils. Kim *et al.* in [51] described the process of integrating a micro X-Y stage using silicon on glass substrate. Although the scanning range is as large as 50 mm, the center moving platform for the recording media is only less than 20% of the total stage area. Alfaro *et al.* presented a micro media actuator for position the recording media in X-Y directions in [3]. Silicon wafer double-side etching and wafer-to-wafer bonding processes are proposed for device fabrication.

In this chapter, a novel design of the micro X-Y stage with large movable media coated platform of dimensions 6 mm × 6 mm is presented for nanopositioning. The recording media area is 36% of the total stage area. The fabrication

process, including the integration of PMMA (PolyMethyl-MethAcrylate) recording media, is detailed and the prototype of the device is fabricated by micromachining techniques. The proposed CSSA circuit shown in the previous chapter is verified with experimental results and a robust decoupling control scheme based on open loop H_∞ shaping [28] is designed.

8.2   MEMS Micro X-Y Stage

The layout design of the micro X-Y stage is shown in Figure 8.1. It consists of
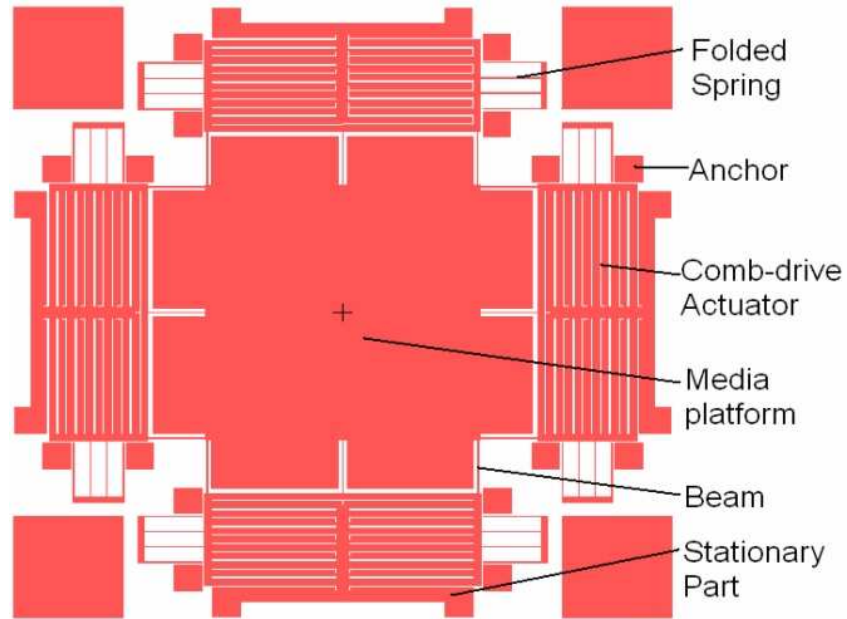
Figure 8.1: Simplified layout of a micro X-Y stage with 6×6 mm^2 recording media.

a movable media platform, comb-drive actuators, X and Y suspensions, springs and stationary parts. The media platform is connected to the suspensions via supporting beams, and the suspensions are connected to the anchors through the folded springs. All anchors are fixed on the SOI (Silicon-On-Insulator) substrate

with which the suspensions are electrically isolated from the stationary parts. Such kind of suspension design provides not only larger media area but also small mechanical cross-talk coupling issues [60], which are critical concerns for nano-scale bit size and spacing, for high storage capacity in smaller-form-factor probe storage device. Four sets of comb-drive actuators are used to drive the media platform moving in X and Y directions. In each actuator, comb-drive interdigital capacitance electrodes, attached to the arms of the suspensions and stationary parts, are used to generate electrostatic actuation.

The electrostatic driving force F is expressed by

$$F = \frac{\varepsilon h n V^2}{g} \tag{8.1}$$

where ε is the permittivity of air, h is the height of the structure, n is the number of the electrode pairs, V is the driving voltage, and g is the gap width of the comb-drive fingers. The detail parameters of the micro X-Y stage is shown below in Table 8.1.

Table 8.1: Design parameters of micro X-Y stage

Over size	1 cm $\times$ 1 cm
Finger width	4 μm
Finger gap	3 μm
Comb-finger pairs	1920
Spring width	8 μm
Height of spring/finger	60 μm
Spring length	1 mm
Media platform	6 mm $\times$ 6 mm

When a 55 V voltage is applied to one set of comb-drive actuators, the overall

electrostatic forces are calculated as 1 mN. Applying the electrostatic forces to the comb fingers for the X-axis actuation and running the static analysis in ANSYS, the displacement of the micro X-Y stage is determined, which is shown below in Figure 8.2. The displacement of the media platform in X-axis is achieved 20 μm. At
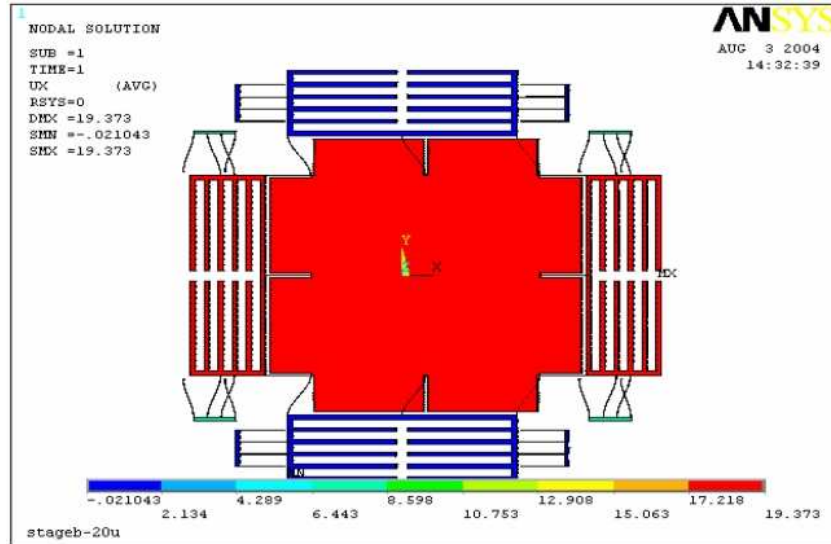
Figure 8.2: Displacement 20 μm of the recording media in X-axis under the driving voltage 55 V.

the same time, the displacement in Y-axis is 0.13 μm which is very small comparing to the comb-drive gap 3 μm. As such, the displacement decouple ratio $\frac{y}{x}$ is 0.6% at the driving voltage of 55 V.

8.2.1 Design and Simulation of Micro X-Y Stage

To investigate the dynamic performance of the micro X-Y stage, modal analysis and harmonic analysis are carried out using ANSYS. Figure 8.3 shows the in plane mode of the micro X-Y stage at the first and second resonant frequency of 440 Hz. The frequency response of the media platform to an exciting force 1 mN in X-axis
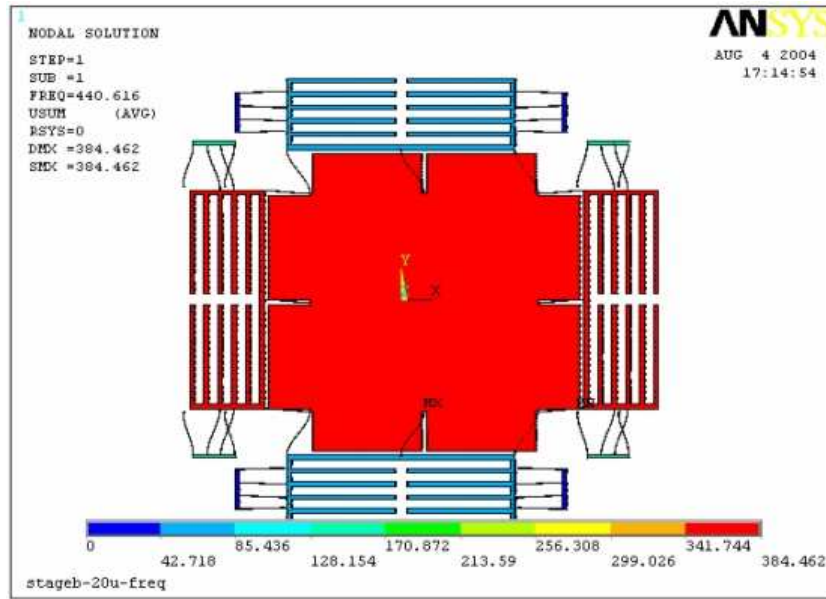
Figure 8.3: The first two resonant frequencies are at 440 Hz. The mode is an in-plane sway mode.

is shown in Figure 8.4.

8.2.2 Prototype of the MEMS Micro X-Y Stage

An integrated fabrication procedure for micro X-Y stage and ultra-thin recoding media layer is shown in Figure 8.5. The fabrication process starts from a SOI wafer. Openings for releasing the large area media platform are etched until the buried oxide layer from the SOI backside. An ultra-thin layer (PMMA), which is used as recoding media in probe storage systems, is formed on the topside by the spin-coat technique. The thickness of the PMMA film deposited is about 40 nm. A silicon dioxide layer is then deposited by PECVD (Plasma Enhanced Chemical-Vapour-Deposited) technique. The silicon dioxide layer is patterned as both protective layer and PMMA patterning mask. After PMMA patterned by oxygen plasma, thick photoresist AZ4620 is spin-coated to cover the oxide protective layer and
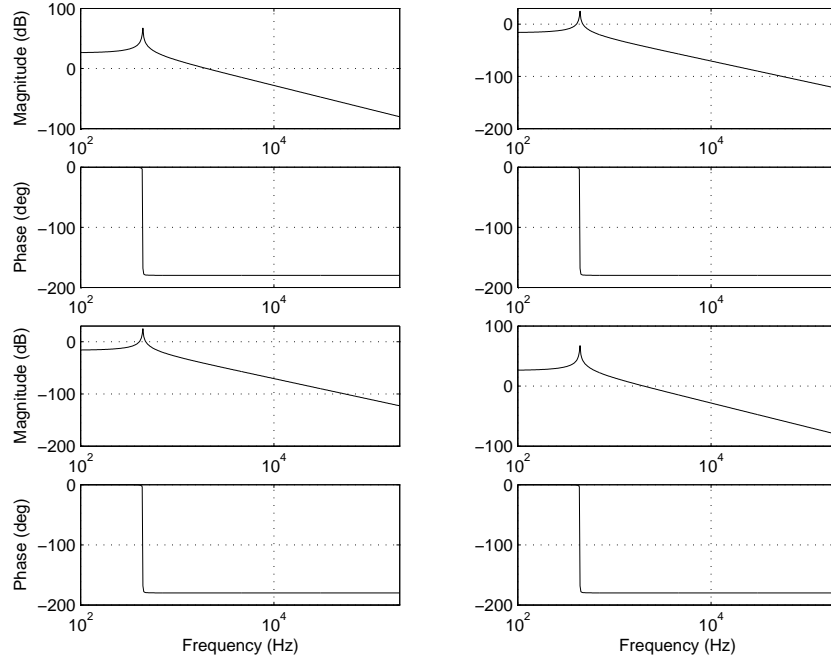
Figure 8.4: Frequency response of the media platform to an exciting force 1 mN in X-axis.

the patterned PMMA. After resist processing, the patterned photoresist AZ4620 is used as a mask for X-Y stage etching process. Next, the X-Y stage structures, including comb-drives, springs, beams and suspensions are patterned by DRIE (Deep Reactive Ion Etching). The photoresist is removed by oxygen plasma. Finally, the X-Y stage with the moveable exposed PMMA layer platform is fully released after the silicon dioxide protective layer and SOI buried dioxide layer are removed by BOE (Buffered Oxide Etching).

Figure 8.6 shows the partial view of the X-Y stage under SEM (Scanning Electron Microscopy). The large area recoding media platform is released from the SOI wafer substrate and suspended by 12 supporting beams. All the movable parts are suspended by 8 pairs of folded springs. Details of the comb-drives and the suspensions are shown in Figure 8.7. The finger width is 4 μm and the gap is 3 μm. The length of the finger is 75 μm. The overlap of each pair of fingers
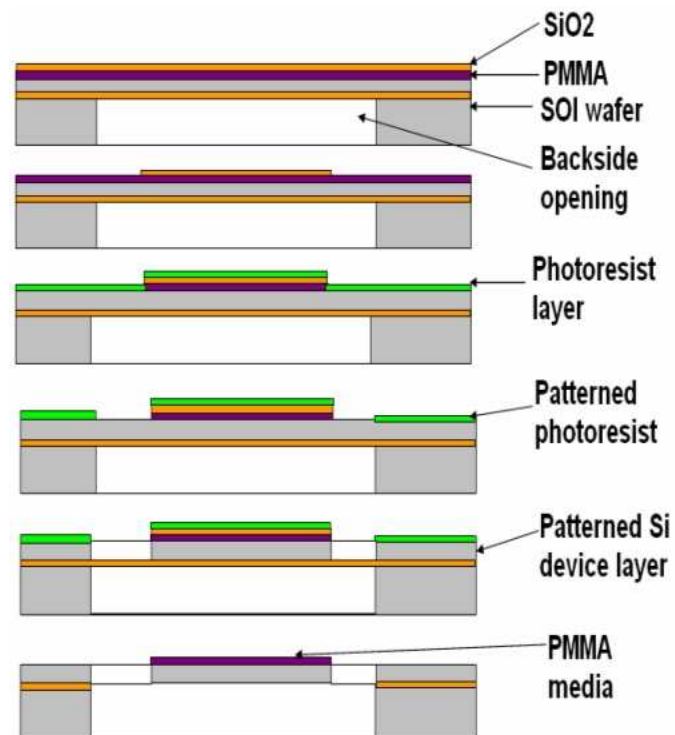
Figure 8.5: Fabrication process flow.
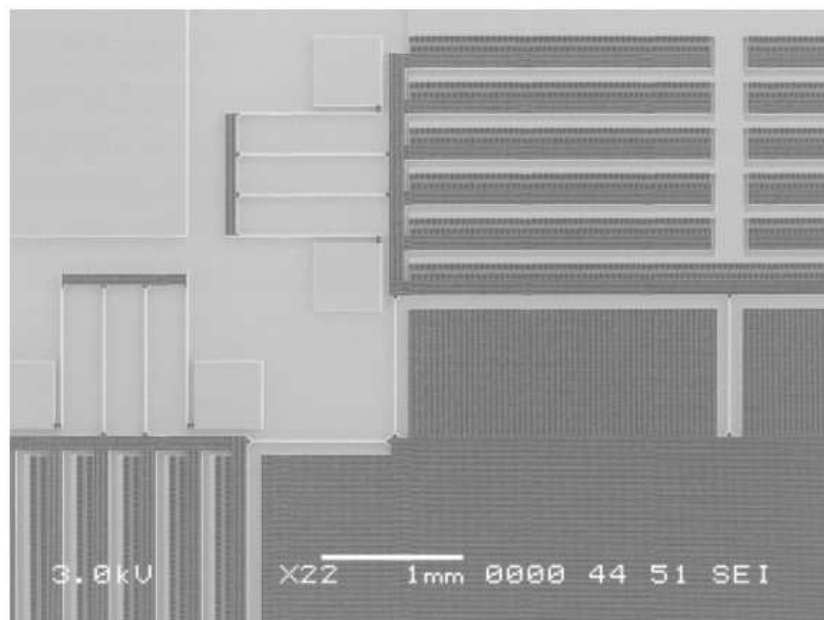
Figure 8.6: Partial view of the X-Y stage under SEM.

185
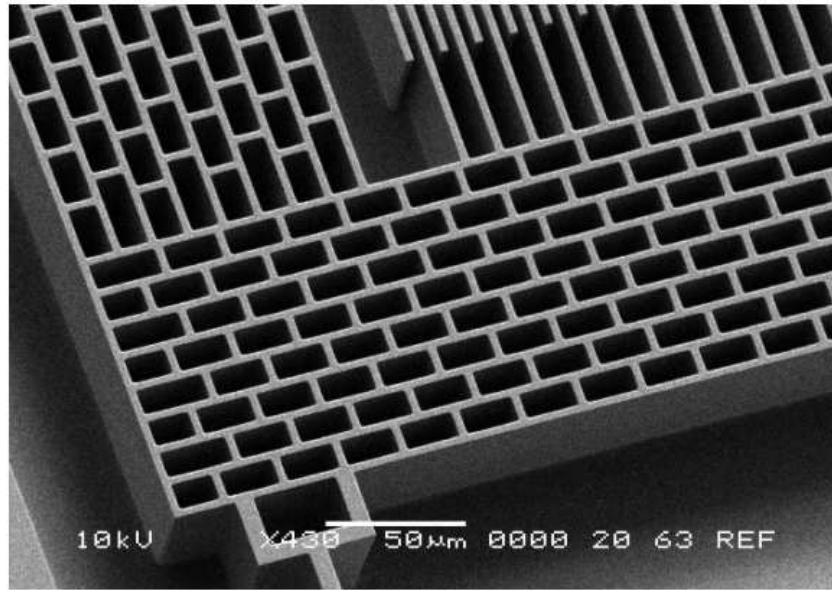
Figure 8.7: Details of comb-drives under SEM. Plan view of the fingers (top right).

is 30 μm.
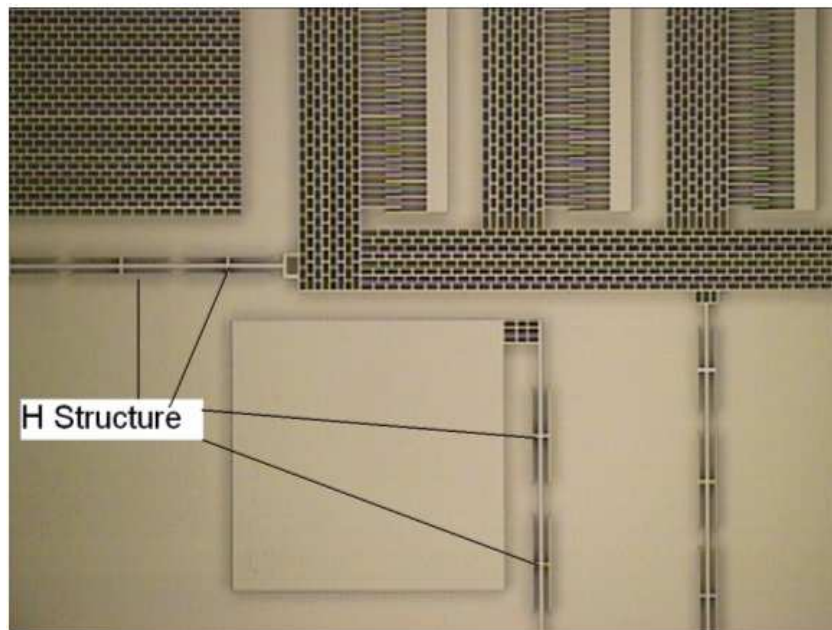
H Structure

Figure 8.8: "H" structures for protecting side wall of springs during DRIE etching process.

As shown in Figure 8.8, the "H" structures are fabricated to protect the sidewall of the folded springs and supporting beams during DRIE etching since the structure-area-density of the springs and beams is lower than other areas such as suspensions or comb-drives. The undercut of the spring width and the beam width is reduced and the designed width 8 μm is kept properly.

8.3   Capacitive Self-Sensing Actuation (CSSA)

Since the actuation of the MEMS micro X-Y stage is in the in-plane direction, non-intrusive online measurements of axial displacements and velocities are not possible even upon release of the MEMS micro X-Y stage from the wafer. As such, offline measurements from high speed cameras coupled with image processing techniques are commonly used for frequency response measurements. Dissimilar to the "Millipede" project where probe tips are integrated and thermal sensors are used to detect the absolute position of the heated tips, a CSSA (Capacitive Self-Sensing Actuation) scheme proposed earlier in Figure ?? is used here.

The main motivation of using the CSSA is to achieve actuation and sensor capabilities simultaneously, similar to SSA in piezoelectric actuators. However as mentioned earlier in Chapter 2, an external sinusoidal modulator signal is essential to achieve high SNR capacitive sensing and to actuate the MEMS micro X-Y stage for obtaining readback signal needed in PES demodulation.

For our experiments, capacitors in the pico Farad range and a sinusoidal modulator signal of 5 kHz are used. The demodulator, low pass filter of corner frequency at 10 kHz, and intrapolator in Equation (6.42) are implemented in a dSPACE system at a sampling frequency of 400 kHz. The experimental results of proposed

CSSA showing linearity of output DC voltage v_{DC} and change in capacitance ΔC with an identified relationship of

$$v_{DC} = -0.07\Delta C - 0.11 \tag{8.2}$$

and is shown in Figure 8.9 [63].
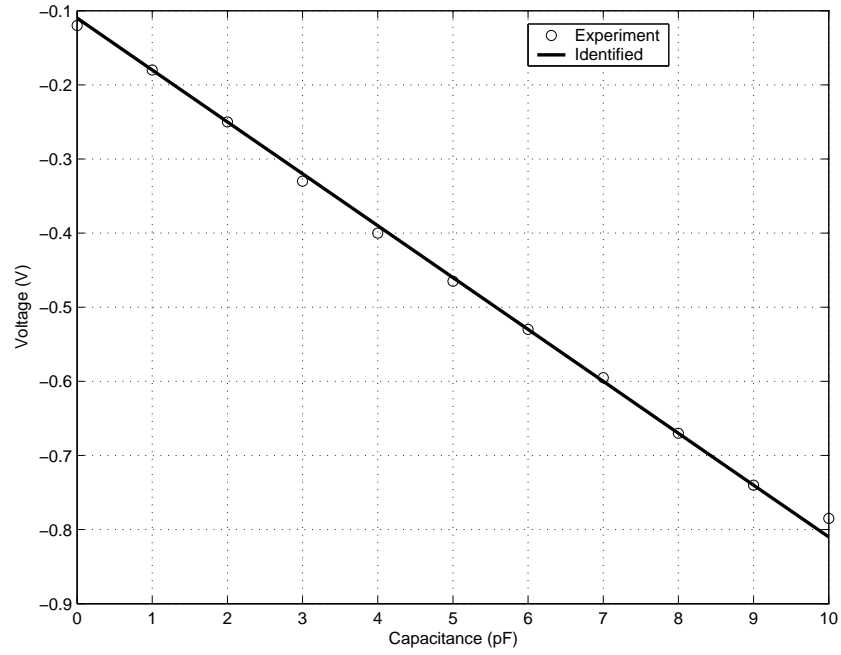
Figure 8.9: Experimental results of proposed CSSA [63].

It can be seen from Figure 8.9 that the output DC voltage is linear with change in capacitance which is in turn, is proportional to displacement of the MEMS micro X-Y stage. The proposed CSSA scheme calibrated with the measurements from the high speed cameras upon structural release can be used for absolute displacement sensing in both axial X and Y directions. Together with written in PES, both information will be used to track-seeking and track-following control.

8.4 Robust Decoupling Controller Design

To ensure robustness against parametric uncertainties in the actual micro X-Y stage during fabrication process and release, we exploit the "clean" high frequency double integrator properties of MEMS actuators. The $\mathcal{H}_\infty$ loop shaping method for MIMO controller design detailed in [28] will be modified and explored here. This one step approach is used as the open loop bandwidth (gain crossover frequency) is commonly used as a measurement of error rejection capabilities in data storage systems. Also, the loop shape at gain crossover frequency f_c of 4.5 kHz (about 10 times above the first in-plane sway mode of the micro X-Y stage at 440 Hz) can be improved for better gain and phase margins.

Before we carry out robust stabilization of the micro X-Y stage with normalized left coprime factorization, we shall cascade shaping filters W_1 and W_2 to shape the largest singular values into the shaped plant G_s as

$$G_s = W_2 G W_1 \tag{8.3}$$

For our application, W_1 is chosen as an identity matrix to ease controller synthesis and implementation. W_2 is chosen as a notch filter to compensate for the small damping and large gain at the resonant frequency at 440 Hz and a lead compensator at f_c for stability. A decoupler is also included to further reduce the axial coupling for independent axial control. This shaping filter also prevents any numerical stability while synthesizing the robust controller. As such, we obtain W_2 as

$$
\begin{aligned}
W_2 &= \frac{s^2 + 2(0.0009)2\pi 440 s + (2\pi 440)^2}{s^2 + 2(1)2\pi 440 s + (2\pi 440)^2} \cdots \\
&\times K_c \frac{s + \frac{2\pi f_c}{2\alpha}}{s + 2\pi} \frac{s + \frac{2\pi f_c}{\alpha}}{s + 2\alpha 2\pi f_c}
\begin{bmatrix}
1 & -0.006 \\
-0.006 & 1
\end{bmatrix}
\end{aligned}
\tag{8.4}
$$

where $5 < \alpha < 10$ used typically [87]. By setting $|W_2(j2\pi f_c)G_{xx}(j2\pi f_c)| = 1$, K_c is tuned to ensure maximum phase lead at desired f_c. The frequency response of the shaping filter W_2 is shown in Figure 8.10.
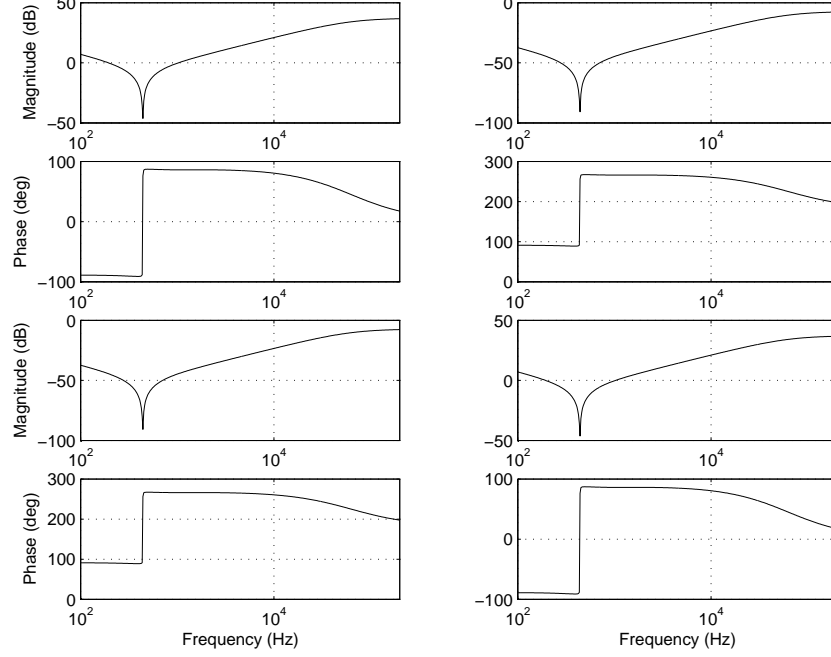
Figure 8.10: Frequency response of $W_2(s)$.

Without CSSA, written in PES on the PMMA remains as the only position information available for feedback control. Using the shaping filters designed, the robust stabilization controller K is synthesized by solving the robust stabilization problem, assuming that the shaped plant G_s has a normalized coprime factorization of $G_s = M_s^{-1}N_s$.

Assume that the micro X-Y stage is perfectly decoupled by the decoupler in $W_2(s)$. The controller design can now be carried out independently for each axis with the diagonal and symmetrically shaped plant $G_s(s)$. With A, B, C and D as the system's dynamics state-space matrix quadruple of the micro X-Y stage's identified mathematical model shown previously in Equation (2.5), the

micro X-Y stage can be represented by a strictly proper system with no feedthrough (*i.e.* $D = 0$). As such, the controller which ensures that

$$\left\| \begin{bmatrix} K_x \\ I \end{bmatrix} (I - G_{xs}K)^{-1} M_{xs}^{-1} \right\|_\infty \leq \gamma \tag{8.5}$$

for a specified $\gamma > \gamma^*$ where γ^* is the $\mathcal{H}_\infty$-norm of Equation (8.5), is given by [28][132]

$$K_x = \begin{bmatrix} A + BF + \gamma^2 (L^T)^{-1} Z C^T C & \gamma^2 (L^T)^{-1} Z C^T \\ B^T X & 0 \end{bmatrix} \tag{8.6}$$

where G_{xs} is the shaped micro X-Y stage in the X-axis and M_{xs} is the left coprime factorization of G_{xs}. F and L are then given by

$$F = -B^T X \tag{8.7}$$

$$L = (1 - \gamma^2)I + XZ \tag{8.8}$$

with Z and X being the unique positive definite solution to the following AREs respectively

$$AZ + ZA^T - ZC^T CZ + BB^T = 0 \tag{8.9}$$

$$A^T X + XA - XBB^T X + C^T C = 0 \tag{8.10}$$

Obviously, Z and X can be obtained by performing Schur's complements and solving using LMI (Linear Matrix Inequalities) techniques. In the next section, the controller is synthesized and simulation results are presented.

8.5   Simulation Results

1) Controller synthesis: On controller synthesis, a $\gamma^* = 1.4705$ is obtained. By choosing a $\gamma > \gamma^* = 2.0$ which results in suboptimal $\mathcal{H}_\infty$ controller, a 50% per-

turbation of magnitude of coprime uncertainty can be tolerated before instability. The frequency response of the synthesized K_x is shown below in Figure 8.11.
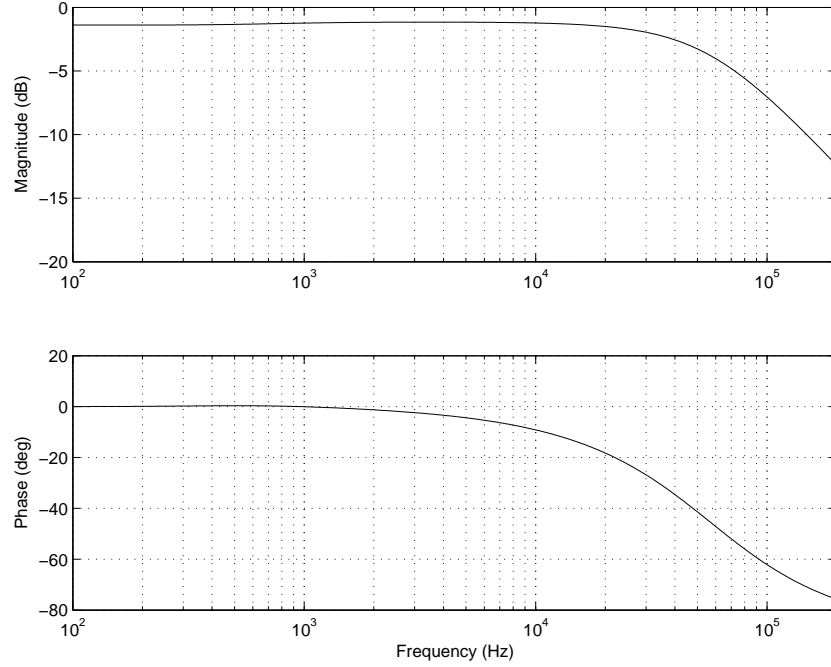
Figure 8.11: Frequency response of K_x.

The synthesized K_x effectively reduces the low frequency gain and the gain crossover frequency slightly, while increases roll off at high frequencies for robust stability. The final controller K for the micro X-Y stage will thus be

$$K = \begin{bmatrix} K_x & 0 \\ 0 & K_y \end{bmatrix} W_2 \tag{8.11}$$

and $K_y = K_x$ after decoupling control. The frequency response of K is shown in Figure 8.12 below.

2) Frequency responses: The frequency responses of largest singular values in shaped plant G_s and open loop transfer function KG_s are plotted in Figure 8.13. It can be seen that the overall loop shape is generally unaltered, but a gentler
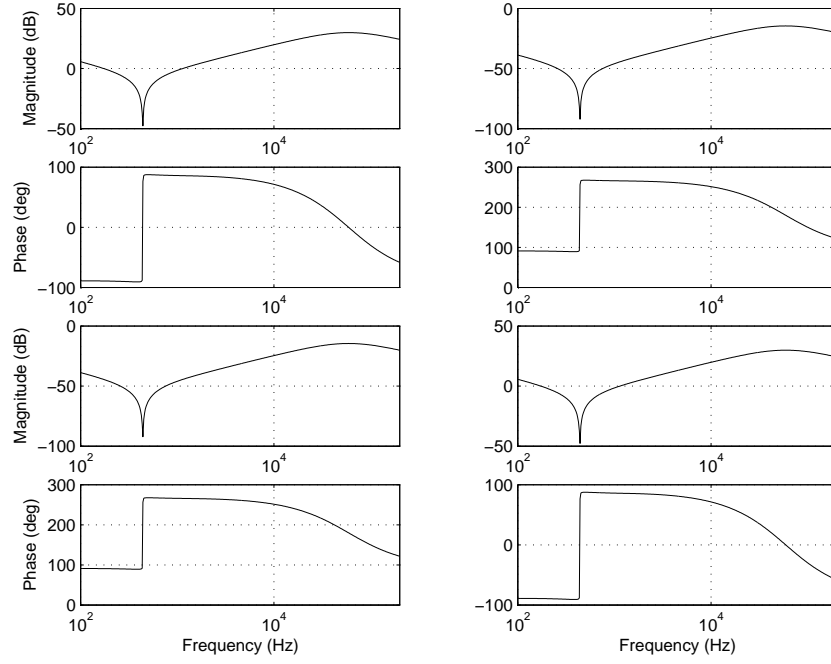
Figure 8.12: Frequency response of K.

slope is observed near the crossover frequency f_c translating into larger stability margins.

The block diagram for digital control of micro X-Y stage in both axes is shown in Figure 8.14. The two-input-two-output control $K(z)$ is obtained by discretizing the $K(s)$ at sampling frequency of 400 kHz with bilinear transformation.

3) Time responses: For fast user data access, the overshoot of the micro X-Y stage during seek operations should be kept to a minimum. As such, a nonlinear saturator is added to $K(z)$ to ensure that the control signal does not exceed the maximum allowable voltage of 55 V. $K(z)$ must also be able to decouple the micro X-Y stage such that the interaction in the main axes is kept to a minimum. The step response of the micro X-Y stage with 20 μm for 2 ms followed by 14 μm in the X-axis is shown below in Figure 8.15.
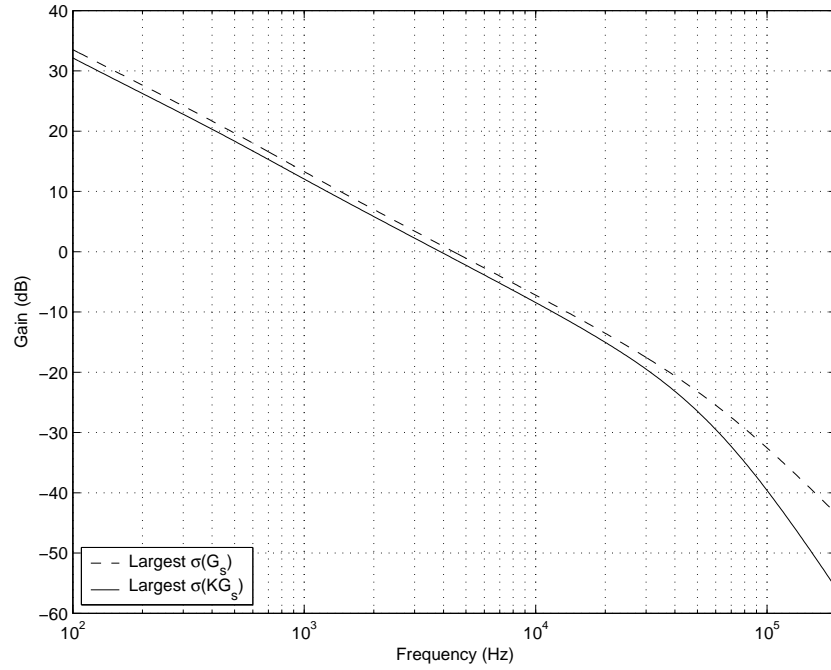
Figure 8.13: Plots of largest singular values.
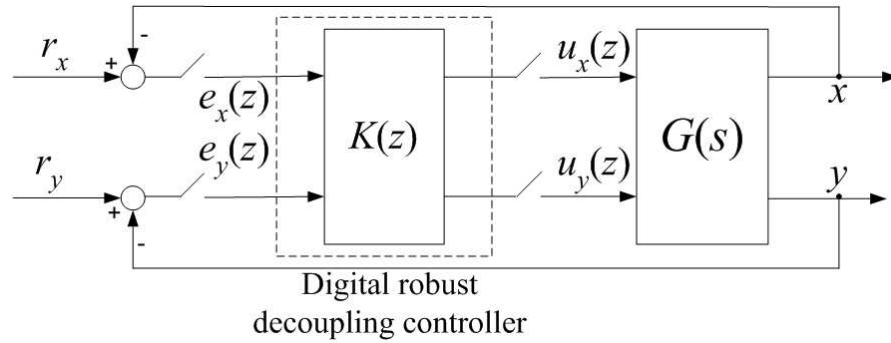
Figure 8.14: Block diagram for digital control of micro X-Y stage.

The step response of the micro X-Y stage with 14 μm at 1 ms for 2 ms followed by 6 μm in the Y-axis is on the same figure. It can be seen that the actuation in both axes is decoupled and the interactions in both axes are in orders magnitudes of 10^{-12} m.

The corresponding control signals are shown below in Figure 8.16. The large span seek operations with little overshoot are achieved within the control signal

194
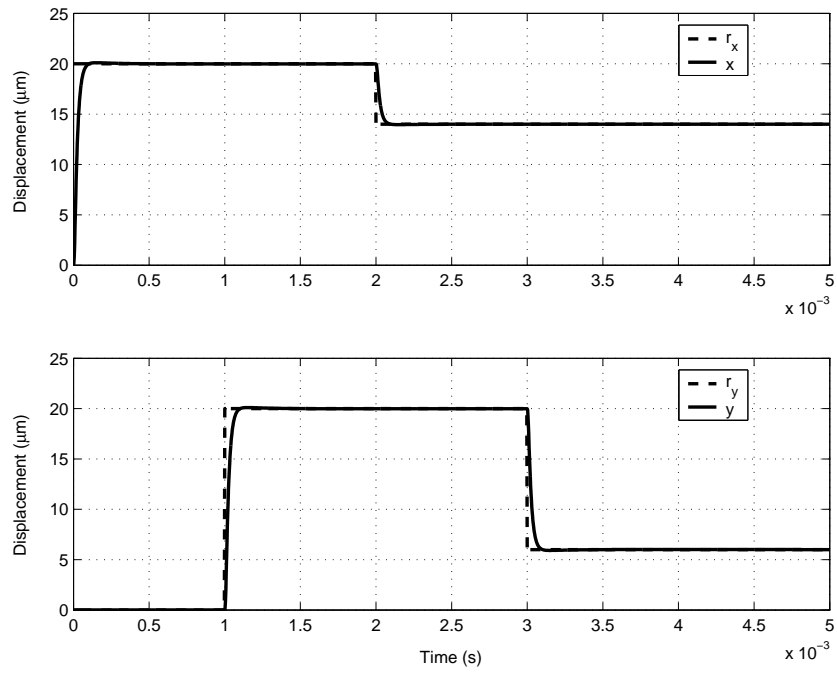
Figure 8.15: Step responses.

limitations.
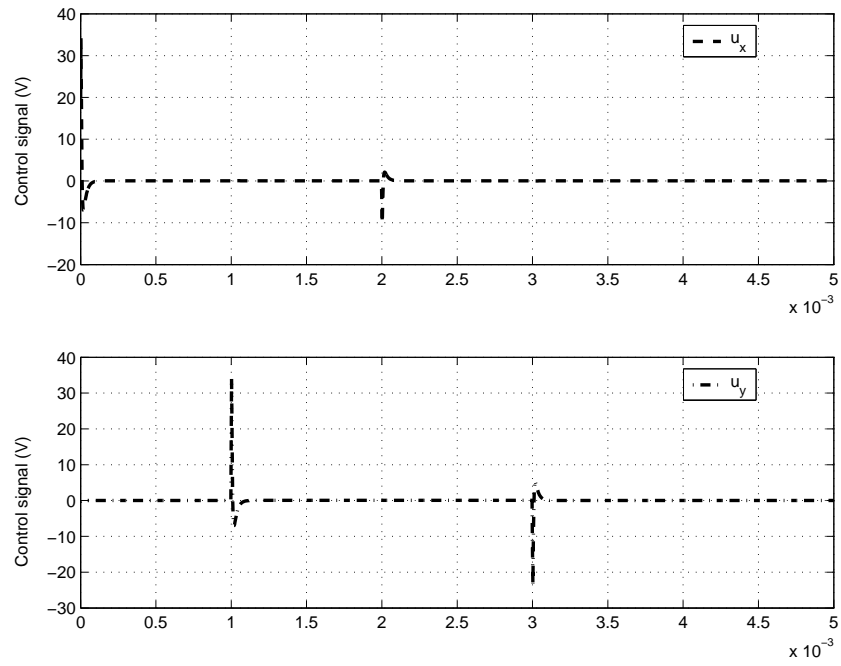
Figure 8.16: Control signals.

4) Robustness analysis: Most MEMS actuators demonstrate double integrator properties at high frequencies with little uncertainties. As such, only the largest singular value of G is perturbed with $\pm 50\%$ to demonstrate the robustness of the digital controller $K(z)$. The step responses are simulated with the reference sequences r_x and r_y again and are shown in Figure 8.17. The closed-loop digital
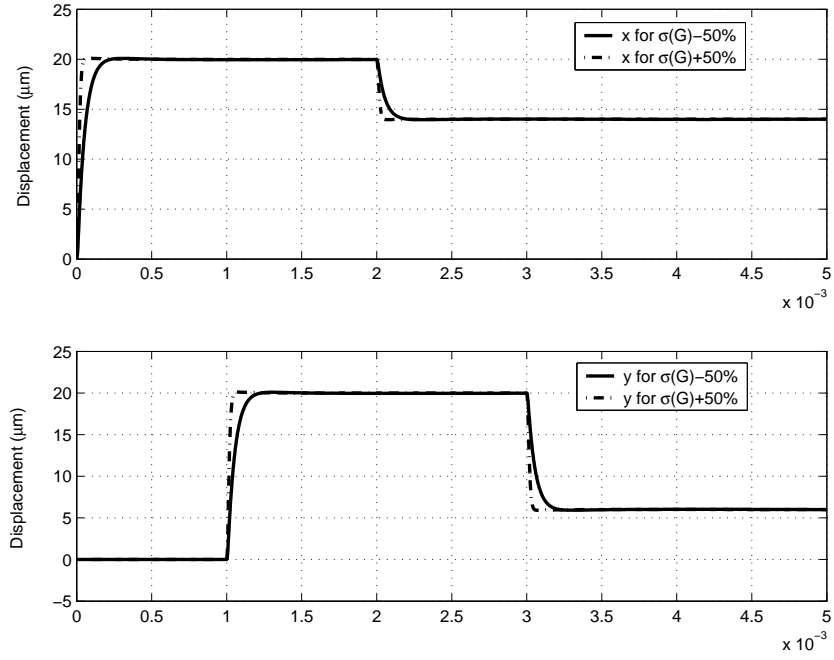
Figure 8.17: Step responses for perturbed system.

control system is robustly stable with the controller K. In future, the CSSA interface will be integrated to verify the proposed controller with the micro X-Y stage on the same wafer to eliminate the noises.

8.6   Summary

In this chapter, a novel design of the MEMS micro X-Y stage with 6 mm $\times$ 6 mm recording media platform is presented and proposed to integrate 40 nm PMMA

film (recording media). The displacement of the media platform is 20 μm with the driving voltage of 55 V and a CSSA (Capacitive Self-Sensing Actuation) scheme is detailed with experimental results. With the first two resonant in plane modes of the MEMS micro X-Y stage at 440 Hz, a robust decoupling controller scheme is proposed. Simulation results show that the digital servo MIMO system has strong error and vibration rejection capabilities.

Chapter 9

Conclusion and Future Work

The trend of increasing storage capacities for ultra-high data density mobile data storage devices demands strong disturbance rejection capabilities. This dissertation focuses on developing control technologies with extraneous sensors and multi- or self-sensing solutions in future storage servo systems for ultra-strong disturbance suppression in next generation of high performance data storage devices.

The main findings and results presented in this dissertation are :

1. Composing an OICA (Online Iterative Control Algorithm) with and without extraneous sensors to minimize the square of $\mathcal{H}_2$-norm from NRRO disturbances to true PES using experimental gradient estimates, without prior knowledge of the dominant input and output disturbances spectra. The TMR budget is optimized on a PZT-actuated spinstand servo system with baseline NRRO suppression and an reduction of 22% in 3σ NRRO without solving AREs and LMIs.

2. Designing a practical add-on DDO (Disturbance Decoupling Observer) and

DDOS (DDO with extraneous Sensor) parameterized by a single ε using SPT (Singular Perturbation Theory) to strengthen the disturbance rejection performances in sampled-data servo systems. The DDOs are capable of rejecting the dominant input and output disturbances simultaneously, with possible attenuation of noise using the DDOS. An experimental setup with a PZT-actuated suspension mimicking today high end drives shows an improvement in 3σ PES of up to 69.2%.

3. Advancing on the SPT to decompose a general LTI mechanical system with rigid and flexible body modes into slow and fast subsystems for active vibration control. Experimental results show effective suppression of the VCM's as well as PZT active suspension's flexible modes and an improvement of 39.9% of 3σ PES during track-following in a single stage HDD with PZT active suspension as sensor and fast observer is observed.

4. Constructing a PZT microactuator's displacement sensor with SSA to enable inner loop compensation and direct design as depicted in SPT. Experimental results show a high correlation, high SNR measurement up to nanometer resolution superior than that of the LDV. A robust AMD (Active Mode Damping) controller is then designed to actively damp the PZT micro-actuator's sway and torsion modes as well as decouple the dual-stage loop for individual loop control and sensitivity optimization. A low sensitivity servo system with improvement of up to 20% in 3σ PES is observed.

5. Proposing a CSSA (Capacitive SSA) and robust decoupling controller for the fabricated MEMS micro X-Y stage with integrated recording media used for probe-based storage servo system demonstration. The minimal uncertainty feature at high frequencies of MEMS devices is exploited to design a high bandwidth servo system with strong disturbance and vibration rejection

capabilities.

Future storage systems must be mobile, coupled with ultra high storage densities with ultra fast access times. As such, excellent disturbance rejection capabilities enabled with high SNR and resolution sensors for ultra precise servo positioning will be essential. In view of the results obtained, the following work should be emphasized in future research:

1. Sensor collocation on sensitivity limitations in dual-stage HDDs:

   For the PZT micro-actuator in dual-stage HDDs as shown below in Figure 9.1, a study of the non-collocation of the sensor, spillover phenomenon using active control and disturbance sources will be analyzed. Theoretical developments on relationships between sensor collocation, Discrete Bode's Integral Theorem and robust active vibration control will be studied upon. The disturbances $w(k)$ (due to windage mainly) occur at length x from a
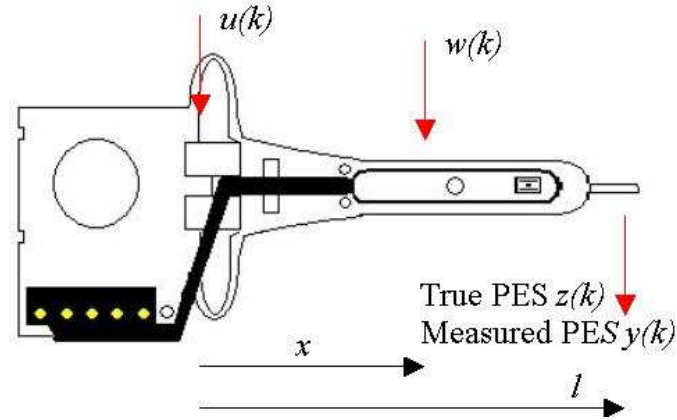
Figure 9.1: Input and output signals of PZT micro-actuator.

PZT micro-actuator of length l and the control input $u(k)$ is injected by the PZT elements at the base of the actuator. The only available signal is measured PES $y(k)$, which is a contaminated version of the true PES $z(k)$ and is

measured at the tip of the PZT microactuator. The moments from $w(k)$ and its effects on $z(k)$ can only be compensated by $u(k)$ at the base. As such, the R/W head and PZT elements are a non-collocated actuator and sensor pair. With these, the following equations hold

$$G(z) = \begin{bmatrix} G_{zw}(z) & G_{zu}(z) \\ G_{yw}(z) & G_{yu}(z) \end{bmatrix} \sim \begin{bmatrix} A & B & D_1 \\ E_1 & 0 & 0 \\ C & 0 & 0 \end{bmatrix} \tag{9.1}$$

$$L(z) = G_{yu}(z)G_c(z) \tag{9.2}$$

$$S(z) = \frac{1}{1 + L(z)} \tag{9.3}$$

$$\tilde{G}_{zw}(z) = S_p(z)S(z) \tag{9.4}$$

and $\tilde{G}_{zw}(z)$ is the closed-loop transfer function from disturbance $w(k)$ from windage on the PZT active suspension to true PES $z(k)$. Theoretical developments on optimal active vibration controller based on spillover transfer function $S_p(z)$ will be carried out and the effectiveness of the synthesized controller $G_c(z)$ will be tested with experiments.

2. SPT with nonlinearity considerations [56][57][62]:

SP design methodologies which involve decomposing system dynamics into fast and slow subsystems on two time scales are known to solve the non-collocated sensor/actuator pair issue which creates non-minimum phase zero dynamics that degrades tracking performance. As such, the stable resonant pole anti-resonant zero pairs in piezoelectric actuators can be used for creating the fast dynamics for inner loop cascade control with SSA [89][87]. Neural networks [62] can be incorporated to compensate for the effects of hysteresis and "creep" commonly encountered in piezoelectric actuators.

3. Iterative control algorithm for low sensitivity servos:

To reduce the positive area under sensitivity transfer function S further, we

observe that

$$\ln S \;=\; \ln |S| + j\angle S \tag{9.5}$$

With $S = \frac{1}{1+L}$ where L is the open loop transfer function, we get

$$
\begin{aligned}
\ln |S| &= \ln \frac{1}{1+L} + j\angle \frac{1}{1+L} \\
&= -\ln(1+L) - j\angle(1+L) \tag{9.6}
\end{aligned}
$$

Parameterizing in terms of controller parameters μ and noting that $L = K(\mu)P$ where K is the controller and P is the plant to be controlled, we can get for the first term on the right hand side as

$$
\begin{aligned}
\ln(1+L) &= L - \frac{L^2}{2} + \frac{L^3}{3} - \cdots \\
&\approx -K(\mu)P + \frac{K(\mu)^2 P^2}{2} \tag{9.7}
\end{aligned}
$$

using Taylor's expansions. A similar approximation expansion can be derived for the second term and hence the logarithmic magnitude of sensitivity transfer function S can be parameterized in terms of current controller $K_i(\mu)$ at each iteration i. An iterative updating control law to ensure fast convergence and closed-loop stability will also be derived and tested.

4. Experimental results for robust decoupling control of MEMS micro X-Y stage:

   Following the fabrication of MEMS micro X-Y stage and development of robust decoupling control scheme with CSSA, the proposed algorithms will be tested on the MEMS micro X-Y stage with integrated recording media after its release from the wafer. Bit indentations with R/W/E operations will be tested on the closed-loop system to obtain bit and track densities. Novel PES coding, encoding and demodulation schemes will also be designed for the proposed probe-based storage system.

Bibliography

[1] D. Abramovitch and G. Franklin, "A Brief History of Disk Drive Control," *IEEE Control Systems Magazine*, Vol. 22, No. 3, pp. 28–42, June 2002.

[2] D. Abramovitch, T. Hurst, and D. Henze, "The PES Pareto Method : Uncovering the Strata of Position Error Signals in Disk Drives," in *Proceedings of the 1997 American Control Conference*, pp. 421–428, Albuquerque, NM, USA, June 4–6, 1997.

[3] J. F. Alfaro and G. Fedder, "Actuation for Probe-Based Mass Data Storage," in *Technical Proceedings of the Fifth International Conference on Modeling and Simulation of Microsystems*, pp. 202–205, San Juan, Puerto Rico, April 22–25, 2002.

[4] A. Al-Mamun, T. H. Lee, G. Guo, W. E. Wong, and W. Ye, "Measurement of Position Offset in Hard Disk Drive using Dual Frequency Servo Bursts," *IEEE Transactions on Instrumentation and Measurement*, Vol. 52, No. 6, pp. 1870–1880, December 2003.

[5] T. Arisaka, T. Shimizu, T. Atsumi, H. Masuda, and T. Yamaguchi, "Development on In-Phase Actuator Mechanism in Hard Disk Drives," in *Proceedings of the Asia-Pacific Magnetic Recording Conference APMRC 2004*, Seoul, Korea, August 16–19, 2004.

[6] K. J. Åström, P. Hagander, and J. Sternby, "Zeros of Sampled Systems," *Automatica*, Vol. 20, No. 1, pp. 31–38, 1984.

[7] K. J. Åström and B. Wittenmark, *Adaptive Control*, Addison-Wesley, 2nd Edition, 1995.

[8] K. J. Åström and B. Wittenmark, *Computer Controlled Systems : Theory and Design*, Prentice Hall, 3rd Edition, 1997.

[9] L. R. Carley, J. A. Main, G. K. Fedder, D. W. Greve, D. F. Guillou, M. S. C. Lu, T. Mukherjee, S. Santhanam, L. Abelmann, and S. Min, "Single-chip Computers with Microelectromechanical Systems-Based Magnetic Memory," *Journal of Applied Physics*, Vol. 87, No. 9, pp. 6680–6685, May 2000.

[10] B. M. Chen, *Robust and H_∞ Control*, Springer-Verlag, New York, London, 2000 (Communications and Control Engineering Series).

[11] B. M. Chen, T. H. Lee, C. -C. Hang, Y. Guo, and S. Weerasooriya, "An H_∞ Almost Disturbance Decoupling Robust Controller Design for a Piezoelectric Bimorph Actuator with Hysteresis", *IEEE Transactions on Control Systems Technology*, Vol. 7, No. 2, pp. 160–174, March 1999.

[12] B. M. Chen, T. H. Lee, K. Peng, and V. Venkataramanan, *Hard Disk Drive Servo Systems*, 2nd Edition, Springer (Advances in Industrial Control Series), New York, 2006.

[13] B. M. Chen, T. H. Lee, and V. Venkataramanan, *Hard Disk Drive Servo Systems*, Springer-Verlag (Advances in Industrial Control Series), New York, London, 2002.

[14] J. Choi, H. Park, K. Y. Kim, and J. U. Jeon, "Electromagnetic Micro x-y Stage for Probe-Based Data Storage," *Journal of Semiconductor Technology and Science*, Vol. 1, No. 1, pp. 84–93, March 2001.

[15] J. E. Dennis and R. B. Schnabel, *Numerical Methods for Unconstrained Optimization and Nonlinear Equations*, Philadelphia, PA: SIAM, 1996.

[16] Z. Y. Dong, C. K. Pang, and P. Zhang, "Power System Sensitivity Analysis for Probabilistic Small Signal Stability Assessment in a Deregulated Environment," *International Journal of Control Automation and Systems (Special Issue on Recent Advances in Power System Control)*, Vol. 3, No. 2 (Special Edition), pp. 355–362, June 2005.

[17] J. C. Doyle, B. A. Francis, and A. R. Tannenbaum, *Feedback Control Theory*, Macmillan, 1992.

[18] C. Du, J. Zhang, and G. Guo, "Vibration Analysis and Control Design Comparison of Fluid Bearing and Ball Bearing HDDs," in *Proceedings of 2002 American Control Conference*, pp. 1380–1385, Anchorage, AK, USA, May 8–10, 2002.

[19] C. Du, L. Xie, G. Guo, J. Zhang, Q. Li, B. Hredzak, and J. N. Teoh, "A Generalized KYP Lemma Based Control Design and Application for 425 kTPI Servo Track Writing," accepted for 2006 American Control Conference, Minneapolis, MN, USA, June 14-16, 2006.

[20] C. Duan, "Robust Periodic Disturbance Compensation via Multirate Control," *M. Eng. Thesis*, National University of Singapore, 2005.

[21] E. Eletheriou, T. Antonakopoulos, G. K. Binning, G. Cherubini, M. Despont, A. Dholakia, U. Dürig, M. A. Lantz, H. Pozidis, H. E. Rothuizen, and P.

Vettiger, "Millipede–A MEMS-Based Scanning-Probe Data-Storage System," *IEEE Transactions on Magnetics*, Vol. 39, No. 2, pp. 938–945, March 2003.

[22] R. Evans, J. Griesbach, and W. Messner, "Piezoelectric Micro-Actuator for Dual-Stage Control," *IEEE Transactions on Magnetics*, Vol. 35, No. 2, pp. 977–982, March 1999.

[23] G. F. Franklin, J. D. Powell, and M. Workman, *Digital Control of Dynamic Systems*, Addison-Weasley, 3rd Edition, 1997.

[24] J. Freudenberg, R. Middleton, and A. Stefanopoulou, "A Survey of Inherent Design Limitations," in *Proceedings of the 2000 American Control Conference*, pp. 2987–3001, Chicago, IL, USA, June 28–30, 2000.

[25] M. I. Friswell and D. J. Inman, "The Relationship Between Positive Position Feedback and Output Feedback Controllers," *Smart Materials and Structures*, Vol. 8, No. 3, pp. 285-291, June 1999.

[26] Fujitsu Company Website [Online], Fujitsu develops HDD Read-Head Technology for 300 Gb/in^2 Densities, *http://pr.fujitsu.com/en/news/2002/05/15-1.htm*, May 2002.

[27] H. Fujita, K. Suzuki, M. Ataka, and S. Nakamura, "A Microactuator for Head positioning System of Hard Disk Drives," *IEEE Transactions on Magnetics*, Vol. 35, No. 2, pp. 1006–1010, March 1999.

[28] K. Glover and D. McFarlane, "Robust Stabilization of Normalized Coprime Factor Plant Descriptions with H_∞ Bounded Uncertainty," *IEEE Transactions on Automatic Control*, Vol. 34, No. 8, pp. 821–830, August 1989.

[29] T. B. Goh, Z. Li, B. M. Chen, T. H. Lee, and T. Huang "Design and Implementation of a Hard Disk Drive Servo System Using Robust and Perfect

Tracking Approach," *IEEE Transactions on Control Systems Technology*, Vol. 9, No. 2, pp. 221–233, March 2001.

[30] G. C. Goodwin, "Predicting the Performance of Soft Sensors as a Route to Low Cost Automation," *Annual Reviewers in Control*, Vol. 24, pp. 55–56, 2000.

[31] E. Grochowski, Hitachi Global Storage Technologies Company Website [Online], *www.hitachigst.com/hdd/hddpdf/tech/hdd_technology2003.pdf*, 2003.

[32] G. Guo, Q. Hao, and T. S. Low, "A Dual-Stage Control Design for High Track Per Inch Hard Disk Drives," *IEEE Transactions on Magnetics*, Vol. 37, No. 2, pp. 860–865, March 2001.

[33] L. Guo, D. Martin, and D. Brunnett, "Dual-Stage Actuator Servo Control for High Density Disk Drives," in *Proceedings of the 1999 IEEE/ASME International Conference on Advanced Intelligent Mechatronics*, pp. 132–137, Atlanta, GA, USA, September 19–23, 1999.

[34] G. Guo, D. Wu, and T. C. Chong, "Modified Dual-Stage Controller for Dealing With Secondary-Stage Actuator Saturation," *IEEE Transactions on Magnetics*, Vol. 39, No. 6, pp. 3587–3592, November 2003.

[35] G. Guo and J. Zhang, "Feedforward Control for Reducing Disk-Flutter-Induced Track Misregistration," *IEEE Transactions on Magnetics*, Vol. 39, No. 6, pp. 2103–2108, July 2003.

[36] Guzik Company Website [Online], Spin Stand Products Information,*http://www.guzik.com*, 2006.

[37] Q. Hao, R. Chen, G. Guo, S. Chen, and T. S. Low, "A Gradient-Based Track-Following Controller Optimization for Hard Disk Drive," *IEEE Transactions on Industrial Electronics*, Vol. 50, No. 1, pp. 108–115, February 2003.

[38] Z. He, E. H. Ong, and G. Guo, "Optimization of a Magnetic Disk Drive Actuator with Small Skew Actuation," *Journal of Applied Physics* Vol. 91, No. 10, pp. 8709–8711, May 2002.

[39] G. Herrmann and G. Guo, "HDD Dual-Stage Servo-Controller Design Using a μ-Analysis Tool," *Control Engineering Practice*, Vol. 12, No. 3, pp. 241–251, March 2004.

[40] T. Hirano, L. Fan, W. Lee, J. Hong, W. Imaino, S. Pattanaik, S. Chan, P. Webb, R. Horowitz, S. Aggarwal, and D. Horsley, "High Bandwidth High Accuracy Rotary Microactuator for Magnetic Hard Disk Drive Tracking Servos," *IEEE/ASME Transactions on Mechatronics*, Vol. 3, No. 3, pp.156–165, September 1998.

[41] H. Hjalmarsson, M. Gevers, S. Gunnarsson, and O. Lequin, "Iterative Feedback Tuning: Theory and Applications," *IEEE Control Systems Magazine*, Vol. 18, No. 4, pp. 26–41, August 1998.

[42] J. Hong and D. S. Bernstein, "Bode Integral Constraints, Colocation, and Spillover in Active Noise and Vibration Control," *IEEE Transactions on Control Systems Technology*, Vol. 6, No. 1, pp. 111–120, January 1998.

[43] R. Horowitz and B. Li, "Adaptive Track-Following Servos for Disk File Actuators," *IEEE Transactions on Magnetics*, Vol. 32, No. 3, pp. 1779–1786, May 1996.

[44] F. Y. Huang, W. Imaino, F. Lee, and T. Semba, "Active Damping in HDD actuator," *IEEE Transactions on Magnetics*, Vol. 37, No. 2, pp. 847–849, March 2001.

[45] P. A. Ioannou, E. B. Kosmatopoulos, and A. M. Despain, "Position Error Signal Estimation at High Sampling Rates Using Data and Servo Sector Measurements," *IEEE Transactions on Control Systems Technolgy*, Vol. 11, No. 3, pp. 325–334, May 2003.

[46] *IEEE Standard on Piezoelectricity*, ANSI/IEEE Standard 176, 1987.

[47] IBM Company Website [Online], Limits of Magnetic Recording, *http://www.almaden.ibm.com/st/projects/limits*, May 2002.

[48] Q. W. Jia, F. C. Cai, and Z. F. Wang "Repeatable Runout Disturbance Compensation with a New Data Collection Method for Hard Disk Drive," *IEEE Transactions on Magnetics*, Vol. 41, No. 2, pp. 791–796, February 2005.

[49] C. -I. Kang and C. -H. Kim, "An Adaptive Notch Filter for Suppressing Mechanical Resonance in High Track Density Disk Drives," *Microsystem Technologies* Vol. 11, No. 8, pp. 638–652, August 2005.

[50] M. Karaman and W. C. Messner, "Robust Dual-Stage HDD Track Follow Control Systems Design for Hand Off Shaping," in *Digest of the 2002 Asia-Pacific Magnetic Recording Conference*, pp. BA5-01–BA5-02, Singapore, August 27–29, 2002.

[51] C. Kim and Y. -K. Kim, "Micro XY-Stage using Silicon on a Glass Substrate," *Journal of Micromechanics and Microengineering*, Vol. 12, No. 2, pp. 103–107, March 2002.

[52] M. Kobayashi, S. Nakagawa, T. Atsumi and T. Yamaguchi, "High Bandwidth Servo Control Designs for Magnetic Disk Drives," in *Proceedings of the 2001 IEEE/ASME International Conference on Advanced Intelligent Mechatronics*, Vol. 2, pp. 1124–1129, Como, Italy, July 8–12, 2001 .

[53] M. Kobayashi, S. Nakagawa, and S. Nakamura, "A Phase-Stabilized Servo Controller for Dual-Stage Actuators in Hard-Disk Drives," *IEEE Transactions on Magnetics*, Vol. 39, No. 2, pp. 844–850, March 2003.

[54] M. Kobayashi, T. Yamaguchi, T. Yoshida, and H. Hirai, "Multi-Sensing Servo with Carriage-Acceleration Feedback for Magnetic Disk Drives," in *Proceedings of the 1998 American Control Conference*, pp. 3038–3042, Philadelphia, PA, USA, June 24–26, 1998.

[55] S. Koganezawa, K. Takashi, Y. Uematsu, T. Yamada, S. Hasegawa, and T. Ueno, "A Flexural Piggyback Milli-Actuator for Over 5 GBit/in^2 Density Magnetic Recording," *IEEE Transactions on Magnetics*, Vol. 32, No. 5, pp. 3908–3910, September 1996.

[56] P. V. Kokotović, "Applications of Singular Perturbation Techniques to Control Problems," *SIAM Review*, Vol. 26, No. 4, pp. 501–550, October 1984.

[57] P. V. Kokotović, H. K. Khalil, and J. O'Reilly, *Singular Perturbation Methods in Control: Analysis and Design*, Academic Press, London, 1986.

[58] H. S. Lee, "Controller Optimization for Minimum Position Error Signals of Hard Disk Drives," *IEEE Transactions on Industrial Electronics*, Vol. 48, No. 5, pp. 945–950, October 2001.

[59] S. -H. Lee, C. C. Chung, and C. W. Lee, "High Frequency Vibration Rejection in Hard Disk Drives," in *Proceedings of the 2003 JSME-IIP/ASME-ISPS Joint MIPE'03*, MC-10, pp. 24–25, Yokohama, Japan, June 16–18, 2003.

[60] R. Legtenberg, A. W. Groeneveld, and M. Elwenspoek, "Comb-drive Actuators for Large Displacement," *Journal of Micromechanics and Microengineering*, Vol. 6, No. 3, pp. 320–329, September 1996.

[61] F. L. Lewis, *Applied Optimal Control & Estimation*, Prentice-Hall International Inc., New Jersey, 1992.

[62] F. L. Lewis, S. Jagannathan and A. Yeşildirek, *Neural Network Control of Robot Manipulators and Nonlinear Systems*, Taylor and Francis, London, 1999.

[63] C. Li, "Design and Implementation of Position Error Signals for Probe-based Storage Systems," *B. Eng. Thesis*, National University of Singapore, 2005.

[64] Z. Li, G. Guo, B. M. Chen, and T. H. Lee "Optimal Track-Following Design for the Highest Tracks per Inch in Hard Disk Drives," *Journal of Information Storage and Processing Systems*, Vol. 3, No. 1–2, pp. 27–41, April 2001.

[65] Y. Li, R. Horowitz, and R. Evans, "Vibration Control of a PZT Actuated Suspension Dual-Stage Servo System Using a PZT Sensor," *IEEE Transactions on Magnetics*, Vol. 39, No. 2, pp. 932–937, March 2003.

[66] Z. Lin and B. M. Chen, "Solutions to General H_∞ Almost Disturbance Decoupling Problem with Measurement Feedback and Internal Stability for Discrete-Time Systems," *Automatica*, Vol. 36, pp. 1103–1122, 2000.

[67] L. Ljung, *System Identification: Theory for the User*, Prentice Hall, 2nd Edition, 1999.

[68] Y. Lou, P. Gao, B. Qin, G. Guo, E. H. Ong, A. Takada and K. Okada, "Dual-Stage Servo with On-Slider PZT Microactuator for Hard-Disk Drives," *IEEE Transactions on Magnetics*, Vol. 38. No. 5, pp. 2183–2185, September 2002.

[69] M. S. -C. Lu and G. K. Fedder, "Position Control of Parallel-Plate Microactuators for Probe-Based Data Storage," *Journal of Microelectromechanical Systems*, Vol. 13, No. 5, pp. 759–769, October 2004.

[70] Y. Lu, C. K. Pang, J. Chen, H. Zhu, J. P. Yang, J. Q. Mou, G. Guo, B. M. Chen, and T. H. Lee, "Design, Fabrication and Control of a Micro X-Y Stage with Large Ultra-Thin Film Recording Media Platform," in *Proceedings of the 2005 IEEE/ASME International Conference on AIM*, MA1-04, pp. 19–24, Monterey, CA, USA, July 24–28, 2005.

[71] D. H. S. Maithripala, J. M. Berg, and W. P. Dayawansa, "Control of an Electrostatic Microelectromechanical System Using Static and Dynamic Output Feedback," *Transactions of the ASME G: Journal of Dynamic Systems Measurement and Control*, Vol. 127, No. 3, pp. 443–450, September 2005.

[72] H. J. Maminm, B. D. Terris, L. S. Fan, S. Hoen, R. C. Barrett, and D. Rugar, "High-Density Data Storage using Proximal Probe Techniques," *IBM Journal of Research and Development*, Vol. 39, No. 6, pp. 681–700, November 1995.

[73] Maxtor Company Website [Online], PC Storage Solutions, *http://www.maxtor.com/en/solutions/enterprise/desktop_computing-/pc_storage/index.htm*, January 2003.

[74] W. Messner and R. Ehrlich, "A Tutorial on Controls for Disk Drives," in *Proceedings of the 2001 American Control Conference*, pp. 408–420, Arlington, VA, June 25–27, 2001.

[75] S. O. R. Moheimani, "A Survey of Recent Innovations in Vibration Damping and Control Using Shunted Piezoelectric Transducers," *IEEE Transactions on Control Systems Technology*, Vol. 11, No. 4, pp. 482–494, July 2003.

[76] C. Mohtadi, "Bode's Integral Theorem for Discrete-Time Systems," *IEE Proceedings*, Vol. 137, Pt. D., No. 2, pp. 57–66, March 1990.

[77] S. Nakagawa, M. Kobayashi, and T. Yamaguchi, "A Higher Bandwidth Servo Design with Strain Feedback Control for Magnetic Disk Drives," in *Proceedings of the 2003 American Control Conference*, pp. 2547–2552, Denver, CO, USA, June 4–6, 2003.

[78] I. Naniwa, S. Nakamura, S. Saegusa, and K. Sato, "Low Voltage Driven Piggy-Back Actuator of Hard Disk Drives," in *Proceedings of the 12th IEEE Micro-Electro-Mechanical-Systems Conference*, pp. 49–52, Orlando, FL, USA, January 17–21, 1999.

[79] Nano Scale Servo [Online], *http://mizugaki.iis.u-tokyo.ac.jp/nss/* (in Japanese).

[80] NHK Spring: Precision Springs and Components Division [Online], *http://info-sec.nhkspg.co.jp/eng/prod/disk.html*.

[81] K. Ohnishi, "A New Servo Method in Mechatronics," *Transactions of the Japanese Society of Electrical Engineering*, Vol. 107-D, pp. 83–86, 1987.

[82] C. K. Pang, "Vibration Analysis and Control in Hard-Disk Drives Servo Systems," *M. Eng. Thesis*, National University of Singapore, 2003.

[83] C. K. Pang, Z. Y. Dong, P. Zhang, and X. Yin, "Probabilistic Analysis of Power System Small Signal Stability Region," in *Proceedings of 2005 IEEE ICCA*, pp. 503–509, Budapest, Hungary, June 27–29, 2005.

[84] C. K. Pang, G. Guo, B. M. Chen, and T. H. Lee, "Enhanced Disturbance Suppression in Sampled-Data Systems and its Applications to High Density Data

Storage Servos," in *Proceedings of the 2006 ASME/JSME Joint Conference on MIPE*, S34_04, Santa Clara, CA, USA, June 21-23, 2006.

[85] C. K. Pang, G. Guo, B. M. Chen, and T. H. Lee, "Enhanced Disturbance Suppression in Sampled-Data Systems and its Applications to High Density Data Storage Servos," *Microsystem Technologies*, in press.

[86] C. K. Pang, G. Guo, B. M. Chen, and T. H. Lee, "Nanoposition Sensing and Control in HDD Dual-Stage Servo Systems," in *Proceedings of 2004 IEEE International CCA*, pp. 551–556, Taipei, Taiwan, September 2–4, 2004.

[87] C. K. Pang, G. Guo, B. M. Chen, and T. H. Lee, "Self-Sensing Actuation for Nanopositioning and Active-Mode Damping in Dual-Stage HDDs," *IEEE/ASME Transactions on Mechatronics*, Vol. 11, No. 3, pp. 328–338, June 2006.

[88] C. K. Pang, F. L. Lewis, S. S. Ge, G. Guo, B. M. Chen, and T. H. Lee, "Singular Perturbation Control for Vibration Rejection with a PZT Active Suspension," in *Proceedings of the 45th IEEE CDC*, FrIP12.14, pp. 6599–6604, San Diego, CA, USA, December 13–15, 2006.

[89] C. K. Pang, F. L. Lewis, S. S. Ge, G. Guo, B. M. Chen, and T. H. Lee, "Singular Perturbation Control for Vibration Rejection with a PZT Active Suspension as Fast Subsystem Observer", *IEEE Transactions on Industrial Electronics*, in press.

[90] C. K. Pang, E. H. Ong, and G. Guo, "Experimental Dynamic Modeling and Characterizations of Disk Platter Resonances," in *Digest of Technical Papers IEEE International INTERMAG Europe*, BS–12, Amsterdam, The Netherlands, April 28–May 2, 2002.

[91] C. K. Pang, S. C. Tam, G. Guo, B. M. Chen, F. L. Lewis, and T. H. Lee, "Improved Disturbance Rejection with Online Adaptive Pole-Zero Compensation on a Φ-Shaped PZT Active Suspension," submitted to 2007 ISPS, February 2007.

[92] C. K. Pang, W. E. Wong, G. Guo, B. M. Chen, and T. H. Lee, "NRRO Rejection using Online Iterative Control for High Density Data Storage," *IEEE Transactions on Magnetics*, in press.

[93] C. K. Pang, W. E. Wong, G. Guo, B. M. Chen, and T. H. Lee, "NRRO Rejection using Online Iterative Control for High Density Data Storage on a PC-Based Spinstand Servo System," to be presented at the 2007 ACC, New York City, NY, USA, July 11-13, 2007.

[94] C. K. Pang, D. Wu, G. Guo, T. C. Chong, and Y. Wang, "Suppressing Sensitivity Hump in HDD Dual Stage Servo Systems," in *Proceedings of 2003 JSME-IIP/ASME-ISPS Joint MIPE*, MC–11, pp. 26–27, Yokohama, Japan, June 16–18, 2003.

[95] C. K. Pang, D. Wu, G. Guo, T. C. Chong, and Y. Wang, "Suppressing Sensitivity Hump in HDD Dual Stage Servo Systems," *Microsystem Technologies*, Vol. 11, No. 8–10, pp. 653–662, August 2005.

[96] A. Pantazi, M. A. Lantz, G. Cherubini, H. Pozidis, and E. Eleftheriou, "A Servomechanism for a Micro-Electro-Mechanical-System based Scanning-Probe Data Storage Device," *Nanotechnology*, Vol. 15, No. 10, S612–S621, October 2004.

[97] S. W. Park, J. Jeong, H. S. Yang, Y. P. Park, and N. C. Park, "Repetitive Controller Design for Minimum TMR in HDD," *IEEE Transactions on Magnetics*, Vol. 41, No. 9, pp. 2522–2528, September 2005.

[98] H. Park, J. Jung, D.-K. Min, S. Kim, S. Hong, and H. Shin, "Scanning Resistive Probe Microscopy: Imaging Ferroelectric Domains," *Applied Physics Letters*, Vol. 84, No. 10, pp. 1734–1736, March 2004.

[99] K. Peng, B. M. Chen, T. H. Lee, and V. Venkataramanan, "Design and Implementation of a Dual-stage Actuated HDD Servo System via Composite Nonlinear Control Approach," *Mechatronics*, Vol. 14, No. 9, pp. 965–988, September 2004.

[100] H. Podizis, Private Communication, A*STAR Data Storage Institute, Singapore, 2006.

[101] M. Rakowski, Transfer Function Approach to Disturbance Decoupling Problem, *Linear Algebra for Control Theory*, Springer-Verlag, New York, 1994.

[102] A. Saberi, P. Sannuti, and B. M. Chen, H_2 *Optimal Control*, Prentice Hall International (UK) Limited, 1995.

[103] A. Saberi, B. M. Chen and P. Sannuti, *Loop Transfer Recovery: Analysis and Design*, Springer, London, 1993.

[104] A. H. Sacks, "Position Signal Generation in Magnetic Disk Drives", *Ph.D. Thesis*, Carnegie Mellon University, 1995.

[105] S. J. Schroeck, W. C. Messner, and R. J. McNab, "On Compensator Design for Linear Time Invariant Dual-Input Single-Output Systems", *IEEE/ASME Transactions on Mechatronics*, Vol. 6, No. 1, pp. 50-57, March 2001.

[106] T. Semba, T. Hirano, J. Hong, and L-S. Fan, "Dual-Stage Servo Controller for HDD using MEMS Microactuator," *IEEE Transactions on Magnetics*, Vol. 35, No. 5, pp. 2271–2273, September 1999.

[107] Y. Soeno, S. Ichikawa, T. Tsuna, Y. Sato, and I. Sato, "Piezoeletric Piggy-Back Microactuator for Hard Disk Drive," *IEEE Transactions on Magnetics*, Vol. 35, No. 2., pp. 983-987, March 1999.

[108] S. Skogestad and I. Postlethwaite, *Multivariable Feedback Control: Analysis and Design*, John Wiley & Sons Ltd., 1996.

[109] M. Sri-Jayantha, A. Sharma, H. Dang, and H. Suzuki, "Repeatable Runout Free Servo Architecture in Direct Access Storage Device," *United States Patent*, Patent Number 6097565, August 1, 2000.

[110] M. Tomizuka, "Zero Phase Error Tracking Algorithm for Digital Control," *Journal of Dynamic Systems, Measurement and Control, Transactions of the ASME*, Vol. 109, pp. 65–68, March 1987.

[111] M. Tokuyama, T. Shimizu, M. Masuda, S. Nakamura, M. Hanya, O. Iriuchijima, and J. Soga, "Development of a Φ-Shaped Actuated Suspension for 100 kTPI Hard-Disk Drives," *IEEE Transactions on Magnetics*, Vol. 37, No. 4, pp. 1884–1886, July 2001.

[112] H. Uchida and T. Semba, "A Study of the Residual Vibration During the Seek-Settling Period for Hard Disk Drives," in *Digest of the 2000 Asia-Pacific Magnetic Recording Conference*, pp. MP19-1–MP19-2, Tokyo, Japan, November 6–8, 2000.

[113] V. Venkataramanan, K. Peng, B. M. Chen, and T. H. Lee, "Discrete-Time Composite Nonlinear Feedback Control With an Application in Design of a Hard Disk Drive Servo System," *IEEE Transctions on Control Systems Technology*, Vol. 11, No. 1, pp. 16–23, January 2003.

[114] P. Vettiger *et al.*, "The 'Millipede'—Nanotechnology Entering Data Storage," *IEEE Transctions on Nanotechnology*, Vol. 1, No. 1, pp. 39–55, March 2002.

[115] P. Vettiger and G. K. Binnig, "The Nanodrive Project," *Scientific American*, Vol. 228, No. 1, pp.46–53, January 2003.

[116] P. Vettiger, M. Despont, U. Drechsler, U. Dürig, W. Häberle, M. I. Lutwyche, H. E. Tothuizen, R. Stutz, R. Widmer, and G. K. Binnig, "The "Millipede"– More Than One Thousand Tips for Future AFM Data Storage," *IBM Journal of Research and Development*, Vol. 44, No. 3, pp. 323–340, May 2000.

[117] M. T. White and W. Lu, "Hard Disk Drive Bandwidth Limitations due to Sampling Frequency and Computational Delay," in *Proceedings of the 1999 IEEE/ASME International Conference on Advanced Intelligent Mechatronics*, pp. 120–125, Atlanta, GA, USA, September 19–23, 1999.

[118] M. T. White, M. Tomizuka, and C. Smith, "Improved Track Following in Magnetic Disk Drives using a Disturbance Observer," *IEEE/ASME Transactions on Mechatronics* Vol. 5, pp. 3–11, No. 1, March 2000.

[119] B. Widrow and E. Walach, *Adaptive Inverse Control*, Prentice Hall, 1996.

[120] W. E. Wong, L. Feng, Z. He, J. Liu, C. M. Kan, and G. Guo, "PC-Based Position Error Signal Generation and Servo System for a Spinstand," *IEEE Transactions on Magnetics*, Vol. 41, No. 11, pp. 4315–4322, November 2005.

[121] W. E. Wong, G. Guo, A. Al-Mamum, W. Ye, and J. Zhang, "Detection of Track Misregistration within User Data Channel," US Application no. 10/888,493, filed on 09 Jul 2004 (priority Singapore Patent Application No. 200304108-4 filed 10 July 2003).

[122] R. W. Wood, J. Miles, and T. Olson, "Recording Technologies for Terabit per Square Inch Systems," *IEEE Transactions on Magnetics*, Vol. 38, No. 4, pp. 1711–1718, July 2002.

[123] D. Wu, "Study on High Performance Dual-Stage Servomechanism in Hard-Disk Drives," *Ph. D. Thesis*, National University of Singapore, 2002.

[124] D. Wu, G. Guo, and T. C. Chong, "Adaptive Compensation of Microactuator Resonance in Hard Disk Drives," *IEEE Transactions on Magnetics*, Vol. 36, No. 5, pp. 2247–2250, September 2000.

[125] D. Wu, G. Guo, and T. C. Chong, "Midfrequency Disturbance Suppression via Micro-Actuator in Dual-Stage HDDs," *IEEE Transactions on Magnetics*, Vol. 38, No. 5, pp. 2189–2191, September 2002.

[126] B. Wu and E. Jonckheere, "A Simplified Approach to Bode's Theorem for Continuous-Time and Discrete-Time Systems," *IEEE Transactions on Automatic Control*, Vol. 36, No. 11, pp. 1797–1802, November 1992.

[127] Z. Xu, Z. Y. Dong, and C. K. Pang, "Spinning Reserve Procurement in an Integrated Energy and Ancillary Market," in *Proceedings of AUPEC'03*, Paper 71, Christchurch, New Zealand, September 28–October 1, 2003.

[128] H. Yamada, M. Sasaki, and Y. Nam, "Control of a Micro-Actuator for Hard-Disk Drives Using Self-Sensing," in *Proceedings of the 8th IEEE International Workshop on Advanced Motion Control*, pp. 147–152, Kawasaki, Japan, March 25–28, 2004.

[129] T. Yamaguchi, H. Numasato, and H. Hirai, "A Mode-Switching Control for Motion Control and its Application to Disk Drives: Design of Optimal Mode-Switching Conditions," *IEEE/ASME Transactions on Mechatronics* Vol. 3, No. 3, pp. 202–209, September 1998.

[130] H. Ye, V. Sng, C. Du, J. Zhang, and G. Guo, "Radial Error Propagation Issues in Self-Servo Track Writing Technology," *IEEE Transactions on Magnetics*, Vol. 38, No. 5, pp. 2180–2812, September 2002.

[131] Z. Zhang *et al.*, "Magnetic Recording Demonstration Over 100 Gb/in^2," *IEEE Transactions on Magnetics*, Vol. 38, No. 5, pp. 1861–1866, September 2002.

[132] K. Zhou and J. C. Doyle, *Essentials of Robust Control*, Prentice Hall, September 1997.

[133] K. Zhou, J. C. Doyle, and K. Glover, *Robust and Optimal Control*, Prentice Hall, 1996.

List of Publications

The research work related to this dissertation resulted in the following publications:

a) International refereed journals

1. C. K. Pang, G. Guo, B. M. Chen, and T. H. Lee, "Enhanced Disturbance Suppression in Sampled-Data Systems and its Applications to High Density Data Storage Servos," *Microsystem Technologies*, in press.

2. C. K. Pang, W. E. Wong, G. Guo, B. M. Chen, and T. H. Lee, "NRRO Rejection using Online Iterative Control for High Density Data Storage," *IEEE Transactions on Magnetics*, in press.

3. C. K. Pang, F. L. Lewis, S. S. Ge, G. Guo, B. M. Chen, and T. H. Lee, "Singular Perturbation Control for Vibration Rejection with a PZT Active Suspension as Fast Subsystem Observer", *IEEE Transactions on Industrial Electronics*, in press.

4. C. K. Pang, G. Guo, B. M. Chen, and T. H. Lee, "Self-Sensing Actuation for Nanopositioning and Active-Mode Damping in Dual-Stage HDDs," *IEEE/ASME Transactions on Mechatronics*, Vol. 11, No. 3, pp. 328–338, June 2006.

b) Invited sessions

1. C. K. Pang, G. Guo, B. M. Chen, and T. H. Lee, "Nanoposition Sensing and Control in HDD Dual-Stage Servo Systems," Invited Session on Control

of Disk Drive Storage System, presented at IEEE Joint CCA/ISIC/CACSD 2004, Taipei, Taiwan, September 2, 2004.

c) International conferences

1. C. K. Pang, W. E. Wong, G. Guo, B. M. Chen, and T. H. Lee, "NRRO Rejection using Online Iterative Control for High Density Data Storage on a PC-Based Spinstand Servo System," to be presented at the 2007 ACC, New York City, NY, USA, July 11-13, 2007.

2. C. K. Pang, F. L. Lewis, S. S. Ge, G. Guo, B. M. Chen, and T. H. Lee, "Singular Perturbation Control for Vibration Rejection with a PZT Active Suspension," in *Proceedings of the 45th IEEE CDC*, FrIP12.14, pp. 6599–6604, San Diego, CA, USA, December 13–15, 2006.

3. C. K. Pang, G. Guo, B. M. Chen, and T. H. Lee, "Enhanced Disturbance Suppression in Sampled-Data Systems and its Applications to High Density Data Storage Servos," in *Proceedings of the 2006 ASME/JSME Joint Conference on MIPE*, S34_04, Santa Clara, CA, USA, June 21-23, 2006.

4. Y. Lu, C. K. Pang, J. Chen, H. Zhu, J. P. Yang, J. Q. Mou, G. Guo, B. M. Chen, and T. H. Lee, "Design, Fabrication and Control of a Micro X-Y Stage with Large Ultra-Thin Film Recording Media Platform," in *Proceedings of the 2005 IEEE/ASME International Conference on AIM*, MA1-04, pp. 19–24, Monterey, CA, USA, July 24–28, 2005.

5. C. K. Pang, G. Guo, B. M. Chen, and T. H. Lee, "Nanoposition Sensing and Control in HDD Dual-Stage Servo Systems," in *Proceedings of 2004 IEEE International CCA*, pp. 551–556, Taipei, Taiwan, September 2–4, 2004.

His other publications include:

a) International refereed journals

1. C. K. Pang, D. Wu, G. Guo, T. C. Chong, and Y. Wang, "Suppressing Sensitivity Hump in HDD Dual Stage Servo Systems," *Microsystem Technologies*, Vol. 11, No. 8–10, pp. 653–662, August 2005.

2. Z. Y. Dong, C. K. Pang, and P. Zhang, "Power System Sensitivity Analysis for Probabilistic Small Signal Stability Assessment in a Deregulated Environment," *International Journal of Control Automation and Systems (Special Issue on Recent Advances in Power System Control)*, Vol. 3, No. 2 (Special Edition), pp. 355–362, June 2005.

b) International conferences

1. C. K. Pang, S. C. Tam, G. Guo, B. M. Chen, F. L. Lewis, and T. H. Lee, "Improved Disturbance Rejection with Online Adaptive Pole-Zero Compensation on a Φ-Shaped PZT Active Suspension," submitted to 2007 ISPS, February 2007.

2. C. K. Pang, Z. Y. Dong, P. Zhang, and X. Yin, "Probabilistic Analysis of Power System Small Signal Stability Region," in *Proceedings of 2005 IEEE ICCA*, pp. 503–509, Budapest, Hungary, June 27–29, 2005.

3. Z. Xu, Z. Y. Dong, and C. K. Pang, "Spinning Reserve Procurement in an Integrated Energy and Ancillary Market," in *Proceedings of AUPEC'03*, Paper 71, Christchurch, New Zealand, September 28–October 1, 2003.

4. C. K. Pang, D. Wu, G. Guo, T. C. Chong, and Y. Wang, "Suppressing Sensitivity Hump in HDD Dual Stage Servo Systems," in *Proceedings of 2003*

JSME-IIP/ASME-ISPS Joint MIPE, MC–11, pp. 26–27, Yokohama, Japan, June 16–18, 2003.

5. C. K. Pang, E. H. Ong, and G. Guo, "Experimental Dynamic Modeling and Characterizations of Disk Platter Resonances," in *Digest of Technical Papers IEEE International INTERMAG Europe*, BS–12, Amsterdam, The Netherlands, April 28–May 2, 2002.